Field tuning of spin dynamics in low dimensional Ising-like quantum magnets probed by neutron scattering

Leonie Woodland

Lincoln College

University of Oxford

A thesis submitted for the degree of

Doctor of Philosophy

Trinity 2024

Acknowledgements

I would like to thank all of the people who made this work possible, whether by their contributions to the work itself or by their support and guidance.

First and foremost, my supervisor Radu Coldea, for teaching me so much about neutron scattering and quantum magnetism and for his kindness, generosity with his time and copious feedback. The experiments and analysis in this thesis would not have been possible without many collaborators. I would like to thank Dharmalingam Prabhakaran for the synthesis of the $CoNb_2O_6$ samples and Ryutaro Okuma for growing and coaligning the $Na_2BaCo(PO_4)_2$ samples, and David Macdougal, Ivelisse Cabrera, Jordan Thompson, Robert Bewley and Mark Telling, alongside Radu Coldea again, for taking the data analysed in several chapters of this thesis. I am grateful to the instrument scientists at the ISIS Neutron and Muon source — Christian Balz and Ross Stewart on LET and Dmitry Khalyavin, Pascal Manuel and Fabio Orlandi on WISH — without whom data could not have been taken. Thanks also to all the technicians at ISIS who helped the experiments run smoothly. I wish to thank Izabella Lovas and Leon Balents for their significant contributions to the $CoNb_2O_6$ in low transverse field project including their insightful theoretical models. Thanks also to Michele Fava for very helpful discussions about his exact diagonalization code, to Cristian Batista for his suggestion of using biquadratic exchange to stabilize more collinear phases in simulations of $Na_2BaCo(PO_4)_2$, and to Alexander Chernyshev for useful comments on the exposition of the refined Hamiltonian for $CoNb_2O_6$.

I would also like to thank the various past and present members of the group who have taught me skills I have used in this thesis and during my DPhil. Thanks to Kylie MacFarquharson and Amalia Coldea for teaching me to use the Physical Property Measurement System, Hwanbeom Cho for teaching me to use the x-ray diffractometers and to refine diffraction data with Fullprof, Matthew Pearce for teaching me about cryogenics and dilution fridges and Daniel Antoniou for teaching me to handle gas cylinders. Outside of my group, thanks to Pascal Manuel for teaching me to use Jana.

I am grateful to everyone who has made my DPhil enjoyable. Thanks go to the various occupants of Clarendon 107 over the years and especially Viviane Peçanha-Antonio and Siobhan Tobin for their support and encouragement. Thanks to Daniel

Antoniou, Matthew Steggles, Matthew Pearce and Charles Godfrey for keeping me supplied with tea and biscuits, to Andrew Boothroyd for inviting me to tea with his group, and to everyone else who has made the Clarendon an enjoyable place to work including but not limited to Miska Elliot, Koushik Karmakar, Kylie Macfarquharson, Archie Morfoot, John Pearce, Hiroto Takahashi and Hank Wu.

In the world outside of the physics department, thanks go to the members of the institution that is (online) boardgames night — Jack McIntyre, Daniel Sherlock and Julia Stadlmann — for being a weekly point of socialising throughout my DPhil, even in the middle of lockdown. Thanks also to the extended quiz chat community, for general support and endless supplies of animal photos and to the Oxford Singers for being so welcoming and brightening my Thursday evenings. I am very grateful to my parents and step-parents and my grandmother for their endless support and for having always encouraged my interest in science. And last but by no means least, thanks to Jacob Robertson for everything from late night pasta to detailed theoretical discussions and for being a brilliant friend, flatmate and undergraduate lab partner.

I acknowledge graduate scholarship funding from the Oxford-John and Pat Cuckney Graduate Scholarship from Lincoln College and the University of Oxford, and from the European Research Council under the European Union's Horizon 2020 research and innovation programme, Grant Agreement Number 788814 (EQFT), with my thesis supervisor as Principal Investigator.

Abstract

This thesis presents inelastic neutron scattering (INS) studies of spin dynamics in two different Ising-like quantum magnetic materials as a function of applied magnetic field.

The first material explored is the ferromagnetic Ising chain $CoNb_2O_6$. The excitations in an Ising chain are independent domain wall quasiparticles, however, additional interactions beyond pure one-dimensional Ising exchange can lead to the formation of a variety of bound states in different regimes of applied magnetic field. The excitations in $CoNb_2O_6$ are first studied as a function of applied near-longitudinal field. This causes domain walls to become confined into bound states, with the confinement potential tuned by the applied field, from the limit of weak field where there is a Zeeman ladder of bound states to strong field where only two remain. Next, a quantum spin Hamiltonian is refined based on a global fit to the spectrum observed in zero field and in high field applied along two orthogonal directions. A novel method is developed using a combination of linear spinwave theory and exact diagonalization on finite chains to capture the observed bound states as well as the weak interactions between the different chains. Calculations using the refined Hamiltonian quantitatively reproduce not only the spectra to which the data were fit, but also the rich behaviour observed in low transverse field. An intuitive physical picture and fully analytically solved model is proposed for this behaviour based on novel bound states stabilized by the competition between an off-diagonal exchange and transverse field. Finally, the magnetization of $CoNb_2O_6$ is measured as a function of field up to 16 T, observing evidence for the proximity to the expected transverse-field induced quantum critical point.

The other material studied in this thesis is the frustrated triangular lattice quantum Ising-like antiferromagnet $Na_2BaCo(PO_4)_2$, whose spectrum is measured using INS as a function of transverse field. In high field, sharp magnons are observed and a spin Hamiltonian is refined based on the observed magnon dispersions. At fields below the transition to the field polarized phase, strong continuum scattering is observed, which dominates at low fields where no magnons are observed. The observed spectrum cannot be explained even qualitatively at low field using a linear spinwave approach including one and two magnon excitations.

Contents

List of Figures

1 Introduction

This thesis presents studies of spin dynamics in two different Ising-like quantum magnetic materials as a function of applied magnetic field. The materials both have low dimensional magnetic interactions, with $CoNb_2O_6$ being a ferromagnetic spin chain material, while $Na_2BaCo(PO_4)_2$ is a triangular lattice antiferromagnet. The main technique used to study these materials is single crystal inelastic neutron scattering, which is used to reveal information about their magnetic excitations.

The next chapter — Chapter 2 — introduces the ideas in quantum magnetism that will be of relevance to this thesis. First, single-ion physics is discussed, followed by an overview of some key ideas that will be discussed in this thesis: quantum phase transitions, frustration and fractionalization. Next the physics of Ising-like chains and of triangular lattice antiferromagnets is discussed in more detail, and finally the key analytical techniques which will be used — linear spinwave theory and exact diagonalization — are discussed. Chapter 3 then introduces the experimental techniques of neutron scattering as well as vibrating sample magnetometry.

Chapters 4 to 7 report experimental and theoretical results on the ferromagnetic Ising chain material $CoNb_2O_6$. The Ising chain realizes the fundamental paradigm of spin fractionalization, where locally flipping a spin creates two independent domain wall quasiparticles that can separate apart at no energy cost. However, additional

interactions beyond pure one-dimensional Ising exchange can lead to the formation of a variety of bound states in different regimes of applied magnetic field.

In Chapter 4, the regime of $CoNb_2O_6$ in near-longitudinal (along Ising axis) magnetic field is explored. In this regime, the applied field acts as an effective linear potential in the separation between domain walls, confining them together into a series of bound states, and tuning the applied field tunes this effective potential. Using high-resolution single crystal inelastic neutron scattering, the evolution of the spectrum is directly observed. In the regime of very weak confinement at low field, a Zeeman ladder of many closely spaced bound states with energies scaling as the field strength to the power 2/3 is observed, while in the regime of very strong confinement at high field, the spectrum consists of a magnon and a dispersive two-magnon bound state, with a linear field dependence. At intermediate fields, the crossover between these two regimes and the disappearance of the higher-order bound states from the spectrum is explored.

Next, in Chapter 5, a quantum spin Hamiltonian for $CoNb_2O_6$ is refined based on a global fit to the spectrum observed in zero field and in high field applied along two orthogonal directions. A novel method is developed using a combination of linear spinwave theory (LSWT) and exact diagonalization (ED) on finite chains to capture the observed bound states as well as the weak interactions between the different chains. The interchain couplings are first quantitatively parameterized using LSWT in the regime of high applied field, where LSWT is expected to capture the interchain dispersions well. A global fit is then performed to the observed spectrum in zero field and high field applied along two orthogonal directions corrected for interchain dispersion, using exact diagonalization methods for a 1D chain. A refined single-chain and interchain Hamiltonian is thus proposed that quantitatively reproduces not only the spectra to which the data were fit, but also spectra observed at intermediate fields.

In particular, it is found that the Hamiltonian refined in Chapter 5 quantitatively reproduces the spectrum observed for $CoNb_2O_6$ in low transverse field, and this regime is explored in Chapter 6. In this regime, high-resolution single crystal

inelastic neutron scattering measurements observe that small transverse fields lead to a breakup of the spectrum into three parts, each evolving very differently upon increasing field. An intuitive physical picture and fully analytically solved model is proposed for this behaviour based on novel bound states of domain wall quasiparticles. In this regime, both the applied transverse field and an off-diagonal exchange term allow domain walls to hop, but these hopping effects have opposite signs. The novel bound states arise near the special field where the sizes of the hopping effects match so that domain walls become localized. The theoretical model qualitatively captures a variety of nontrivial features in the observed spectrum, providing insight into the underlying physics of these bound states.

In Chapter 7, the magnetization of $CoNb_2O_6$ is measured as a function of field up to 16 T along three orthogonal crystallographic directions. For field along b, where a quantum critical point is present at $B_c = 5.5$ T, the key features of the field and temperature dependence of the magnetization M, its derivatives, and of the magnetic entropy S at temperatures above 2 K and fields near B_c are well captured by calculations for a minimal model of an exactly solvable Ising chain in transverse field at finite temperature. The temperature and field dependent magnetization curves are quantitatively compared to calculations using exact diagonalization of the quantum spin chain Hamiltonian refined in Chapter 5 and good agreement is found.

The other material studied in this thesis is the frustrated triangular lattice quantum Ising-like antiferromagnet $Na_2BaCo(PO_4)_2$, which is discussed in Chapter 8. Inelastic neutron scattering experiments observe the spectrum as a function of transverse (in-plane) field. In high field, sharp, resolution-limited magnons are observed, which are well described by a minimal nearest-neighbour XXZ quantum spin Hamiltonian. The parameters of this spin Hamiltonian are refined based on a global fit to the observed magnon dispersions at several fields reported here, as well as to data reported in the literature for field applied along the easy-axis direction. In transverse fields below the transition to the field polarized phase, there are two intermediate field phases and strong continuum scattering is observed in both. While the spectrum in the higher field phase can be understood based

on a picture of magnon broadening due to decay into the continuum, at the lowest fields, no magnons are observed at all and instead continuum scattering dominates. The data are compared to the results of calculations in linear spinwave theory including both one- and two-magnon contributions and it is found that this semi-classical calculation cannot account for the strong continuum scattering observed experimentally, suggesting much stronger quantum fluctuations than can be captured by a spinwave approximation.

2 Quantum magnetism

This chapter introduces the theoretical background relevant to the work reported in this thesis. First, the physics of localized magnetic moments in insulators is discussed. An overview is then given of some important concepts in quantum magnetism which are of relevance to this thesis: quantum phase transitions, frustration and fractionalization. Next, the physics of the low dimensional spin systems relevant to this thesis — Ising-like chains and triangular antiferromagnets — is discussed in more detail. Finally, linear spinwave theory and exact diagonalization, which are the analytical techniques used throughout this thesis, are introduced.

2.1 Introduction

The existence of magnetic materials of any sort, i.e., materials whose equilibrium properties are affected by the presence of a magnetic field, intrinsically requires the existence of quantum physics, as proved by the Bohr-van Leeuwen theorem [1]. Many materials, however, can be very well described using semi-classical approximations. The field of quantum magnetism encompasses those materials that cannot adequately be described semi-classically, and these display a wide variety of emergent phenomena [2].

The purpose of this chapter is to introduce briefly the various topics within quantum magnetism which will be of particular relevance in this thesis. First, in Sec. 2.2, a brief description is given of the origins of localized magnetic moments in insulators and how they interact. This section focusses on the single-ion physics of Co^{2+}, as this is the magnetic ion in both the materials studied in this thesis. Next, in Sec. 2.3, a brief overview is given of some phenomena which are realised in a broad range of systems within quantum magnetism: quantum phase transitions, frustration and fractionalization. In Sec. 2.4, the physics relevant to the low dimensional systems described in this thesis will be described in more detail. Ising-like chains, of relevance for describing $CoNb_2O_6$, are discussed with several models, each of which are relevant for describing this material in different regimes. Triangular lattice antiferromagnets, which are relevant for an understanding of $Na_2BaCo(PO_4)_2$, are also discussed. Finally, Sec. 2.5 introduces the two main analysis techniques which will be used throughout this thesis for comparing experimental results to theoretical predictions, namely linear spin wave theory (LSWT) and exact diagonalization (ED).

2.2 Local moments and their interactions

The materials discussed in this thesis are both insulators, so the magnetism is caused by electrons which are localized within the electronic shell of certain ions rather than itinerant throughout the crystal.

2.2.1 The origin of local moments

Localized magnetic moments can be found when ions have a net total electronic spin $\boldsymbol{S}$ or orbital angular momentum $\boldsymbol{L}$. For an ion in free space, the ground state $\boldsymbol{S}$ and $\boldsymbol{L}$, as well as their sum $\boldsymbol{J}$, can be predicted using Hund's rules. When the ion is embedded in a crystal lattice, the effects of the crystal field (i.e., the electrostatic fields from neighbouring ions) need to be considered. For f-block elements (rare earths), Hund's rules continue to work well because the f-electrons are closer to the nucleus than the outer filled s- and p-electron shells, which screen the Coulomb interaction between f-electrons and ligands. However, for d-block ions

such as Co^{2+}, while the total spin and orbital angular momentum are in general determined by Hund's rules, the crystal field strength is in general much larger than the spin-orbit coupling, and so Hund's third rule, which determines the total angular momentum, is not obeyed [1, 3].

Once crystal field and spin-orbit coupling have been included, the lowest ground state multiplet can in general be described as an effective spin S_{eff} where the degeneracy of the multiplet is $2(S_{\text{eff}} + 1)$. This allows the low energy excitations to be described in terms of a 'spin Hamiltonian' in the effective spins, which can apply to both the interactions between spins and the local anisotropy expressed as a single-ion Hamiltonian [3]. The magnetic moment $\boldsymbol{\mu}$ is related to the effective spin S_{eff} by $\boldsymbol{\mu} = -\mu_B \tilde{g} \boldsymbol{S}$ where $\tilde{g}$ is the g-tensor which is in general anisotropic.

As both materials studied in this thesis, $CoNb_2O_6$ and $Na_2BaCo(PO_4)_2$, contain Co^{2+} ions in distorted octahedral environments, this case will be considered in more detail as an example.

2.2.1.1 The Co^{2+} ion in a distorted octahedral environment

For ions in a distorted octahedral environment, it is usually possible to treat the dominant crystal field as exactly cubic and then treat distortions as perturbations. While this does not give quantitatively correct results when the distortion is fairly large, it will be a useful approach to gain a qualitative understanding of the single-ion spectrum.

A cubic octahedral environment splits the 5-fold degenerate d-orbitals of the free ion into a lower energy triplet and higher energy doublet, as shown in Fig. 2.1A, labelled as t_{2g} and e_g respectively, according to the representation of the cubic point group under which they transform. The orbitals are then filled according to their energy, with the competition between the crystal field strength and the on-site repulsion determining whether higher energy orbitals are singly occupied before lower energy orbitals are doubly occupied. The Co^{2+} ion has a $3d^7$ electron configuration and both materials studied here correspond to the intermediate field strength regime, in which the higher energy orbitals are first singly occupied, as

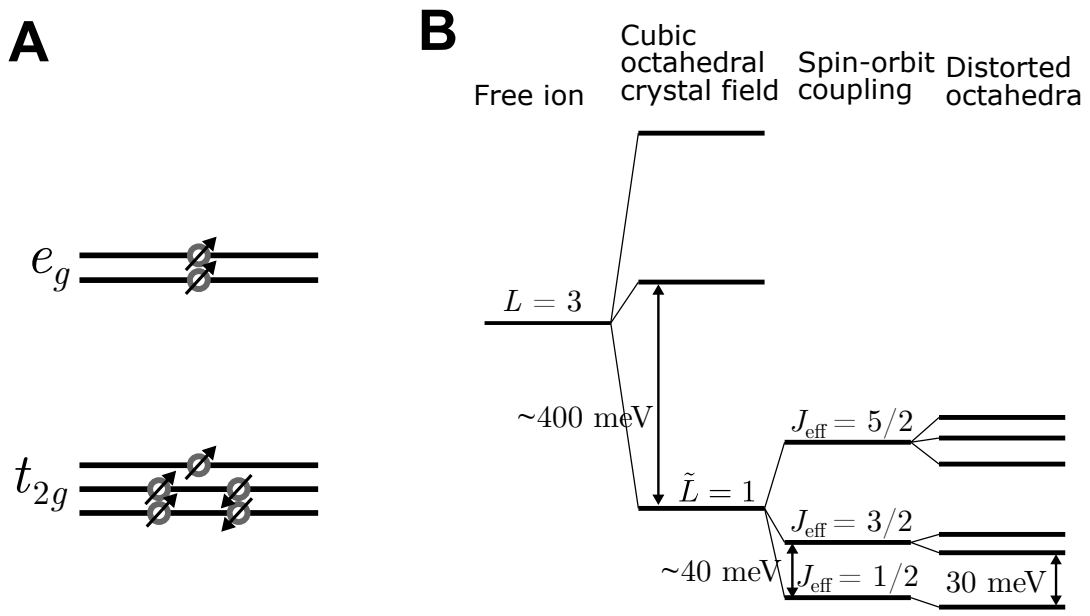

Figure 2.1: A) The splitting of the single electron d-orbital levels induced by the cubic octahedral crystal field environment and their occupation in the 'high spin' d^7 configuration. The circles represent electrons while the lines represent the orbitals. The e_g orbitals are higher energy than the t_{2g} orbitals and in cubic octahedral symmetry, the orbitals would be degenerate within these multiplets and are only shown separated for clarity. B) The splitting of the multi-electron Hund's rules $L = 3$, $S = 3/2$ ground state manifold at different levels of perturbation theory. The cubic octahedral crystal field splits the orbital septet such that the lowest energy manifold is an orbital triplet with effective orbital angular momentum $\tilde{L} = 1$. The spin-orbit coupling then splits the $3 \times 4 = 12$-fold degenerate spin-orbit manifold according to $J_{\text{eff}} = \tilde{L} + S$ [3, 4]. Finally the distortion (monoclinic for $CoNb_2O_6$, trigonal for $Na_2BaCo(PO_4)_2$) lifts the remaining degeneracy as far as is allowed by Kramers theorem, that is, all levels in the final column are Kramers doublets. The energy splittings indicated in the second and third column have been estimated by combining the parameters given in Ref. [5] for $CoNb_2O_6$ with formulae from Ref. [3]. Similar splittings are appropriate for $Na_2BaCo(PO_4)_2$ [6]. In both panels, energy is shown as increasing up the page.

shown in Fig. 2.1A. This leads to a total spin of $S = 3/2$ with configuration $t_{2g}^5 e_g^2$, as predicted by Hund's rules, known as the high-spin state [7]. In very strong crystal fields, the alternative $S = 1/2$ state with configuration $t_{2g}^6 e_g^1$ is possible.

In order to understand the effect of the crystal field on the total orbital angular momentum $L = 3$ states predicted by Hund's rules, it is useful to express the crystal field potential in terms of operator equivalents, built out of powers of the total orbital angular momentum operator $\boldsymbol{L}$. The allowed terms are highly constrained by the point group symmetry at the ion site [3]. Both the cubic octahedral terms

and any distortions can be expressed in this formalism. The effect of the cubic terms is to split the $L = 3$ manifold into two triplets and a singlet, with one the triplets being lowest in energy [3], as shown in Fig. 2.1B. Since this manifold is a triplet, its wavefunctions can be described by an effective orbital angular momentum $\tilde{\boldsymbol{L}} = 1$, with eigenvalues such that the matrix elements of $\boldsymbol{L}$ are equivalent to those of $-\frac{3}{2}\tilde{\boldsymbol{L}}$ over the restricted Hilbert space of $\tilde{\boldsymbol{L}} = 1$ states [3].

The spin-orbit coupling can then be considered, written as $\lambda\tilde{\boldsymbol{L}} \cdot \boldsymbol{S}$ with $\lambda > 0$. This splits the combination of the $\tilde{L} = 1$ and $S = 3/2$ into multiplets with $\boldsymbol{J}_{\text{eff}} = \tilde{\boldsymbol{L}} + \boldsymbol{S} = 1/2, 3/2, 5/2$, i.e., a doublet, a quartet and a sextet, with the doublet being the lowest energy [3], as shown in Fig. 2.1B. This is a Kramers doublet, arising because of the odd number of electrons in Co^{2+}, meaning that it is protected by time-reversal symmetry. It therefore cannot be further split by distortions of the octahedra. In cubic point group symmetry, the g-tensor for the Co^{2+} ions would be isotropic (spherical) with value $g = 4\frac{1}{3}$ in all directions [3]. Distorting the octahedra admixes in the higher $\boldsymbol{J}_{\text{eff}}$ levels into the lowest doublet, which can lead to a highly anisotropic g-tensor [3]. In the rest of this thesis, the symbol S will, unless otherwise specified, represent the *effective* spin determined by the degeneracy of the lowest spin-orbit multiplet, which in the case of Co^{2+} is a Kramers doublet in both cubic and non-cubic local crystal field environments.

2.2.2 Interactions of local moments

The interactions between local moments are often far stronger than can be explained by dipolar interactions between magnetic moments. These interactions are instead due to a combination of electrostatic interactions and energy gain from delocalization: electrons can gain energy if they can virtually hop to neighbouring sites, and whether this process is allowed or not depends on the relative orientation of the spins of the electrons on these neighbouring sites [1]. In practice, there is often little overlap between the orbitals of magnetic ions and the hopping happens via anion ligands, often O^{2-} ions, in a process called superexchange. The sign of the superexchange

interaction depends on the angle made by the magnetic ions and the anion, since this affects which orbitals are involved [8, 9].

If exchange interactions only involved pure spin states, they would be Heisenberg, i.e., isotropic in spin-space. However, in the presence of spin-orbit couplings, the effective spin Hamiltonian can become anisotropic in spin-space, as the electron wavefunctions have mixed spin-orbital character and exchange through some orbitals can be energetically more favourable than exchange between other orbitals. This effectively leads to couplings between some spin components being more favourable than couplings between other spin components, and thus anisotropic exchange, which can in principle be bond-dependent [10].

2.3 Quantum effects in magnetism

This section will contain a brief survey of some of the main theoretical ideas of broad applicability in this thesis. These concepts are not all limited to quantum magnetic systems, but play an important role in them.

2.3.1 Quantum phase transitions

Quantum phase transitions are phase transitions that happen at zero temperature as some tuning parameter is varied [11]. In the cases of relevance to this thesis, this tuning parameter is an applied magnetic field, but in other systems the tuning parameter could be pressure, or chemical doping, among others. Of particular interest are second order (continuous) quantum phase transitions. This means that the order parameter goes continuously to zero as the quantum critical point is approached from the phase with spontaneous symmetry breaking. Quantum phase transitions are not restricted to magnetic systems and examples of interest to the condensed matter community at large are found in a wide variety of electronic systems [12].

In some ways, quantum phase transitions are very similar to classical finite-temperature phase transitions. At second order phase transitions of both types, thermodynamic quantities (as well as correlation lengths) scale as the critical point

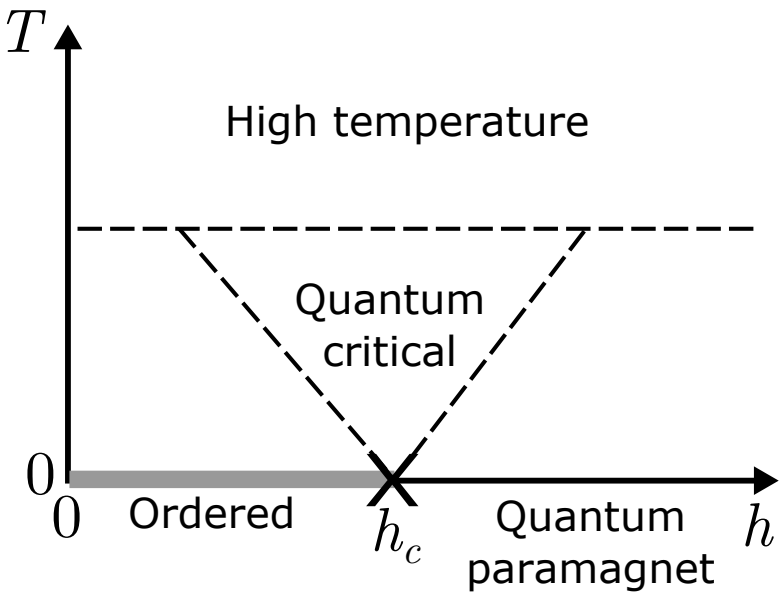

Figure 2.2: A sketch of a phase diagram for a model with a quantum critical point and no finite temperature phase transition, such as the transverse field Ising chain (see Sec. 2.4.1.1). The cross labels the quantum critical point while the thick grey line indicates the ordered region, which exists only at zero temperature. The dashed lines indicate crossovers between different regimes. The crossovers between the quantum critical regime and the low temperature regimes are determined by the size of the gap. The crossover into the regime labelled 'High temperature' occurs when sufficiently energetic states are populated that the effects of the lattice cannot be neglected. The behaviour in the quantum critical regime is dictated by the quantum critical point. Figure adapted from Ref. [11].

is approached as power laws with so-called 'critical exponents' which are universal, that is they do not depend on the microscopic details of the system [11, 13]. In fact, quantum phase transitions occurring in systems with d dimensions can be exactly mapped to classical phase transitions in $d+1$ dimensions [11, 14], and quantum phase transitions often occur as the end point of a line of classical phase transitions.

However, quantum phase transitions also differ from classical phase transitions in important respects, for instance, quantum phase transitions are driven by quantum fluctuations rather than thermal fluctuations. In addition, the presence of a quantum critical point can influence the behaviour of the system even at relatively high temperatures [11]; the region of the phase diagram whose behaviour is governed by the quantum critical point is known as a 'quantum critical fan'. A schematic of a phase diagram which includes a quantum critical point is shown in Fig. 2.2,

on which the quantum critical fan is shown. This region roughly corresponds to the region in which the temperature is larger than some characteristic energy scale such as the gap to excitations Δ (although the temperature cannot be so large as to overcome the correlations altogether).

The fact that quantities scale with critical exponents in the vicinity of quantum critical points is an example of a broader phenomenon of universality, whereby the behaviour of the system on sufficiently large length scales depends only on the dimensionalities of the system and the order parameter (and on whether the interactions are long ranged) [11]. Universality can also constrain, for example, the long wavelength excitations of the system near the quantum critical point.

A paradigmatic example of quantum phase transitions, and the one that will be of most relevance in this thesis, is the Ising chain in transverse field (TFIC). This will be discussed in more detail in Sec. 2.4.1.1.

It is important to note that according to the Mermin-Wagner theorem, continuous symmetries cannot be broken at finite temperature in $d \leq 2$, or at any temperature (even zero) in $d = 1$ [14, 15]. However, a phase transition in systems with $d = 2$ at finite temperature (equivalently $d = 1$ at zero temperature) is possible for systems which have an $O(2)$ symmetry. These phase transitions, named for Berenzinskii, Kosterlitz and Thouless, do not break symmetry, so do not fit into the Landau paradigm, and occur due to the formation of vortices [14]. Note also that in $d = 1$, it is possible to break even discrete Ising symmetry only at $T = 0$ [11].

2.3.2 Frustration

Frustration occurs when it is not possible fully to satisfy all interactions simultaneously. In the context of magnetism, this means that some pairs of spins are not in a configuration relative to each other that minimizes their interaction energy. The prototypical example used to illustrate this concept is a triangle with Ising spins (i.e., spins constrained to only be either up or down) located at its vertices with an antiferromagnetic interaction between them, as shown in Fig. 2.3. The energy for any given pair of spins is minimized if they are anti-parallel, but once

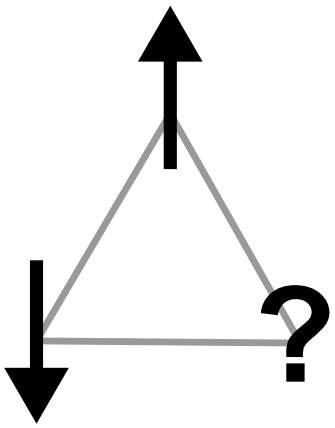

Figure 2.3: Frustration of antiferromagnetic Ising spins on a triangular lattice. Once the first two spins have been placed pointing in opposite directions to each other, the possibilities for the third spin both leave a bond unsatisfied.

two spins have been placed on the vertices pointing opposite to each other, the third spin can only be anti-parallel to one of them, such that whether the third spin is up or down, both configurations are equally poor at satisfying the interactions. Taking into account the ways the spins could be permuted, there are thus six configurations which minimize the energy [16]. One could imagine creating a whole lattice of triangles, either sharing edges (this is what is usually referred to as a triangular lattice) or sharing corners (the kagomé lattice), and a similar argument would apply on a macroscopic scale.

These arguments imply that when frustrated spins are classical, frustration leads to highly degenerate ground states. Indeed, it has been known for many years that the ground state of the Ising triangular lattice antiferromagnet is a classical spin liquid, i.e., a superposition of all the possible states which minimize the energy [17]. When the spins are quantum however, quantum fluctuations lift the degeneracy of this ground state manifold and are expected to select a unique ground state (or at least, a sub-extensive number of ground states if symmetry breaking occurs) [16]. It has been suggested that in some cases, the ground state of such systems could be a quantum spin liquid, in which the system is in a complex entangled state consisting of a superposition of many of the low energy configurations with well defined phases between them. In this case, the system would not magnetically order all the way down to absolute zero. While the first systems

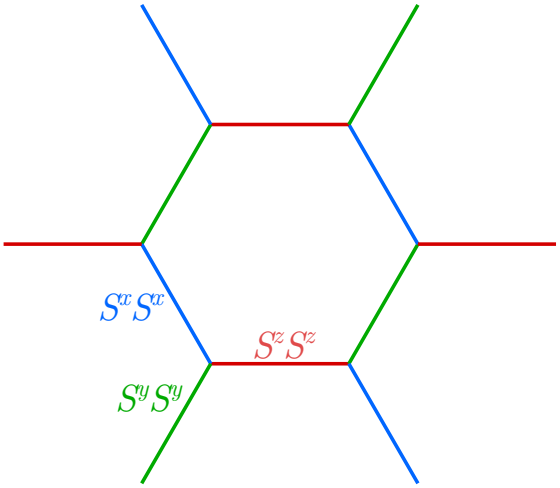

Figure 2.4: Interactions in the Kitaev model [21]. On each bond, the interaction is Ising, but the Ising axis depends on the bond as shown, with the red (horizontal), green (pointing up and right), and blue (pointing up and left) bonds being z, y and x bonds respectively, where x, y, z are Cartesian axes.

that were proposed to be quantum spin liquids — triangular lattice antiferromagnets — have since been shown to have ordered ground states [18–20], this ordering tends to occur at temperatures significantly below what would be expected based on their interaction strength and using a mean field model [16]. The frustration parameter $f = \theta_{\mathrm{CW}}/T_C$, where θ_{CW} is the Curie-Weiss temperature extracted from fits to the high temperature susceptibility and T_C is the ordering temperature, is thus a useful measure of frustration [16].

The triangular lattice antiferromagnet, mentioned above, will be discussed in more detail in Sec. 2.4.2. It is an example of 'geometric frustration', as the frustration occurs due to the arrangement of the antiferromagnetic bonds. It is also possible for frustration to occur instead due to the form of the interactions themselves. An example of this is the Kitaev model [21], consisting of spins on a honeycomb lattice which interact via Ising interactions, but with the Ising axis depending on the bond, see Fig. 2.4. This model has been the subject of significant attention, due in part to the fact that it is exactly solvable with a quantum spin liquid ground state, but no experimental realisations have yet been found of systems where terms in the Hamiltonian beyond the pure Kitaev form were sufficiently

small to avoid inducing long range order at low temperatures. Similar interactions have also been studied in other geometries [22, 23].

The high classical degeneracy of the ground states of frustrated systems has important consequences. Firstly, it leads to multiple competing ground states, implying that the ground state is sensitive to perturbations and often leading to rich phase diagrams. Secondly, there are many low lying excitations, and thirdly, the form of the excitations is often exotic. In particular, the excitations in spin liquids (both classical and quantum) often display fractionalization, which will be discussed next. This is because the ground states of frustrated systems often have local constraints (e.g., minimizing the sum of the magnetization on a given triangle), and a local perturbation, such as flipping a spin, violates this constraint in two places [16, 21, 24].

2.3.3 Fractionalization

Usually in condensed matter systems, excitations are either electron-like, carrying spin $S = 1/2$ and charge ± 1 in units of the electron charge (holes are here being counted as electron-like), or magnon-like, carrying no charge and spin $S = \pm 1$. In systems where fractionalization occurs, this is not the case, as quasiparticles 'break up' into smaller parts, which carry fractional spin and/or charge.

Perhaps the simplest example of fractionalization can be found in the ordered phase of the Ising chain. This is illustrated in Fig. 2.5A and will be discussed more quantitatively in Sec. 2.4.1.1. While the Ising chain only has two (symmetry breaking) ground states, the excitation spectrum is highly degenerate. This is because the energy of the Ising chain depends only on the number of domain walls between regions of up spins and down spins and not the distance between them, since a domain wall in a one-dimensional system breaks exactly one bond. Flipping a single spin creates two domain walls, and rather than this spin flip propagating coherently as a magnon, the two domain walls can separate apart independently from each other. In the presence of a transverse field, the domain walls can hop and they become the true quasiparticles of the system. This behaviour

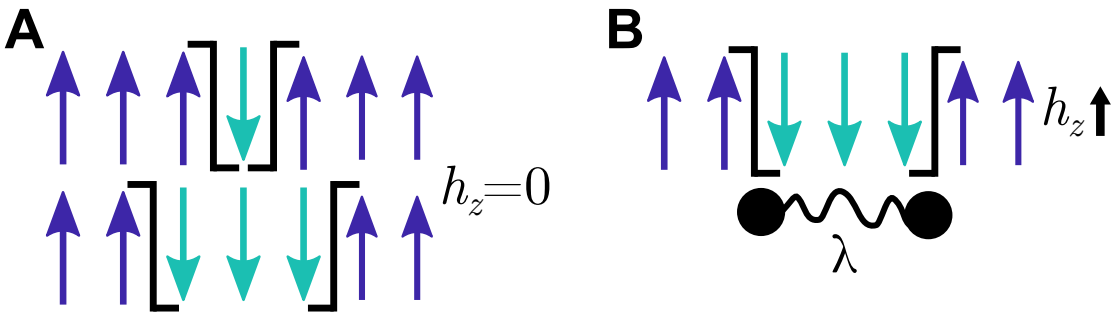

Figure 2.5: A) In a ferromagnetic Ising chain, domain walls (solid lines) can separate apart at no energy cost. B) In a finite longitudinal field h_z, there is an energy cost linear in the separation, as if the two domain walls interacted via a string tension λ (curly line between solid dots), which stabilizes confinement bound states.

applies to Ising chains whether they are ferromagnetic or antiferromagnetic and has been observed experimentally [25].

A key feature of fractionalized excitations is that it is not possible to create them individually. This means that the spectrum observed, for instance, in inelastic neutron scattering, does not contain sharp dispersions but a continuum of excitations, corresponding to different ways that the energies and momenta of the individual fractionalized quasiparticles can combine. The presence of continua of excitations in scattering spectra is therefore a key signature of fractionalization, although these continua can also be due to other effects such as disorder.

A variety of other systems are also predicted to display fractionalization, and it has been observed experimentally in some of them. A few examples will now be briefly mentioned. The fractional quantum Hall effect is an example of charged quasiparticles fractionalizing [26]. The antiferromagnetic Heisenberg chain has been both predicted and observed to have fractionalized spinon excitations [27–29], while magnetic monopoles are expected to exist in (classical) spin ice systems [30–32]. Fractionalized quasiparticles have also been observed in distorted triangular antiferromagnets [33].

Quantum spin liquids are expected in general to have fractionalized excitations [16]. While the ground state of the pure nearest-neighbour Heisenberg triangular lattice antiferromagnet is an ordered state, a quantum spin liquid ground state is predicted in the presence of next-nearest-neighbour interactions [34]. This might

have spinon type excitations. The exactly solvable Kitaev model, which is also predicted to have a quantum spin liquid ground state, also has fractionalized excitations, which in this case are propagating Majorana fermions and static fluxes [21, 35].

2.4 Low dimensional magnetism

While both materials studied in this thesis have a fully three dimensional crystal structure, the arrangement of the magnetic ions within them means that the interactions are much weaker along one or two of the directions than in the others, such that the dimensionality of the magnetic system is effectively reduced. This means that a useful understanding of the behaviour of these materials can be gained by considering models of independent chains or layers which are effectively one- or two-dimensional, respectively. The effects of the weak interchain or interlayer interactions can then be considered as perturbations [36].

2.4.1 Ising-like chains

The spin chain material $CoNb_2O_6$, which will be the focus of Chapters 4 to 7, is a good example of an Ising-like chain. However, additional interactions beyond the pure Ising exchange mean that different approximations are most useful in different regimes of applied field. These will be discussed in some detail below.

2.4.1.1 The transverse field Ising chain

The transverse field Ising chain (TFIC), with Hamiltonian

$$\mathcal{H} = \sum_j \left[-JS_j^z S_{j+1}^z - hS_j^x \right], \tag{2.1}$$

where $J > 0$ is a ferromagnetic Ising exchange and h is an externally applied transverse field, is an important model in condensed matter physics because it displays the key paradigms of both a continuous quantum phase transition from an ordered phase to a quantum paramagnetic phase as a function of field, as well as, in

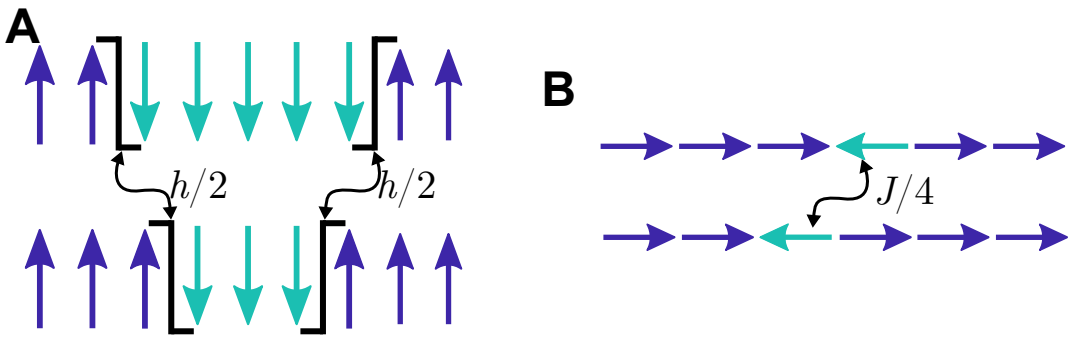

Figure 2.6: Excitations of the transverse field Ising chain. A) In the ordered phase, the excitations are domain walls that can hop due to the transverse field. B) In the quantum paramagnetic phase, excitations are spin flips against the applied field, which can hop due to the Ising exchange.

the ordered phase, of fractionalization of local spin flips into pairs of domain wall quasiparticles (also known as spinons or solitons) [11], as discussed in Sec. 2.3.3.

It is helpful first to gain a qualitative understanding of this model. The behaviour in the ordered phase can be understood by starting from zero field, where, as discussed in Sec. 2.3.3, the excitations are pairs of domain walls between regions of up spins and down spins, see Fig. 2.5A. The transverse field term in (2.1)

$$\sum_j -hS_j^x = \sum_j -h\frac{S_j^+ + S_j^-}{2} \tag{2.2}$$

flips single spins. If the spin flip occurs in the middle of a domain, this introduces an extra two domain walls, costing Ising energy J, and so the effect of mixing with states with higher numbers of domain walls can be neglected. If the spin that is flipped is at the end of a domain, however, this process can happen without changing the number of domain walls and the effect is instead to cause the domain wall to hop by one site, as illustrated in Fig. 2.6A. The transverse field thus gives domain walls kinetic energy. When this kinetic energy matches the potential energy cost to create domain walls in the first place, the gap closes and the transition occurs. The behaviour in the quantum paramagnetic phase meanwhile can be understood starting from the limit of very high field, where the spins are all aligned along the field direction, see Fig. 2.6B, and it is therefore useful to rotate to a

new basis, $S_j^{z'} = S_j^x$, $S_j^{x'} = -S_j^z$, such that $S_j^z = -(S^{+'} + S^{-'})/2$. In this frame, the nearest-neighbour Ising interaction term in 2.1 becomes

$$\sum_j -JS_j^z S_{j+1}^z = -\frac{J}{4}\sum_j \left(S_j^{+'}S_{j+1}^{+'} + S_j^{-'}S_{j+1}^{-'} + S_j^{+'}S_{j+1}^{-'} + S_j^{-'}S_{j+1}^{+'}\right). \tag{2.3}$$

The first two terms on the right create or destroy pairs of spin flips, thus changing the energy by h, which is assumed large and so the effect of these terms can be neglected in a first approximation. The last two terms, however, allow spin flips to hop by one site, such that in this phase, the Ising interaction term gives the quasiparticles kinetic energy. The quantum phase transition can thus equivalently be seen as occurring when the kinetic energy of these spin-flip quasiparticles matches the potential energy cost to create them.

The transverse field Ising chain can be quantitatively discussed via a mapping to spinless fermion variables [37, 38], which in the ordered phase represent these solitons, while in the quantum paramagnetic phase, they represent spin flips against the direction of the field. The derivation will be presented here because these steps will be used in Chapter 7 and will follow the discussion of Ref. [11]. The mapping proceeds via the non-local Jordan-Wigner transformation from spin operators to fermion operators [11]

$$S_j^{z'} = \frac{1}{2} - c_j^\dagger c_j \tag{2.4}$$

$$S_j^{+'} = \prod_{j'<j}(1 - 2c_{j'}^\dagger c_{j'})c_j \tag{2.5}$$

$$S_i^{-'} = \prod_{j'<j}(1 - 2c_{j'}^\dagger c_{j'})c_j^\dagger, \tag{2.6}$$

with the primed axes related to the unprimed axes via a 90° rotation about the y-axis, as above, and where the $c^\dagger$ and c are fermion creation and annihilation operators, respectively. The products in (2.5), (2.6) are known as Jordan-Wigner strings and are required to preserve the correct commutation relations for the spin operators, $\left[S_j^{z'}, S_{j'}^{\pm'}\right] = \pm S_j^{\pm'}\delta_{jj'}$, $\left[S_j^{+'}, S_{j'}^{-'}\right] = 2S_j^{z'}\delta_{jj'}$ and all commutators of spins on different sites vanishing. The fermion operators thus create spins which

are flipped against the field direction. The Jordan-Wigner transformation in the original unprimed frame then becomes [11]

$$S_j^x = \frac{1}{2} - c_j^\dagger c_j \tag{2.7}$$

$$S_j^z = -\frac{1}{2}\prod_{j'<j}(1-2c_{j'}^\dagger c_{j'})(c_j + c_j^\dagger), \tag{2.8}$$

and after substitution of these expressions into (2.1), the Hamiltonian becomes

$$\mathcal{H} = -\sum_j \left[\frac{J}{4}\left(c_j^\dagger c_{j+1} + c_{j+1}^\dagger c_j + c_j^\dagger c_{j+1}^\dagger + c_{j+1}c_j\right) - hc_j^\dagger c_j + \frac{h}{2}\right]. \tag{2.9}$$

This Hamiltonian is quadratic in the fermion operators and can be solved exactly as follows. First the fermion operators are Fourier transformed, using

$$c_j = \frac{1}{\sqrt{N}}\sum_k c_k e^{ikj}, \tag{2.10}$$

where N is the number of sites in the chain and it has been assumed that the spacing between consecutive sites is 1, yielding

$$\mathcal{H} = \frac{1}{4}\sum_k \left[(4h - 2J\cos k)c_k^\dagger c_k + iJ\sin k(c_{-k}^\dagger c_k^\dagger + c_{-k}c_k) - 2h\right] \tag{2.11}$$

$$= E_0 + \frac{1}{4}\sum_k \begin{pmatrix} c_k^\dagger & c_{-k}\end{pmatrix}\begin{pmatrix}(2h - J\cos k) & -iJ\sin k \\ iJ\sin k & -(2h - J\cos k)\end{pmatrix}\begin{pmatrix} c_k \\ c_{-k}^\dagger\end{pmatrix} \tag{2.12}$$

where E_0 is a constant (which depends on h).

The quadratic part of the Hamiltonian can then be diagonalized via a canonical transformation of the fermion operators to new operators γ, known as a Bogoliubov transformation,

$$\begin{pmatrix}\gamma_k \\ \gamma_{-k}^\dagger\end{pmatrix} = \begin{pmatrix} u_k & -iv_k \\ iv_k & u_k\end{pmatrix}\begin{pmatrix} c_k \\ c_{-k}^\dagger\end{pmatrix} \tag{2.13}$$

where the u_k and v_k are real, and can be parameterized as $\cos(\theta_k/2)$ and $\sin(\theta_k/2)$. The requirement that the Hamiltonian be diagonal in the γ_k operators becomes

$$\tan\theta_k = \frac{J\sin k}{2h - J\cos k} \tag{2.14}$$

and the Hamiltonian thus becomes

$$\mathcal{H} = E_{\mathrm{GS}} + \sum_k \epsilon_k \gamma_k^\dagger \gamma_k, \tag{2.15}$$

where E_{GS} is the ground state energy and where the quasiparticle excitation energy is

$$\epsilon_k = \frac{1}{2}\sqrt{J^2 + 4h^2 - 4hJ\cos k}. \tag{2.16}$$

These expressions will be used in Chapter 7.

Note that the energy of a quasiparticle with zero momentum according to (2.16) is

$$\epsilon_0 = \frac{1}{2}|J - 2h|, \tag{2.17}$$

such that the gap closes (i.e. the quantum phase transition occurs) at the critical field $h_c = J/2$, with the gap depending linearly on $|h - h_c|$ on both sides of the transition. On the low field side of the transition, there is a spontaneous magnetization $\langle S_j^z \rangle \neq 0$, and the $c_k^\dagger$ represent (dressed) domain wall creation operators. Since domain walls are created in pairs by local perturbations, the gap in the ordered phase is $\Delta = 2\epsilon_0 = 2(h - h_c)$. In the high field phase, there is no spontaneous magnetization. The character of the state is however quite different to a thermal paramagnet, due to the quantum correlations, so the term quantum paramagnet is used [11]. The excitations in this phase have the character of spin flips against the field direction (magnons) and the gap is $\Delta = \epsilon_0 = h - h_c$.

Many results are known about the properties of the transverse field Ising chain, especially near the quantum critical point, where continuum limits can be taken, for instance, many of the critical exponents can be calculated exactly [11]. A major difference, however, between the TFIC and a real material such as $CoNb_2O_6$ is that while the Ising chain only has long range order at zero temperature, weak interactions between chains, always present in a real material, lead to a finite temperature three-dimensional ordered phase.

2.4.1.2 The Ising chain in tilted field

It is insightful to discuss also the case of the Ising chain in a tilted field with both a transverse as well as a longitudinal (along the Ising axis) component. This will be relevant for understanding in a first approximation the effects of the weak interchain

couplings, as in the ordered phase they effectively create a longitudinal mean field [39]. The relevant single-chain Hamiltonian in this case is

$$\mathcal{H} = \sum_j \left[-JS_j^z S_{j+1}^z - h_x S_j^x - h_z S_j^z \right]. \tag{2.18}$$

This can no longer be solved exactly using the methods of Sec. 2.4.1.1, because the Jordan-Wigner strings no longer cancel, leading to highly non-local interactions. The behaviour in certain regimes can nonetheless be well understood.

First consider the case where $h_z \ll h_x \ll J$, which will be considered further in Chapter 4, and which was explored in Refs. [40, 41]. In this case, it is a good approximation to start from a picture of delocalized domain wall quasi-particles. The constraint $h_x \ll J$ means that the low energy excited states will contain exactly two of these domain walls, which can hop due to the transverse field term h_x. The longitudinal field can be considered to create an attractive interaction between the domain walls, which is linear in the separation between them, since flipping each additional spin between them costs the same amount of energy, as illustrated in Fig. 2.5B. This emergent linear potential is reminiscent of the linear potential between quarks in mesons [41] and confines the domain walls into bound states. If the condition $h_z \ll h_x$ is satisfied, then the kinetic term h_x is much greater than the confining potential term h_z, and a continuum approximation can be taken. This results in a Schrödinger equation for the separation between the domain walls, which can be rearranged to have the form of the mathematically well-known Airy equation, as will be discussed further in Chapter 4.

The other regime of significant interest is that where $h_x = h_c$. This point is exactly solvable in the long wavelength limit, resulting in a spectrum of eight quasiparticles whose energies are determined by the properties of the E8 Lie algebra [42], and which have been observed in $CoNb_2O_6$ [25, 43].

2.4.1.3 XXZ chain

Another model which will be useful for understanding the behaviour of $CoNb_2O_6$ is the XXZ chain. In this material, in the regime of large (near) longitudinal field ($h_z >$

J), the perturbation to the pure Ising limit which most strongly affects the physics seems to be an XY exchange interaction. The relevant minimal Hamiltonian is

$$\mathcal{H}_{\mathrm{XXZ}} = -J\sum_j \left[S_j^z S_{j+1}^z + \lambda_S(S_j^x S_{j+1}^x + S_j^y S_{j+1}^y)\right] - \sum_j h_z S_j^z. \tag{2.19}$$

The spectrum of this Hamiltonian can be solved exactly by making the ansatz that spin flips relative to a fully polarized state ($\| z$) travel as plane waves even when more than one spin-flip is present in the system, with interactions only serving to change the allowed momenta [36, 44]. In the case of ferromagnetic J, the ground state is the fully polarized state and the excitations have small numbers of spins flipped against the field.

The excitations with a single spin flipped are conventional magnon excitations with wavevector dependent energies [44]

$$m_1(l) = h_z + J(1 - \lambda_S \cos \pi l), \tag{2.20}$$

where the wavevector has been expressed in reciprocal lattice units corresponding to two sites per unit cell along the chain, for relevance to Chapter 4.4. The excitations with two spin flips come in two types. The first is a conventional continuum of two independently propagating single spin flips. The second is a bound state of two spin flips (i.e. two adjacent spin flips hopping as a pair, a two-magnon bound state), with dispersion relation [44]

$$m_2(l) = 2h_z + J\left[1 - \frac{\lambda_S^2}{2}(\cos \pi l + 1)\right]. \tag{2.21}$$

The corresponding (un-normalized) wavefunctions are

$$|m_1\rangle = \sum_j e^{i\pi l j} |\ldots\uparrow\uparrow\uparrow\downarrow_j\uparrow\uparrow\uparrow\ldots\rangle \tag{2.22}$$

and

$$\begin{aligned} |m_2\rangle = \sum_j e^{i\pi l j}\Big(&|\ldots\uparrow\uparrow\downarrow_j\downarrow\uparrow\uparrow\uparrow\ldots\rangle \\ &+ \lambda_S e^{i\pi l/2}\cos\frac{\pi l}{2}|\ldots\uparrow\uparrow\downarrow_j\uparrow\downarrow\uparrow\uparrow\ldots\rangle + \mathcal{O}(\lambda_S^2)\Big). \end{aligned} \tag{2.23}$$

The full un-normalized wavefunction up to all orders in λ_S for the m_2 mode is given in Ref. [44].

Note that the m_1 and the m_2 modes are both dispersive, but the m_1 mode will in general have a significantly larger bandwidth than the m_2 mode. This is because, for the m_1 mode, the dispersion comes at first order in the XY exchange $J\lambda_S$, while for the m_2 mode, the hopping process occurs in two stages via an intermediate state in which the spin flips are separated by one site [second term in (2.23)], therefore the hopping process is second order in the XY exchange, which leads to the dispersive term proportional to $J\lambda_S^2$ in (2.21).

The spectrum of the XXZ Hamiltonian (2.21) in fact contains bound states of arbitrarily many spin flips, all of whose dispersions can be obtained analytically [45]. However, these will in general overlap with states in the multiparticle continuum and are therefore susceptible to decay in the presence of additional terms beyond the pure XXZ Hamiltonian. On the other hand, the m_2 bound state is stabilized against decay by being below the threshold for creation of two independent m_1 particles by approximately the Ising energy J. This can be understood because two independent spin flips have 4 domain walls, whereas a bound state of two adjacent spin flips only has 2 domain walls. Therefore, the two-magnon m_2 bound state is robust against perturbations away from the pure XXZ limit, and indeed is observed in $CoNb_2O_6$ for high (near)-longitudinal fields, as reported in Chapter 4.

2.4.2 Triangular lattice antiferromagnets

The material $Na_2BaCo(PO_4)_2$, which will be the focus of Chapter 8, is an example of a triangular Ising-like XXZ antiferromagnet. To understand its behaviour as a function of temperature and applied transverse field, it is instructive first to consider the Ising and Heisenberg limits.

2.4.2.1 The triangular Ising antiferromagnet

The Ising antiferromagnet on a triangular lattice has already been briefly discussed in Sec. 2.3.3 as a paradigmatic example of frustration. The ground state in zero

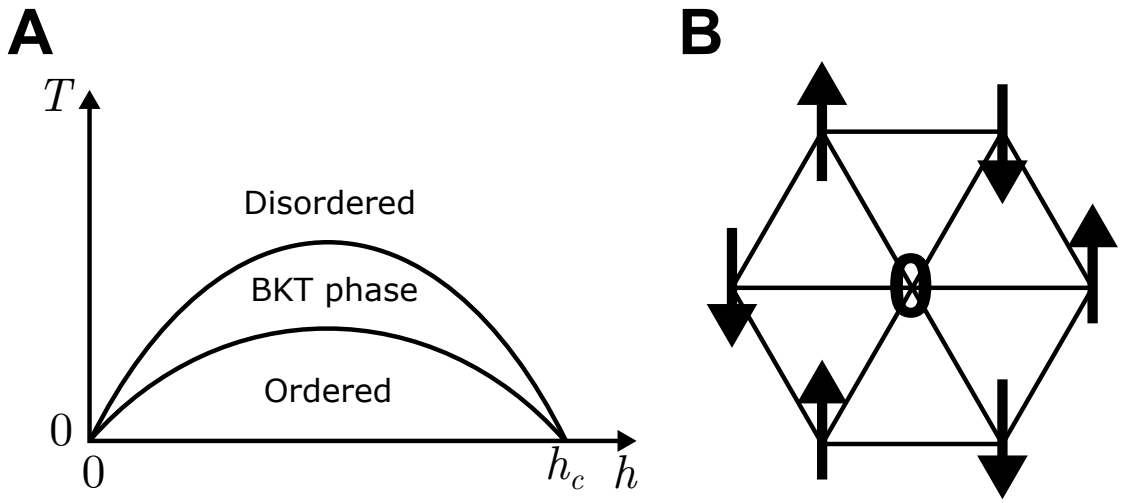

Figure 2.7: A) The phase diagram of the triangular Ising antiferromagnet in transverse field. BKT phase stands for Berezinskii-Kosterlitz-Thouless, while the arrangement in the ordered phase is shown in B. Figure adapted from Ref. [49]. B) Arrangement of spins in the ordered phase. The Ising axis is vertical. The 0 state can be understood as pointing along the field direction, meaning that its expectation value along the Ising axis is 0.

field is a classical spin liquid [17]. This means that there is a local constraint, that on any given triangle there should be two spins pointing in one direction and one spin pointing in the opposite direction (in the Ising limit, spins can only point up or down). There are many ways in which this constraint can be satisfied, and so the ground state on average only has power law correlations [46], so the dynamics is very different from conventionally ordered magnets and the excitations consist of defect triangles in which all spins are aligned [47, 48].

When an infinitesimal transverse field is applied, the system acquires quantum dynamics as up and down spins can now be mixed, and the system orders into a three sublattice structure with magnetizations +1, -1 and 0 along the Ising direction on the different sublattices [49, 50], see Fig. 2.7. At sufficiently high field, the system becomes polarized along the field direction. At intermediate fields, the system enters the ordered phase via two Kosterlitz-Thouless transitions as the temperature is decreased [50]. The excitations in the low temperature intermediate field phase are still the subject of much theoretical research and also appear to be unconventional [24].

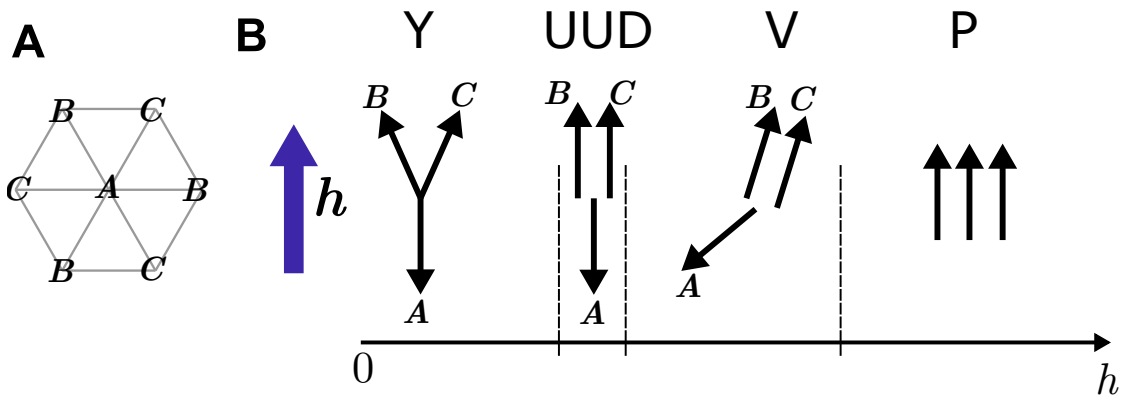

Figure 2.8: A) Triangular lattice with the ABC sublattices for magnetic phases with a $\sqrt{3} \times \sqrt{3}$ unit cell shown. B) Zero temperature phase diagram of the Heisenberg antiferromagnet in applied field pointing up, as indicated by the dark blue arrow. Field is shown increasing left to right. In zero field, the coplanar 120° order can have the A sublattice pointing in any direction, and the B and C spins pointing in a plane containing the A spin, at a relative angle in that plane of ±120°. An infinitesimal applied field causes the A spin to align against the field, forming a Y shaped phase. As the field is increased, the B and C spins rotate towards the field until the up-up-down (UUD) phase is reached. At fields higher than this, the B and C spins remain parallel, and rotate together first away from the field then back towards the field again, whilst the A spin is rotated all the way from opposite to the field to along the field; this is the V phase. Finally, the field polarized phase (P) is reached, with all spins aligned along the field. Dashed vertical lines indicate phase transitions. Panel B is adapted from Ref. [19] and is not drawn to scale.

2.4.2.2 The triangular Heisenberg antiferromagnet

The pure two dimensional triangular Heisenberg antiferromagnet cannot order at finite temperature by the Mermin-Wagner theorem [15]. It was proposed that the system might not order even down to zero temperature, as the ground state was proposed to be a quantum spin liquid composed of resonating valence bonds [18, 51]. However, it is now robustly theoretically established that the ground state is in fact ordered with a 120° phase [20, 52, 53]. The low energy excitations would therefore be expected to be sharp spinwaves, which are gapless at the K point of the hexagonal Brillouin zone due to the continuous symmetry breaking. Indeed, both numerical simulations and experiment observe sharp magnons throughout the Brillouin zone [54, 55]. This even extends into the region where decay of magnons into the two-magnon continuum would be expected, but which does not occur and is attributed to strong interactions between the continuum states and the magnons,

which cause level repulsion and push the magnons to lower energies, where they no longer overlap with the continuum, and so are stable against decay [54].

Several phases are observed when a magnetic field is applied to a triangular Heisenberg antiferromagnet. Note that the behaviour does not depend on the direction of the applied field as the interactions are isotropic in spin space. Even in applied field, the classical Heisenberg antiferromagnet retains a large degree of degeneracy, and the ground state is chosen by zero-point quantum fluctuations [19]. As the field is increased from 0, the system initially remains in the 120° ordered phase but with one spin pointing exactly against the field, forming a Y phase, see Fig. 2.8B. As the field is increased, the B and C spins (see Fig. 2.8A) gradually rotate towards the field until an up-up-down phase is reached. Semi-classically, this up-up-down phase would only exist at a single point in the phase diagram, but quantum fluctuations favouring collinear ordering stabilize this phase over a finite extent in field. As the field is increased still further, the A spin starts to rotate towards the field with the B and C spins also rotating, initially in the opposite direction, in order to cancel the transverse polarization induced by the A spins, creating the V phase [19], as illustrated in Fig. 2.8B. Finally, the system enters a field polarized phase.

2.4.2.3 The triangular XXZ antiferromagnet

The triangular Ising-like XXZ antiferromagnet,

$$\mathcal{H} = \sum_{\langle ij \rangle} J_{xy} \left(S_i^x S_j^x + S_i^y S_j^y \right) + J_z S_i^z S_j^z, \tag{2.24}$$

where $J_z > J_{xy} > 0$, has properties between those of the Ising and Heisenberg case. While a quantum spin-liquid ground state was originally proposed in zero field [56], the ground state has since been shown to be ordered in a coplanar Y phase, in which one spin (labelled as A) points along the Ising direction, and the other two make angles $\pm\theta$ with the Ising axis in the opposite sense, see Fig. 2.9 [57]. The angle θ ranges from 60° in the Heisenberg limit to 0° in the Ising limit

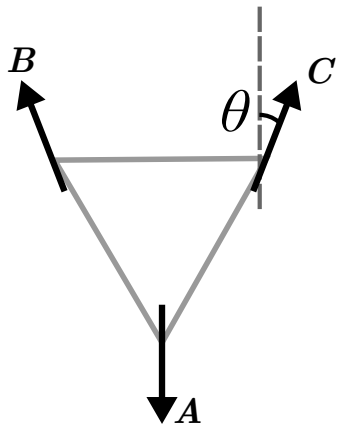

Figure 2.9: The Y phase ground state of the XXZ triangular antiferromagnet in zero field. The A, B and C sublattices are indicated along with the definition of the angle θ. Figure adapted from Ref. [57].

and is given at the mean field level by [57]

$$\cos\theta = \frac{1}{\frac{J_{xy}}{J_z} + 1}. \tag{2.25}$$

The degeneracy of this ground state is $U(1) \times Z_3 \times Z_2$. This corresponds to the choice of the direction in the xy plane in which spins B and C are pointing, the possible permutations of the 3 sublattices between them and whether the unique spin points along $+z$ or $-z$.

It is important to note that the degeneracy of the classical mean field ground state is much greater, being $U(1) \times U(1) \times Z_3$. The second $U(1)$ is an artefact of the mean field approximation, as the angle of the A spin relative to the Ising axis in the ordering plane can be continuously varied while remaining within the ground state manifold, provided that the directions of the B and C spins are adjusted accordingly, leading to an additional $U(1)$ classical degeneracy in addition to the rotational $U(1)$ symmetry of the Hamiltonian (2.24) about the z direction. Quantum fluctuations select the Y phase out of this classically degenerate manifold.

At the linear spinwave level, one expects three spinwave branches in the Y phase, due to the three site unit cell, with one of these gapless at the K point due to breaking of the $U(1)$ rotational symmetry about the z-direction, i.e. a Goldstone mode. In addition, at the linear spinwave level, there is another gapless magnon mode due to the additional classical mean-field $U(1)$ degeneracy, however, this mode is expected

to acquire a small gap due to quantum fluctuations that select the Y phase. As will be discussed in Chapter 8, this is not however what is observed experimentally. Numerical methods seem to reproduce this experimentally observed behaviour [58–60], while an explanation has been suggested in terms of a proximate quantum spin liquid [61], implying that quantum fluctuations in the Ising-like XXZ model are much stronger than can be captured semi-classically by the spinwave approximation.

The ordering described above in zero field is expected to occur as temperature is decreased from the high temperature paramagnetic phase, and to proceed via two transitions in which first the z component, then the xy components order [62]. The zero temperature phase diagram as a function of transverse field is a subject of active study [63, 64], with the phases that are observed depending on the ratio J_{xy}/J_z [63], and will be discussed in detail in Chapter 8.

2.5 Analysis techniques

The two main techniques used in this thesis for detailed comparison between theoretical predictions of given Hamiltonians and experimental data are linear spinwave theory (LSWT) and exact diagonalization (ED). These will each be discussed in turn.

2.5.1 Linear spinwave theory

Linear spinwave theory can be used to calculate dispersions of magnon modes, as well as the correlation functions which are needed to calculate intensities in inelastic neutron scattering, when the ground state of the system can be approximated by a classical mean-field ground state. This requires the spin reduction compared to a classical ground state to be small. Linear spinwave theory is thus generally accurate when a sufficiently large magnetic field is applied that the system is well into the field polarized phase, where quantum fluctuations are entirely absent if the Hamiltonian has rotational symmetry about the applied field direction, or asymptotically suppressed when this is not the case. It can also work within

ordered phases, but corrections to the linear approximation are more likely to be applicable, especially if the spin is small.

A general spin Hamiltonian for spins with quantum number S will be written in terms of the components of the spin S_j^x, S_j^y, S_j^z on each site j. The first step in the linear spinwave calculation is to rotate the spin axes on each sublattice such that the ground state magnetization lies along the *local* z direction [65]. The spin components can then be written in terms of boson creation and annihilation operators $a_j^\dagger$ and a_j according to the Holstein-Primakoff transformation [66, 67]

$$S_j^+ = S_j^x + iS_j^y = \sqrt{2S}\sqrt{1 - \frac{a_j^\dagger a_j}{2S}}a_j \tag{2.26}$$

$$S_j^- = S_j^x - iS_j^y = \sqrt{2S}a_j^\dagger\sqrt{1 - \frac{a_j^\dagger a_j}{2S}} \tag{2.27}$$

$$S_j^z = S - a_j^\dagger a_j. \tag{2.28}$$

It can be seen from these relations that the Holstein-Primakoff bosons create deviations of the spin from its maximal value and it can be verified that these expressions satisfy the usual spin commutation relations. The factor $\sqrt{1 - a_j^\dagger a_j/(2S)}$ enforces that no more than $2S$ bosons can be present on a given site, as required for this mapping to be valid. In linear spinwave theory however, this factor is set equal to 1, which is permissible if the average number of bosons per site is much less than $2S$. Note that a different species of boson is required for each magnetic sublattice.

These expressions can then be substituted into the original spin Hamiltonian. This will in general result in a constant term of order S^2, terms quadratic in the boson operators of order S and terms higher order in both $1/S$ and the boson operators. In linear spinwave theory, only the terms up to quadratic order in the boson operators are kept. This is often justified by treating $1/S$ as a small parameter, which would imply that LSWT cannot be used when $S = 1/2$. While it is true that the spectrum with $S = 1/2$ is often somewhat renormalized from the linear spinwave prediction, LSWT nonetheless often produces much better results than would be expected based on an expansion which treats $1/S$ as a small parameter even when $S = 1/2$. This can be understood by realising that this

expansion also treats $a_j^\dagger a_j$ as a small parameter, and can therefore be of use even if $1/S$ is not small as long as the spin deviation is small.

Due to the lattice translational invariance (a periodic crystal structure is assumed), the magnetic excitations will have well defined momentum and the next step is therefore to Fourier transform the boson operators. This can be done by substituting in the expression

$$a_j = \frac{1}{\sqrt{N}} \sum_{\boldsymbol{k}} a_{\boldsymbol{k}} e^{-i\boldsymbol{k}\cdot\boldsymbol{R}_j}, \tag{2.29}$$

where $\boldsymbol{k}$ is the wavevector, $\boldsymbol{R}_j$ is the position of the jth site, and N is the number of unit cells. Again, a species of Fourier transformed boson is needed for each sublattice in the magnetic unit cell.

After making these substitutions, the Hamiltonian can be written as [68]

$$\mathcal{H} = E_{\mathrm{GS}} + \frac{1}{2} \sum_{\boldsymbol{k}} \mathsf{X}_{\boldsymbol{k}}^\dagger \mathsf{H}_{\boldsymbol{k}} \mathsf{X}_k. \tag{2.30}$$

Here,

$$\mathsf{X}_{\boldsymbol{k}} = \begin{pmatrix} \boldsymbol{a}_{\boldsymbol{k}} \\ \boldsymbol{a}_{-\boldsymbol{k}}^\dagger \end{pmatrix}, \tag{2.31}$$

where $\boldsymbol{a}_{\boldsymbol{k}}$ is an n-element column vector of boson annihilation operators corresponding to the n magnetic sublattices in the magnetic unit cell.

Similarly to the way in which the TFIC Hamiltonian was solved in Sec. 2.4.1.1, this Hamiltonian can be diagonalized by a Bogoliubov transformation, i.e., the column vector of operators $\mathsf{X}_{\boldsymbol{k}}$ is written as

$$\mathsf{X}_{\boldsymbol{k}} = \mathsf{S}_{\boldsymbol{k}} \mathsf{X}'_{\boldsymbol{k}}, \tag{2.32}$$

where the transformation matrix $\mathsf{S}_{\boldsymbol{k}}$ does not have to be unitary. This time, it is boson commutation relations that must be conserved rather than fermion commutation relations. This can be done by using the procedure of Ref. [68], which is as follows. The matrix g is defined to be the matrix of commutators of the boson operators, i.e.,

$$\mathsf{g} = \mathsf{X}\mathsf{X}^\dagger - \mathsf{X}^\dagger\mathsf{X} = \begin{pmatrix} \mathbb{1} & 0 \\ 0 & -\mathbb{1} \end{pmatrix}, \tag{2.33}$$

where $\mathbb{1}$ is the $n \times n$ identity matrix. The matrix $\mathsf{S}_{\boldsymbol{k}}$ is then chosen to be the one that diagonalizes the product $\mathsf{g}\mathsf{H}_{\boldsymbol{k}}$, i.e.,

$$\mathsf{S}_{\boldsymbol{k}}^{-1}\mathsf{g}\mathsf{H}_{\boldsymbol{k}}\mathsf{S}_{\boldsymbol{k}} = \Lambda_{\boldsymbol{k}}, \tag{2.34}$$

where $\Lambda_{\boldsymbol{k}}$ is diagonal. It is found that $\Lambda_{\boldsymbol{k}} = \mathsf{g}\Omega_{\boldsymbol{k}}$, where $\Omega_{\boldsymbol{k}}$ is diagonal and its entries are the n energies of the spinwave modes, followed by the same values again. By diagonalizing $\mathsf{H}_{\boldsymbol{k}}$ at each wavevector of interest, it is possible to calculate the dispersion relation for each of the n magnon modes. It is also possible to use more computationally efficient methods to compute S and Ω which take advantage of the fact that H is Hermitian and positive definite [69].

The elements of the transformation matrix $\mathsf{S}_{\boldsymbol{k}}$ can be used in order to calculate the predicted inelastic neutron scattering intensities. As will be discussed in Chapter 3.1.1.3, inelastic neutron scattering intensities are determined by the components of the dynamical structure factor,

$$S^{\alpha\beta}(\boldsymbol{Q},\omega) = \sum_{\lambda}\langle \mathrm{GS}|S^{\alpha}(-\boldsymbol{Q})|\lambda\rangle\langle\lambda|S^{\beta}(\boldsymbol{Q})|\mathrm{GS}\rangle\delta(E_{\lambda}-\hbar\omega), \tag{2.35}$$

where the g-factors and Bohr magneton have been omitted for simplicity, $|\mathrm{GS}\rangle$ is the ground state, λ labels excited states, with E_{λ} being the energy above the ground state, and it has been assumed that the calculation is being done at zero temperature.

Now, it is useful to note that due to the form of the column vector $\mathsf{X}_{\boldsymbol{k}}$, the matrix $\mathsf{S}_{\boldsymbol{k}}$ must be such that the transformation (2.32) can be written as

$$a_{\boldsymbol{k},j} = \sum_{m} u^{*}_{jm}(-\boldsymbol{k})b_{\boldsymbol{k},m} + v_{jm}(\boldsymbol{k})b^{\dagger}_{-\boldsymbol{k},m} \tag{2.36}$$

$$a^{\dagger}_{-\boldsymbol{k},j} = \sum_{m} v^{*}_{jm}(-\boldsymbol{k})b_{\boldsymbol{k},m} + u_{jm}(\boldsymbol{k})b^{\dagger}_{-\boldsymbol{k},m}, \tag{2.37}$$

where j labels the sublattices and $b^{\dagger}_{\boldsymbol{k},m}$ are the normal mode (magnon) creation operators. The normal mode annihilation operators have the property that $b_{\boldsymbol{k},m}|\mathrm{GS}\rangle = 0$ for any $\boldsymbol{k}, m$, which can be understood as there being no magnons present in the ground state. Using these relations, together with the definitions (2.35) and

(2.26)-(2.28), it can be readily seen that

$$S^{xx}(\boldsymbol{Q},\omega) = \sum_m \left| \sum_j u_{jm}(\boldsymbol{Q}) + v_{jm}(\boldsymbol{Q}) \right|^2 \delta(\hbar\omega_m(\boldsymbol{Q}) - \hbar\omega), \tag{2.38}$$

$$S^{yy}(\boldsymbol{Q},\omega) = \sum_m \left| \sum_j v_{jm}(\boldsymbol{Q}) - u_{jm}(\boldsymbol{Q}) \right|^2 \delta(\hbar\omega_m(\boldsymbol{Q}) - \hbar\omega), \tag{2.39}$$

$$\begin{aligned} S^{xy}(\boldsymbol{Q},\omega) =& S^{yx}(\boldsymbol{Q},\omega)^* = -S^{yx}(\boldsymbol{Q},\omega) \\ =& i \sum_m \left(\sum_{j'} v_{jm}(\boldsymbol{Q}) - u_{jm}(\boldsymbol{Q}) \right)^* \left(\sum_j v_{jm}(\boldsymbol{Q}) + u_{jm}(\boldsymbol{Q}) \right) \delta(\hbar\omega_m(\boldsymbol{Q}) - \hbar\omega). \end{aligned} \tag{2.40}$$

It can be seen that $S^{xy} = -S^{yx}$ and these components will therefore cancel each other in an unpolarized neutron experiment (see Chapter 3.1.1.3) [70] but can be measured separately using polarization analyis.

The contributions to S^{zz} come in two types. This can be seen by substituting (2.28) into (2.35), and examining the action of S^z on the ground state $|\mathrm{GS}\rangle$. The action of S (here a pure number) on the ground state is simply to multiply it by a constant, so $S|\mathrm{GS}\rangle$ has no overlap with excited states, and this term therefore contributes to Bragg scattering, as will be discussed in Chapter 3.1.1.3. The action of the $a^\dagger a$ term can be seen by expanding it in terms of normal mode operators. The only term in the expansion that does not kill the ground state (and therefore contributes to S^{zz} at zero temperature) is the term with two magnon creation operators. The corresponding two magnon annihilation operators are required in the other factor in order to return to the ground state. The inelastic contribution to S^{zz} is therefore given by

$$S^{zz}(\boldsymbol{Q},\omega) = \sum_{\boldsymbol{k},\boldsymbol{k'}} \delta\left(\boldsymbol{Q} - \boldsymbol{k} - \boldsymbol{k'}\right) \sum_{m,m'} \delta\left(\hbar\omega - E^m_{\boldsymbol{k}} - E^{m'}_{\boldsymbol{k'}}\right) f_{m,m'}(\boldsymbol{k},\boldsymbol{k'}), \tag{2.41}$$

$$f_{m,m'}(\boldsymbol{k},\boldsymbol{k'}) = \sum_{j,j'} u^*_{jm}(\boldsymbol{k}) v^*_{jm'}(\boldsymbol{k'}) u_{j'm}(\boldsymbol{k}) v_{j',m'}(\boldsymbol{k'}). \tag{2.42}$$

The components $S^{xz}, S^{yz}, S^{zx}, S^{zy}$ are 0 because if the excited state $|\lambda\rangle$ is reached by adding two magnons to the ground state, it is not possible to get back to the ground state by removing only one magnon. Note that the expressions given here for $S^{\alpha\beta}$ are in the local frame. The physically relevant components

of $S^{\alpha\beta}$ must be computed in the global frame, and general expressions for these will be given in Chapter 8.5.2.

While linear spinwave theory is not accurate when there are strong quantum fluctuations, it is nonetheless useful for gaining an understanding of the spectrum, especially well into the field polarized phase when quantum fluctuations are suppressed. For one or two sublattice systems, linear spinwave calculations can be done fully analytically. When the magnetic unit cell contains multiple sublattices, the one-magnon dispersions and scattering intensities can be calculated numerically using software such as SpinW [65].

2.5.2 Exact diagonalization

The other technique used extensively in this thesis is exact diagonalization, i.e., numerically diagonalizing the Hamiltonian on small system sizes. This technique is very computationally intensive since the number of basis states scales as $(2S+1)^N$, for spin S and number of sites N. Nonetheless, it can be very powerful as it is exact, and is particularly useful when the system can be treated as one-dimensional, since the number of basis states then scales as $(2S+1)^L$, where L is the linear dimension of the system, rather than $(2S+1)^{L^2}$ or $(2S+1)^{L^3}$ for two or three dimensional systems, which is even more prohibitive [36]. This is important because finite size effects and wavevector resolution both depend on L.

The code used for the exact diagonalization calculations in Chapters 4 to 7 was custom written, starting from the code used in Ref. [71], and a brief description of the way it works will now follow.

The Hamiltonian for a given number of sites can be constructed as a matrix, and the natural basis in which to do this is the tensor product of the individual site S^z bases. Concretely, taking the example of $S = 1/2$, which is both the simplest case and the one of relevance here, this is the basis $|\downarrow\downarrow\ldots\downarrow\downarrow\rangle$, $|\downarrow\downarrow\ldots\downarrow\uparrow\rangle$, $|\downarrow\downarrow\ldots\uparrow\downarrow\rangle$ and so on; in the case $S = 1/2$, these states can be represented by numbers written in binary. The Hamiltonian can be constructed using sums and products of spin

operators. The single site spin operators S^α can be constructed explicitly. The α component of the spin operator on site j, S_j^α can then be constructed as

$$S_j^\alpha = \underbrace{\mathbb{1} \otimes \mathbb{1} \otimes \ldots}_{j-1} \otimes S^\alpha \otimes \underbrace{\mathbb{1} \otimes \ldots}_{N-j} \tag{2.43}$$

where $\mathbb{1}$ is the $(2S+1) \times (2S+1)$ identity operator and $\otimes$ is the Kronecker product operation (which is built-in in languages such as Matlab [72] in which this code was written). The computation requires significantly less memory if the Hamiltonian is constructed using sparse matrices, as, assuming that interactions are short-ranged, most elements of the Hamiltonian matrix will be zero [36]. In all of the calculations in this thesis, the Hamiltonian was constructed to have periodic boundary conditions in order both to avoid edge effects and to be invariant under lattice translations so that the excitations have well defined momentum.

The Hamiltonian can then be numerically diagonalized. For the calculations reported in this thesis, only the low energy subspace was required, and the speed and memory usage of the calculation can therefore be significantly improved by using Lanczos algorithms to retain only the eigenvectors corresponding to the lowest eigenvalues. The relevant algorithms are also implemented as built-in functions in Matlab [72]. Letting the number of eigenvectors kept in the calculation be n, the result of the diagonalization is thus a diagonal $n \times n$ matrix of eigenvalues Ω and a $(2S+1)^N \times n$ matrix of eigenvectors V.

Many quantities can be extracted using the eigenvalues Ω and eigenvectors V of the Hamiltonian. First, the $(2S+1)^N \times (2S+1)^N$ matrices S_j^α are transformed to the energy eigenstate basis resulting in $n \times n$ matrices $\tilde{S}_j^\alpha$ as

$$\tilde{S}_j^\alpha = V^\dagger S_j^\alpha V. \tag{2.44}$$

In order to extract the dynamical structure factor in Chapters 4 to 6, Fourier transformed spin operators were constructed as

$$\tilde{S}^\alpha(\boldsymbol{Q}) = \frac{1}{N} \sum_j e^{i\boldsymbol{Q}\cdot\boldsymbol{R}_j} \tilde{S}_j^\alpha \tag{2.45}$$

where $\boldsymbol{R}_j$ is the position of site j. The dynamical structure factor was then calculated using the expression (2.35), using the elements of the relevant Fourier transformed matrices and the corresponding energy eigenvalues. The results of these calculations were multiplied by the relevant g-factors as necessary (see Chapter 3.1.1.3) in order to calculate the predicted inelastic neutron scattering intensity, as displayed in Chapters 4 to 6. These calculations have finite wavevector resolution since the only physically meaningful momenta are those with the momentum along the chain satisfying $Q = 2\pi m/(N_{\text{cell}}a)$ where m is an integer, N_{cell} is the number of unit cells used in the calculation (in general different from the number of sites) and a is the length of the unit cell. The energies of particular modes as a function of wavevector, required for the fits performed in Chapter 5, were calculated based on which eigenstates had non-negligible values of S^{xx} at which wavevectors, following the method used in Ref. [71]. This method would not have worked if the states of interest had no overlap with states accessible from the ground state by flipping a single spin, but such states would also not have been observable in inelastic neutron scattering.

In order to extract the magnetization, as used in Chapter 7, the spin operators $\tilde{S}^{\alpha}_j$ on each site were averaged to give $\tilde{S}^{\alpha} = \frac{1}{N}\sum_j \tilde{S}^{\alpha}_j$. The expectation value of the spin along the α direction per site at a temperature T was then calculated as

$$\langle \tilde{S}^{\alpha} \rangle = \frac{1}{Z} \sum_{\lambda} e^{-\frac{\Omega_\lambda}{k_B T}} \tilde{S}^{\alpha}_{\lambda\lambda} \tag{2.46}$$

where λ labels eigenstates, Ω_λ is the energy of state λ, the $\tilde{S}^{\alpha}_{\lambda\lambda}$ are the diagonal elements of the matrix $\tilde{S}^{\alpha}$, and Z is the partition function $Z = \sum_\lambda \exp\{[-\Omega_\lambda/(k_B T)]\}$. The results were then multiplied by the relevant g-factors, as detailed in Appendix B.

The advantages of exact diagonalization are that no approximations have to be made, such that the technique is unbiased [36], and that there is no restriction on the character of the states that can be accessed in this way[1] or on the complexity of the Hamiltonian. The disadvantages are that, as previously mentioned, the

[1] While the algorithm used in this thesis can only identify the wavevector dependence of modes with a finite overlap with a single spin-flip mode, it is also possible to avoid this issue by using a basis of momentum eigenstates from the start, as implemented in QuSpin [73], which was not used in this thesis in order to integrate more easily with existing code and allow more flexibility in the quantities that were being calculated.

calculation is very computationally costly, so only small numbers of sites can be used. This leads to finite size effects:

- Only finite wavevector resolution is available, as discussed above.
- Only a finite number of states can be accessed which means that the energy spacing of states is always discrete. This makes it difficult to identify continua unambiguously.
- Long wavelength behaviour is not well captured. This becomes important near quantum critical points and means that the gap closing behaviour is not well reproduced.
- There is no spontaneous symmetry breaking, as this only happens in the thermodynamic limit. Therefore, in order to obtain numerically a single magnetic domain in ordered phases (rather than a superposition of the symmetry breaking states), it is necessary to add to the Hamiltonian an additional (small) biasing field, which can be implemented as a self-consistent mean field.

For these reasons, while exact diagonalization is used extensively in this thesis, other techniques are sometimes used instead or in addition.

3 Experimental techniques

This chapter describes the experimental techniques that are used in this thesis. The main technique used is neutron scattering and this is therefore described in some depth. First, the cross-section for neutron scattering will be discussed, both for nuclear scattering and for magnetic scattering, as the latter especially is important for interpreting the results of this thesis. Most of the neutron scattering experiments reported in this thesis were time-of-flight inelastic neutron scattering (neutron spectroscopy, INS), and the experimental considerations relevant to this technique are discussed next. Time-of-flight neutron diffraction results are reported in Chapter 8, and relevant considerations are also discussed. Chapter 7 uses vibrating sample magnetometry (VSM), which is also described, as well as the tools that were developed for checking the alignment of samples once attached to the VSM holder.

3.1 Neutron scattering

Neutrons are a very valuable tool for investigating condensed matter systems. Their mass of $m_n = 1.675 \times 10^{-27}$ kg means that their dispersion relation is very well suited to probing condensed matter systems: neutrons which are thermalized at room temperature (i.e. with an energy of 25.3 meV) have a wavelength of 1.798 Å [74], which means that their energy is comparable to the energies of lattice vibrations

and their wavelength is comparable to the lattice parameters of condensed matter systems. The other important property of neutrons for the systems investigated in this thesis is that they have a magnetic moment, meaning that they can interact with magnetic field gradients and thus measure magnetic structures and magnetic excitations, as will be discussed more in the following subsection. In addition, while neutrons do have a magnetic moment, they do not have an electric charge. This means that they do not interact strongly with matter, making them highly penetrating. While this means that large samples are needed, it also means that measurements are not sensitive to surface effects and that neutrons can penetrate many sample environments. For all of these reasons, neutron scattering is the main technique which has been used in this thesis. It will only be possible to give a relatively brief discussion of the technique here; for more details see, e.g. [70, 74–76].

3.1.1 The neutron scattering cross-section

The following discussion will largely follow the discussions in Refs. [70] and [74].

3.1.1.1 Definitions

The total scattering cross-section is defined by the relation [70, 77]

$$\sigma = \frac{n_{\text{scattered}}}{\Phi}, \tag{3.1}$$

where $n_{\text{scattered}}$ is the total number of neutrons scattered in all directions per unit time and Φ is the incident flux of neutrons, defined as the number of incident neutrons per unit time per unit area. As expected, σ has units of area.

Since in real instruments, there are only ever detectors in certain directions, it will also be useful to consider the differential cross-section

$$\frac{\mathrm{d}\sigma}{\mathrm{d}\Omega} = \frac{\mathrm{d}n_{\text{scattered}}(2\theta, \phi)}{\Phi \mathrm{d}\Omega}, \tag{3.2}$$

where $\mathrm{d}n_{\text{scattered}}(2\theta, \phi)$ is the number of neutrons scattered per second into a solid angle $\mathrm{d}\Omega$ in the direction $(2\theta, \phi)$, see Fig. 3.1. This is the quantity measured by instruments which do not have energy analysis [70].

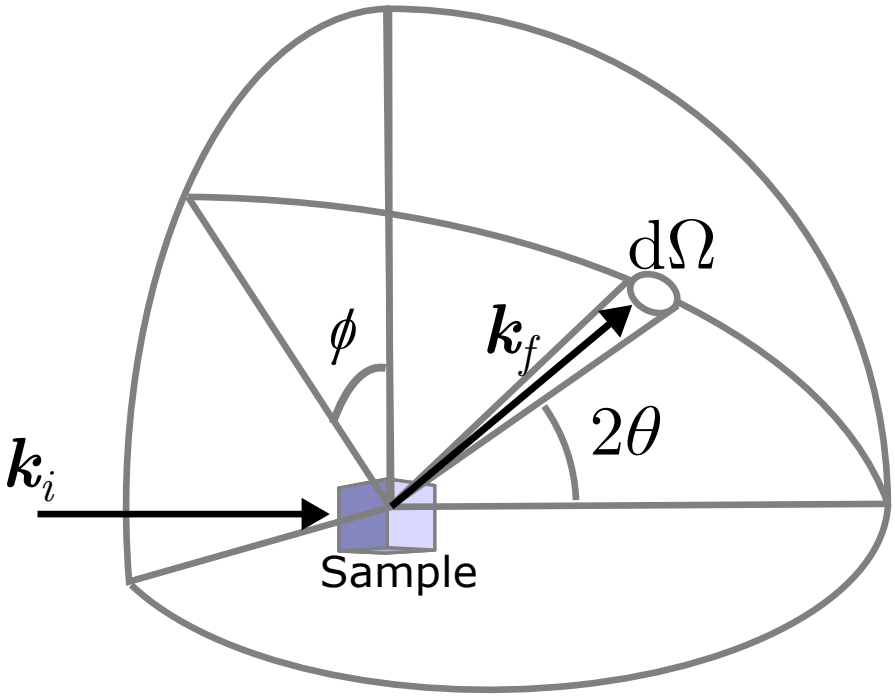

Figure 3.1: Definitions of $\boldsymbol{k}_i$, $\boldsymbol{k}_f$, 2θ, ϕ and $\mathrm{d}\Omega$. $(2\theta, \phi)$ are spherical angles of $\boldsymbol{k}_f$ in a coordinate system with $z \parallel \boldsymbol{k}_i$. Figure adapted from Ref. [74].

The quantity measured by instruments which do have energy analysis is the partial differential cross section. This is given by

$$\frac{\mathrm{d}^2\sigma}{\mathrm{d}\Omega \mathrm{d}E_f} = \frac{\mathrm{d}^2 n_{\mathrm{scattered}}(2\theta, \phi, E_f)}{\Phi \mathrm{d}\Omega \mathrm{d}E_f}, \tag{3.3}$$

where $\mathrm{d}^2 n_{\mathrm{scattered}}(2\theta, \phi, E_f)$ is the number of neutrons scattered per second into a solid angle $\mathrm{d}\Omega$ in the direction $2\theta, \phi$, with final energy between E_f and $E_f + \mathrm{d}E_f$ [70, 74].

More specifically, the quantity

$$\left(\frac{\mathrm{d}^2\sigma}{\mathrm{d}\Omega \mathrm{d}E_f}\right)_{(\boldsymbol{k}_i, s_i, \lambda_i) \to (\boldsymbol{k}_f, s_f, \lambda_f)} \tag{3.4}$$

will be considered, where $\boldsymbol{k}$ is the wavevector of the neutron, s is the spin of the neutron and λ labels the state of the sample, and where the i and f subscripts stand for 'initial' and 'final'. Now, the states $\lambda_{i,f}$ cannot be known, and in this thesis, polarization analysis of the neutrons will not be considered. Therefore, the possible initial states must be averaged over and the possible final states summed

over [74], such that the measured quantity is

$$\left(\frac{\mathrm{d}^2\sigma}{\mathrm{d}\Omega\mathrm{d}E_f}\right)_{\boldsymbol{k}_i\to\boldsymbol{k}_f} = \sum_{s_i s_f} P_{s_i} \sum_{\lambda_i\lambda_f} P_{\lambda_i} \left(\frac{\mathrm{d}^2\sigma}{\mathrm{d}\Omega\mathrm{d}E_f}\right)_{(\boldsymbol{k}_i,s_i,\lambda_i)\to(\boldsymbol{k}_f,s_f,\lambda_f)}, \tag{3.5}$$

where P_{s_i} and P_{λ_i} are the respective probabilities for the neutron to start in the spin state s_i and for the sample to start in state λ_i. This expression can be written as

$$\left(\frac{\mathrm{d}^2\sigma}{\mathrm{d}\Omega\mathrm{d}E_f}\right)_{\boldsymbol{k}_i\to\boldsymbol{k}_f} = \sum_{s_i s_f \lambda_i\lambda_f} P_{s_i} P_{\lambda_i} \frac{W_{(\boldsymbol{k}_i,s_i,\lambda_i)\to(\boldsymbol{k}_f,s_f,\lambda_f)}\mathrm{d}\Omega\mathrm{d}E_f}{\Phi\mathrm{d}\Omega\mathrm{d}E_f}, \tag{3.6}$$

where $W_{(\boldsymbol{k}_i,s_i,\lambda_i)\to(\boldsymbol{k}_f,s_f,\lambda_f)}$ is the rate of transition from the state $(\boldsymbol{k}_i, s_i, \lambda_i)$ to the state $(\boldsymbol{k}_f, s_f, \lambda_f)$.

Some approximations can now be made to evaluate this expression. Firstly, the incident neutrons are assumed to be plane waves, such that their flux is the product of their velocity and their density. The neutrons used in scattering experiments from condensed matter are non-relativistic so their speed is $\hbar k_i/m_n$ where $k_i{=}|\boldsymbol{k}_i|$, and assuming a single incident neutron in a box of volume $\mathcal{V}$, the flux becomes

$$\Phi = \frac{\hbar k_i}{\mathcal{V} m_n}. \tag{3.7}$$

Next, the transition rates $W_{(\boldsymbol{k}_i,s_i,\lambda_i)\to(\boldsymbol{k}_f,s_f,\lambda_f)}$ can be evaluated using Fermi's golden rule (see most books on quantum mechanics, e.g. Ref. [78]). This states that

$$W_{(\boldsymbol{k}_i,s_i,\lambda_i)\to(\boldsymbol{k}_f,s_f,\lambda_f)} = \frac{2\pi}{\hbar} g(\boldsymbol{k}_f) |\langle \boldsymbol{k}_f s_f \lambda_f | V | \boldsymbol{k}_i s_i \lambda_i \rangle|^2 \delta(E_i + E_{\lambda_i} - E_f - E_{\lambda_f}). \tag{3.8}$$

Here, V is the interaction potential, $E_{i,f}$ are the initial and final neutron energies, $E_{i,f} = \hbar^2 k_{i,f}^2/(2m_n)$, and $g(\boldsymbol{k}_f)\mathrm{d}E_f\mathrm{d}\Omega$ is the number of neutron momentum states with energy between E_f and $E_f + \mathrm{d}E_f$ in the direction of $\mathrm{d}\Omega$. Assuming again that the neutron is in a box of volume $\mathcal{V}$, and that the outgoing neutron is also a plane wave, the density of states is [74]

$$g(\boldsymbol{k}_f)\mathrm{d}E_f\mathrm{d}\Omega = k_f \frac{\mathcal{V} m_n}{(2\pi)^3\hbar^2}\mathrm{d}E_f\mathrm{d}\Omega. \tag{3.9}$$

Now, it can be assumed that the state $|\boldsymbol{k}s\lambda\rangle$ can be written as a tensor product of the states for the neutron position, the neutron spin and the sample state, i.e.

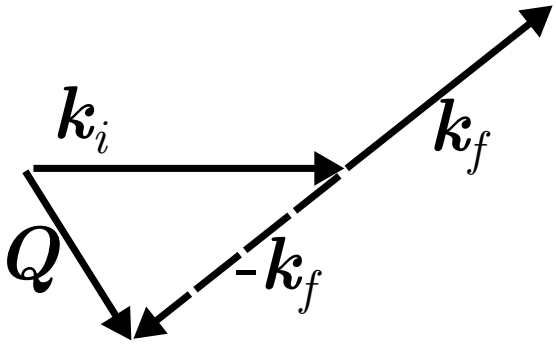

Figure 3.2: The scattering triangle, showing the definitions of $\boldsymbol{Q}$, $\boldsymbol{k}_i$ and $\boldsymbol{k}_f$.

$|\boldsymbol{k}s\lambda\rangle = |\boldsymbol{k}\rangle|s\rangle|\lambda\rangle$. The wavefunction for the state $|\boldsymbol{k}\rangle$ is[1]

$$\psi_{\boldsymbol{k}}(\boldsymbol{r}) = \frac{1}{\sqrt{\mathcal{V}}} e^{i\boldsymbol{k}\cdot\boldsymbol{r}}. \tag{3.10}$$

The matrix element in (3.8) can now be partly evaluated by performing the integral over the spatial coordinates of the neutron. This gives

$$\begin{aligned}\langle \boldsymbol{k}_f s_f \lambda_f | V | \boldsymbol{k}_i s_i \lambda_i \rangle =& \langle s_f \lambda_f | \langle \boldsymbol{k}_f | V | \boldsymbol{k}_i \rangle | s_i \lambda_i \rangle \\ =& \frac{1}{\mathcal{V}} \langle s_f \lambda_f | \int \mathrm{d}\boldsymbol{r}^3 e^{-i\boldsymbol{k}_f\cdot\boldsymbol{r}} V(\boldsymbol{r}) e^{i\boldsymbol{k}_i\cdot\boldsymbol{r}} | s_i \lambda_i \rangle \\ =& \langle s_f \lambda_f | V(\boldsymbol{Q}) | s_i \lambda_i \rangle, \end{aligned} \tag{3.11}$$

where $\boldsymbol{Q} = \boldsymbol{k}_i - \boldsymbol{k}_f$ is the wavevector transfer (see Fig. 3.2) and $V(\boldsymbol{Q})$ is the Fourier transform of $V(\boldsymbol{r})$ with respect to $\boldsymbol{Q}$, into which the factor of $1/\mathcal{V}$ has been absorbed.

Combining together (3.6) to (3.9) and (3.11), the final expression for the partial differential cross-section is [70]

$$\begin{aligned}&\left(\frac{\mathrm{d}^2\sigma}{\mathrm{d}\Omega \mathrm{d}E_f}\right)_{\boldsymbol{k}_i \to \boldsymbol{k}_f} \\ &= \frac{k_f}{k_i}\left(\frac{m_n}{2\pi\hbar^2}\right)^2 \sum_{s_i s_f \lambda_i \lambda_f} P_{s_i} P_{\lambda_i} |\langle s_f \lambda_f | V(\boldsymbol{Q}) | s_i \lambda_i \rangle|^2 \delta(E_{\lambda_f} + E_f - E_{\lambda_i} - E_i). \end{aligned} \tag{3.12}$$

This equation will be the basis for the remainder of the discussion in this subsection. If unpolarized neutrons are used, then $P_{s_i} = 1/2$ for every s_i, and assuming that the sample is thermalized at a temperature T, $P_{\lambda_i} = \exp\left[-E_{\lambda_i}/(k_B T)\right]$. It will be

[1] The assumption that wavefunctions of the incoming and outgoing neutrons are both plane waves applies in the Born approximation, which is valid when scattering is weak, as is always the case when scattering neutrons.

useful in the following to introduce the notation $\hbar\omega = E_i - E_f$. It will also be useful to introduce the scattering function, $S(\boldsymbol{Q}, \omega)$ defined such that

$$\left(\frac{\mathrm{d}^2\sigma}{\mathrm{d}\Omega \mathrm{d}E_f}\right)_{\boldsymbol{k}_i \to \boldsymbol{k}_f} = \frac{k_f}{k_i} S(\boldsymbol{Q}, \omega). \tag{3.13}$$

3.1.1.2 Nuclear scattering

Neutrons interact both with nuclei, via the strong nuclear force, and with magnetic moments, via the electromagnetic interaction. While the main focus of this thesis will be on magnetic scattering, nuclear scattering is also present in all materials. Nuclear scattering can be treated somewhat more simply than magnetic scattering, so several ideas that will also be important for magnetic scattering will first be introduced in this context.

Nuclear scattering length The nucleus (and the range of the strong nuclear force) is very small ($\approx 10^{-15}$ m) compared to the size of the atom and to the wavelengths of the neutrons ($\approx 10^{-10}$ m) used in scattering experiments from condensed matter, so it can be considered as a point particle. As such, the wave scattered from a single (fixed) nucleus will be spherical and can be written as [70, 74]

$$\psi_{\text{scattered}} = -\frac{b}{r} e^{ik_f r}, \tag{3.14}$$

where r is the distance from the nucleus and the quantity b is known as the 'scattering length', which parameterizes the strength of the scattering. The total cross-section for scattering from such a nucleus can be readily seen, using the definition (3.1) above, to be

$$\sigma = 4\pi b^2. \tag{3.15}$$

The scattering length depends on the nuclide (different isotopes of the same element can have different scattering lengths) and varies across the periodic table in a way with no obvious pattern. The scattering length also depends on the relative spin orientation of the neutron and the nucleus and it can be positive or negative [70]. The former fact means that elastic neutron scattering (diffraction) can

distinguish between neighbouring elements more readily than x-ray diffraction and is equally sensitive to light elements as heavy elements. The fact that the scattering length also depends on both the isotope and the total spin of the nucleus-neutron system means that there will nearly always be random variation in the scattering length, even in a perfectly chemically ordered sample.

Because the nuclear interaction is so short ranged, the corresponding interaction potential can be assumed to be a delta function (this is the 'Fermi pseudo-potential'). Inserting a delta function into (3.12) and integrating, and comparing the result to (3.15) to find the pre-factors, the result is found to be [74]

$$V(\boldsymbol{r}) = \frac{2\pi\hbar^2}{m_n} b\delta(\boldsymbol{r}). \tag{3.16}$$

Coherent and incoherent scattering Consider now the scattering from an array of nuclei labelled j, with scattering lengths b_j at positions $\boldsymbol{R}_j$. Combining equations (3.12) and (3.16) gives [74]

$$\begin{aligned}&\left(\frac{\mathrm{d}^2\sigma}{\mathrm{d}\Omega \mathrm{d}E_f}\right)_{\boldsymbol{k}_i \to \boldsymbol{k}_f} \\ &= \frac{k_f}{k_i} \sum_{s_i s_f \lambda_i \lambda_f} P_{s_i} P_{\lambda_i} |\sum_j b_j \langle s_f \lambda_f | e^{i\boldsymbol{Q}\cdot\boldsymbol{R}_j} | s_i \lambda_i \rangle|^2 \delta(E_{\lambda_f} + E_f - E_{\lambda_i} - E_i).\end{aligned} \tag{3.17}$$

Now,

$$|\sum_j b_j \langle s_f \lambda_f | e^{i\boldsymbol{Q}\cdot\boldsymbol{R}_j} | s_i \lambda_i \rangle|^2 = \sum_{j,j'} b_j b_{j'} \langle s_i \lambda_i | e^{-i\boldsymbol{Q}\cdot\boldsymbol{R}_j} | s_f \lambda_f \rangle \langle s_f \lambda_f | e^{i\boldsymbol{Q}\cdot\boldsymbol{R}_{j'}} | s_i \lambda_i \rangle. \tag{3.18}$$

If a sufficiently large system is studied (as will always be the case in practice), the scattering lengths can be replaced with average values. In particular, assuming no correlations between different sites, such that [74]

$$\begin{aligned}\overline{b_j b_{j'}} &= \left(\bar{b}\right)^2, & j \neq j' \\ \overline{b_j b_{j'}} &= \overline{b^2}, & j = j',\end{aligned} \tag{3.19}$$

then,

$$\sum_{j,j'} \overline{b_j b_{j'}} \langle s_i\lambda_i|e^{-i\boldsymbol{Q}\cdot\boldsymbol{R}_j}|s_f\lambda_f\rangle\langle s_f\lambda_f|e^{i\boldsymbol{Q}\cdot\boldsymbol{R}_{j'}}|s_i\lambda_i\rangle = \sum_{j,j'} \left(\overline{b}\right)^2 \langle s_i\lambda_i|e^{-i\boldsymbol{Q}\cdot\boldsymbol{R}_j}|s_f\lambda_f\rangle\langle s_f\lambda_f|e^{i\boldsymbol{Q}\cdot\boldsymbol{R}_{j'}}|s_i\lambda_i\rangle + \sum_j \left[\overline{b^2} - \left(\overline{b}\right)^2\right] \langle s_i\lambda_i|e^{-i\boldsymbol{Q}\cdot\boldsymbol{R}_j}|s_f\lambda_f\rangle\langle s_f\lambda_f|e^{i\boldsymbol{Q}\cdot\boldsymbol{R}_j}|s_i\lambda_i\rangle. \quad (3.20)$$

Here, the first term on the right corresponds to coherent scattering. This depends on correlations between different nuclei, therefore resulting in interference effects [74], and is responsible for, e.g., Bragg peaks (see next paragraph) and scattering from phonons [79]. The second term on the right corresponds to incoherent scattering. This only depends on correlations of a single nucleus with itself in time. To see this, it is helpful to rewrite (3.17) as

$$\left(\frac{\mathrm{d}^2\sigma}{\mathrm{d}\Omega\mathrm{d}E_f}\right)_{\boldsymbol{k}_i\to\boldsymbol{k}_f} = \frac{k_f}{k_i} \sum_{s_i s_f \lambda_i \lambda_f} P_{s_i} P_{\lambda_i} \sum_{jj'} b_j b_{j'} \int \mathrm{d}t\, e^{-i\omega t} \langle s_i\lambda_i|e^{-i\boldsymbol{Q}\cdot\boldsymbol{R}_{j'}(0)} e^{i\boldsymbol{Q}\cdot\boldsymbol{R}_j(t)}|\lambda_i s_i\rangle. \quad (3.21)$$

Here, the notation $\hbar\omega = E_i - E_f$ has been used, and $\boldsymbol{R}_j(t)$ is the time evolved operator in the Heisenberg picture. A derivation of this result can be found in many sources [70, 74–76], and proceeds by re-writing the delta function in (3.17) as a Fourier transform, using the fact that the E_λ are eigenstates of the scattering system's Hamiltonian, and then introducing Heisenberg operators. As in (3.20), it is then possible to take averages and split the expression into one part which depends on correlations between different sites and the other which depends only on single sites, that is, the incoherent part. The incoherent scattering therefore does not result in interference effects, and thus has only very weak wavevector dependence. In inelastic neutron scattering, the incoherent scattering contributes a strong peak in energy (though less strong than the Bragg peaks) centred on the elastic line at all wavevectors. The rest of this discussion will focus on coherent scattering, as the effects of incoherent scattering will be considered to be background for the purposes of this thesis. The above discussion assumes only one element (or no chemical order

if multiple elements are present) but the ideas can be readily extended for cases with different elements at different sites in the unit cell.

Elastic and inelastic scattering Elastic coherent scattering is also known as diffraction and obeys Bragg's law. To see this, consider again (3.17), and keep only the coherent part, which is equivalent to replacing b_i with $\bar{b}_m$, where it is now assumed that there could be distinct sites labelled m and the average is only over the nuclei that can occupy that site. Elastic scattering is scattering where the state of the system does not change, i.e., $\lambda_f = \lambda_i$, so $E_f = E_i$ which implies $k_f = k_i$. In addition, it is not possible for the spin of the neutron to change during elastic nuclear scattering. Assuming now a crystalline material with unit cells labelled by j at positions $\boldsymbol{R}_j$ and sites labelled m within the unit cell corresponding to atoms at $\boldsymbol{R}_j + \boldsymbol{r}_m$, the coherent elastic nuclear partial differential cross-section is therefore given by

$$\left(\frac{\mathrm{d}^2\sigma}{\mathrm{d}\Omega \mathrm{d}E_f}\right)_{\text{coh, el}} = \sum_{s_i s_f \lambda_i \lambda_f} P_{s_i} P_{\lambda_i} \Big| \sum_{\substack{\text{unit cells,} \\ j}} \sum_{\substack{\text{unit cell} \\ \text{sites,} m}} \bar{b}_m e^{i\boldsymbol{Q}\cdot\boldsymbol{R}_j} e^{i\boldsymbol{Q}\cdot\boldsymbol{r}_m} \Big|^2 \delta(E_f - E_i), \quad (3.22)$$

where the subscript $\boldsymbol{k}_i \to \boldsymbol{k}_f$ has been dropped for brevity. If the $\boldsymbol{R}_j$ form a perfect static lattice, it can be seen that this expression will cancel out for all $\boldsymbol{Q}$ except where $\boldsymbol{Q}$ is a reciprocal lattice vector, defined as $e^{i\boldsymbol{Q}\cdot\boldsymbol{R}_j} = 1$ for all $\boldsymbol{R}_j$, i.e.

$$\left(\frac{\mathrm{d}^2\sigma}{\mathrm{d}\Omega \mathrm{d}E_f}\right)_{\text{coh, el}} = N \sum_{s_i s_f \lambda_i \lambda_f} P_{s_i} P_{\lambda_i} \sum_l \delta(\boldsymbol{Q} - \boldsymbol{G}_l) |F_{\text{nuclear}}(\boldsymbol{Q})|^2 \delta(E_f - E_i), \quad (3.23)$$

where $\boldsymbol{G}_l$ are the reciprocal lattice vectors, N is the number of sites and

$$F_{\text{nuclear}}(\boldsymbol{Q}) = \sum_{\substack{\text{unit cell} \\ \text{sites,} m}} \bar{b}_m e^{i\boldsymbol{Q}\cdot\boldsymbol{r}_m} \quad (3.24)$$

is the nuclear structure factor.

All scattering which is not elastic is inelastic and in this case $\lambda_f \neq \lambda_i$. Inelastic nuclear scattering is due to the creation or absorption by the neutron of one or more phonons. Inelastic (coherent) magnetic scattering is due to the creation (or absorption) of magnons, or more exotic excitations, such as were discussed in Chapter 2 and which will be discussed in much more detail in Chapters 4 and 6.

The Debye-Waller factor In reality, crystalline lattices are never perfectly static, due to thermal vibrations and zero-point quantum motion even at the lowest temperatures. It can be shown that in this case (see, e.g. Refs. [70] or [74]), the structure factor becomes

$$F_{\text{nuclear}}(\boldsymbol{Q}) = \sum_{\substack{\text{unit cell} \\ \text{sites},m}} \bar{b}_m e^{i\boldsymbol{Q}\cdot\boldsymbol{r}_m} e^{-W_m(\boldsymbol{Q})}. \tag{3.25}$$

In this expression, $e^{-W_m(\boldsymbol{Q})}$ is known as the 'Debye-Waller factor' and quantifies the displacement of atom m from its ideal position. In the general case it is given by [80]

$$e^{-W_m(\boldsymbol{Q})} = \exp\left(-2\pi^2 \sum_{l}^{3}\sum_{l'}^{3} Q_l \langle \Delta x^l \Delta x^{l'} \rangle Q_{l'}\right), \tag{3.26}$$

where Δx^l is the displacement along the lth crystallographic direction in units of the lattice parameters and $\langle\rangle$ denotes a general statistical average. The tensor quantities $\beta^{ll'} = 2\pi^2\langle \Delta x^l \Delta x^{l'} \rangle$ are known as the anisotropic displacement parameters.

3.1.1.3 Magnetic scattering

The magnetic interaction While nuclear scattering is due to the interaction of neutrons with atomic nuclei via the strong nuclear force, magnetic scattering is due to the interaction of neutrons with the magnetic field generated by the electrons. This discussion will again largely follow Refs. [70] and [74].

The energy of the neutron magnetic moment in a magnetic field $\boldsymbol{B}_{\text{eff}}$ due to the electrons is given by [70, 76]

$$\mathcal{H} = -\boldsymbol{\mu}_n \cdot \boldsymbol{B}_{\text{eff}}, \tag{3.27}$$

where μ_n is the magnetic moment of the neutron and is given by [70]

$$\boldsymbol{\mu}_n = -2\gamma\mu_N \boldsymbol{s}_n. \tag{3.28}$$

Here, μ_N is the nuclear magneton, $\mu_N = e\hbar/(2m_p)$ where e is the electron charge and m_p is the mass of a proton [74], $\gamma = 1.913$ is a constant, and $\boldsymbol{s}_n$ is the neutron spin, which has eigenvalues $s = \pm 1/2$. Equation (3.27) can be taken to define the magnetic interaction potential.

The effective magnetic field $\boldsymbol{B}_{\text{eff}}$ due to the jth electron has contributions from both the electron spin and the electron orbital motion. The contribution at the origin from the spin of the electron (taken to be at $\boldsymbol{R}_j$) is [70, 74]

$$\boldsymbol{B}_{s,j} = -\frac{\mu_0}{4\pi}\boldsymbol{\nabla} \times \left(\frac{\boldsymbol{\mu}_{e,j} \times \hat{\boldsymbol{R}}_j}{R_j^2}\right), \tag{3.29}$$

where $R_j = |\boldsymbol{R}_j|$, $\hat{\boldsymbol{R}}_j = \boldsymbol{R}_j/R_j$ and

$$\boldsymbol{\mu}_{e,j} = -g_e \mu_B \boldsymbol{s}_{e,j} \tag{3.30}$$

is the electron's magnetic moment. Here, $\mu_B = e\hbar/(2m_e) = 1/17.276$ meV/T is the Bohr magneton, where m_e is the electron mass, g_e is the electron spin g-factor and will be taken to be 2 and $\boldsymbol{s}_{e,j}$ is the spin of the jth electron. The orbital current contribution to the magnetic field can be calculated using the Biot-Savart law [74] and is given by

$$\boldsymbol{B}_{L,j} = \frac{\mu_0 \mu_B}{2\pi\hbar} \frac{\boldsymbol{p}_{e,j} \times \hat{\boldsymbol{R}}_j}{R_j^2}, \tag{3.31}$$

where $\boldsymbol{p}_{e,j}$ is the momentum of the jth electron. The interaction potential for interaction between the neutron and the jth electron is then [74, 75]

$$V_{m,j} = \gamma \mu_N \mu_B \frac{\mu_0}{\pi} \boldsymbol{s}_n \cdot \left[\boldsymbol{\nabla} \times \left(\frac{\boldsymbol{s}_{e,j} \times \hat{\boldsymbol{R}}_j}{R_j^2}\right) + \frac{1}{\hbar}\frac{\boldsymbol{p}_{e,j} \times \hat{\boldsymbol{R}}_j}{R_j^2}\right]. \tag{3.32}$$

The total interaction potential is the sum of these contributions from all of the electrons in the system.

To proceed, it is then necessary to find the matrix elements of this interaction potential with the states $|\boldsymbol{k}s\lambda\rangle$. As with the nuclear contribution, it is possible to carry out the integration over the spatial coordinates of the neutron first, i.e., calculate the matrix element $\langle \boldsymbol{k}_f | V_{m,j} | \boldsymbol{k}_i \rangle$, which is equivalent to taking the Fourier transform of the interaction potential. By making use of some vector calculus identities, it can be shown that [70, 74, 75]

$$\langle \boldsymbol{k}_f | V_{m,j} | \boldsymbol{k}_i \rangle = -4\gamma \mu_N \mu_B \mu_0 \boldsymbol{s}_n \cdot \left[\hat{\boldsymbol{Q}} \times (\boldsymbol{s}_{e,j} \times \hat{\boldsymbol{Q}}) + \frac{i}{\hbar Q}(\boldsymbol{p}_{e,j} \times \hat{\boldsymbol{Q}})\right] e^{i\boldsymbol{Q}\cdot\boldsymbol{R}_j}. \tag{3.33}$$

Substituting this expression into (3.12), and summing over all the electrons in the system, the expression for the partial differential cross-section becomes [70, 74, 79]

$$\left(\frac{\mathrm{d}^2\sigma}{\mathrm{d}\Omega \mathrm{d}E_f}\right)_{\boldsymbol{k}_i \to \boldsymbol{k}_f} = \frac{k_f}{k_i}(2\gamma r_0)^2 \sum_{s_i s_f \lambda_i \lambda_f} P_{s_i} P_{\lambda_i} |\langle s_f \lambda_f | \boldsymbol{s}_n \cdot \boldsymbol{D}_\perp(\boldsymbol{Q}) | s_i \lambda_i \rangle|^2 \delta(E_{\lambda_f} + E_f - E_{\lambda_i} - E_i). \tag{3.34}$$

where $r_0 = \mu_0 e^2/(4\pi m_e)$ is the classical radius of the electron and

$$\boldsymbol{D}_\perp(\boldsymbol{Q}) = \sum_j \left[\hat{\boldsymbol{Q}} \times (\boldsymbol{s}_{e,j} \times \hat{\boldsymbol{Q}}) + \frac{i}{\hbar Q}(\boldsymbol{p}_{e,j} \times \hat{\boldsymbol{Q}})\right] e^{i\boldsymbol{Q}\cdot\boldsymbol{R}_j} \tag{3.35}$$

is the magnetic interaction operator. It can be shown that [81]

$$\boldsymbol{D}_\perp(\boldsymbol{Q}) = -\frac{1}{2\mu_B}\hat{\boldsymbol{Q}} \times \left[(\boldsymbol{M}_S(\boldsymbol{Q}) + \boldsymbol{M}_L(\boldsymbol{Q})) \times \hat{\boldsymbol{Q}}\right], \tag{3.36}$$

where $\boldsymbol{M}_{S,L}(\boldsymbol{Q})$ are the Fourier transforms of the magnetization due to the spin and orbital moments respectively. The total (Fourier transformed) magnetization is $\boldsymbol{M} = \boldsymbol{M}_S + \boldsymbol{M}_L$.

Partial response functions Now, $\boldsymbol{s}_n$ acts only on the neutron spin part of the wavefunction $|s\rangle$, whereas $\boldsymbol{D}_\perp$ acts only on the electron part of the wavefunction $|\lambda\rangle$. Noting also the identity

$$\boldsymbol{D}_\perp^\dagger(\boldsymbol{Q}) \cdot \boldsymbol{D}_\perp(\boldsymbol{Q}) = \frac{1}{(2\mu_B)^2} \sum_{\alpha\beta} \left(\delta_{\alpha\beta} - \hat{Q}_\alpha \hat{Q}_\beta\right) M_\alpha M_\beta, \tag{3.37}$$

where † indicates a Hermitian conjugate, it can then be shown that, if unpolarized neutrons are used, the partial differential cross-section can be written as [70, 75]

$$\left(\frac{\mathrm{d}^2\sigma}{\mathrm{d}\Omega \mathrm{d}E_f}\right)_{\boldsymbol{k}_i \to \boldsymbol{k}_f} = \frac{k_f}{k_i}\left(\frac{\gamma r_0}{2\mu_B}\right)^2 \sum_{\alpha\beta} \left(\delta_{\alpha\beta} - \hat{Q}_\alpha \hat{Q}_\beta\right) \tilde{S}^{\alpha\beta}(\boldsymbol{Q}, \omega), \tag{3.38}$$

where the partial magnetic response functions are [70]

$$\tilde{S}^{\alpha\beta}(\boldsymbol{Q}, \omega) = \sum_{\lambda_i \lambda_f} P_{\lambda_i} \langle \lambda_i | M_\alpha^\dagger(\boldsymbol{Q}) | \lambda_f \rangle \langle \lambda_f | M_\beta(\boldsymbol{Q}) | \lambda_i \rangle \delta(E_{\lambda_f} - E_{\lambda_i} - \hbar\omega). \tag{3.39}$$

Using a similar procedure to that used to derive (3.21), it can be shown that the expressions for $\tilde{S}^{\alpha\beta}$ can be factorized into a part depending on the atomic positions

and a part depending on the electron spin state, each of which is a sum of a static part and a dynamic part [70, 74]. For the purposes of this thesis, when discussing magnetic scattering, a completely static lattice will be assumed.

The dipole approximation It now remains to find a useful expression for $\boldsymbol{M}(\boldsymbol{Q})$. For a Bravais lattice, with the magnetization localized to delta function orbitals in direct space, $\boldsymbol{M}(\boldsymbol{Q})$ would be a lattice of delta function orbitals in reciprocal space, all with the same intensity. In reality, the magnetization is due to electron clouds which have finite extent, i.e., in direct space the magnetization is a convolution between a lattice of delta functions and the magnetization density of the electron cloud of a single magnetic ion. In reciprocal space, as can be seen from the convolution theorem, $\boldsymbol{M}(\boldsymbol{Q})$ is therefore a product between a lattice of delta functions and the Fourier transform of the magnetization density of a single ion, $\boldsymbol{M}_1(\boldsymbol{Q})$. Multi-sublattice systems can be considered in a similar way, introducing a structure factor as was done in the case of nuclear scattering.

It is therefore necessary to find an expression for the Fourier transform of the magnetization density of a single ion, and to do this, the 'dipole approximation' is used. This approximation holds when the neutron wavelength is much larger than the atomic size, a situation which holds for all the data presented in this thesis. When the orbital angular momentum is unquenched, the dipole approximation states that the Fourier transform of the magnetization due to a single site can be written as

$$\boldsymbol{M}_1(\boldsymbol{Q}) = -\mu_B f(Q)(\boldsymbol{L} + 2\boldsymbol{S}), \tag{3.40}$$

where $\boldsymbol{L}$ and $\boldsymbol{S}$ are the total orbital and spin angular momenta for that single site and $f(Q)$ is the dipole magnetic form factor. It is possible to expand $f(Q)$ as a sum of exponentials; values of the coefficients relevant for different ions have been tabulated [82]. Both materials discussed in this thesis contain Co^{2+} ions in distorted octahedral environments, for which the orbital angular momentum is partially quenched [6, 7]. In this regime, the dipole approximation states that for a single ion [70],

$$\boldsymbol{M}_1(\boldsymbol{Q}) = -g\mu_B f(Q)\tilde{\boldsymbol{S}}, \tag{3.41}$$

where g is the empirically observed g-factor (assumed for the moment to be isotropic) and $\tilde{\boldsymbol{S}}$ is the effective spin of that single ion.

When the dipole approximation holds, it is possible to write the partial differential cross-section for unpolarized neutrons as [70]

$$\left(\frac{\mathrm{d}^2\sigma}{\mathrm{d}\Omega \mathrm{d}E_f}\right)_{\boldsymbol{k}_i \to \boldsymbol{k}_f} = \frac{k_f}{k_i}\left(\frac{\gamma r_0}{2\mu_B}\right)^2 f^2(Q) e^{-2W} \sum_{\alpha\beta}\left(\delta_{\alpha\beta} - \hat{Q}_\alpha \hat{Q}_\beta\right) S^{\alpha\beta}(\boldsymbol{Q},\omega), \quad (3.42)$$

where e^{-W} is the Debye-Waller factor defined above and $S^{\alpha\beta}$ are the 'reduced partial response functions'. These will also be referred to as the components of the 'dynamical structure factor' and are given by [70]

$$S^{\alpha\beta}(\boldsymbol{Q},\omega) = g^2\mu_B^2 \sum_{\lambda_i\lambda_f} P_{\lambda_i} \langle\lambda_i|S^\alpha(-\boldsymbol{Q})|\lambda_f\rangle\langle\lambda_f|S^\beta(\boldsymbol{Q})|\lambda_i\rangle \delta(E_{\lambda_f} - E_{\lambda_i} - \hbar\omega), \quad (3.43)$$

where

$$\boldsymbol{S}(\boldsymbol{Q}) = \sum_j e^{i\boldsymbol{Q}\cdot\boldsymbol{R}_j}\boldsymbol{S}_j \quad (3.44)$$

is the Fourier transformed (effective) spin.[2]

In the materials discussed in this thesis, the g-factor is not isotropic, and must be replaced by a g-tensor. If the g-tensor is diagonal in the $\alpha\beta$ coordinates used, (3.43) can be used with $g^2 \to g^{\alpha\alpha}g^{\beta\beta}$. In a general coordinate system, (3.43) must be generalized to

$$S^{\alpha\beta}(\boldsymbol{Q},\omega) = \mu_B^2 \sum_{\lambda_i\lambda_f\gamma\delta} P_{\lambda_i} \langle\lambda_i|g^{\alpha\gamma}S^\gamma(-\boldsymbol{Q})|\lambda_f\rangle\langle\lambda_f|g^{\beta\delta}S^\delta(\boldsymbol{Q})|\lambda_i\rangle \delta(E_{\lambda_f} - E_{\lambda_i} - \hbar\omega). \quad (3.45)$$

These last two forms are used throughout this thesis.

Elastic and inelastic magnetic scattering Now consider a ground state which is aligned along a local z-axis. The S^z operator can be written as $S^z = S - \delta S$ where δS is the spin reduction operator due to quantum fluctuations. There are thus two contributions to S^{zz}: Bragg peaks on the elastic line, and fluctuations in the size of the ordered moment, which cause inelastic scattering.

[2] The tilde denoting effective spins will from now on be dropped for simplicity.

The S^x operator can be written as $S^x = (S^+ + S^-)/2$, and similarly the S^y operator can be written as $S^y = (S^+ - S^-)/(2i)$. If the ground state $|\text{GS}\rangle$ is fully aligned along z (i.e. there is no spin reduction) then $S^+|\text{GS}\rangle = 0$ and also there is no inelastic contribution to S^{zz}. Therefore, the inelastic scattering due to a state $|\psi\rangle$ is related to its overlap $|\langle\psi|1\text{s.f.}\rangle|^2$ with a state $|1\text{s.f.}\rangle$ related to the ground state $|\text{GS}\rangle$ by flipping a single spin.

3.1.2 Neutron spectroscopy

This subsection will give a brief overview of the techniques involved in measuring inelastic neutron scattering (INS). A much more detailed account of neutron instrumentation is available in Ref. [83].

3.1.2.1 Types of neutron source

A variety of techniques are used to measure neutron scattering, depending on both the type of source and on the aim of the experiment. The data discussed in this thesis were all collected at the ISIS Neutron and Muon source in Oxfordshire, shown in Fig. 3.3. This is a spallation source, meaning that neutrons are produced by accelerating protons using a synchrotron, cyclotron or linear accelerator, and then colliding them with a heavy metal target. Spallation sources typically produce neutrons in pulses, each time a bunch of protons collides with the target [83]. The fact that neutrons are produced in pulses means that their speed and thus their energy can be calculated based on how long it takes them to reach a point some distance away from the target. Instruments at pulsed sources therefore often use 'time-of-flight' methods in order to exploit this fact. Time-of-flight instruments will be discussed in more detail below.

The other major type of neutron source is a reactor source. These operate by nuclear fission of uranium in a chain reaction, and thus produce a continuous flux of neutrons. The most common type of spectrometer used at reactor sources is the triple axis spectrometer. These use Bragg reflection from a crystal monochromator in order to select both the incident energy E_i and the outgoing energy E_f. By varying

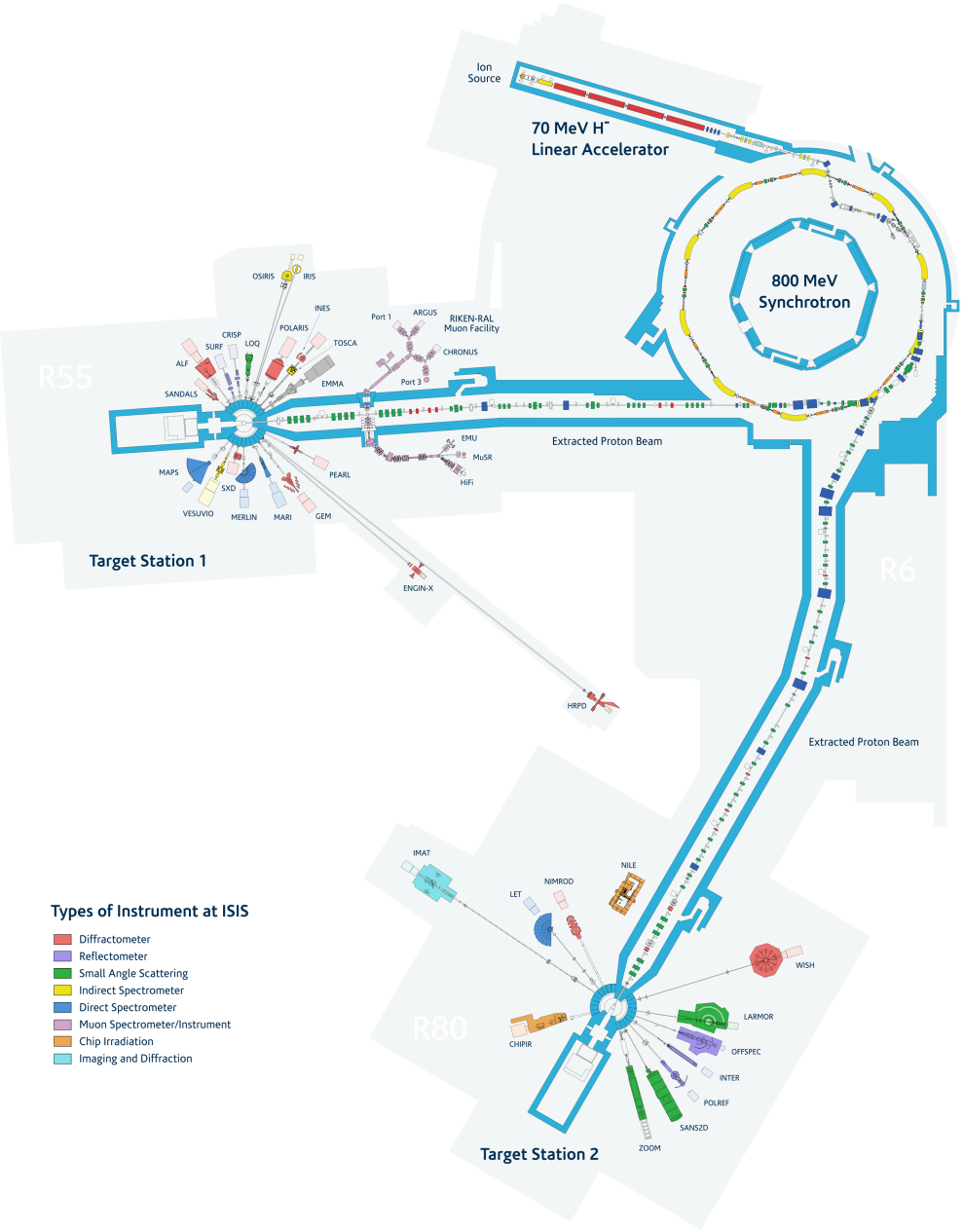

Figure 3.3: The layout of the ISIS Neutron and Muon source. Image credit: STFC.

the scattering angle from these crystals, it is possible to change the wavelength of scattered neutrons and thus select a fixed energy. The third axis of rotation is the scattering angle at the sample. By varying all three of these angles, it is possible to measure the scattering at a range of points in the $(\boldsymbol{Q}, \omega)$ space in the horizontal scattering plane [83]. The disadvantage of this method over time-of-flight methods is that the scattering must typically be measured point by point. In addition, the monochromating and analysing crystals can sometimes introduce

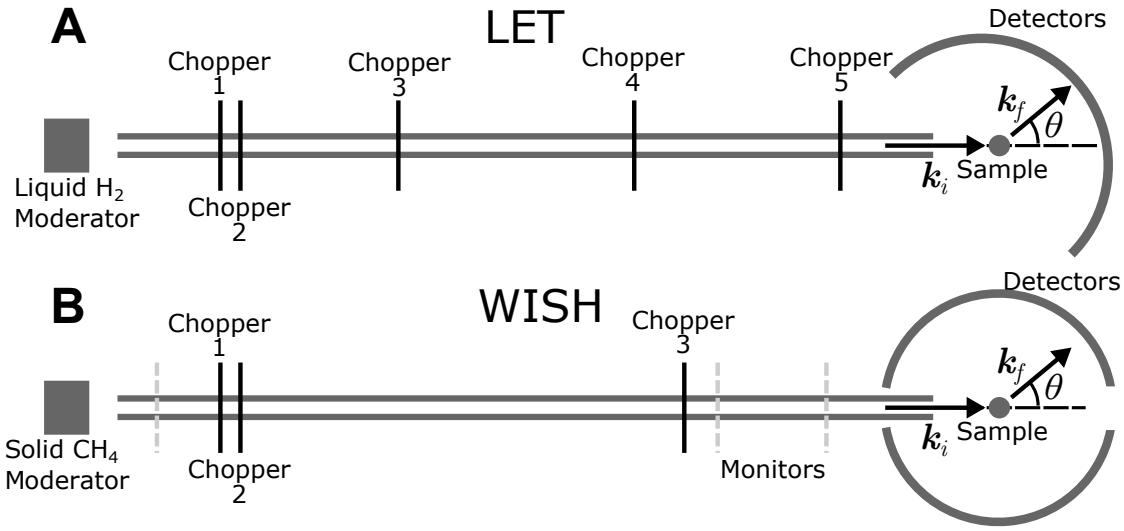

Figure 3.4: A) Schematic of the layout of LET. Neutrons are first slowed using a liquid hydrogen moderator. The overall effect of choppers 1 to 4 is to prevent frame overlap and shape the pulse. Chopper 5 is a double counter-rotating disk chopper which selects the incident energy. The detector bank is made up of 4 m long position sensitive detectors. The distance from the moderator to the sample is 25 m. Figure adapted from Ref. [84]. B) Schematic of the layout of WISH. The neutrons are slowed using a solid methane moderator. In this case, the purpose of the choppers is to prevent frame overlap and select the wavelength range. The grey dashed vertical lines indicate monitors; the counts recorded in the right-most monitor are used to normalize the wavelength-dependent flux. The detector bank is made up of 1 m long position sensitive detectors and the distance from the moderator to the sample is 40 m. Figure adapted from Ref. [85]. Neither panel is drawn to scale.

spurious features into the data [70], such as λ/m scattering where λ is the neutron wavelength and m is a small integer.

3.1.2.2 Direct geometry time-of-flight spectrometers

The INS data presented in Chapters 4, 5 and 8 were all taken on LET [84] at ISIS, which is an example of a direct geometry time-of-flight spectrometer. Figure 3.4A shows a schematic of LET, which stands for Low Energy Transfer as this instrument is optimized for use with small incident energy E_i.

Choppers Direct geometry instruments use choppers to select a fixed incident energy. These work by only allowing neutrons to get through which reach the chopper at a particular time after the neutrons were created, and are therefore travelling

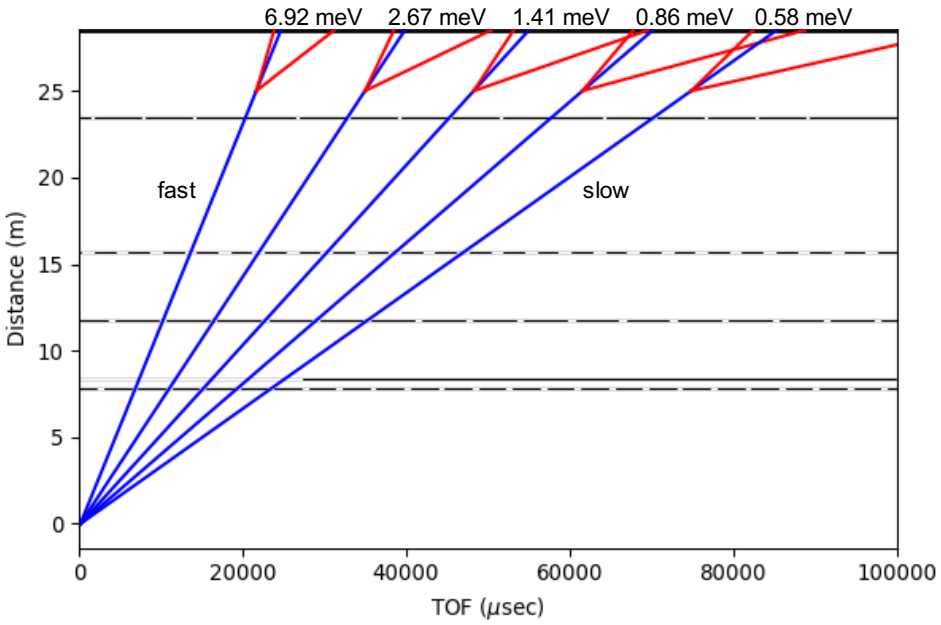

Figure 3.5: Distance-time diagram for LET showing the effect of each chopper. Blue lines show the trajectory of elastically scattered neutrons with each available incident energy, while red lines show the range of trajectories of neutrons of each incident energy that scatter inelastically. When red lines of adjacent monochromatic pulses overlap then frame overlap occurs and data is unusable in that region. Figure made using PyChop [88] with the configuration used for the measurements in Chapter 8.

at a particular speed. Many direct geometry instruments (e.g. MERLIN [86]) use Fermi choppers, which are spinning cylinders with curved slits [83]. Instruments which are optimized for low E_i however, such as LET, instead use a system of counter-rotating disks [70]. Many instruments also have various other choppers, such as a t_0 chopper, which closes at the time the proton pulse strikes the target in order to avoid background from gamma rays or high energy neutrons, and choppers to shape the beam and to prevent frame overlap [70]. On some instruments, such as LET, it is possible to operate in repetition rate multiplication mode [87], where multiple incident energies can be measured at the same time. This is shown on a distance-time diagram in Fig. 3.5.

Detectors After the neutrons pass the resolution chopper (i.e., the chopper used for energy selection) they then travel towards the sample, where they scatter, as described in Sec. 3.1.1. Many modern direct geometry instruments have large banks

of detectors in order to be able to detect scattering over a wide range of solid angle. On LET, these detector banks are made up of 4 m long tubes filled with ^{3}He which detect neutrons based on the cascade of charged particles released when a ^{3}He nucleus reacts with a neutron to form a ^{3}H nucleus and a proton. By measuring the relative size of the charge released at both ends of the tube, it is possible to infer how far along the detector the neutron was detected [76, 83]. Using these techniques, direct geometry instruments are able to split each detector tube into many much smaller detectors, so the whole detector area is effectively split into over 90,000 independent detectors (pixels) of area ≈ 1 inch^2. A large range of reciprocal space is thus measured simultaneously. The final neutron energy (and hence the energy transfer) is measured by timing how long it takes the neutron to reach the detector, and the final neutron wavevector (and hence the wavevector transfer) is measured based on the direction of the detector pixel relative to the sample and also the timing.

Single crystal spectroscopy experiments As there are only three degrees of freedom in a single crystal time-of-flight INS measurement (polar and azimuthal angle of the detector relative to the sample, and time for the neutron to travel), it is not possible to independently measure all four components of $\boldsymbol{Q} - \omega$ space at once. Instead, a three-dimensional manifold is measured, with a non-trivial relation between the components. In order to measure the full four-dimensional $\boldsymbol{Q} - \omega$ space, a fourth degree of freedom must be introduced, and this is the rotation angle of the sample. Raw runs recording neutron counts as a function of time can be converted to counts as a function of energy transfer using software such as MANTID [88]. Individual runs at a fixed angle can be analysed as a function of $\boldsymbol{Q}$ and ω using MSLICE [89] or combined together to cover the full 4 dimensional $\boldsymbol{Q} - \omega$ space using HORACE [90]. Slices and cuts along desired directions can then be extracted.

While triple-axis spectrometers have historically been preferred to time-of-flight instruments for their ability to measure specific paths in $\boldsymbol{Q} - \omega$ space, the very wide detector coverage of modern time-of-flight instruments makes up for this by allowing a large portion of reciprocal space to be measured simultaneously, which is

very useful when it is not known where in reciprocal space the interesting features will be. The technique is also particularly useful for measuring materials in which the magnetic interactions are primarily one- or two-dimensional (i.e., the dispersion of the excitations is flat along at least one direction), as the data can be integrated along that direction to increase the counting statistics. Both materials studied in this thesis belong to this category. Direct geometry instruments also have the advantage of having very low background compared to other instruments. This is because the high energy neutrons which are not of interest will arrive at the beginning of the pulse and do not overlap with the main signal [70]. While direct geometry spectrometers do not suffer from the same spurious features that affect triple axis and indirect geometry spectrometers due to the analyser crystals, spurions (spurious features which look like they could be real signal) can still be present, due to scattering from the sample environment. However, these can be easily identified and characterized.

Direct geometry spectrometers can also be used as diffractometers by removing the resolution chopper, i.e., working in white beam mode [76]. The operation of time-of-flight diffractometers will be discussed in more detail in Sec. 3.1.3.2. Spectrometers are used in this 'white beam' mode at the beginning of experiments in order to align the sample.

3.1.2.3 Indirect geometry spectrometers

The data presented in Chapter 6 were taken on the indirect time-of-flight spectrometer OSIRIS [91], also at ISIS. I was not involved in carrying out those measurements, so this discussion will be briefer than the discussion above and is included for completeness.

Indirect geometry time-of-flight spectrometers operate at a fixed final energy E_f. This is selected by means of analyser crystals (often pyrolitic graphite), while the incident energy is determined by measuring the time-of-flight. As with direct geometry instruments, the wave-vector transfer is a function of both the time-of-flight and the scattering angle. Compared to direct geometry instruments, the range of $\boldsymbol{Q} - \omega$ space that is kinematically accessible is different: in direct

geometry instruments, the energy transfer cannot be greater than the incident energy, whereas indirect geometry instruments do not have this restriction. In addition, indirect geometry spectrometers which are set up to be used in a 'back-scattering' geometry can have very high energy resolution. Back-scattering means that the total scattering angle 2θ at the analyser crystal is close to 180°, and this configuration exploits the wavelength spread as given by Bragg's law to achieve an energy resolution which is dominated by the analyser crystal perfection rather than by the spread in angle of the beam [70].

The disadvantages of indirect geometry in comparison to direct geometry are that the detector area is in general smaller as analyser crystals are needed for each detector. No position sensitivity is available and integration of the data along the detector tube is therefore inevitable. In addition, scattering at the analyser crystals can introduce spurious background features into the data due to a white beam being incident on the sample. These spurions need to be well characterized and subtracted off.

3.1.3 Neutron diffraction

Elastic neutron scattering is generally known as neutron diffraction and can be used to investigate the crystal and/or magnetic structure of materials. A brief overview of the techniques and experimental considerations relevant to diffraction will be given in this section.

3.1.3.1 General considerations

Most neutron diffractometers do not have energy analysis, and so measure

$$\frac{\mathrm{d}\sigma}{\mathrm{d}\Omega} = \int \mathrm{d}E_f \, \frac{\mathrm{d}^2\sigma}{\mathrm{d}\Omega \mathrm{d}E_f}, \tag{3.46}$$

which is proportional to

$$S(\boldsymbol{Q}) = \int \mathrm{d}\omega \, S(\boldsymbol{Q}, \omega). \tag{3.47}$$

It is in general assumed that this quantity will be dominated by elastic scattering, such that it can be assumed that $k_i = k_f$.

It is sometimes the case that measurements seek only to identify the location of Bragg peaks in reciprocal space; if there are Bragg peaks in locations other than where those of the structural unit cell are expected, this can identify the presence of supercells, which are often present if there is magnetic order.

In addition, the relation (3.23) can be used to relate the intensity of Bragg peaks to the position of atoms within the unit cell, and similar relations hold for magnetic diffraction. In particular (3.23) states that the measured intensity $I(\boldsymbol{Q})$ is proportional to $|F(\boldsymbol{Q})|^2$, where F can be the nuclear structure factor as defined in (3.24) or the generalization to magnetic scattering. Now, if the quantities $F(\boldsymbol{Q})$ were known, it would be possible to invert (3.24) to obtain the density of scattering length as a function of position in the unit cell. However, it is experimentally only possible to extract the modulus of F, meaning that it is not possible to perform this inverse Fourier transform. This 'phase problem' means that it is instead necessary to refine the parameters of a model in an iterative process. Various different software tools are available to do this, such as FULLPROF [92] and JANA [93].

In order to refine a structure, it is thus important to understand exactly how the measured neutron counts relate to the differential cross-section $\frac{\mathrm{d}\sigma}{\mathrm{d}\Omega}$. Scale factors which affect all the peaks uniformly can be refined (since the scattering lengths of different elements are known), however, if effects affect different peaks differently, they need to be treated with care. There are various effects that need to be taken into account.

- *Neutron flux*: As per the definition (3.2), in order to relate the differential cross-section to the number of neutrons scattered in a particular direction, it is important to know the flux of incoming neutrons. In particular, if intensities taken across multiple counting times are combined, it is important for the neutron counts to be normalized by the time-integrated flux of incoming neutrons. In addition, if a broad range of neutron wavelengths are used as in time-of-flight instruments (see Sec. 3.1.3.2), it is important to know the flux distribution as a function of wavelength, so that the intensities of peaks corresponding to different neutron wavelengths can be compared. Incoming

neutron flux can be measured using a monitor, which is a low efficiency neutron detector [70, 83].

- *Detector efficiency*: While some experimental set-ups have only a single detector, many set-ups have multiple detectors in order to be able to probe reciprocal space more efficiently by measuring the scattering across a wider range of solid angle. Subtle differences between detectors, e.g. differences in gas pressure inside gas tube based detectors, can affect their efficiency. In addition, detector efficiency will in general depend on wavelength. The relative efficiencies of detectors and their wavelength dependence can be calibrated by using a standard which scatters isotropically. A good standard for this purpose is elemental vanadium, because it has a large incoherent cross-section and a very small coherent cross-section [70, 83].

- *Absorption and extinction*: Absorption of neutrons by nuclei decreases the number that can be scattered, while extinction affects strong Bragg reflections and is due to a decrease in the flux of incident neutrons as a function of distance into the sample because of some of them having already been scattered [70]. Both of these effects depend on both the sample geometry and neutron wavelength.

- *The Lorentz factor*: The Bragg peaks in a real experiment are not δ-functions but have a finite spread due to a combination of instrumental resolution and sample imperfections. This means that the intensities measured in a real experiment are integrated intensities across the width of the peak. While the required quantities are integrals in $\boldsymbol{Q}$-space, the experiment measures quantities as a function of some combination of sample orientation, angle to the detector and neutron wavelength. The conversion between these integrals therefore requires the Jacobian of the transformation between these coordinates, which is known as the 'Lorentz factor'.

As with spectrometers, different types of neutron source tend to employ different types of diffractometer. Reactor sources use constant wavelength diffractometers which use an analyser crystal to select a fixed incident wavelength and move the sample and detector to perform scans through $\boldsymbol{Q}$-space. Different geometries are available depending on constraints such as the sample environment [70, 83]. Pulsed sources on the other hand, use time-of-flight methods, which will be discussed next. Diffraction measurements at both types of source can be carried out on either single crystals or on powders.

3.1.3.2 Time-of-flight single crystal neutron diffraction

The data reported in Chapter 8.3 were taken on the time-of-flight neutron diffractomer WISH at the ISIS facility [85]. A schematic of WISH (Wide angle In a Single Histogram) is shown in Fig. 3.4B.

Time-of-flight diffractometers work similarly to spectrometers, in that the time that it takes the neutron to travel is used to calculate its energy. In this case, neutrons of all energies (with a profile corresponding to the temperature of the moderator used to slow down the neutrons) will be incident on the sample. As elastic scattering dominates over inelastic, it is assumed that $E_i = E_f$ and the time-of-flight is used to measure $k = k_i = k_f$. The use of time-of-flight means that many wavelengths can be measured simultaneously, while the use of large banks of position sensitive detectors (WISH has particularly wide angle coverage with banks from 10° to 170° on both sides) means that a large solid angle is measured. This makes the technique efficient for measuring large regions of reciprocal space, which is particularly useful when it is not known in advance at which wavevectors diffraction peaks will be observed. The disadvantage is that refinement of structures is more complicated. This is because all the correction factors described above are wavelength dependent and strongly varying — the Lorentz factor for time-of-flight measurements is $\lambda^4/\sin^2\theta$ where λ is the neutron wavelength [70, 83] — and measuring many wavelengths simultaneously therefore requires this wavelength dependence to be well characterized.

3.2 Vibrating sample magnetometry

Vibrating sample magnetometry (VSM) was used for the magnetization measurements presented in Chapter 7. In this technique, a sample is oscillated rapidly up and down, passing in and out of a set of pick-up coils, and the voltage induced in the coils is measured [1]. More specifically, the voltage V induced in a set of coils is related to the rate of change of magnetic flux Φ through the coils by Faraday's law,

$$V = -\frac{\mathrm{d}\Phi}{\mathrm{d}t} = -\frac{\mathrm{d}\Phi}{\mathrm{d}z}\frac{\mathrm{d}z}{\mathrm{d}t}, \tag{3.48}$$

where z is the vertical position of the sample [94]. Assuming that the sample oscillates sinusoidally, and such that its position is given by $z = A\sin\omega t$, the voltage measured in the coil is

$$V = \omega C m A \cos\omega t \tag{3.49}$$

where m is the magnetization of the sample and C is a constant of proportionality, known as the sensitivity function [95] that relates m to $\mathrm{d}\Phi/\mathrm{d}z$ [94]. It is possible to calculate C under the assumption that the sample is a point-like dipole but in general, magnetometers are also calibrated using a standard sample. Eq. (3.49) shows that the measured voltage depends on not only the sample magnetic moment but also on the oscillation frequency and oscillation amplitude. In practice, ω is in general fixed for a given set-up, and is chosen to maximize the signal while keeping the forces on the sample holder to within limits that it can withstand, as these forces scale as ω^2 [96]. The oscillation amplitude is limited by the design of the pick-up coil and the requirement for linear approximations to hold. A sample with a large magnetic moment was used for the measurements reported in this thesis, so achieving sufficient sensitivity was not a problem.

The measurements presented in this thesis used the vibrating sample magnetometer option of a Quantum Design Physical Property Measurement System (PPMS). In this set-up, a pick-up coil is placed at the bottom of the sample chamber, and the sample is attached to the end of a sample rod. An external magnetic field up to 16 T can be applied, and the axis of the pick up coil, the motion of the sample rod and the

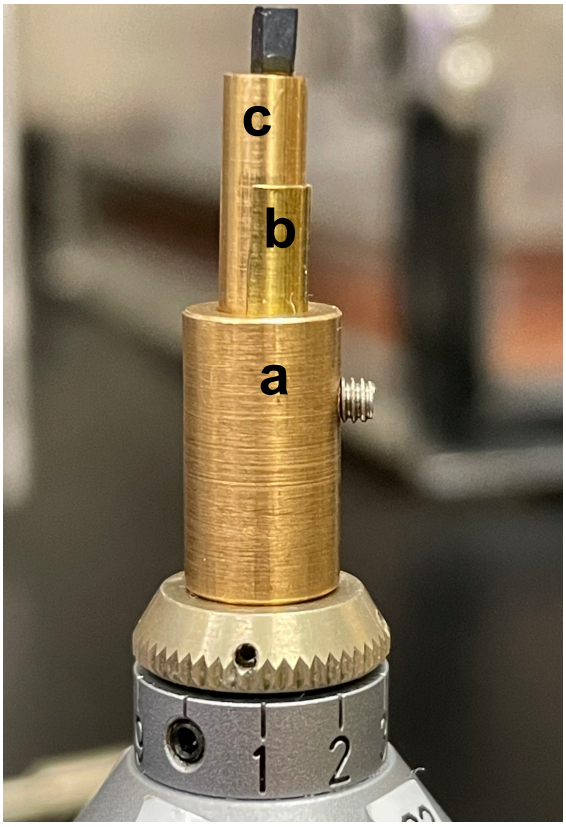

Figure 3.6: The mount used for measuring the alignment of the sample when mounted in the VSM. The pieces are (a) the x-ray diffractometer holder. This can be used in either the Supernova diffractometer or the Laue diffractometer. b) A brass half tube, designed to replicate the end of the half tube VSM mount. This is for holding the quartz piece so that the quartz piece does not get scratched by the grub screw. c) The quartz cylinder. The photo was taken using a brass replica of the quartz cylinder. The sample (dark cuboid) is glued to the top with GE varnish. This photo is for illustration purposes of the principle of the method, and the sample shown is not the actual sample that was used in the experiment.

applied magnetic field are all parallel and vertical [94]. This 'axial' arrangement is the most common [95], but different arrangements of the coils relative to the motion of the rod can be used to measure different components of the magnetization [97].

While various different sample mounts can be used with the PPMS VSM, the one that was used in this thesis consists of a brass half tube, in which a sample can be braced into position with two quartz cylinders. For the measurements presented here, it was important to know the orientation of the sample relative to the axis of the applied field and pick-up coils as precisely as possible. Therefore, an adapter was designed such that the sample could be glued to the end of one of the quartz

cylinders, and the quartz cylinder could then be inserted into the holder for an x-ray diffractometer so that the orientation of the sample as it would be during the experiment could be determined to a high degree of precision. This adapter is shown in Fig. 3.6. This measurement assumed that the quartz cylinder would be perfectly vertical in both the x-ray diffractometer and in the VSM. Therefore a very snug fit was required for the adapter components in the x-ray diffractometer. The fit of the quartz cylinder into the brass half-tube VSM holder is very snug by design, and it has been assumed that deflections of the sample rod are small. However, the sample holder experiences large forces due to the oscillations and large torques when the magnetic field is applied along the hard axis of a highly anisotropic sample, such as was done in Chapter 7. Therefore, some small deflection or flapping of the sample rod could possibly have occurred.

It is also important to bear in mind when mounting samples that sample geometry can play an important role. If samples are long and thin, then corrections of up to 30% must sometimes be made compared to calibration based on the approximation of a point dipole sample. If the centre of the sample does not lie on the centre-line of the coil, corrections can also be necessary [94]. In addition, sample geometry affects demagnetization effects, which determine the size of the field experienced within the sample. These will be discussed further in Chapter 7.

4

Tuning of spinon confinement in the Ising chain material $CoNb_2O_6$

The Ising chain realizes the fundamental paradigm of spin fractionalization, where locally flipping a spin creates two domain walls (spinons) that can separate apart at no energy cost. In a quasi-one-dimensional system, the mean-field effects of the weak three-dimensional couplings confine the spinons into a Zeeman ladder of two-spinon bound states. In this chapter, the confinement potential between spinons is experimentally tuned in the quasi-one-dimensional Ising ferromagnet $CoNb_2O_6$ by means of an applied magnetic field with a large component along the Ising direction. Using high-resolution single crystal inelastic neutron scattering, the evolution of the spectrum from the limit of very weak confinement at low field (with many closely spaced bound states with energies scaling as the field strength to the power 2/3) to very strong confinement at high field (where it consists of a magnon and a dispersive two-magnon bound state, with a linear field dependence) is directly observed. At intermediate fields, the disappearance of the higher order bound states from the spectrum as they move to higher energies and overlap with the two-particle continuum is explored. The results of this chapter and the following chapter have been published in Ref. [98].

4.1 Introduction

The material $CoNb_2O_6$ has been of interest for some time, as it is considered to be an excellent experimental realization of a ferromagnetic Ising chain [25, 43, 99–104], the arrangement of the magnetic Co^{2+} ions leading to highly one-dimensional magnetic interactions. While the magnetic properties of $CoNb_2O_6$ were first investigated over 50 years ago [105–108], it gained significant interest in the 1990s when it was discovered to have a very rich phase diagram in low field applied in the *ac*-plane [109–117]. This rich phase diagram arises due to the interplay between strong ferromagnetic Ising-like interactions along the chains and weak antiferromagnetic interactions between the chains which are partially frustrated [118]. Around this time, the possibility of spin-cluster excitations arising from the quasi-one-dimensional nature also began to be investigated [103, 119]. In addition, other material properties of $CoNb_2O_6$ have also been of interest [120–122].

More recently, it was realised that $CoNb_2O_6$ has a low enough exchange energy scale that the full phase diagram in transverse magnetic field is experimentally accessible [25, 123]. This has resulted in $CoNb_2O_6$ being seen as one of the best experimental realizations of transverse field Ising chain (TFIC) physics in a condensed matter system for over a decade [25, 43, 99, 100, 102, 124]. Among the key experimental observations indicative of the quantum phase transition is the qualitative change in the nature of quasiparticles from domain walls in the ordered phase to coherently propagating spin flips in the high-field paramagnetic phase. Moreover, a fine structure of bound states has been observed just below the critical transverse field, consistent with predictions for a universal E8 spectrum expected in the presence of a perturbing longitudinal field, which in this case arises from mean-field effects of the three-dimensional magnetic order [25, 43]. The rich physics arising from the quasi-one-dimensional nature of $CoNb_2O_6$ is why it is the focus of much of this thesis. In the last few years, there has also been renewed interest in $CoNb_2O_6$ due to departures of the Hamiltonian from the pure Ising limit [71, 125–127]. While in this chapter, $CoNb_2O_6$ will mostly be discussed as

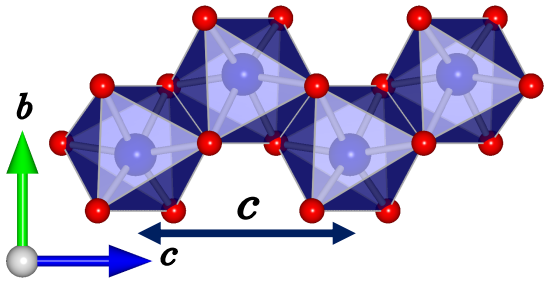

Figure 4.1: A zigzag magnetic chain in $CoNb_2O_6$, showing Co^{2+} ions (blue) inside edge-sharing octahedra (blue shading) of O^{2-} ions (red). Figure made using VESTA [129].

an example of an Ising chain or pure XXZ chain, the full Hamiltonian will be discussed in much more detail in the following chapters.

The magnetic ions in $CoNb_2O_6$ are Co^{2+}, arranged into zigzag chains running along the crystallographic c-direction, with the zigzag in the b-direction, as shown in Fig. 4.1. The crystal structure of $CoNb_2O_6$ corresponds to the columbite family [105, 106, 128], with the orthorhombic space group $Pbcn$, and with the chains forming a distorted triangular lattice in the ab-plane (Fig. 4.2A). The lattice parameters at 2.5 K are $a = 14.1337$ Å, $b = 5.7019$ Å and $c = 5.0382$ Å[114]. The combination of crystal field effects and spin-orbit coupling in $CoNb_2O_6$ leads to an effective $S = 1/2$ Kramers doublet ground state with strong Ising-like character, which is separated from the next lowest Kramers doublet by 30 meV [5]. Weak interactions between chains stabilize magnetic order at low temperatures, and below 1.97 K, the spins are ferromagnetically aligned along each zigzag chain due to a dominant nearest-neighbour Ising exchange, with an antiferromagnetic pattern between chains [110, 114] (Fig. 4.2B and C). The magnetic moments lie in the ac-plane [107, 108], at an angle $\gamma = 30°$ to the c-axis [114], which will be taken here to be the local Ising z-axis; a field applied along the b-axis is then transverse to the Ising axes of all spins.

In addition to the rich physics observed in transverse field, whose relevance to $CoNb_2O_6$ will be discussed further in the following chapters, the ordered phase of the Ising chain also displays the key paradigm of fractionalization, as discussed in Chapter 2.3.3. It is possible to model this rich behaviour with the deceptively

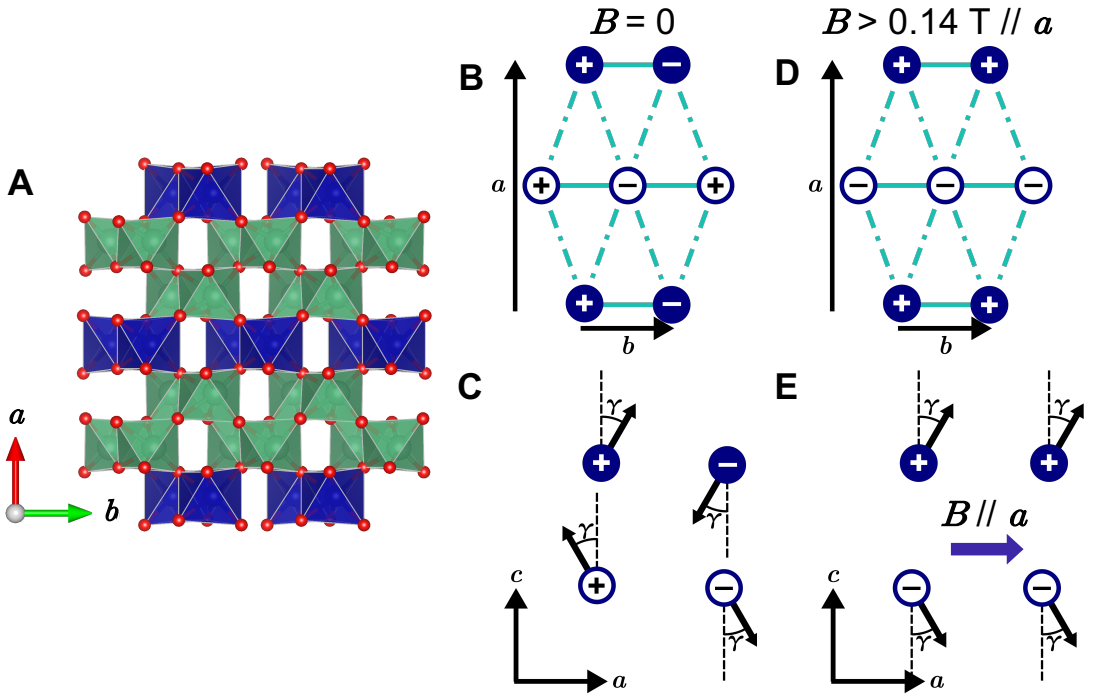

Figure 4.2: A) The crystal structure of $CoNb_2O_6$ projected onto the *ab* plane. Layers of CoO_6 octahedra (blue) in the *bc* plane are separated by two layers of NbO_6 octahedra (green). Within the layers, both the CoO_6 and NbO_6 form zigzag chains along *c*. B) The magnetic structure of $CoNb_2O_6$ in zero field [108, 114]. The filled and open circles represent chains with the easy axis at $\pm 30°$ to the *c*-axis respectively, while the $\pm$ signs represent the projection of the moments (arrows in C) onto the *c*-direction. C) Projection of the zero-field magnetic structure onto the *ac* plane. D) The magnetic structure when fields above 0.14 T are applied along the *a*-axis [116], using the same convention as in B. The directions of the moments are shown in E. Panel A was made using VESTA [129].

simple Hamiltonian for the Ising chain in a tilted field, introduced in Chapter 2.4.1.2

$$\mathcal{H} = \sum_j -JS_j^z S_{j+1}^z - h_x S_j^x - h_z S_j^z, \tag{4.1}$$

with $J > 0$ the Ising exchange, and h_x and h_z applied transverse and longitudinal fields, respectively. As discussed in Chapter 2, a local spin flip, created for example in a neutron scattering process, fractionalizes into a pair of domain wall quasiparticles (spinons, also referred to in Chapter 6 as solitons). When $h_z = 0$, domain walls can separate apart at no energy cost, as illustrated in Fig. 2.5A, and these become the true quasi-particles of the system [37, 38]. However, in the presence of a finite *longitudinal* field $h_z > 0$, domain walls are no longer free but have an attractive interaction, because there is an energy cost proportional to h_z that increases linearly

with their separation. The longitudinal field acts as an effective string tension between the domain walls, not allowing them to separate but confining them into bound states, realizing a one-dimensional analogue of the confinement of quarks into mesons [41]. By tuning the strength of the longitudinal field h_z, one could explore the crossover from the regime of weak confinement (with h_z a small perturbation on the scale of J) where many closely-spaced bound states are expected, with energy separation predicted to scale as a power-law $h_z^{2/3}$, to the regime of strong confinement (h_z comparable to J), where, depending on the relative sizes of J, h_z and h_x and on what other subleading exchange terms may be present in the spin Hamiltonian beyond the minimal model in (4.1), only one, or at most two, bound states are expected, with their energies scaling linearly with h_z. The motivation behind the present studies was to explore the manifestation of this physics experimentally, using an external magnetic field to tune the longitudinal field h_z to cover the full range from weak to strong confinement. The ferromagnetic nature of the dominant interactions in $CoNb_2O_6$, along with their sufficiently small energy scale, makes this material an ideal candidate for this exploration.

In this chapter, high-resolution single crystal inelastic neutron scattering (INS) measurements, that probe the full wavevector-dependence of the spectrum as a function of magnetic field applied along the crystallographic a-axis, with a large longitudinal (along Ising axis) component, are reported. These results complement earlier terahertz (THz) spectroscopy measurements for the same applied field direction, which probed the spectrum at the zone centre (wavevector transfer $\boldsymbol{Q} = 0$) [102, 103], as well as THz spectroscopy and INS measurements previously taken on the Ising material $CoCl_2 \cdot 2\,H_2O$ where the interchain couplings are more significant [130, 131]. In particular, the evolution of the bound state spectrum with field is parameterized and good agreement is found with scaling laws expected in the regimes of weak and strong confinement, corresponding to low and high applied fields, respectively. In low field, many bound states are observed, as expected for a model of a hierarchy of confinement bound states. In high field, only two bound states remain. The character of the bound states in both these regimes is

discussed in detail. In addition, the way that the higher bound states progressively disappear from the spectrum is analysed.

The rest of this chapter is organized as follows. Section 4.2 outlines the inelastic neutron scattering experiments. Experimental results for the spectrum in field applied along a across a wide range of field strengths are then presented in the following sections, from weak confinement (Sec. 4.3) to strong confinement (Sec. 4.4), with the evolution of the high-order bound states presented in Sec. 4.5. Section 4.6 contains the conclusions for this chapter.

4.2 Experimental details

***Attribution note**: The measurements described here were performed before the start of my thesis by an experimental team consisting of David Macdougal and Radu Coldea (University of Oxford) and Robert Bewley (ISIS facility) using a single crystal grown by D. Prabhakaran (University of Oxford). The experimental details are reported here for completeness. The initial processing of the raw time of flight data to convert it into intensity in units of $S(\boldsymbol{Q},\omega)$ using Mantid was also done before I started. I have done all the subsequent analysis presented in this chapter and the next.*

Inelastic neutron scattering measurements of the magnetic excitation spectrum were performed using the direct geometry time-of-flight spectrometer LET at the ISIS facility [84]. The sample was a large single crystal (4.59 g) of $CoNb_2O_6$ grown using the floating-zone technique, as described in Ref. [132], and mounted in the $(0kl)$ horizontal scattering plane, where the wavevector transfer $\boldsymbol{Q}$ is labelled as (hkl) in reciprocal lattice units of the structural orthorhombic unit cell, so $\boldsymbol{Q} = 2\pi\left(\frac{h}{a}, \frac{k}{b}, \frac{l}{c}\right)$. The sample was mechanically fixed in place using copper brackets so that it would not move or rotate due to the torques from the applied field. The sample was cooled using a dilution refrigerator insert and all data were collected below 0.14 K. A magnetic field up to 9 T was applied vertically, along the crystallographic a-axis, which has a longitudinal field component $h_z = g_z\mu_B B \sin\gamma$, where B is the externally applied field magnitude.

LET was operated to measure simultaneously the inelastic scattering of incident neutrons with energies of $E_i = 2.46$, 4.30 and 9.33 meV; the measured energy resolutions (full width half maximum, FWHM) on the elastic line were 0.038(1), 0.085(1), and 0.274(2) meV, respectively. To obtain the overview of the field dependence of the spectrum, the scattering was measured at each field for one fixed sample orientation chosen such that data projected along the chain direction covered a large part of the along-chain Brillouin zone. For these measurements, the sample was aligned with the (010) axis at an angle of 8° to the incident beam direction, and scattering was measured for a typical counting time of 3 hours per field at an average beam current of 40 μA of protons on target. In addition to the single orientation measurements, multi-angle (Horace) scans were performed to obtain a full four-dimensional data set of scattering intensity as a function of three momentum directions and energy at two representative fields, 1.5 and 8 T. For these, the sample was rotated about the vertical a axis in steps of 2° over an angular range of 88 and 108°, with 11 and 17 minutes counting per step, respectively.

The raw time-of-flight neutron data were converted to scattering intensities $S(\boldsymbol{Q}, \omega)$ using MANTID [88], and the resulting data were then analysed using the HORACE [90] and MSLICE [89] packages.

4.3 Weak confinement regime

In the limit of small longitudinal field $h_z \ll J$, the confinement of domain walls into bound states can be captured via a Schrödinger equation for the domain wall separation distance x in the continuum limit [40, 41, 133]

$$-\frac{\hbar^2}{\mu}\frac{d^2\psi_n(x)}{dx^2} + \lambda|x|\psi_n(x) = (m_n - 2m_0)\psi_n(x), \tag{4.2}$$

where μ is the reduced mass for the domain wall pair, $\lambda = 2h_z/c$ is an effective string tension between the domain walls, $c/2$ is the spacing of sites along the chain, and m_0 is the energy cost to create a single domain wall. For the Hamiltonian (4.1), $m_0 = J/2 - h_x$ [11]. Eq. (4.2) can be recast as the Airy equation, and

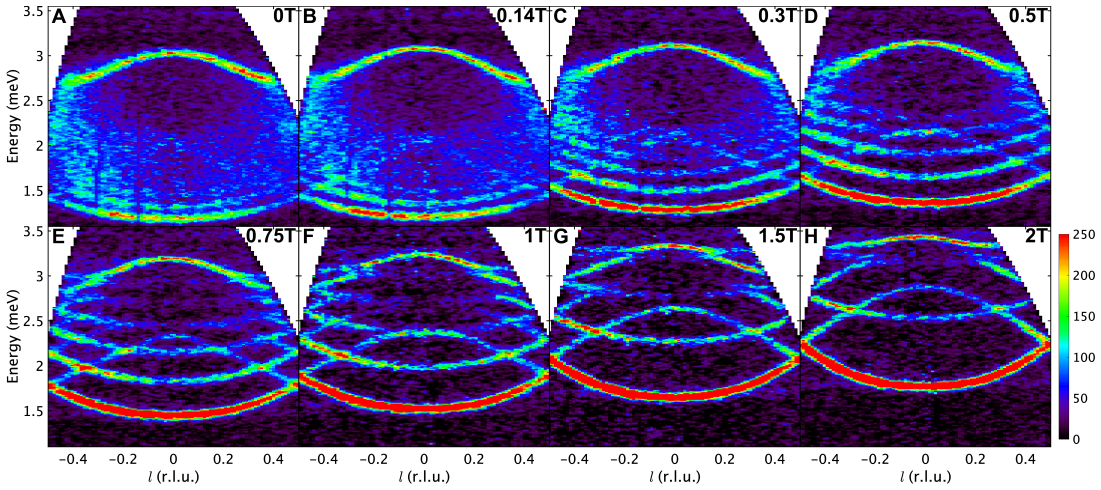

Figure 4.3: INS spectrum as a function of field from 0 to 2 T $\parallel a$, in the weak to intermediate confinement regimes, with field increasing from left to right and top to bottom. Colour is the raw neutron scattering intensity (i.e., no background has been subtracted) on an arbitrary scale, collected using a high-resolution configuration ($E_i = 4.30$ meV) for a fixed sample orientation, with wavevectors projected along the chain direction.

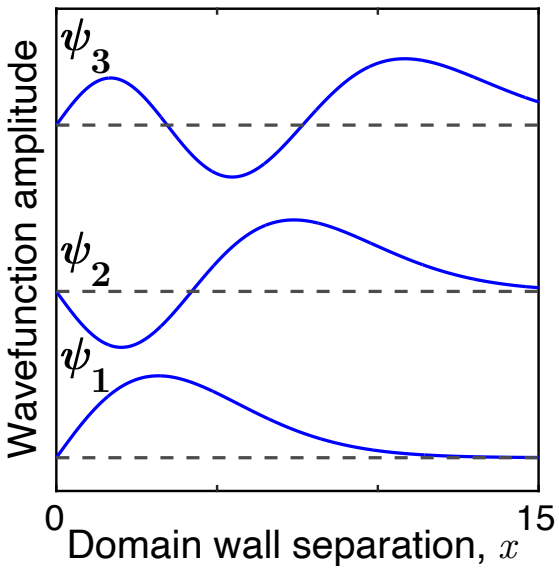

Figure 4.4: In the weak confinement regime ($h_z \ll J$), many bound states exist, which are coherent superpositions of states with the two domain walls separated by many sites. Solid lines are the Airy wavefunctions for the first three bound states as per (4.4) for parameters $\lambda\mu/\hbar^2 = 0.072$, relevant for the longitudinal mean field due to interchain interactions in $CoNb_2O_6$ [25]. The domain wall separation, x, is in units of the spacing along the chain $c/2$.

enforcing the boundary condition $\psi_n(0) = 0$, arising because domain walls cannot overlap, results in energy eigenvalues

$$m_n = 2m_0 + \left(\frac{\hbar^2}{\mu}\right)^{1/3} \lambda^{2/3} z_n, \tag{4.3}$$

where $-z_n$ are the zeros of the Airy Ai function; the corresponding eigenstates are

$$\psi_n(x) = \mathrm{Ai}\left(\left(\frac{\mu}{\hbar^2}\lambda\right)^{1/3}\left(x - \frac{m_n - 2m_0}{\lambda}\right)\right). \tag{4.4}$$

The wavefunctions for the lowest three bound states are sketched in Fig. 4.4. This shows that the bound states in the weak confinement regime are expected to be superpositions of many states, with finite amplitude even for states with large separations between domain walls.

Eq. (4.2) is applicable for $CoNb_2O_6$ even in the absence of an externally applied field. This is because i) there is a finite longitudinal (internal) mean field due to the weak interchain interactions $h_z = 2J\lambda_{\mathrm{MF}}\langle S^z\rangle$, with J and λ_{MF} defined in Chapter 5.4.1 and $\langle S^z\rangle$ the expectation value of the spin component along the Ising axis; and ii) there are terms in the spin exchange Hamiltonian beyond the dominant Ising exchange (as will be shown in Chapter 5) that lead to domain wall propagation, so a finite μ. The bound state spectra observed in previous zero-field INS [25] and THz spectroscopy experiments [43, 102] have shown good agreement with the predictions of (4.2) with h_z interpreted as the interchain longitudinal mean field, which has the same magnitude for all sites in the zero-field antiferromagnetic phase. Zero-field data collected in the current experimental setting are shown in Fig. 4.3A, where the three lowest bound states are clearly visible at the lowest energies. Also notable is the sharp mode at the top of the spectrum with a dispersion curving the opposite way to the lower modes. This mode, which is stabilized by a different mechanism from the low-energy confinement bound states, is a single-spin-flip bound state stabilized by a subleading term in the spin Hamiltonian of the form $-J\lambda_S \sum_j \left(S_j^+ S_{j+1}^- + S_j^- S_{j+1}^+\right)/2$. This XY exchange term allows a single-spin-flip state (i.e., two domain walls on adjacent sites) to

hop between nearest-neighbour sites along the chain as a single entity and this state was therefore dubbed a kinetic bound state [25].

The zigzag nature of the magnetic chains illustrated in Fig. 4.1 leads to a doubling of the unit cell along the chain direction compared to straight chains, therefore a doubling of the number of magnetic modes, so each 'primary' mode with dispersion $\omega(h,k,l)$ has a 'shadow' version with dispersion $\omega(h,k,l+1)$ obtained from the 'primary' version by Brillouin zone folding. In zero field, in the approximation of decoupled chains, the intensities of these modes are proportional to $\cos^2(2\pi k\zeta)$ and $\sin^2(2\pi k\zeta)$ respectively, where the magnetic ions alternate in position along the b direction as $\pm\zeta b$ between consecutive sites along the zigzag chain ($\zeta = 0.165$) [134]. In Fig. 4.3A, the top mode (the kinetic bound state) is a shadow mode with finite intensity only because of finite k, whereas all low-energy confinement modes are primary. Throughout this chapter and the following one, the nth lowest energy (primary) mode at $l = 0$ is referred to as m_n, in both the weak confinement and strong confinement regimes. Modes with the same label in these two regimes have very different character, but there is a smooth crossover between the two regimes.

The remaining panels in Fig. 4.3 show the evolution of the spectrum upon increasing field. It is known that low fields applied along a induce a series of spin-flip transitions such that above a threshold field of 0.14 T, all spin components along a are parallel to the applied field [115, 116, 135], see Fig. 4.2D. All finite field INS data were therefore collected at fields at and above this threshold field to ensure all spin sites experience the same magnitude longitudinal and transverse fields. Upon increasing the applied field, all bound states move up in energy, with the higher order ones moving at a faster rate. This is because the higher order bound states contain in their superposition more weight for states with domain walls further apart [see Fig. 2.5C], so with more spins flipped opposite to the applied field direction, and therefore higher Zeeman energy or higher effective g-factor. Since the higher modes increase in energy more quickly, the relative energy separation between adjacent modes increases and modes become better resolved, such that whilst at 0.14 T (panel B) only m_1 to m_3 are resolved, at 0.5 T (panel D), m_1 to m_7 can be

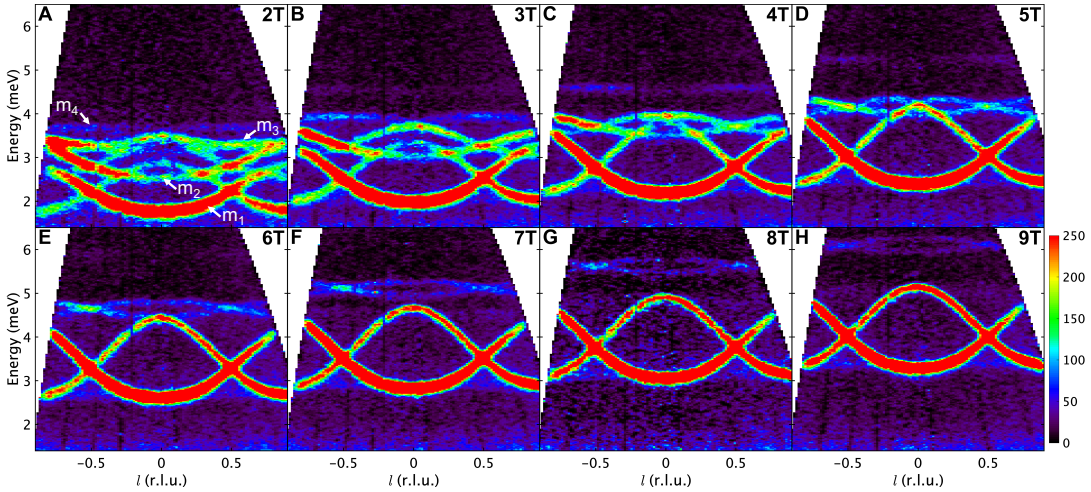

Figure 4.5: INS spectrum as a function of field from 2 to 9 T $\parallel a$, covering the intermediate to strong confinement regimes, with field increasing from left to right and top to bottom. Colour is the raw neutron scattering intensity on an arbitrary scale (different from Fig. 4.3), collected using a high-coverage coarser-resolution configuration ($E_i = 9.33$ meV) for the same fixed sample orientation as in Fig. 4.3, with wavevectors projected along the chain direction. Panel A is at the same field as the higher-resolution data in Fig. 4.3H.

resolved. The kinetic bound state, however, increases in energy relatively slowly since it is a single-spin-flip state, such that the confinement bound states move past it as field is increased. Upon increasing field, the extent of the spectrum covers a progressively wider energy range and so, to probe the full spectrum above 2 T, a higher incident energy, coarser-resolution configuration is used, with data plotted in Fig. 4.5. Data at 2 T are shown in both configurations, [compare Fig. 4.3H and Fig. 4.5A]. At 2 T (panel A), modes m_1 to m_4 (faint horizontal line near 3.7 meV) are clearly resolved, but, upon further increasing field, modes m_3 and m_4 become progressively fainter and above 6 T, in the strong confinement regime, only m_1 and m_2 remain (panels F to H). In the following, first the strong confinement regime is discussed, then the intermediate field regime is discussed in detail.

4.4 Strong confinement regime

The INS spectrum at 8 T, representative of the strong confinement regime, is shown in Fig. 4.6A. Two dispersive modes, lower energy m_1 and higher energy m_2, are seen, each with both a (stronger intensity) primary and a (weaker intensity) shadow

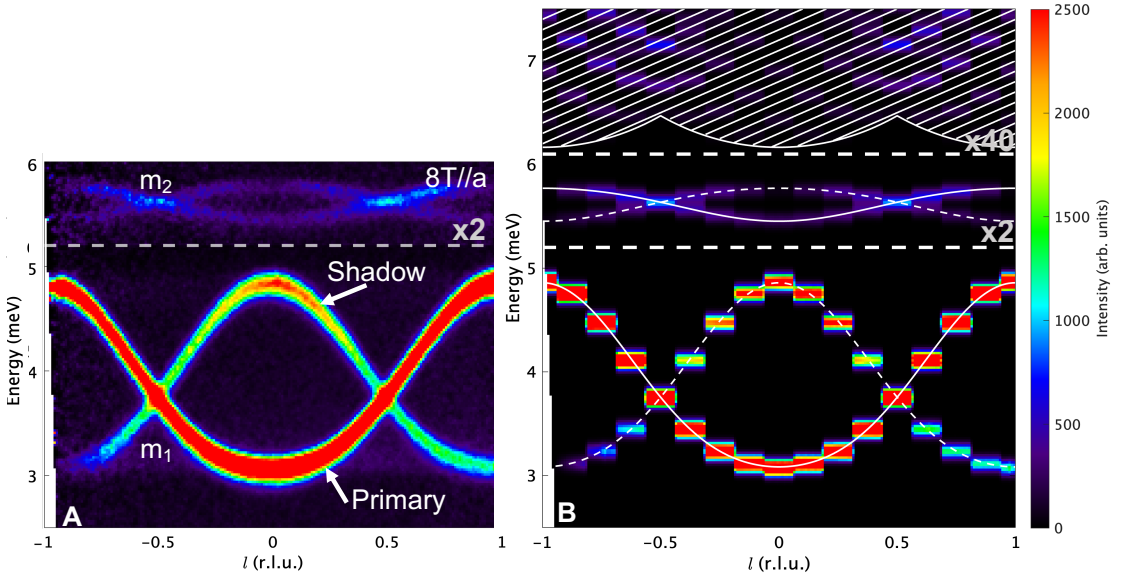

Figure 4.6: A) INS spectrum at 8 T, deep in the strong confinement regime, obtained by averaging a multi-angle scan over the transverse wavevector range $|h| \leq 1.5$ and $|k| \leq 1.5$. Intensities above the dotted line have been scaled up by a factor of 2 to make them more clearly visible. The incident energy used is the same as in Fig. 4.5. B) Calculated intensity $S(\boldsymbol{Q}, \omega)$ as defined in (5.26) for the single-chain Hamiltonian in (5.21), where interchain interactions are included in a mean-field approximation as per (5.28), calculated using exact diagonalization (ED) on a chain of $n = 16$ sites ($n/2$ zigzag unit cells) with periodic boundary conditions. ED gives the spectrum for a discrete set of wavevectors spaced by $\Delta l = 2/n$; for visualization purposes, the spectrum is plotted as constant over the interval Δl around each discrete wavevector. The ED results have been convolved with a Gaussian in energy of FWHM 0.16 meV, representative of the experimental resolution in this energy range and obtained by a fit to the observed peak lineshapes. The white curves are the best fit single-chain dispersion relations with solid and dashed curves showing primary and shadow modes (obtained via $l \to l + 1$ translation) respectively. The hatched region represents the $2m_1$ continuum obtained by assuming that quasiparticles do not interact. Note that m_2 is below the $2m_1$ continuum at all wavevectors. The m_2 and $2m_1$ intensities have been multiplied by factors of 2 and 40, respectively.

version (obtained from the primary via an $l \to l + 1$ translation). In this regime, m_1 is a magnon mode, a coherently propagating single spin flip, as expected for the lowest energy excitation in a field-polarized paramagnet. Meanwhile, the m_2 mode can be understood as a dispersive two-spin-flip state, i.e. a bound state of two m_1 magnons. To understand why a two-magnon state can still exist in this limit of high fields, and why it is dispersive, albeit with a much suppressed bandwidth compared to m_1, it is insightful to consider a minimal Ising-like XXZ model in longitudinal field as discussed in Chapter 2. It is proposed in this work that the

m_2 state seen experimentally has the same qualitative content as the two-spin-flip bound state for the minimal model in (2.19), but with modifications appropriate for the relevant Hamiltonian, such that the m_2 dispersion relation depends on all λ's in (5.21), to be discussed in the following chapter. The dynamical correlations calculated for this model are shown in Fig. 4.6B and capture all key features of the dispersions and intensities of both the m_1 and m_2 modes.

Note that a two-spin-flip state cannot usually be seen in inelastic neutron scattering [it would not be observable for the Hamiltonian in (2.19)], since the scattering intensity of a given state is determined by its overlap with a single spin flip created in a neutron scattering process. However, in the present case, the external field is applied along the crystallographic a-axis, which makes a finite angle $90° - \gamma$ with the Ising direction, and so the field is not perfectly longitudinal but also has a finite transverse component. In addition, as is discussed in the following chapter, there are also sub-leading exchange terms in the spin Hamiltonian that break spin conservation. Both the finite (large) transverse field and the (relatively much smaller) exchange terms in the Hamiltonian that break spin conservation lead to some mixing between states with different numbers of spin flips, allowing the predominantly two-spin-flip m_2 state to have a finite admixture of a single-spin-flip state and therefore to be visible in the present INS experiments.

It is notable that the m_2 mode is expected to survive up to indefinitely large field (although the intensity would become progressively weaker as the mixing with the single-spin-flip state would progressively decrease upon increasing Zeeman energy). This is because the binding energy of m_2 relative to the $2m_1$ continuum for the minimal model in (2.19, 2.20, 2.21) is $m_2 - 2m_1 = -J$ in the limit $\lambda_S \to 0$, i.e. the two magnons gain Ising energy if they are next to one another. The fact that the m_2 mode is lower in energy than the $2m_1$ continuum means that it is not energetically possible for it to decay, hence it survives as a sharp mode.

It is also important to note that at these high fields the m_1 state has non-negligible dispersion bandwidth perpendicular to the chain direction because of the finite interchain couplings; this is again discussed further in the following chapter.

This has the consequence that the lineshape of the m_1 mode in Fig. 4.6A appears artificially broadened because the data are integrated over a large range in the wavevector direction transverse to the chains. The interchain dispersion at high field is non-negligible because the hopping strength between chains for a single spin flip is first order in the interchain exchange. In contrast, at lower fields, even the lowest energy mode (m_1) has multiple spin flips, as illustrated in Fig. 4.4 for ψ_1, so the interchain dispersion is higher order in the interchain exchange strength and is thus much suppressed, such that it is essentially undetectable at low field.

Note also that the bottom of the m_1 dispersion is visibly flattened compared to a perfect sinusoid [see Fig. 4.6A], indicating a double Fourier component along l, suggesting hopping to next-nearest-neighbour sites along the chain, which will be further discussed in the following chapter.

4.5 Fate of higher order bound states

4.5.1 Disappearance of the higher bound states

The evolution of the INS spectrum upon increasing field from 2 to 9 T is shown in Fig. 4.5. A notable feature is that, upon increasing field, the higher order bound states progressively become less dispersive and rapidly lose spectral weight, with the highest ones doing so at the fastest rate. In detail, at 2 T (panel A), m_1 and m_2 have similar intensities and bandwidths, m_3 is fairly flat and m_4 is very flat and fairly weak. Upon increasing field, m_4 moves up in energy and becomes weaker until it disappears between 4 and 4.5 T. At those fields, m_3 is completely flat and weaker in intensity, then becomes undetectable above 6.5 T.

The field dependence of the m_3 mode is summarized in Fig. 4.7A. The intensity (red triangles and right vertical axis) drops off very rapidly upon increasing field, decreasing by more than an order of magnitude between 1 and 4 T. In this field range, the m_3 energy (blue round symbols, left axis) is below the estimated $2m_1$ continuum lower boundary (dashed line), so the m_3 mode should be stable, with no mechanism for decay; nevertheless, its intensity drops off very fast upon increasing field. A qualitatively similar behaviour is observed for the m_4 mode (panel B):

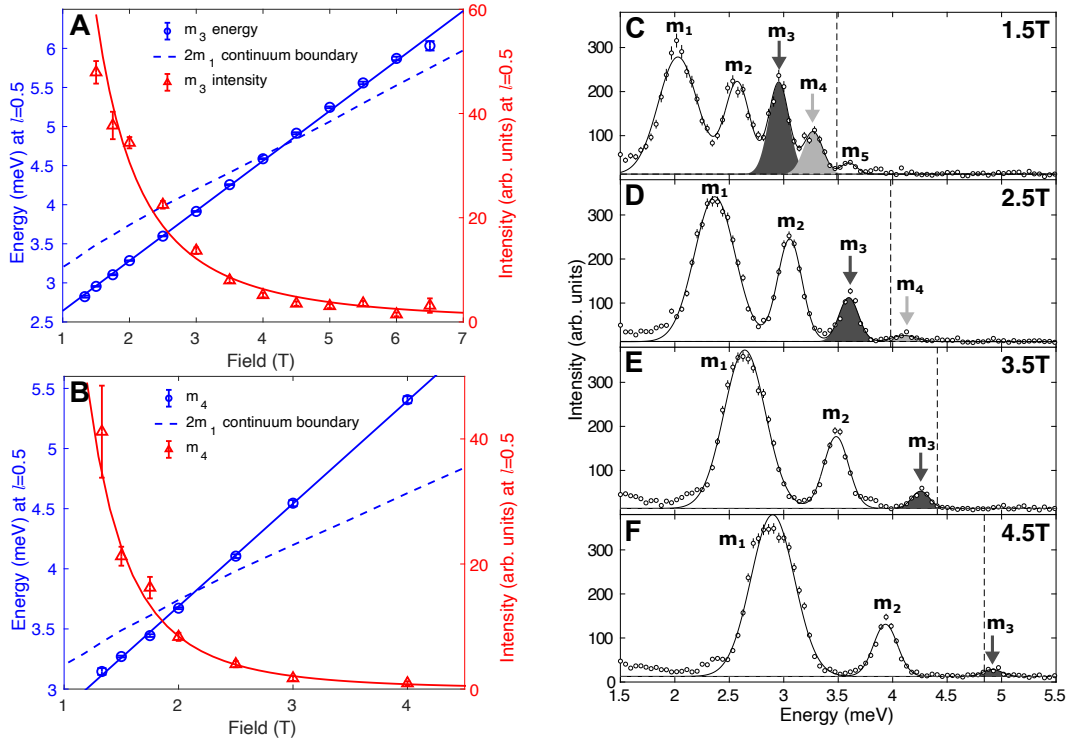

Figure 4.7: A,B) Energies (blue symbols, left axes) and integrated intensities (red symbols, right axes) deduced from multi-Gaussian fits of the m_3 (A) and m_4 (B) mode at $l = 0.5$, extracted from cuts from data in the same configuration as in Fig. 4.5. Solid lines are guides to the eye and the dashed lines show the estimated $2m_1$ continuum lower boundary at the same l-value. C-F) Energy scans showing the field dependence of the various modes (integrated over $0.4 < l < 0.6$), solid lines are fits to multi-Gaussian peaks. Intensities are raw neutron scattering intensities on an arbitrary scale (the same for all panels). Note that a clear signal at the expected $m_{3,4,5}$ energy is present even after crossing the $2m_1$ continuum lower boundary (dashed vertical line in panels C-F), which has been calculated using fitted dispersion relations for the m_1 mode and assuming that m_1 particles do not interact with each other.

the intensity drop-off is an even steeper function of increasing field and again the intensity decreases very quickly even before 2 T, above which m_4 enters the $2m_1$ continuum. Within the sensitivity of the experiments, no systematic intensity change occurs for either of the $m_{3,4}$ modes as they enter the continuum and their signal could be followed even up to significantly higher fields, when the modes should be deep into the continuum energy range [see Fig. 4.7C-F]. This might suggest that the matrix elements for the decay processes $m_{3,4} \rightarrow m_1 + m_1$ are relatively weak, and that the dominant effect leading to the fast intensity drop-off

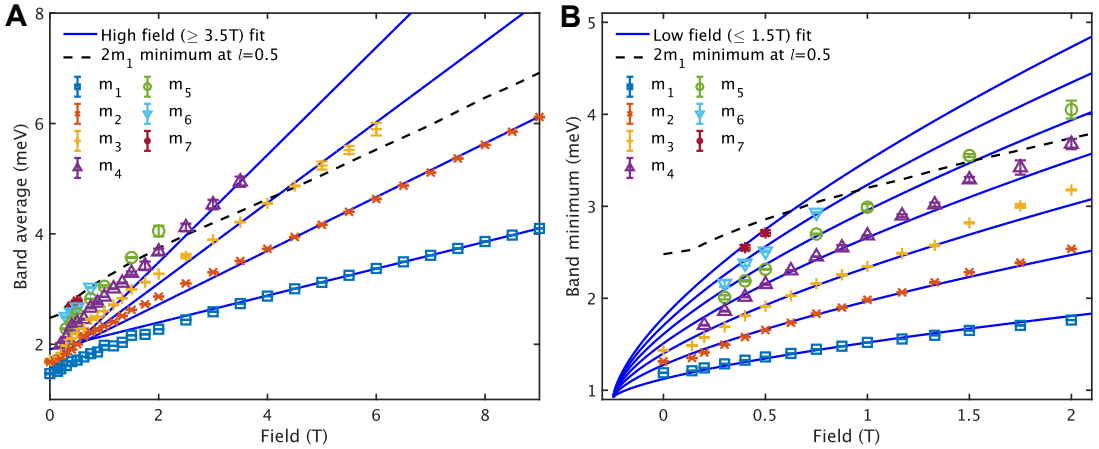

Figure 4.8: A) Band averages fit (solid lines) to a form $E_n = ng\mu_B B + E_{0n}$ where n labels modes, $g = 4.20(2)$ is an effective g-factor (for fields along a) and E_{0n} is an effective zero-field energy. The fit only includes data for $B \geq 3.5$ T. B) One-dimensional band minima, corrected for the effects of interchain hopping, as a function of field in the low field regime. The band minima have been simultaneously fit (solid lines) to a form $E_n = \alpha z_n |B - B_0|^{2/3} + E_0$ as per (4.2), where $-z_n$ are the zeroes of the Airy Ai function, $B_0 = -0.24(2)$ T is a field offset due to the mean field effects of the antiferromagnetic interchain interactions, $\alpha = 0.221(2)$ meV $\mathrm{T}^{-2/3}$ is a constant of proportionality related to $(\hbar^2/\mu)^{1/3}$, and $E_0 = 0.92(2)$ meV is the energy required to create a pair of domain walls. The fit only includes data in the field polarized paramagnetic regime for $0.14 \leq B \leq 1.5$ T; the zero field data were omitted from the fit as the magnetic structure is different from that above 0.14 T such that a different value of B_0 would be needed. In both panels, the dashed line shows the energy of the lower boundary of the $2m_1$ continuum at $l = 0.5$ under the assumption that the quasiparticles do not interact.

with increasing field is the progressively reduced mixing of the single-spin-flip state into the wavefunction of the $m_{3,4}$ modes, as upon increasing field the number of spin flips becomes a progressively better approximation for a good quantum number. This picture is consistent with the results of exact diagonalization (ED) calculations, which indicate that while there is some decay of the bound states when they overlap with the continuum, the predicted broadening is of order 0.01 meV, which is not resolvable within the experimental results presented here.

4.5.2 Crossover from weak to strong confinement

As well as studying the disappearance of the higher bound states, the crossover between the weak and the strong confinement regimes was quantitatively tested by doing fits to the expected field dependence of the mode energies. In the high field

regime, a linear dependence of mode energy on field is expected. This is because, in this regime, the number of spin flips in the mode is approximately a good quantum number, with the m_n mode containing states with n spins flipped compared to the field-polarized state. Thus, the Zeeman energy is expected to scale linearly with both mode number and field. Indeed, the band averages are well fit by a linear dependence of energy on field and mode number, i.e., a fit where the gradients of the m_2, m_3 and m_4 lines are constrained to be 2, 3 and 4 times, respectively, the gradient of the m_1 line, as illustrated in Fig. 4.8A. A cutoff field of 3.5 T, assumed to be close enough to the high field limit, was used, and only data at fields above this were included in the fit, which was performed simultaneously to the four lowest energy modes. The quality of this fit, especially for the m_1 and m_2 modes, also adds evidence that these are single-spin-flip and two-spin-flip modes respectively, i.e., derived from modes with wavefunctions given in (2.22) and (2.23). The fit in this regime used the band averages, as the band minima in this regime were found to be affected by the tilting of the local magnetization towards the field, which leads to a field-dependent bandwidth. This effect is quantitatively understood and is discussed in more detail in the following chapter.

Fig. 4.8A also illustrates that the linear fit breaks down at low fields. This is expected, since at low field the number of spin flips ceases to be even approximately a good quantum number, and instead the weak confinement physics described in Sec. 4.3 holds. In this low field regime, a fit was performed simultaneously to the band minima of all the modes, as shown in Fig. 4.8B, with the field dependence having a 2/3 power law form, as per (4.3), and the spacing between the energy levels being constrained by the zeros of the Airy function. The band minima were corrected for the effects of interchain dispersion by fitting the experimentally-extracted dispersion points to a parameterized three-dimensional (3D) dispersion relation of the form given in Chapter 5.3.2.1, then setting the interchain hopping terms in those parameterizations to zero to correct for the small energy shifts due to interchain dispersion. The good agreement obtained between the field dependence of the bound state energies and the different expected power-law behaviours in

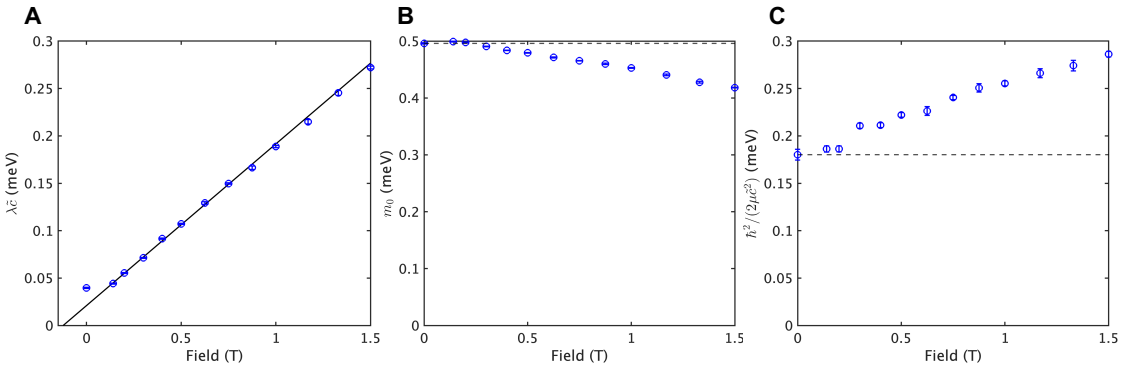

Figure 4.9: Field dependence of $\lambda\tilde{c}$ (A), m_0 (B), and $\hbar^2/(2\mu\tilde{c})$ (C), extracted from fits to the $|l| < 0.3$ dispersion of the modes in the low field regime. In A, the black line is a straight line fit; the slope is given by $g_{\text{eff}}\mu_B$, from which $g_{\text{eff}} = 2.95$. This is to be compared with $g_z \sin\gamma = 3.45$. The non-zero value of the x-intercept (-0.12 T) is due to the effect of interchain interactions. In B and C, the dashed lines are guides to the eye indicating the zero field value. While the assumption that λ has a linear dependence on field holds well, the assumptions that m_0 and μ are constant hold less well, which is attributed to the fact that the transverse component of field increases alongside the longitudinal component, as discussed in the text.

the two field limits in Fig. 4.8 (solid lines) lends support to the proposal that, in $CoNb_2O_6$, the interchain couplings are sufficiently small relative to the dominant in-chain exchange, and the Ising character sufficiently strong, that both the weak and the strong spinon confinement regimes are realized experimentally via tuning of the applied field. The crossover region is approximately between 1.5 and 3.5 T. Note that, according to the Hamiltonian and parameters refined in the following chapter, this crossover region is where the kinetic term for domain walls and the Zeeman term are comparable, such that the continuum approximation used in (4.2) for the weak confinement regime is no longer applicable.

The fits in Fig. 4.8B were done using the form (4.2), and assuming that λ was linearly related to the applied field while m_0 and μ remained constant. It is possible to verify this assumption by doing fits to a finite l-region around the band minima, rather than just the band minima, independently at each field. Fits were therefore done to the data with $|l| < 0.3$ with the form [25]

$$\hbar\omega_n(l) = 2m_0 + 2\left(\frac{\hbar^2}{2\mu\tilde{c}^2}\right)\left(\frac{\pi l}{2}\right)^2 + z_n\left(\lambda\tilde{c}\right)^{\frac{2}{3}}\left(\frac{\hbar^2}{\mu\tilde{c}^2}\right)^{1/3}, \tag{4.5}$$

where $\tilde{c} = c/2$ is the spacing of sites along the chain, and $\omega_n(l)$ is the energy of the nth mode at wavevector l. In this equation, m_0 determines the gap to the first mode, μ determines the curvature of the bands and λ determines the spacing between the modes. Equation (4.5) implies that the curvature of all the bands is the same, and this is only true up to about 1.5 T, which was also the upper limit for the weak confinement regime found through fits to the band minima. The results of these fits, shown in Fig. 4.9, are therefore only shown up to 1.5 T. It can be seen (panel A) that the assumption that λ depends linearly on field is a good one. Figure 4.9B and C shows that the assumptions that m_0 and μ remain constant with increasing field do not hold however. The fact that m_0 decreases with increasing field can be understood to be due to the cost of creating domain walls decreasing as the moments tilt towards the field. The fact that $\hbar^2/(2\mu\tilde{c})$ increases with field is likely due to the interplay between the transverse component of the applied field and additional terms in the Hamiltonian which will be discussed in the following chapters, as both the transverse field and these additional terms allow domain walls to hop. If it were possible to apply the field perfectly parallel to the local easy axes, the agreement between the data and the fits shown in Fig. 4.8B might perhaps be even stronger.

4.6 Conclusions

In summary, the confinement potential between spinons in the ferromagnetic Ising chain material $CoNb_2O_6$ was tuned by applying an external magnetic field along the crystallographic a-direction, such that there was a large longitudinal (along Ising axis) field component. In the low field, weak confinement regime, a hierarchy of bound states was found, with their energy varying as field to the 2/3 power and the spacing between modes determined by the zeros of the Airy function, as expected in a picture of domain walls in a linear confining potential proportional to the strength of the longitudinal field. Upon increasing field, higher order bound states increase more quickly in energy and progressively disappear from the spectrum such that in the limit of high field, in the strong confinement regime, only two bound states were found, whose energies depend linearly on field. The higher

energy of these two bound states is a dispersive two-spin-flip bound state which is stabilized by the proximity to the Ising limit.

5

Refinement of the quantum spin Hamiltonian of $CoNb_2O_6$

Near the quantum critical point, $CoNb_2O_6$ exhibits the universal properties of the transverse field Ising chain. Away from criticality, however, rich non-universal physics is observed due to additional terms in the Hamiltonian beyond the pure Ising limit. A quantitative understanding of this physics requires a parameterization of these non-Ising terms. In this chapter, a method is proposed to refine both the in-chain and inter-chain interactions using a two step method. The interchain couplings are first quantitatively parameterized using linear spinwave theory (LSWT) in the regime of high applied field, where LSWT is expected to capture the interchain dispersions well. A global fit is then performed to the observed spectrum in zero field and high field applied along two orthogonal directions corrected for the interchain dispersions, using exact diagonalization methods for a 1D chain. A refined single-chain and interchain Hamiltonian is thus proposed that quantitatively reproduces the dispersions of all observed modes and their field dependence. The results of this chapter have been published in Ref. [98], Sec. IV.

5.1 Introduction

The material $CoNb_2O_6$ constitutes one of the best condensed matter realizations of the transverse field Ising chain. A detailed understanding of the ways in which this material both exhibits and deviates from the expected universal behaviour is therefore very important; this requires an understanding of the additional terms in the spin Hamiltonian for $CoNb_2O_6$, beyond the pure Ising limit. It has been known for some time that additional terms are needed to explain the spectrum observed in zero field; for instance, the kinetic bound state observed at the Brillouin zone boundary requires the presence in the Hamiltonian of an XY exchange term of magnitude $\approx 20\%$ of the dominant Ising exchange [25]. In addition, the fact that domain walls are dispersive even in zero field, as mentioned in Chapter 4, requires an explanation. While this was initially modelled with a phenomenological transverse field term [25, 136, 137], the domain wall motion has recently been explained as being due to an off-diagonal staggered exchange term, which is allowed by the glide symmetry of the crystal [71]. This term also accounts for the quasiparticle breakdown observed in high transverse field [71, 138]. In addition, the weak interchain interactions are crucial for both the confinement physics observed in zero field and the E8 physics observed near the quantum critical point [25, 43]. A detailed characterization of these interchain interactions is thus important for understanding this physics.

In this chapter, the high field inelastic neutron scattering (INS) data discussed in Chapter 4 enable a further refinement of the microscopic model for $CoNb_2O_6$ beyond the minimal in-chain Hamiltonian proposed in Ref. [71], which was refined based only on the spectrum observed in zero field. The effects of the interchain couplings on the high-field dispersive modes are first parameterized for fields along both a and b to extract pure one-dimensional (1D) dispersion relations. In the course of this, a minimal model of the interchain interactions previously proposed to explain the dispersions in large transverse field [134] is revised and extended, such that the high field dispersions for field along both a and b directions can be consistently reproduced. These parametrized high field dispersions, along with the

spectrum observed in zero field, are then compared with exact diagonalization (ED) calculations to arrive at a refined spin Hamiltonian that quantitatively reproduces all the features seen in the full wavevector dependence of the inelastic neutron scattering data, across a wide range of applied fields.

The rest of this chapter is organized as follows. In Sec. 5.2, experimental details for additional measurements beyond those described in Chapter 4 are briefly discussed. The quantitative parameterization of the interchain dispersions obtained in Sec. 5.3 makes it possible to obtain effective 1D dispersion relations to which a single-chain Hamiltonian can be fit, which is done in Sec. 5.4; Sec. 5.4.1 introduces the proposed single-chain Hamiltonian and Sec. 5.4.2 describes the fitting method. In Sec. 5.5, it is shown that other models which have been proposed are not able to quantitatively describe the full set of data presented here. In Sec. 5.6, it is demonstrated that this proposed Hamiltonian also quantitatively captures the behaviour of the magnetic excitations in $CoNb_2O_6$ away from the fields at which the fit was performed and that the proposed Hamiltonian can account for the spectrum observed in THz spectroscopy in Ref. [125]. Finally, Sec. 5.7 contains the conclusions.

5.2 Experimental details

The analysis presented in this chapter is based on data in field applied in two orthogonal directions, which were collected in two different experiments. The data in field applied along the crystallographic a-direction were already presented in Chapter 4, along with the details of that experiment. The other data was a Horace scan collected in high field along b, and details of the experiment in which this data set was collected are presented below.

Attribution note: *The experiment described in this section was carried out before the start of my thesis by an experimental team consisting of Ivelisse Cabrera, Jordan Thompson and Radu Coldea (University of Oxford) and Robert Bewley (ISIS facility), using a single crystal grown by D. Prabhakaran (University of Oxford).*

Experimental details are included for completeness. I performed the processing of the raw time-of-flight data and all of the subsequent analysis.

Inelastic neutron scattering measurements were performed on LET at the ISIS facility. The measurements were carried out at 0.14 K in a field of 9 T $\parallel b$ on the same crystal as in Ref. [134], which was mounted in the $(h0l)$ horizontal scattering plane. For these measurements, the incident energies used were $E_i = 2.14$, 4.02 and 10.17 meV, and the angular range was 145° covered in steps of 1° with 6 minutes counting per step. The Horace scans in field along both a and b were used to quantitatively parameterize the interchain dispersions, as detailed in Sec. 5.3.

As in Chapter 4, raw time-of-flight neutron data were converted to scattering intensities $S(\boldsymbol{Q}, \omega)$ using MANTID [88], and the resulting data were then analysed using the HORACE [90] and MSLICE [89] packages.

5.3 Interchain dispersions

5.3.1 Characterization of the interchain dispersions in high field

INS data probing the dispersions in the interchain directions in high field are plotted in Fig. 5.1. Panel A shows that in large field along a, no systematic dispersion bandwidth is detected along h within the experimental resolution used. Therefore, all data taken with field along a presented in the rest of this chapter and the previous one were integrated across the entire range of h in the data, that is, over $-1.5 < h < 1.5$. Along k, however, there is visible dispersion and further, the bandwidth and even sign of the dispersion depends on the mode energy, i.e., on l. This is illustrated in Fig. 5.1B, where the lower energy and higher energy modes have k dispersions that are of opposite signs (white solid lines are fits as described in Sec. 5.3.2.1). Note that the bottom mode is the shadow version of the primary m_1 mode wavevector-translated from $l = 0$ whereas the top mode is the primary m_1 mode at $l = 1$. This coupled kl dispersion is accounted for by the exchange pathways shown schematically in Fig. 5.1I and is discussed mathematically in the following subsection.

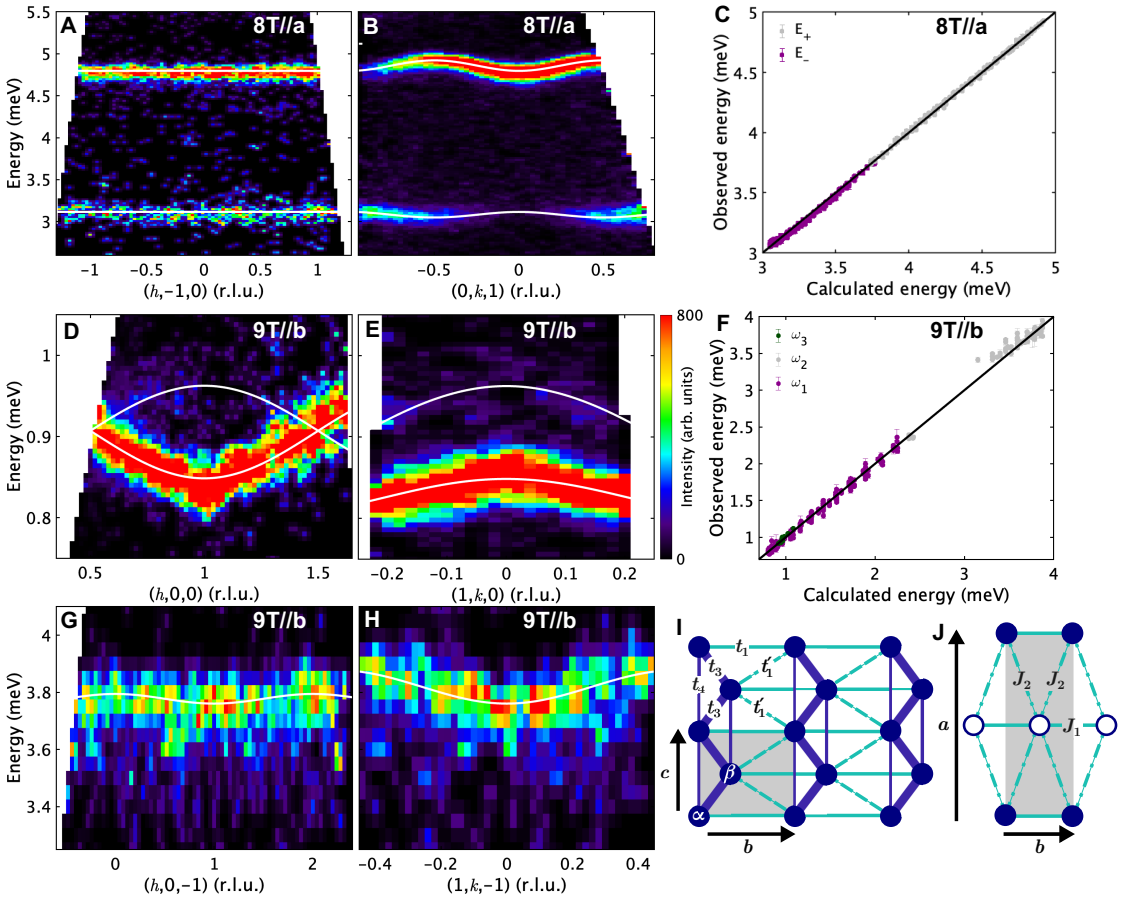

Figure 5.1: Interchain dispersions at 8 T $\parallel a$ (A, B) and 9 T $\parallel b$ (D, E, G, H). White curves represent best fit dispersion relations. Colour is the raw neutron scattering intensity on an arbitrary scale. The incident energies E_i used were 9.33 meV (A, B), 2.14 meV (D, E) and 10.17 meV (G, H), and the overall intensity scale is different for each experimental configuration. C, F) Comparison of observed and calculated energies with best fit parameters for the 8 T $\parallel a$ hopping dispersion (5.2) and 9 T $\parallel b$ linear spin wave theory dispersion respectively, with $\omega_{1,2}(\boldsymbol{Q}) = \omega_{\pm}(\boldsymbol{Q})$ and $\omega_3(\boldsymbol{Q}) = \omega_{-}(\boldsymbol{Q} + \boldsymbol{a}^*)$, with $\omega_{\pm}$ as per (5.8). I, J) Exchange interaction paths in the bc and ab planes, respectively. Labels $t_{1,3,4}$ and t_1' are hopping parameters for the dispersion model in (5.2), while J_1 and J_2 refer to the Hamiltonian (5.4). Dark/light colored lines indicate in-chain/interchain bonds, respectively. The grey shaded area indicates the structural unit cell shifted from the conventional $Pbcn$ unit cell such that the origin is at one Co^{2+} site. The site labels α and β are used in the hopping calculations for the Hamiltonian in (5.1) and in the linear spin wave theory calculations for the full interchain Hamiltonian in (5.4). Filled/open circles represent spins with the local Ising axis at an angle $\pm\gamma$ to the c direction respectively. The experimental data were averaged in the transverse wavevector directions as follows: $-1.05 \leq k \leq -0.95$, $-0.05 \leq l \leq 0.05$ (A); $-1.5 \leq h \leq 1.5$, $0.95 \leq l \leq 1.05$ (B); $-0.1 \leq k \leq 0.1$, $-0.05 \leq l \leq 0.05$ (D); $0.8 \leq h \leq 1.2$, $-0.05 \leq l \leq 0.05$ (E); $-0.1 \leq k \leq 0.1$, $-1.05 \leq l \leq -0.95$ (G); $0.8 \leq h \leq 1.2$, $-1.05 \leq l \leq -0.95$ (H).

Panels D, E, G and H of Fig. 5.1, meanwhile, show the dispersions in the directions perpendicular to the chains in a transverse field, 9 T $\parallel$ b. It can be seen that in this regime, there is interchain dispersion along both h and k, of similar magnitude to that seen along k for $B \parallel a$. However, while the dispersion along k remains of similar magnitude but switches sign when moving from $l = 0$ (Fig. 5.1E) to $l = -1$ (Fig. 5.1H), i.e. from the bottom to the top of the dispersion, similarly to what is seen for $B \parallel a$, the dispersion along h is strongly suppressed at $l = -1$ (Fig. 5.1G) compared to at $l = 0$ (Fig. 5.1D). The model proposed in Ref. [134] captures some, but not all, of these interchain dispersion effects. In particular, it predicts that the interchain bandwidth is suppressed at higher energy (i.e. $l = -1$ compared to $l = 0$). This is indeed seen along h, but not along k. The same model also predicts that there will be very little interchain dispersion for near-longitudinal field, which is again seen along h but not along k; in fact, the dispersion bandwidth along k at $l = 1$ in near longitudinal field is approximately the same as in transverse field (the $l = 0$ transverse field k dispersion bandwidth is enhanced by the bonds in the ab-plane). In this work, the interchain interaction model in Ref. [134] is therefore expanded and revised with the proposal that the bonds with a component along the a-direction (the dash-dot light blue J_2 paths in Fig. 5.1J) are approximately Ising, whereas those in the bc plane [the solid and dashed light blue paths in Fig. 5.1I, i.e., J_1 (t_1) and J_1' (t_1')] are approximately Heisenberg.

5.3.2 Parameterization of the dispersion relations in high field

Parameterization of the interchain dispersion relations was done by assuming that the dispersion of single spin flips in directions perpendicular to the chains could be quantitatively captured using a linear spinwave formalism, but with in-chain parameters which may be renormalized compared to those deduced from the exchange Hamiltonian. The linear spinwave formalism is expected to be asymptotically exact in the limit of high field (when the gap is much larger than the bandwidth). In this limit, the linear spinwave dispersion relation can be

perturbatively expanded to become equivalent to a spin-flip quasiparticle hopping (or tight-binding) formalism. As the hopping formalism depends only on the exchange pathways, this same formalism can also be applied to quasiparticles composed of multiple spin-flips. In the case of field along the a-direction, a parameterization of the dispersion of bound states of various different numbers of spin flips within a single formalism is sought, and a hopping formalism is therefore used. For high transverse field, a parameterization of only a single magnon mode is sought, but in a case where the gap is fairly small compared to the bandwidth such that a perturbative expansion in terms of a hopping formalism does not hold; a linear spinwave theory formalism is therefore used.

5.3.2.1 Hopping model parameterization of the 3D dispersions in high near-longitudinal field ($\parallel a$)

In order to account for the coupled kl dispersion observed in high field $\parallel a$ (see Fig. 5.1B), a hopping model was proposed, shown schematically in Fig. 5.1I, where solid and dashed bonds indicate paths across which excitations could hop. This approach was used in order to be able to describe both the m_1 and the m_2 modes using the same formalism. The effects of the Ising parts of the interchain coupling are taken into account at a mean-field level (see Sec. 5.6) which affects both the m_1 and m_2 states. This more phenomenological formalism is also able to capture the full 3D dispersions of higher bound states in lower fields. In Fig. 5.1I, the dark blue lines represent in-chain bonds (parameterized by t_3 and t_4), whose Hamiltonian is described in detail in (5.21), while the light blue lines represent interchain bonds (parameterized by t_1 and t_1'). The next-nearest-neighbour in-chain hopping (t_4) accounts for the flattening of the bottom of the dispersion [see Fig. 4.6A] while the diagonal interchain bonds (t_1') explain why the dispersion bandwidth along k depends on l.

This hopping model for the paths illustrated in Fig. 5.1I can be written as a two sublattice model (a single zigzag chain with two sites per effective unit cell) with sublattices labelled α and β. The different Ising directions on the two chains in the structural unit cell can be neglected as interactions along the a direction

are not included in the hopping model, since no dispersion along h is detected within the resolution of the experiment. This is consistent with the picture of the interchain couplings presented in the following subsection where the only coupling with a component along a, J_2, is Ising-like. This means that the hopping induced by J_2 is suppressed by a factor of $\sin^2\theta$ where θ is the angle between the local Ising axis and the local magnetization direction, and is small even for large fields along a. Therefore, in high field along a, the Hamiltonian can be approximated as being decoupled into bc planes with hopping interactions within planes and it is written as

$$\begin{aligned}\mathcal{H}_{\text{hopping}} = \sum_{\boldsymbol{R}} & \omega_0 \left(c^\dagger_{\boldsymbol{R},\alpha} c_{\boldsymbol{R},\alpha} + c^\dagger_{\boldsymbol{R},\beta} c_{\boldsymbol{R},\beta}\right) \\ & + \Big[t_3 \left(c^\dagger_{\boldsymbol{R},\alpha} c_{\boldsymbol{R},\beta} + c^\dagger_{\boldsymbol{R},\beta} c_{\boldsymbol{R}+\boldsymbol{c},\alpha}\right) + t_4 \left(c^\dagger_{\boldsymbol{R},\alpha} c_{\boldsymbol{R}+\boldsymbol{c},\alpha} + c^\dagger_{\boldsymbol{R},\beta} c_{\boldsymbol{R}+\boldsymbol{c},\beta}\right) \\ & + t_1 \left(c^\dagger_{\boldsymbol{R},\alpha} c_{\boldsymbol{R}+\boldsymbol{b},\alpha} + c^\dagger_{\boldsymbol{R},\beta} c_{\boldsymbol{R}+\boldsymbol{b},\beta}\right) + t_1' \left(c^\dagger_{\boldsymbol{R},\beta} c_{\boldsymbol{R}+\boldsymbol{b},\alpha} + c^\dagger_{\boldsymbol{R},\beta} c_{\boldsymbol{R}+\boldsymbol{b}+\boldsymbol{c},\alpha}\right) \\ & + \text{Hermitian conjugate} \Big]. \end{aligned} \tag{5.1}$$

where $c^\dagger_{\boldsymbol{R},\alpha}$ ($c_{\boldsymbol{R},\alpha}$) creates (annihilates) a quasiparticle on the α sublattice in the unit cell with origin at $\boldsymbol{R}$. The sum runs over all single-zigzag-chain unit cells, with primitive lattice vectors $(\boldsymbol{a}-\boldsymbol{b})/2$, $\boldsymbol{b}$ and $\boldsymbol{c}$ (the projection of the primitive unit cell in the ab plane is shown by the shaded area in Fig. 5.2B). The dispersion relations in this two sublattice model are then obtained as

$$\begin{aligned} E_\pm &= A \pm |B|\,, \\ A &= \omega_0 + 2t_4 \cos 2\pi l + 2t_1 \cos 2\pi k, \\ B &= 2\cos \pi l \left(t_3 e^{4\pi i k\zeta} + t_1' e^{-2\pi i(1-2\zeta)k}\right). \end{aligned} \tag{5.2}$$

Here, t_i are parameters of the model that ultimately originate from spin exchange interactions between sites connected by the bonds indicated in Fig. 5.1I and ζ is the fractional distance in the b-direction of the Co^{2+} ions from the centre of the zigzag. The $\pm$ signs are to be chosen for the primary/shadow modes respectively for $|l| < 0.5$ and vice-versa for $0.5 < l < 1.5$. If the hopping quasiparticle is a spin

Parameter	Value (meV)
$2t_1$	-0.0147(4)
$2t_1'$	0.0477(6)
J_1	-0.008(2)
J_1'	0.040(2)
J_2	0.023(1)
$J\lambda_{\mathrm{MF}}$	0.0391(7)

Table 5.1: Interchain parameter values. $2t_1$, $2t_1'$ are hopping parameters from the 8 T $\parallel a$ fit to the m_1 dispersion. These should be compared to the values of J_1 and J_1' respectively. The fact that the respective values are comparable is evidence that these bonds are approximately Heisenberg. J_1, J_1' and J_2 are from the fit to 9 T $\parallel b$ data. $J\lambda_{\mathrm{MF}}$ is the value of the zero-field interchain mean field derived from the fit to zero field data. It is expected that $J\lambda_{\mathrm{MF}} = J_1 + J_1' = 0.032(1)$ meV, under the assumption that J_1 and J_1' are Heisenberg. This number is comparable to the fitted value.

flip, the dynamical structure factor in inelastic neutron scattering is expected to be proportional to

$$I_{\pm} = 1 \pm \cos\left(\arg B\right). \tag{5.3}$$

The very good agreement between the observed and calculated m_1 dispersions using the best fit parameter values is shown in Fig. 5.1C and corresponding values for the interchain hopping parameters are listed in Table 5.1. Similarly good agreement is found for the m_2 mode; in this case the interchain parameters t_1 and t_1' were set to zero because the m_2 state is a two-spin-flip state, and so any interchain dispersion would be second order in the interchain interaction strength, and thus expected to be too small to resolve experimentally.

The hopping model dispersion relation in (5.2) was used to parameterize each mode at each field in the $B \parallel a$ data. One-dimensional band characteristics were obtained by setting t_1 and t_1' to zero and calculating the relevant characteristic based on the fitted values of the other parameters, that is ω_0 (the energy offset due to Ising and Zeeman terms), t_3 and t_4. For the fits in Chapter 4.5, these were the band average, $E_{\mathrm{average}} = \omega_0$ and the band minimum, $E_{\mathrm{min}} = \omega_0 + 2t_3 + 2t_4$ (note that t_3 is negative for all bands as the dominant nearest-neighbour interaction is

ferromagnetic). It was found that, as the field decreases, the interchain dispersion decreases, which is consistent with the picture that upon lowering field, quasiparticles acquire a more pronounced multi-spin-flip character and the hopping of multi-spin-flip excitations is suppressed as it is of higher order in the interchain couplings. The kinetic bound state remains dispersive down to 0.14 T, consistent with this being a single-spin-flip mode, but has unresolvable dispersion in zero field, consistent with the zero field magnetic structure, in which the interchain hopping of the single spin flip is suppressed, as shown in Sec. 5.3.3. These trends were extracted from fits to the single orientation data, where the wavevector components k and l are coupled, and were confirmed by investigation of the Horace scan data set at 1.5 T.

Note also that the generic intensity from (5.3) captures the general intensity dependence along the interchain directions as observed, e.g., in Fig. 5.1B. Together with the good agreement with the dispersions, this justifies *a posteriori* the use of a hopping model to parameterize the excitations in this regime.

5.3.2.2 Linear spinwave theory parameterization of the 3D dispersions at high transverse field ($\parallel b$)

The linear spinwave theory formalism used to describe the interchain dispersion in high transverse field ($\parallel b$) is now discussed.

In the actual crystal structure of $CoNb_2O_6$, there are two zigzag chains per structural unit cell, shown in Fig. 5.2A (grey shading), one at the corner of the ab cell (filled circle) with Ising axis tilted at an angle $+\gamma$ away from c towards a, and one chain in the center (open circle) with Ising axis tilted at an angle $-\gamma$. In order to make progress analytically, a reference frame is used where the Ising axes of the central chains are rotated to match those of the chains in the corners, such that the unit cell halves (as shown in Fig. 5.2B), reducing the problem from a four sublattice to a two sublattice problem. This is possible because of a combination of factors which mean that the symmetry of the Hamiltonian is higher than is required by the crystal structure: first the fact that the magnetic field is applied along a high symmetry direction, and secondly the fact that the interchain interactions are

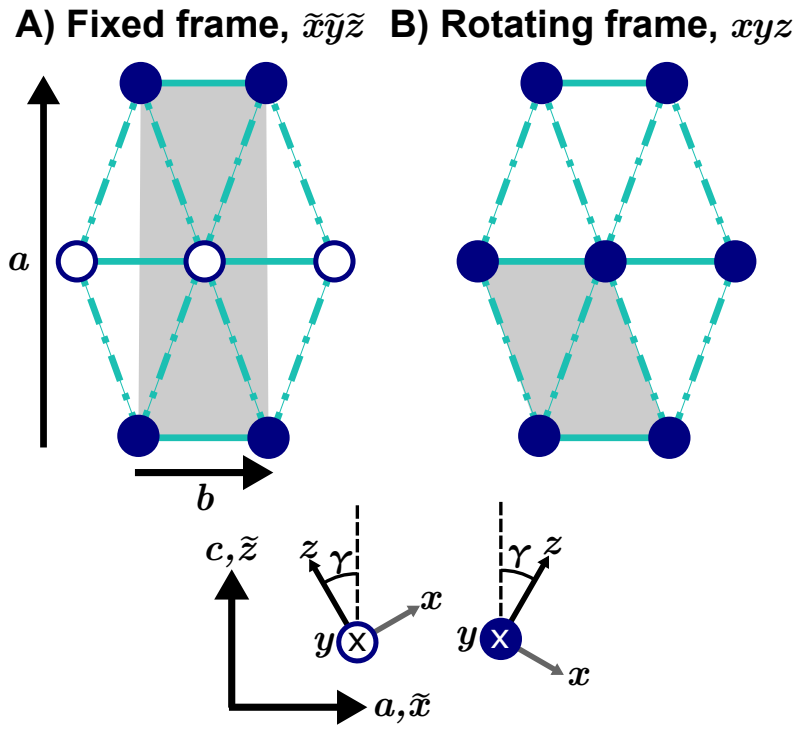

Figure 5.2: A) ab plane of the crystal structure where filled/open circles represent Co^{2+} ions with the local Ising axis at an angle $\pm\gamma$ away from $\boldsymbol{c}$ towards $\boldsymbol{a}$. This alternation of the local Ising axis leads to two zigzag chains per orthorhombic unit cell (rectangular shaded area). These two chains are symmetry-related by both a b glide (mirror in the $\frac{1}{4}\tilde{y}\tilde{z}$ plane followed by translation by $\boldsymbol{b}/2$) and an n-glide (mirror in the $\tilde{x}\tilde{y}\frac{1}{4}$ plane followed by translation by $(\boldsymbol{a}+\boldsymbol{b})/2$) of the $Pbcn$ space group of the crystal structure. Here $\tilde{x}\tilde{y}\tilde{z}$ define the fixed spin axes frame parallel to the orthorhombic abc crystal axes. Lower diagrams show the definition of a mathematically convenient spin axes frame xyz that rotates between the two chains such that z is always along the local Ising axis. B) In this rotating spin axes frame the two chains become equivalent and the unit cell halves (shaded parallelogram).

assumed to have a simple form, such that they are all either Heisenberg or Ising in the rotating frame. In this frame, the Hamiltonian is

$$\begin{aligned}\mathcal{H}_{\text{total}} = &\sum_{\text{chains}} \mathcal{H}_1 + \mathcal{H}_2 \\ &+ \sum_{\boldsymbol{R}} J_1 \left(\boldsymbol{S}_{\boldsymbol{R},\alpha}\cdot\boldsymbol{S}_{\boldsymbol{R}+\boldsymbol{b},\alpha} + \boldsymbol{S}_{\boldsymbol{R},\beta}\cdot\boldsymbol{S}_{\boldsymbol{R}+\boldsymbol{b},\beta}\right) + J_1' \left(\boldsymbol{S}_{\boldsymbol{R},\alpha}\cdot\boldsymbol{S}_{\boldsymbol{R}+\boldsymbol{b},\beta} + \boldsymbol{S}_{\boldsymbol{R},\beta}\cdot\boldsymbol{S}_{\boldsymbol{R}-\boldsymbol{b}+\boldsymbol{c},\alpha}\right) \\ &+ J_2 \left[S^z_{\boldsymbol{R},\alpha}\left(S^z_{\boldsymbol{R}+(\boldsymbol{a}+\boldsymbol{b})/2,\alpha} + S^z_{\boldsymbol{R}+(\boldsymbol{a}-\boldsymbol{b})/2,\alpha}\right) + S^z_{\boldsymbol{R},\beta}\left(S^z_{\boldsymbol{R}+(\boldsymbol{a}+\boldsymbol{b})/2,\beta} + S^z_{\boldsymbol{R}+(\boldsymbol{a}-\boldsymbol{b})/2,\beta}\right)\right].\end{aligned} \tag{5.4}$$

where $\mathcal{H}_{1,2}$ contain in-chain interactions defined in (5.22, 5.23). Here, $\boldsymbol{R}$ runs over all single zigzag chain unit cells, as in (5.1).

This Hamiltonian is now solved in linear spinwave theory, as described in

Chapter 2.5.1. Assuming spins polarized along the b-axis, after a Holstein-Primakoff transformation and a Fourier transform, the Hamiltonian in (5.4) takes the form (up to quadratic order in magnon operators and omitting the constant term)

$$\mathcal{H} = \frac{1}{2}\sum_{\boldsymbol{Q}} \mathsf{X}^\dagger_{\boldsymbol{Q}} \mathsf{H}(\boldsymbol{Q}) \mathsf{X}_{\boldsymbol{Q}}, \tag{5.5}$$

where $\mathsf{X}^\dagger_{\boldsymbol{Q}} = (a^\dagger_{\boldsymbol{Q}}, b^\dagger_{\boldsymbol{Q}}, a_{-\boldsymbol{Q}}, b_{-\boldsymbol{Q}})$ and $a^\dagger_{\boldsymbol{Q}}$ and $b^\dagger_{\boldsymbol{Q}}$ are the magnon creation operators for the two single-chain sublattices. The matrix $\mathsf{H}(\boldsymbol{Q})$ has the form

$$\mathsf{H}(\boldsymbol{Q}) = \begin{pmatrix} A & B & C & D^* \\ B^* & A & D & C \\ C^* & D^* & A & B \\ D & C^* & B^* & A \end{pmatrix}, \tag{5.6}$$

where A, B, C and D are functions of $\boldsymbol{Q}$ and are given by

$$\begin{aligned} A =& J\left(\lambda_S - \lambda_A - \lambda^{xy}_{\mathrm{AF}}\right) - J_1 - J'_1 + g_y \mu_B B \\ &+ J\frac{\lambda_{\mathrm{AF}} + \lambda^{xy}_{\mathrm{AF}}}{2}\cos 2\pi l + J_1 \cos 2\pi k + J_2 \cos \pi h \cos \pi k, \\ B =& \left[-J\frac{(\lambda_S + \lambda_A + 1)}{2} + J'_1 e^{2\pi i k}\right] e^{-4\pi i \zeta k} \cos \pi k, \\ C =& J\frac{\lambda_{\mathrm{AF}} - \lambda^{xy}_{\mathrm{AF}}}{2} e^{-2\pi i l} + J_2 e^{-\pi i h} \cos \pi k, \\ D =& J\frac{\lambda_S + \lambda_A - 1}{2} e^{4\pi i \zeta k} \cos \pi l. \end{aligned} \tag{5.7}$$

Note that the off-diagonal staggered exchange, λ_{yz}, does not appear in these expressions, since this term vanishes in the linear spinwave theory approximation when the ground state is fully aligned along the y direction. However, this term leads to higher order interactions which cause quasiparticle breakdown in the region where this is kinematically allowed [71, 138, 139]. This effect is not captured in the linear spinwave treatment but can be described at higher order in spinwave theory [139].

The spinwave Hamiltonian in (5.5, 5.6) has the same functional form as another two sublattice system discussed in detail in Ref. [4], so the derivation of the dispersion relations and dynamical correlation functions is identical and only key steps are reproduced here.

The dispersion relations are obtained by diagonalizing the matrix $\mathsf{gH}(\boldsymbol{Q})$ where $\mathsf{g} = \mathrm{diag}(1,1,-1,-1)$ and are given by

$$\begin{aligned}\omega_{\pm}^2 =& A^2 + |B|^2 - |C|^2 - |D|^2 \\ &\pm \sqrt{(2AB - CD^* - D^*C^*)(2AB^* - CD - C^*D) + (BD - B^*D^*)^2}. \end{aligned} \quad (5.8)$$

To calculate the neutron scattering intensities, the right eigenvectors of gH are needed. The components of these are

$$\begin{aligned} W(\omega) =& -(A+\omega)(A^2 + |B|^2 - |C|^2 - |D|^2 - \omega^2) + 2A|B|^2 - BDC^* - B^*D^*C, \\ X(\omega) =& (A^2C^* + |B|^2C^* - |C|^2C^* + |D|^2C - C^*\omega^2) - A(BD - B^*D^*) + \omega(BD - B^*D^*), \\ Y(\omega) =& B^*\left[(A+\omega)^2 - |B|^2 + |C|^2\right] - (ACD + ADC^* + CD\omega + C^*D\omega) + BD^2, \\ Z(\omega) =& D(A^2 + C^{*2} - |D|^2 - \omega^2) + B^{*2}D^* - 2AB^*C^*, \end{aligned} \quad (5.9)$$

up to a normalization

$$\mathcal{N}(\omega) = \sqrt{|-|W|^2 + |X|^2 - |Y|^2 + |Z|^2|}. \quad (5.10)$$

From this the following expressions are obtained in the rotating frame,

$$\begin{aligned} S^{xx}(\boldsymbol{Q},\omega) =& |W - X + Y - Z|^2 \frac{[\delta^+(\boldsymbol{Q}) + \delta^-(\boldsymbol{Q})]}{4\mathcal{N}} \\ S^{zz}(\boldsymbol{Q},\omega) =& |W + X + Y + Z|^2 \frac{[\delta^+(\boldsymbol{Q}) + \delta^-(\boldsymbol{Q})]}{4\mathcal{N}} \\ S^{yy}(\boldsymbol{Q},\omega) =& 0. \end{aligned} \quad (5.11)$$

where $\delta^{\pm}(\boldsymbol{Q}) = \delta(\omega - \omega_{\pm}(\boldsymbol{Q}))$.

A transformation is now carried out to global coordinates $\tilde{x}\tilde{y}\tilde{z}$, defined to be parallel to the *abc* crystallographic axes respectively, with the two local z axes defined as $\hat{\boldsymbol{z}}_{\pm} = \tilde{\boldsymbol{z}}\cos\gamma \pm \tilde{\boldsymbol{x}}\sin\gamma$ with the sign alternating between the layers along the a-direction as shown in Fig. 5.2A.

Thus the Fourier transformed spins are

$$\begin{aligned} S^x(\boldsymbol{Q}) =& \sum_{\boldsymbol{r}} (S^{\tilde{x}}\cos\gamma - e^{2\pi i r_{\tilde{x}}/a} S^{\tilde{z}}\sin\gamma) e^{i\boldsymbol{Q}\cdot\boldsymbol{r}}, \\ S^z(\boldsymbol{Q}) =& \sum_{\boldsymbol{r}} (S^{\tilde{z}}\cos\gamma + e^{2\pi i r_{\tilde{x}}/a} S^{\tilde{x}}\sin\gamma) e^{i\boldsymbol{Q}\cdot\boldsymbol{r}}, \\ S^y(\boldsymbol{Q}) =& \sum_{\boldsymbol{r}} S^{\tilde{y}} e^{i\boldsymbol{Q}\cdot\boldsymbol{r}}, \end{aligned} \quad (5.12)$$

where $\boldsymbol{r}$ runs over all magnetic sites and where $r_{\tilde{x}}$ is the component of $\boldsymbol{r}$ along $\tilde{x}$. Transforming the other way,

$$\begin{aligned} S^{\tilde{x}}(\boldsymbol{Q}) &= \sum_{\boldsymbol{r}} (S^x \cos\gamma + e^{2\pi i r_{\tilde{x}}/a} S^z \sin\gamma) e^{i\boldsymbol{Q}\cdot\boldsymbol{r}}, \\ S^{\tilde{z}}(\boldsymbol{Q}) &= \sum_{\boldsymbol{r}} (S^z \cos\gamma - e^{2\pi i r_{\tilde{x}}/a} S^x \sin\gamma) e^{i\boldsymbol{Q}\cdot\boldsymbol{r}}, \\ S^{\tilde{y}}(\boldsymbol{Q}) &= \sum_{\boldsymbol{r}} S^y e^{i\boldsymbol{Q}\cdot\boldsymbol{r}}, \end{aligned} \tag{5.13}$$

such that

$$\begin{aligned} S^{\tilde{x}}(\boldsymbol{Q}) &= S^x(\boldsymbol{Q}) \cos\gamma + S^z(\boldsymbol{Q}+\boldsymbol{a}^*) \sin\gamma, \\ S^{\tilde{z}}(\boldsymbol{Q}) &= S^z(\boldsymbol{Q}) \cos\gamma - S^x(\boldsymbol{Q}+\boldsymbol{a}^*) \sin\gamma. \end{aligned} \tag{5.14}$$

Thus the Fourier transformed magnetization components are (in units of μ_B)

$$\begin{aligned} M^{\tilde{x}}(\boldsymbol{Q}) &= g_x S^x(\boldsymbol{Q}) \cos\gamma + g_z S^z(\boldsymbol{Q}+\boldsymbol{a}^*) \sin\gamma, \\ M^{\tilde{z}}(\boldsymbol{Q}) &= g_z S^z(\boldsymbol{Q}) \cos\gamma - g_x S^x(\boldsymbol{Q}+\boldsymbol{a}^*) \sin\gamma. \end{aligned} \tag{5.15}$$

From this, the dynamical structure factor including the neutron polarization factors is obtained as

$$\begin{aligned} &S(\boldsymbol{Q},\omega) = \\ &\left(1 - \frac{Q_{\tilde{x}}^2}{\boldsymbol{Q}^2}\right) \left(g_x^2 S^{xx}(\boldsymbol{Q},\omega) \cos^2\gamma + g_z^2 S^{zz}(\boldsymbol{Q}+\boldsymbol{a}^*,\omega) \sin^2\gamma\right) \\ &+ \left(1 - \frac{Q_{\tilde{z}}^2}{\boldsymbol{Q}^2}\right) \left(g_z^2 S^{zz}(\boldsymbol{Q},\omega) \cos^2\gamma + g_x^2 S^{xx}(\boldsymbol{Q}+\boldsymbol{a}^*,\omega) \sin^2\gamma\right), \end{aligned} \tag{5.16}$$

where $Q_{\tilde{x},\tilde{z}}$ are the components of $\boldsymbol{Q}$ projected along $\tilde{x}$ and $\tilde{z}$ respectively. In this expression, there are no mixed polarization terms as $S^{xz} = -S^{zx}$, and there are no cross-terms involving Fourier transformed spins at different wavevectors since these are zero by conservation of momentum.

To obtain intensities to compare with experiment, the delta functions in (5.11) are replaced by Gaussians in energy to reflect the finite instrumental energy resolution and the intensity is multiplied by the squared spherical magnetic form factor for Co^{2+}. The two-sublattice analytic calculations presented here of both the dispersions

and the intensities were cross-checked against numerical calculations performed using SpinW [65] with the full four-sublattice model.

The fact that the intensity contains terms with shifted wavevector $\boldsymbol{Q} + \boldsymbol{a}^*$ is a mathematical expression of the real space unit cell doubling (due to alternation of Ising axes) leading to Brillouin zone folding and a consequent shadow mode. This shadow mode is responsible for the additional weak scattering intensity at slightly higher energy than the main mode in Figs. 5.1D and E. It can be seen from (5.16) that the intensity of the shadow mode relative to the primary mode is proportional to $\tan^2\gamma$. Note that this shadow mode is distinct from the shadow mode due to the zigzag of the chains, such that the full model in the fixed frame has a total of four dispersion relations, $\omega_\pm(\boldsymbol{Q})$ and $\omega_\pm(\boldsymbol{Q} + \boldsymbol{a}^*)$.

In order to extract a parameterization of the 3D dispersion in high transverse field, fits were done to the linear spinwave dispersion relations (5.8). The fitted values for the interchain parameters are shown in Table 5.1. Note that these parameters yield minima in the magnon dispersion relations at $(1, \pm q, 0)$ with $q \sim 0.39$ which is compatible with the minima observed at 7 T $\parallel b$ in Fig. 5 of Ref. [134], and can thus be related to the propagation vector $q = 0.37$ of the spontaneous incommensurate spin density wave order that sets in at the magnetic ordering temperature 2.95 K in zero field [114]. To draw a direct comparison with interchain exchange parameters proposed in Ref. [134], the relevant value to compare to J_1 in Ref. [134] is $J_1 + J_1'$ in the present work.

5.3.3 Suppression of the interchain hopping of the kinetic bound state in zero field

A surprising result found experimentally is that the kinetic bound state, the sharp mode near $l = -1$ at the top of the spectrum in zero field (Fig. 5.4A), has no measurable dispersion in either interchain direction, even though it is a single-spin-flip state, and generically one expects interchain dispersion at first order in the interchain couplings. This result is briefly discussed in this subsection, where it is explained that this is due to the combination of the particular antiferromagnetic

order pattern between chains and the form of the interchain couplings. This is done by introducing a simplified toy model.

As the interchain J_2 bonds in Fig. 5.1J are Ising-like, and in zero field the spins are aligned along the Ising axis, the J_2 terms create no hopping along h. The J_2 bonds also do not contribute to a mean field, as the triangular lattice and the antiferromagnetic pattern mean that the effects of the two bonds cancel out. Therefore only the interchain bonds in the bc plane need to be considered. In the simplest approximation, straight ($\zeta = 0$) ferromagnetic Ising chains along the c-direction are considered, with an antiferromagnetic Heisenberg interaction between chains in the b direction, i.e.,

$$\mathcal{H}_{\text{simple}} = \sum_{\boldsymbol{r}} -JS^z_{\boldsymbol{r}}S^z_{\boldsymbol{r}+\boldsymbol{c}/2} + J_1\boldsymbol{S}_{\boldsymbol{r}} \cdot \boldsymbol{S}_{\boldsymbol{r}+\boldsymbol{b}} \tag{5.17}$$

where the sum is over all magnetic sites. In the absence of any applied field, the chains order in an antiferromagnetic pattern along the b-direction (both in this simplified model and in the real material). Therefore, to calculate the linear spinwave spectrum, the quantization axis must be rotated by 180° about the y-direction on alternating chains along the b-direction such that the ordered spin is along the $+z$ direction on all chains. In this rotating frame, the quadratic spinwave Hamiltonian is

$$\frac{1}{2}\sum_{\boldsymbol{Q}} \mathsf{X}^\dagger_{\boldsymbol{Q}}\mathsf{H}(\boldsymbol{Q})\mathsf{X}_{\boldsymbol{Q}} \tag{5.18}$$

where $\mathsf{X}^\dagger_{\boldsymbol{Q}} = (a^\dagger_{\boldsymbol{Q}}, a_{-\boldsymbol{Q}})$ and

$$\mathsf{H}(\boldsymbol{Q}) = \begin{pmatrix} J + J_1 & J_1\cos 2\pi k \\ J_1\cos 2\pi k & J + J_1 \end{pmatrix}. \tag{5.19}$$

This gives a dispersion relation

$$\omega(\boldsymbol{Q}) = \sqrt{(J + J_1)^2 - J_1^2\cos^2 2\pi k}. \tag{5.20}$$

Now, $J_1 \ll J$ (experimentally, $J_1/J \lesssim 2\%$), so this can be Taylor expanded, such that the bandwidth along k is proportional to J_1^2/J, i.e., appears at second order in J_1. This is not experimentally resolvable, which explains why no interchain dispersion is observed for the kinetic bound state in zero field. In contrast, in field $\parallel a$

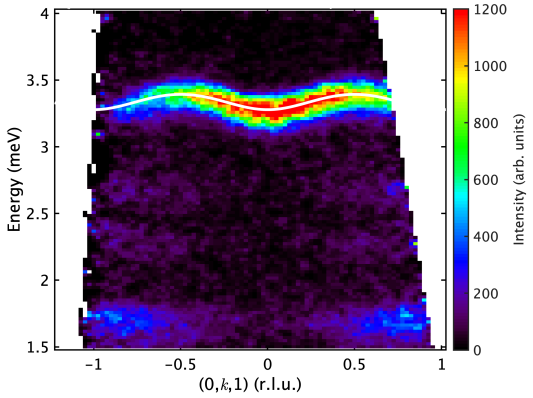

Figure 5.3: Interchain dispersion at 1.5 T$\|$ a. The kinetic bound state, which is the highest energy mode and has the most intensity, is significantly dispersive, with a bandwidth of 0.114(2) meV (white curve). The other, lower energy, modes are much weaker in intensity and much flatter.

above 0.14 T, the spin components along a are all parallel, with the consequence that the interchain dispersion along k appears at first order in J_1. This is experimentally resolvable, and indeed is clearly detected experimentally, with the kinetic bound state at 1.5 T having a bandwidth along k of 0.114(2) meV, as shown in Fig. 5.3.

5.4 Quantitative determination of the single-chain Hamiltonian

5.4.1 Proposed single-chain Hamiltonian

The proposed single-chain Hamiltonian is an extension of one recently proposed on symmetry grounds [71], and it is convenient to write it as

$$\mathcal{H}_{\text{single chain}} = \mathcal{H}_1 + \mathcal{H}_2 + \mathcal{H}_{\text{MF}}, \tag{5.21}$$

where

$$\begin{aligned}\mathcal{H}_1 = J\sum_j \Big[-S_j^z S_{j+1}^z - \lambda_S\left(S_j^x S_{j+1}^x + S_j^y S_{j+1}^y\right) + (-1)^j \lambda_{yz}\left(S_j^y S_{j+1}^z + S_j^z S_{j+1}^y\right)\Big] \\ -\mu_B \sum_j \Big[g_x B_x S_j^x + g_y B_y S_j^y + g_z B_z S_j^z\Big], \end{aligned} \tag{5.22}$$

$$\mathcal{H}_2 = J\sum_j \Big[\lambda_{\text{AF}} S_j^z S_{j+2}^z + \lambda_{\text{AF}}^{xy}\left(S_j^x S_{j+2}^x + S_j^y S_{j+2}^y\right) - \lambda_A\left(S_j^x S_{j+1}^x - S_j^y S_{j+1}^y\right)\Big], \tag{5.23}$$

and where j runs over all sites on a single chain. Here, xyz form an orthogonal right-handed coordinate system with y along the crystallographic b-axis and z defined to be the equilibrium spin direction in zero applied field, which for the Hamiltonian (5.21) coincides with the direction along which the spin components have the largest exchange, i.e., the Ising axis.

It will be shown here that $\mathcal{H}_1$ is the *minimal* Hamiltonian required to *qualitatively* reproduce all key features of the the INS spectra seen in zero field, high field along a, and high purely-transverse field, while $\mathcal{H}_2$ is needed to *quantitatively* capture all details of the spectra.

The first term in $\mathcal{H}_1$ is the dominant Ising exchange. The second (λ_S) is a symmetric XY exchange term, which allows single spin flips to hop, and the third term (λ_{yz}) is an off-diagonal staggered exchange term which allows domain walls to hop. These three terms (together with $\mathcal{H}_{\mathrm{MF}}$, defined below, for zero field and transverse fields below the critical point) can qualitatively account for all of the features seen in the INS spectrum, not only in field parallel to the a-axis presented here, across the full range of field values considered, but also in purely transverse field ($\| b$) below (see following chapter) and above the critical field [71]. In particular, the XY exchange is needed to account for the kinetic bound state seen in zero field (near $l = -1$ in Fig. 5.4A) [25], and for the large m_1 bandwidth seen in field parallel to the a-direction (Fig. 5.4E), as this term allows single spin flips to hop. The staggered off-diagonal exchange term λ_{yz} is needed to account for the fact that domain walls can hop in zero applied field (seen in the fact that the bands around $l = 0$ in Fig. 5.4A are dispersive) [71], as will be discussed further in the following chapter. The key features of the nearest-neighbour exchange are graphically illustrated in Fig. 5.5: the major axis of the ellipsoids at the middle of each bond corresponds to the Ising exchange, the diameter in the perpendicular plane to the Ising direction illustrates the XY exchange λ_S, and the staggered orientation of the ellipsoids is due to the staggered exchange λ_{yz}. Finally, the last term in (5.22) is the Zeeman interaction with an applied magnetic field, where the assumption has been made that the g-tensor is diagonal in the xyz axes.

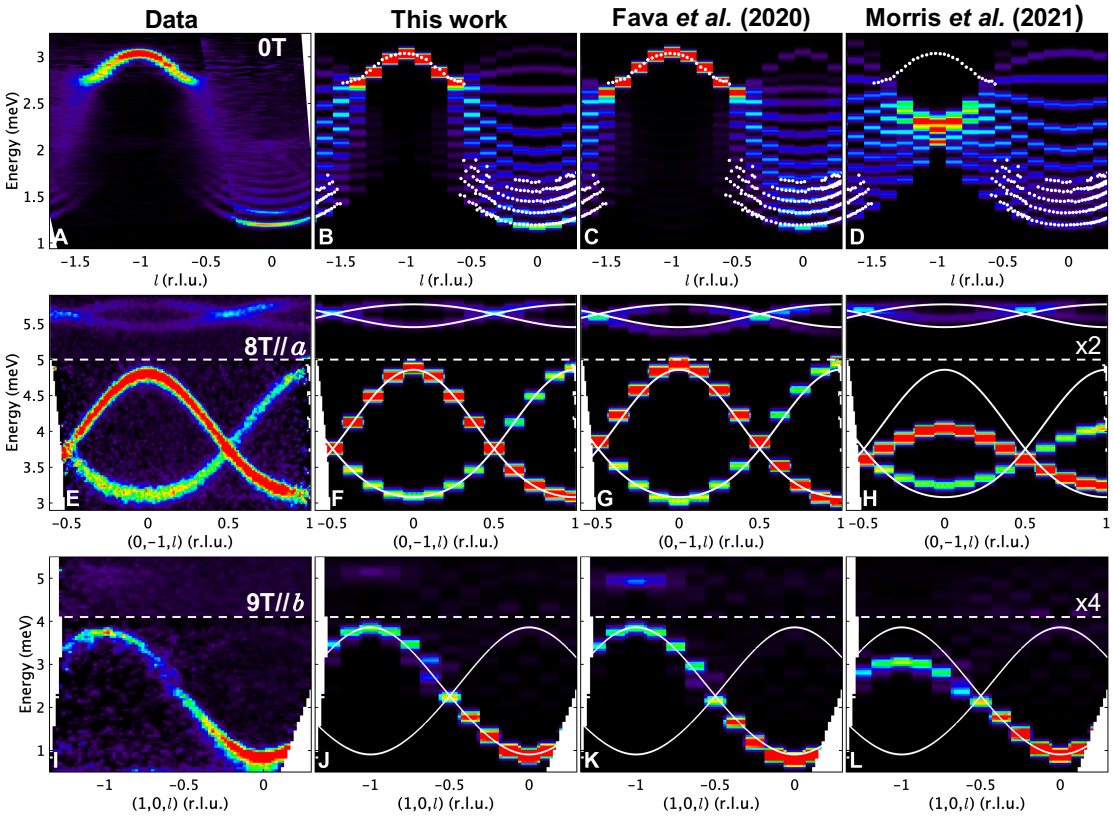

Figure 5.4: INS data in (A) zero field, (E) 8 T $\parallel$ a and (I) 9 T $\parallel$ b compared to dynamical correlations computed via ED for different models for a chain of 16 sites. Panel A is adapted from Ref. [25]. White dots in B-D show experimentally-extracted dispersion points from the data in A; solid white lines in F-H and J-L show the analytic parameterization of the experimental dispersion relations with interchain terms set to 0. The models used were: the model 1D Hamiltonian in (5.21) with parameters in Table 5.2 (B, F, J); the model refined in Ref. [71] with g_x and g_z taken from Table 5.2 (C, G, K); the model used in Ref. [125] with g_x and g_z taken from Table 5.2 (D, H, L). In E-H, data below 5 meV (dashed line) are averaged over $|h| < 1.5$ and $-1.1 < k < -0.9$. Note that the shadow mode is the more intense mode here, as the transverse averaging range has been chosen in order to show the whole dispersion along l while minimizing artificial broadening due to interchain dispersion. Data above 5 meV are averaged over $|h| < 1.5$ and $|k| < 1.5$ and intensities in this region have been multiplied by 2 to make the m_2 mode more clearly visible. In I-L, data below 4.1 meV (dashed line) are averaged over $0.8 < h < 1.2$ and $-0.1 < k < 0.1$. Data above the dashed line have been averaged over $-1 < h < 4$ and $|k| < 1$ and intensities in this region have been multiplied by 4 to make the faint diffuse feature around $l = -1$ at about 5 meV more clearly visible. The ED calculations have been convolved with Gaussians of FWHM 0.066 meV, 0.16 meV and 0.3 meV in B-D, F-H and J-L respectively. In B-D, the intensity shown is $S^{xx}(l, \omega)$, as the data in A have been corrected for the single ion magnetic form factor and the polarization factor under the assumption that $S^{xx} = S^{yy}$ and $S^{zz} = 0$ for inelastic scattering. In F-H and J-L, all components of the dynamical structure factor are included and the averaging range, polarization factor and magnetic form factor have all been accounted for in the calculation.

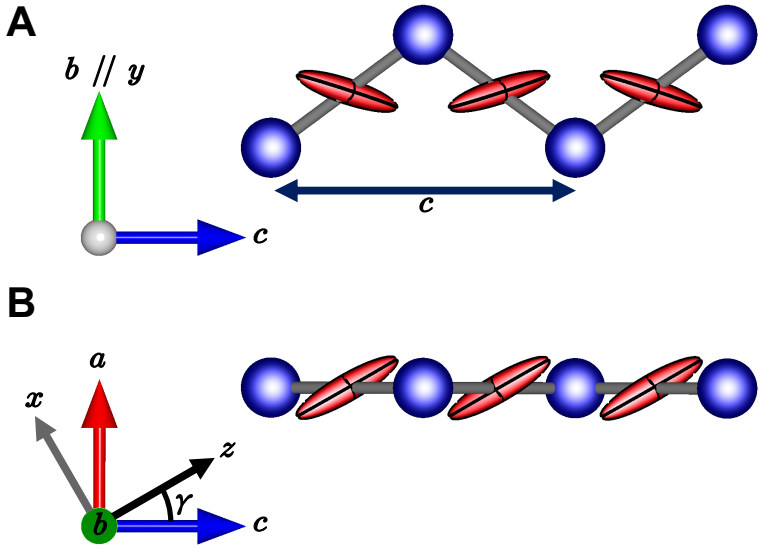

Figure 5.5: Graphical representation of the nearest neighbour part of the exchange Hamiltonian (5.21) projected onto the *bc* (A) and *ac* (B) planes for a single chain. The blue spheres represent cobalt atoms while the red ellipsoids at the mid-point of each nearest-neighbour bond represent the exchange matrix on that bond. The principal axes of the ellipsoids correspond to the principal axes of the exchange matrix, with the lengths of the principal axes proportional to the absolute values of the relevant eigenvalues of the exchange matrix. A) Consecutive bonds along the chain are symmetry-related by the *c*-glide of the crystal structure (mirror in the *ac* plane passing through the middle of each zigzag bond followed by translation by $\boldsymbol{c}/2$), which leads to the staggered orientations of the ellipsoids between consecutive bonds along the chain; this corresponds to the staggered exchange term λ_{yz} in (6.4). B) The Ising z-axis is at an angle γ to the c-axis in the ac plane. The absolute signs of λ_{yz} and angle γ cannot be determined from neutron scattering measurements, only their magnitude, so only one of the four possible orientations of the exchange ellipsoids compatible with the experiments is shown. The other three options are obtained by mirroring the exchange ellipsoid for a reference bond in a plane passing through its centre, parallel to the *ab*, *bc*, or *ac* crystallographic planes. The resulting orientation is then propagated via crystal symmetry operations onto all the other bonds, i.e. via the *c*-glide to obtain the other bonds on the same chain and via the *b* (or *n* glide) to relate bonds on the chain passing through the origin to bonds on the chain passing through the body-centre of the orthorhombic structural cell, as described in Fig. 5.2. The choice shown is compatible with the theoretical ab initio results of Refs. [126, 127], which appeared after the present results were published. Figure made using VESTA [129].

In order to quantitatively account for the full wavevector dependence of the data, however, other, subleading terms are needed, included under $\mathcal{H}_2$: the first term, λ_{AF}, is a next-nearest-neighbour antiferromagnetic Ising term [25, 71] needed to account for the energy of the kinetic bound state. The second term, $\lambda_{\mathrm{AF}}^{xy}$, is an XY part to the next-nearest-neighbour term which accounts for the flattening of the bottom of the m_1 dispersion in high field along a [Fig. 5.4E]. The third term (λ_A) is an asymmetry between the XX and YY exchanges, which is needed to account for the position and bandwidth of the m_2 dispersion in large field along a; without this term, the m_2 mode is too low in energy. These last two terms are only of order 2-3% of the Ising term and the necessity for their inclusion in the parameterization can be seen by comparing Fig. 5.4E with G. The discrepancies illustrated in the latter between the empirical and calculated dispersions motivates the further refinement presented here of the Hamiltonian with the inclusion of the λ_A and $\lambda_{\mathrm{AF}}^{xy}$ terms which were fixed to zero in Ref. [71].

For completeness, it is noted that, as mentioned in Ref. [71], two other nearest-neighbour exchange terms are symmetry allowed, $\lambda_{xz} J \sum_j \left(S_j^x S_{j+1}^z + S_j^z S_{j+1}^x \right)$ and $\lambda_{xy} J \sum_j (-1)^j \left(S_j^x S_{j+1}^y + S_j^y S_{j+1}^x \right)$. However, the definition of the axes used so far — that z is the direction of the equilibrium spin in zero field — places a constraint between these two terms, i.e., only one can vary independently. This is because each of these two terms on their own when added to (5.21) leads to a rotation of the zero-field equilibrium spin direction away from the z-axis, but for a given λ_{xz} one can choose a corresponding λ_{xy} of appropriate magnitude and sign such that, when both terms are present, the zero-field equilibrium spin direction is still along z. However, it is found that allowing finite λ_{xz} and λ_{xy} with the above constraint does not measurably improve the agreement with the present experimental data, so in the following $\lambda_{xz} = \lambda_{xy} = 0$ is assumed.

Finally, $\mathcal{H}_{\mathrm{MF}}$ captures the effects of interchain couplings in a mean-field approximation, where in zero and low transverse field

$$\mathcal{H}_{\mathrm{MF}} = -J \sum_j 2\lambda_{\mathrm{MF}} \langle \boldsymbol{S} \rangle \cdot \boldsymbol{S}_j. \tag{5.24}$$

J	2.48(2)	meV
λ_S	0.251(6)	
λ_A	-0.021(1)	
λ_{yz}	0.226(3)	
λ_{AF}	0.077(3)	
$\lambda_{\mathrm{AF}}^{xy}$	0.031(1)	
g_x	3.29(6)	
g_y	3.32(2)	
g_z	6.90(5)	
λ_{MF}	0.0158(2)	

Table 5.2: Single-chain Hamiltonian parameters used in this work as defined in (5.22)-(5.24).

In fields above 0.14 T applied along the a-direction, the relevant form is instead given in Sec. 5.6, and, at high field, this simplified form is no longer sufficient as excitations acquire a finite interchain dispersion at first order in the interchain couplings. Therefore, in this high field regime, the full explicit form for the relevant interchain exchanges proposed in (5.4) is used.

The refined parameter values are shown in Table 5.2. The Hamiltonian shown above quantitatively reproduces the spectrum seen in zero field, high field $\parallel$ a and high field $\parallel$ b. Furthermore, it also reproduces data at low fields along b, as shown in the following chapter, and at intermediate fields along a, and also accounts for previously published THz spectroscopy data in low transverse field, as is discussed later in Sec. 5.6.

5.4.2 Fitting procedure

The fitting procedure used a global simultaneous fit to the dispersion relations corresponding to data taken in zero field, 8 T $\parallel$ a and 9 T $\parallel$ b, with the aim of arriving at a consistent description of all these different regimes within the same Hamiltonian.

First, cuts were taken through the data as a function of energy transfer at constant wavevector transfer. Dispersion points were obtained by fitting Gaussian peak shapes to these cuts. Many dispersion points were extracted from each data set (over 500 for the 8 T $\parallel$ a data). Empirical dispersion relations were then fitted to

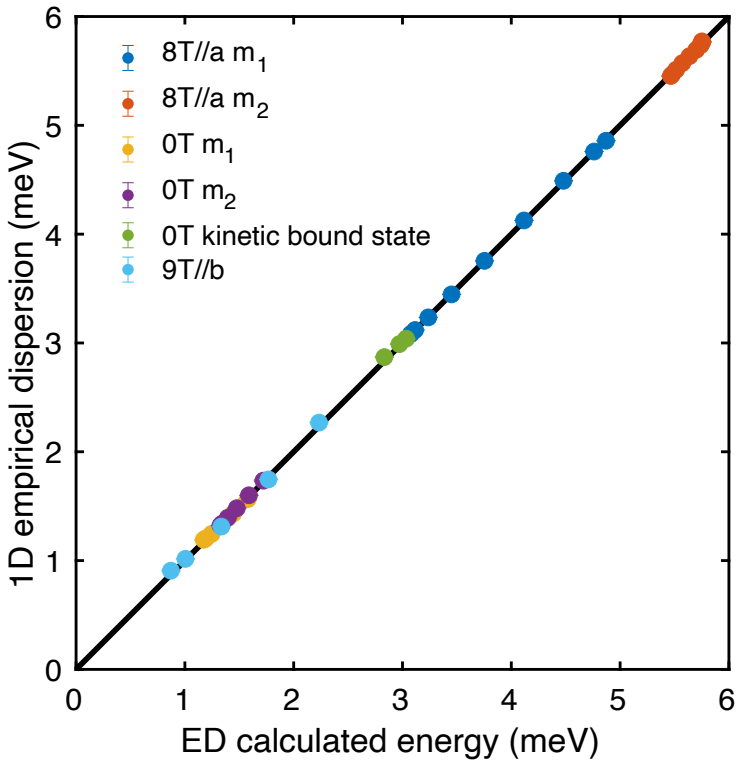

Figure 5.6: Energies of dispersion points as calculated from ED on 16 sites compared to their values as calculated from the empirical dispersion relations. The one-to-one agreement obtained is excellent.

these dispersion points. For the high field data, these were 3D dispersion relations, as per (5.2) and (5.8) for field along a and b respectively. In zero field, the interchain hopping effects are negligible, due to the multi-spin nature of the bound states as well as the antiferromagnetic order pattern between chains, which suppresses interchain hoppings for the kinetic bound state (see Sec. 5.3.3) so a 1D form was used. The single-chain Hamiltonian was then fitted to these empirical dispersion relations with the interchain parameters set to zero. It was not possible to use the parameters derived from linear spinwave theory fits directly, since the predominantly 1D nature of the magnetic interactions together with the small effective spin $S = 1/2$ leads to strong quantum fluctuations that renormalize the dispersions even at the high magnetic fields investigated. In addition, the method used needed to capture the various bound states, i.e. the zero field confinement bound states, as well as the high field $\parallel a$ m_2 bound state; this is not possible in linear spin wave theory. Instead,

exact diagonalization (ED) calculations on finite chains were used, with periodic boundary conditions at the ends of the chains. The fits used calculations on 12 sites as the best compromise between minimal finite size effects and the computation being quick enough to be carried out many times for fitting (for fitting to the kinetic bound state, 10 sites were used as this required more eigenstates to be found and is not strongly affected by finite size effects). Lanczos algorithms were used to diagonalize only the low energy subspace and speed up the calculation. There were 10 parameters in the fit but 13 pieces of information across these different data sets, so the fit was not underconstrained. In particular, the pieces of data used for the fit were the dispersions of the first two confinement bound states and the kinetic bound state from the zero field data [25], the m_1 and m_2 dispersions from the 8 T $\| a$ data, and the magnon dispersion from the 9 T $\| b$ data. For each of these data sets, the squared difference χ^2 between the ED energy E_j^{ED} at each momentum point and the empirical fitted dispersion relation E_j^{fitted} was calculated as

$$\chi^2 = \sum_j \frac{\left(E_j^{\mathrm{ED}} - E_j^{\mathrm{fitted}}\right)^2}{\left(\Delta_j^{\mathrm{fitted}}\right)^2}, \tag{5.25}$$

where j runs over each mode used in the fit at each wavevector accessible by ED at each field included in the fit, and where each term is normalized by the uncertainty on the fitted dispersion relation $\Delta_j^{\mathrm{fitted}}$ as calculated from the covariance matrix of the fitted dispersion parameters; the fit minimized this total χ^2. When calculating χ^2 for the high transverse field data, only the portion of the dispersion for $l \leq 0.5$ was used, as at higher values of l, quasiparticle breakdown occurs [71, 138, 139], meaning that the dispersion relation ceases to be well defined. The optimization used a quasi-Newton algorithm and the initial parameters were varied in order to make sure that a global minimum was found. The very good one-to-one agreement obtained in the simultaneous fits of the ED to the empirical dispersion relations is shown in Fig. 5.6.

Uncertainties on the fitted parameters were estimated by varying the parameters of the empirical dispersion relations according to their covariance matrices. There are significant correlations between some of the parameters, especially between J and λ_S and between λ_S and g_x, and the full correlation matrix is given in

Appendix A. However, while a number of slightly different parameter sets give similar agreement with the features to which the single-chain Hamiltonian was fit, the final parameter set presented in Table 5.2 gives the best agreement not only with the features to which the Hamiltonian was fit, but also to other features in the spectra. These include the relative intensities of different features, the full bandwidth of the magnon in the high transverse field data, the energy and intensity of the faint diffuse feature around $l = -1$ at about 5 meV in the high transverse field data, the field dependence of the bandwidths of the m_1 and m_2 modes in field along a, and the spectra in low transverse field (see the following chapter).

A comparison between the data to which the Hamiltonian was fit and the spectrum calculated by exact diagonalization using this refined Hamiltonian is shown in the first two columns of Fig. 5.4. In these plots, the colour indicates the measured/calculated scattering intensity, while the overlaid white dots/curves show the data points/dispersion relations that were being fit to. It can be seen that very good quantitative agreement is achieved. In these calculations, the plotted intensities are

$$S(\boldsymbol{Q},\omega) = |f(Q)|^2 \sum_{\alpha,\beta} \left(\delta_{\alpha,\beta} - \hat{Q}_\alpha \hat{Q}_\beta\right) S^{\alpha\beta} \tag{5.26}$$

where α, β both run over x, y, z, $f(Q)$ is the magnetic form factor, and $\hat{Q}_\alpha$ is the component along direction α of the unit vector parallel to the wavevector transfer $\boldsymbol{Q}$. The partial dynamical structure factors $S^{\alpha\beta}$ are

$$S^{\alpha\beta} = g_\alpha g_\beta \sum_{\lambda_f} \langle \mathrm{GS}|S^\alpha(-\boldsymbol{Q})|\lambda_f\rangle\langle\lambda_f|S^\beta(\boldsymbol{Q})|\mathrm{GS}\rangle \delta(E_{\lambda_f} - \hbar\omega) \tag{5.27}$$

where the sum is over all excited states $|\lambda_f\rangle$ with energy E_{λ_f} relative to the ground state $|\mathrm{GS}\rangle$ and where the Fourier transformed spin is $S^\alpha(\boldsymbol{Q}) = \sum_{\boldsymbol{r}} S^\alpha_{\boldsymbol{r}} e^{i\boldsymbol{Q}\cdot\boldsymbol{r}}$, summing over all sites $\boldsymbol{r}$.

Parameters fixed	χ^2
None	2008.17
$\lambda_A = 0$	2718.21
$\lambda_{\mathrm{AF}}^{xy} = 0$	5910.82
$\lambda_A = \lambda_{\mathrm{AF}}^{xy} = 0$	7009.55

Table 5.3: Values of χ^2 corresponding to fixing some of the Hamiltonian (5.21) parameters to zero

5.5 Comparison to other Hamiltonian parameter sets

The values of χ^2, as calculated from (5.25), corresponding to fits in which some of the parameters in $\mathcal{H}_2$ are fixed to zero are shown in Table 5.3. A value of zero is only considered for those parameters which were not included in the parameterization of Ref. [71], as the parameters fitted in that work were all shown to be necessary to parameterize just the zero field data. It is seen that it is not possible to fit all features in the data well without using all parameters. These values have not been divided by the number of data points because the fits were not done directly to the data but instead to the empirical 1D dispersion relations corrected for interchain dispersion effects. However, the fit was indirectly performed to many hundreds of data points.

The right hand columns of Fig. 5.4 contain comparisons to previous models that cannot quantitatively or qualitatively account for key features in the experimental data. This comparison provides additional evidence that all of the parameters are indeed needed in order to capture quantitatively all features in the data, as will now be discussed.

The third column of Fig. 5.4 (panels C, G, K) presents calculations using the Hamiltonian model proposed in Ref. [71], with g_x and g_z taken from Table 5.2. The calculation for the 8 T $\|$ a data (panel G) does not fully capture the flattening of the bottom of the m_1 dispersion and the calculated m_2 dispersion is shifted downwards from where it is found empirically. It is found that in order to capture the former effect, it is necessary to include either $\lambda_{\mathrm{AF}}^{xy}$ or λ_A in the fits, and that in order to capture the position and shape of the m_2 dispersion, both of these must be non-zero.

The right-most column of Fig. 5.4 presents calculations using the Hamiltonian model used in Ref. [125], which contains a subset of the nearest-neighbour exchange terms in (5.22) and (5.23) with certain constraints between the parameter values. While that model can capture the energy levels at the zone center ($l = 0$) in zero and transverse field, i.e., the regime probed in Ref. [125], significant qualitative and quantitative discrepancies are found here between calculations using that model and the full spectrum observed via INS. The model does not capture the wavevector dependence of the spectrum either in zero field, where the kinetic bound state near $l = -1$ is not captured at all [compare Fig. 5.4D (calculation) with A (data)], or in field applied along either a or b, where the predicted magnon bandwidths are much smaller than observed experimentally (compare H and L with E and I, respectively). Moreover, in high field along a (panel H), the model does not capture the spectrum even at $l = 0$, as the small magnon bandwidth, which is underestimated by almost a factor of 2, leads to too large a predicted magnon gap. These differences are ascribed here primarily to the fact that, in the model used in Ref. [125], there is no $S^x_j S^x_{j+1}$ exchange term and only a very small $S^y_j S^y_{j+1}$ term. In contrast, in the present work, it is found that the $S^x_j S^x_{j+1}$ and $S^y_j S^y_{j+1}$ exchange terms are of very similar size, and of magnitude comparable to that of the staggered off-diagonal exchange, those being the main subleading terms after the dominant Ising exchange, as already noted in Ref. [71]. The fully refined Hamiltonian model proposed in (5.21) accounts quantitatively not only for the full energy and wavevector dependence of the INS spectrum at all probed fields aligned along two orthogonal directions, but also for the THz spectroscopy data in Ref. [125] without adjusting any parameters, as will be discussed in Sec. 5.6. It is therefore proposed here to be an accurate model of the actual spin Hamiltonian in $CoNb_2O_6$.

5.6 Comparison of the Hamiltonian to experiment at other fields

The refined Hamiltonian can also be compared to the results of INS data taken at fields other than those to which the fit was performed. The data agree significantly

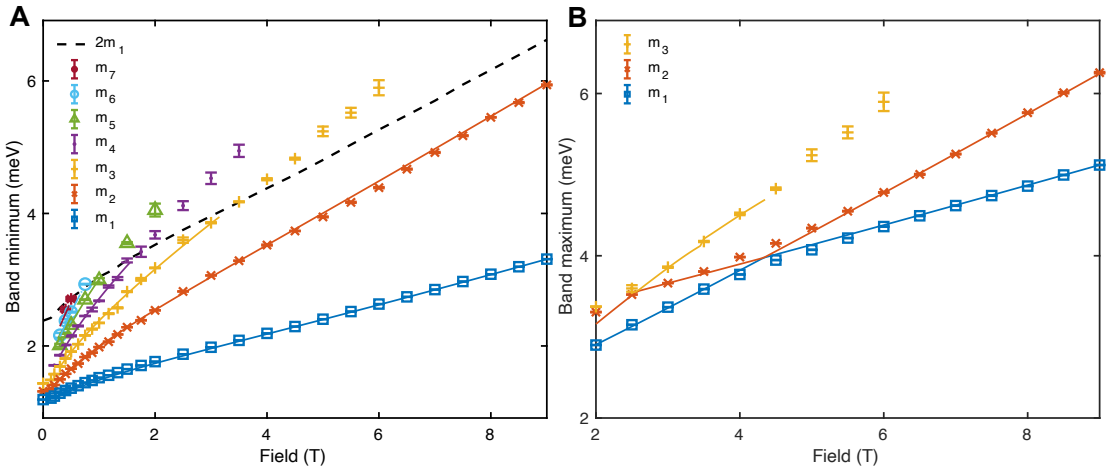

Figure 5.7: Band minima (A) and maxima (B) showing experimentally extracted points (symbols) corrected for interchain dispersion. The results of ED calculations on 16 sites (solid lines) are overlaid in the corresponding color, with effects of interchain couplings included as a mean-field correction. There is good agreement over the whole field range probed. The dependence of the band maxima on field was found to discriminate more strongly between different models than the field dependence of the band minima. Note that the higher bound states cease to be well defined in ED once they overlap with the continuum; for this reason solid lines stop when they intersect the dashed line indicating the lower boundary of the $2m_1$ continuum in A. In B, the discrepancy between ED and experiment where the m_1 and m_2 ED curves touch is due to the fact that experimental values were extracted by fitting to the hopping form (5.2) and points were not extracted in regions where different modes overlapped, as they do in Fig. 4.5C and D. The interchange in the gradient of the maxima of m_1 and m_2 modes with respect to field where they intersect is due to the exchange in character of the top of the mode: between approximately 2 T and 4 T, it is the top of the m_2 mode that has single-spin-flip character around $l = 1$.

better with the calculation when using the fit with all terms included than when omitting any of the terms in $\mathcal{H}_2$.

Fig. 5.7 shows comparisons between ED calculations and the data at fields away from those used for the fits. Excellent quantitative agreement is found. In the calculations shown here, the component of interchain interactions parallel to the magnetization direction was taken into account in a mean field picture. For the field-polarized phase in field above 0.14 T along the a-direction, the form of the interchain mean field in (5.24) does not hold because the ordering pattern of the chains changes, and instead the relevant form of the mean field term is

$$\mathcal{H}_{\mathrm{MF}} = \sum_j 2\left(J_1 + J_1'\right)\langle \boldsymbol{S}\rangle \cdot \boldsymbol{S}_j - 4J_2\langle S^z\rangle S_j^z, \tag{5.28}$$

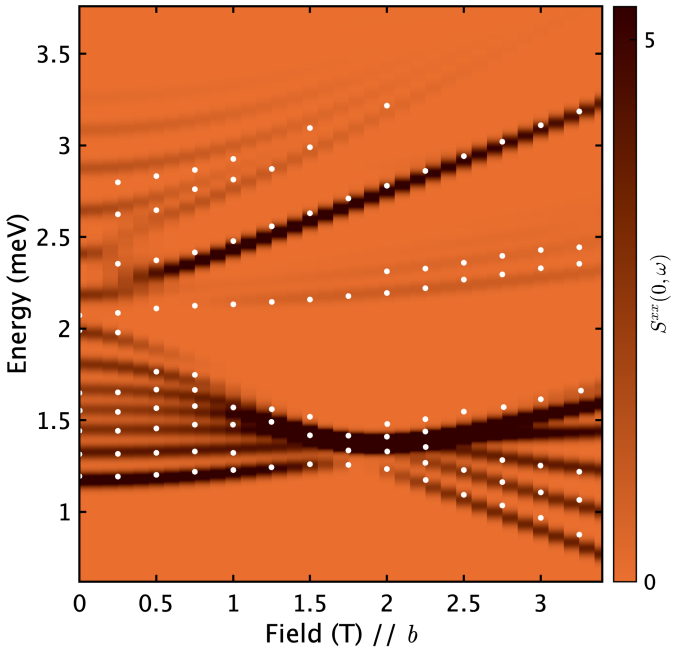

Figure 5.8: Dynamical structure factor at zero momentum transfer as a function of transverse field. Colour indicates $S^{xx}(0,\omega)$ as per (5.27), calculated using ED for a chain of 16 sites for the Hamiltonian in (5.21) and convolved with a Gaussian of FWHM 0.067 meV. White dots are data points extracted from the estimated local intensity maxima in the energy-dependent THz spectroscopy data presented in Ref. [125] at 1.5 K (Fig. 2c of that work).

where the interchain exchanges are defined in Sec. 5.3.2.2. This was the form used in Fig. 5.7.

In addition, in Fig. 5.8, recently reported THz spectroscopy data (white dots) [125] are compared with predictions based on the Hamiltonian proposed here. The comparison is shown for fields up to 3.5 T, which is in the region where ED is sufficiently reliable, as the gap is still large (i.e., finite size effects are small), and interchain effects are also small. All the trends in the THz spectroscopy data are reproduced. The good agreement in the intensities can be seen visually by comparing Fig. 5.8 to Fig. 2c of Ref. [125] (not shown).

5.7 Conclusions

The Hamiltonian for $CoNb_2O_6$ was revisited in order to be able to account for data observed in high field parallel to the a-axis. In order to capture the interchain dispersion as well as bound states and renormalization effects, a two step fitting

method was developed: first the full three dimensional dispersion in the regime of high applied field was parameterized, from which effective one-dimensional dispersions were extracted, i.e., the dispersions that would be observed in the absence of interchain hopping. Then, exact diagonalization methods were used to compare the predictions of a single-chain Hamiltonian to these empirical one-dimensional dispersion relations. By performing a global fit to the full wavevector dependent spectrum observed in various fields, a microscopic Hamiltonian was proposed, including both in-chain and interchain interactions, down to 2% of the dominant Ising exchange. This Hamiltonian quantitatively reproduces the INS data obtained across a wide range of field conditions including zero field, high near-longitudinal field and high transverse field, as well as intermediate fields to which the Hamiltonian was not fit, leading to a fully consistent description of the spin dynamics using a single set of exchange parameters.

6

Excitations in the low transverse field phase of $CoNb_2O_6$

Experimental and theoretical evidence is presented in this chapter of novel bound state formation in the low transverse field ordered phase of the quasi-one-dimensional Ising-like material $CoNb_2O_6$. High-resolution single crystal inelastic neutron scattering measurements observe that small transverse fields lead to a breakup of the spectrum into three parts, each evolving very differently upon increasing field. This can be naturally understood starting from the excitations of the ordered phase of the transverse field Ising model, domain wall quasiparticles (solitons). Here, the transverse field and a staggered off-diagonal exchange create one-soliton hopping terms with opposite signs. It is shown that this leads to a rich spectrum and a special field, when the strengths of the off-diagonal exchange and transverse field match, at which solitons become localized; the highest field investigated in this chapter is very close to this special regime. This case is solved analytically and three two-soliton continua are found, along with three novel bound states. Perturbing away from this novel localized limit, very good qualitative agreement is found with the experimental data. Calculations are also presented using exact diagonalization of a recently refined Hamiltonian model for $CoNb_2O_6$ and using diagonalization of the two-soliton subspace, both of which provide a quantitative

agreement with the observed spectrum. The theoretical models qualitatively and quantitatively capture a variety of nontrivial features in the observed spectrum, providing insight into the underlying physics of bound state formation. The results of this chapter have been published in Ref. [140].

***Attribution note**: The experimental inelastic neutron scattering data in this chapter were collected before I started my thesis, as part of earlier experiments on OSIRIS at ISIS that focussed primarily on the spin dynamics near the critical field, reported in Ref. [25]. The data analysed here were collected as part of the same experiments at low field and not reported previously. Therefore, experimental details are included for completeness as part of this chapter. The raw time-of-flight data were converted to intensities in units of $S(\boldsymbol{Q},\omega)$ and an estimate of the non-magnetic background was subtracted off before I joined this project. The theoretical work in this chapter was a collaboration with theorists Izabella Lovas and Leon Balents (University of California, Santa Barbara), who developed the models described in Sec. 6.4 and 6.5 and wrote the first drafts of Sec. 6.4.1, 6.4.2, 6.5.1 and 6.5.2; these sections are included here for completeness. The details of the analytical calculations in Sec. 6.4.2 were worked out collaboratively, as I derived them independently and wrote code to solve them numerically and produce the figures. I performed all the calculations required for comparison of the theoretical models to the experimental INS data. I also extended the model presented in Sec. 6.5.1 and 6.5.2 in order to take account of additional effects that were important for comparison with the data, as presented in Sec. 6.5.3.*

6.1 Introduction

The transverse field Ising chain (TFIC) is an important model in condensed matter physics because, as discussed in Chapter 2, it displays the key paradigms of both a continuous quantum phase transition from an ordered phase to a quantum paramagnetic phase as a function of field, as well as, in the ordered phase, of fractionalization of local spin flips into pairs of domain wall quasiparticles (solitons, also referred to as spinons in Chapter 4) [11]. The pure TFIC model

can be mapped to non-interacting fermions [37, 38], which in the ordered phase represent these solitons. However, a variety of different additional subleading terms in the spin Hamiltonian, such as a longitudinal field [41], a next-nearest-neighbour antiferromagnetic exchange [141], or an XY exchange [25] can stabilize two-soliton bound states.

In this chapter, a regime is explored where novel bound states can be stabilized by the interplay of applied transverse field and off-diagonal exchange. High resolution single crystal inelastic neutron scattering (INS) data is presented as a function of low to intermediate transverse field in the ordered phase. This regime has also been explored by THz spectroscopy [125], which probes the zone-centre ($\boldsymbol{Q} = 0$) excitations. The INS data reveal a rich evolution of the magnetic spectrum with increasing field: the spectrum splits into three parts with each part behaving very differently. The top two parts are sharp modes, with the top mode becoming progressively flatter and the middle one progressively more dispersive in field, while the lowest energy part is a continuum where the intensity moves from bottom to top upon increasing field.

An explanation for this rich behaviour is sought in terms of the Hamiltonian model for $CoNb_2O_6$ refined in the previous chapter, which proposed all relevant additional exchange terms down to 2% of the Ising exchange. The experimental data are found to agree very well with the results obtained using numerical exact diagonalization (ED) calculations for this full Hamiltonian, where interchain coupling effects are treated in a mean field approximation. To obtain a physical understanding of the spectrum, a picture of soliton quasiparticles, which hop due to both the applied transverse field and the off-diagonal exchange, is taken as a starting point. The competition between these hopping effects leads to soliton hopping terms that alternate along the two legs of the zigzag chain, resulting in two bands with dispersions that are tuned by the applied field. The relevance of a model with alternating hopping of solitons for explaining features in THz spectroscopy data obtained on $CoNb_2O_6$ was already mentioned in Ref. [125], where solitons were treated as non-interacting. Here, the interactions between solitons are fully taken

into account as it is found that this is crucial for a full understanding of the observed spectrum. A spin-flip neutron scattering process creates two-soliton excitations (Fig. 2.5A), which interact via hard-core repulsion and various nearest-neighbour interaction terms. A minimal model is solved in the two-soliton subspace and three continua and up to three bound states are found depending on the values of the Hamiltonian parameters. To understand the character of these bound states, it is found to be helpful to focus first on the limit where solitons are localized due to the hopping term on alternate bonds being zero, a theoretical situation not previously explored. In this limit, novel bound states arise due to hard-core repulsion. Perturbations away from this limit are then considered in first order perturbation theory, such that analytic expressions are obtained for the dispersions and intensities in INS, which give strong qualitative agreement with the data. The results indicate that this regime is indeed realized in $CoNb_2O_6$ at intermediate transverse field.

The rest of this chapter is organized as follows: Sec. 6.2 provides details of the inelastic neutron scattering experiments while Sec. 6.3 introduces the model Hamiltonian and provides a qualitative overview of the experimental results. In Sec. 6.4, the model Hamiltonian is solved in first order perturbation theory in the two-soliton subspace. In Sec. 6.5, a physical picture of the spectrum is provided by starting from the limit where individual solitons are localized and perturbing around this limit. Sec. 6.6 contains the conclusions for this chapter.

6.2 Experimental details

Inelastic neutron scattering measurements of the magnetic excitations were performed on a large single crystal (6.76 g) of $CoNb_2O_6$ grown using a floating-zone technique [132] and already used in previous INS experiments [25]. The magnetic field was applied along the crystallographic b-direction, which is transverse to the local Ising axis of all the spins. The measurements were performed using the indirect geometry time-of-flight spectrometer OSIRIS at the ISIS facility. OSIRIS was operated with PG(002) analyzers to measure the inelastic scattering of neutrons with a fixed final energy of $E_f = 1.82$ meV as a function of energy transfer and

wavevector transfer in the horizontal $(h0l)$ scattering plane. Throughout this chapter, the wavevector transfer in the inelastic neutron scattering experiments is expressed as $\boldsymbol{Q} = (2\pi h/a, 0, 2\pi l/c)$ where $(h, 0, l)$ are expressed in reciprocal lattice units of the orthorhombic structural unit cell, with lattice parameters $a = 14.1337$ Å, $b = 5.7019$ Å and $c = 5.0382$ Å at 2.5 K [114]. The sample was attached to the cold finger of a dilution refrigerator inside a vertical 7.5 T cryomagnet and measurements were taken at a temperature of 0.1 K. The average counting time at each field was around 7 hours.

For each field, two sample orientations were measured (c-axis oriented in the scattering plane at 25° and 60° with respect to the incident beam direction). Throughout this chapter, the data panels presented are a combination of data from these two orientations, with the wavevector projected along the chain direction l as the physics considered is one-dimensional. The two orientations were chosen such that the projected l values covered a large part of the Brillouin zone along the chain direction. The INS data at one of the measured fields (2.5 T, in Fig. 6.1Q) was briefly reported in Ref. [71].

The data shown have had an estimate of the non-magnetic background subtracted off, and have then been divided by the squared isotropic Co^{2+} magnetic form factor $f^2(\boldsymbol{Q})$ and by the neutron polarization factor. The latter was calculated under the assumption that all inelastic scattering is in the polarizations perpendicular to the Ising (z) axes and that the dynamical structure factor satisfies $S^{xx}(\boldsymbol{Q}, \omega) = S^{yy}(\boldsymbol{Q}, \omega)$, an approximation which is found to be valid to a large extent for the model Hamiltonian (6.3) in the low transverse field regime. Here,[1]

$$S^{xx}(\boldsymbol{Q}, \omega) = \sum_{\lambda_f} |\langle \lambda_f | S^x(\boldsymbol{Q}) | \mathrm{GS} \rangle|^2 \delta(E_{\lambda_f} - \hbar\omega), \tag{6.1}$$

where the sum extends over all excited states $|\lambda_f\rangle$ of energy E_{λ_f} relative to the ground state $|\mathrm{GS}\rangle$ and where $S^x(\boldsymbol{Q}) = \sum_j \exp(i\boldsymbol{Q} \cdot \boldsymbol{r}_j) S^x_j$, with j running over all

[1] This definition differs from the one used in other chapters by a factor $g_x^2 \mu_B^2$. As $g_x \approx g_y$ and as $S^{zz}(\boldsymbol{Q}, \omega \neq 0) \approx 0$ in this regime, the lack of scaling by the g-factor and Bohr magneton only affects absolute intensities, not relative intensities. As the intensities in the data were not measured on an absolute scale, this therefore does not affect the conclusions.

sites. Under the above assumption, the wavevector dependence of the neutron polarization factor is

$$\mathscr{P}(\boldsymbol{Q}) = 1 + \frac{\left(\frac{2\pi h}{a}\right)^2 \sin^2\gamma + \left(\frac{2\pi l}{c}\right)^2 \cos^2\gamma}{\boldsymbol{Q}^2}. \tag{6.2}$$

Dividing the raw inelastic neutron scattering intensities by $\mathscr{P}(\boldsymbol{Q})f^2(\boldsymbol{Q})$ then gives $S^{xx}(\boldsymbol{Q},\omega)$ up to an overall scale factor. Eq. (6.2) is appropriate for the experimentally observed zero-field magnetic structure of $CoNb_2O_6$ and takes into account the two different chains per crystallographic unit cell with Ising directions at an angle of $\pm\gamma$ to the c-direction in the ac-plane. The angle γ has been taken to be 30° [114].

6.3 Evolution of the magnetic excitations with applied field

In this section, first the model Hamiltonian is introduced and related to the zero field spectrum, discussed in terms of two-soliton states. In applied field, the spectrum splits into three components with different evolution in field. It is shown in the following sections that this rich behaviour can be naturally understood in a picture of solitons with dispersions tuned by the transverse field.

6.3.1 Model Hamiltonian

The single-chain Hamiltonian model for $CoNb_2O_6$ refined in the previous chapter is used[2]. It is convenient to write this Hamiltonian in three parts and for convenience it is reproduced here:

$$\mathcal{H} = \mathcal{H}_1 + \mathcal{H}_2 + \mathcal{H}_{\mathrm{MF}} \tag{6.3}$$

[2]Note that there is a change in the definition of the sign of the Zeeman term compared to the expression in Chapter 5. This is equivalent to rotating 180° about the x-axis followed by interchanging the definition of odd and even sites.

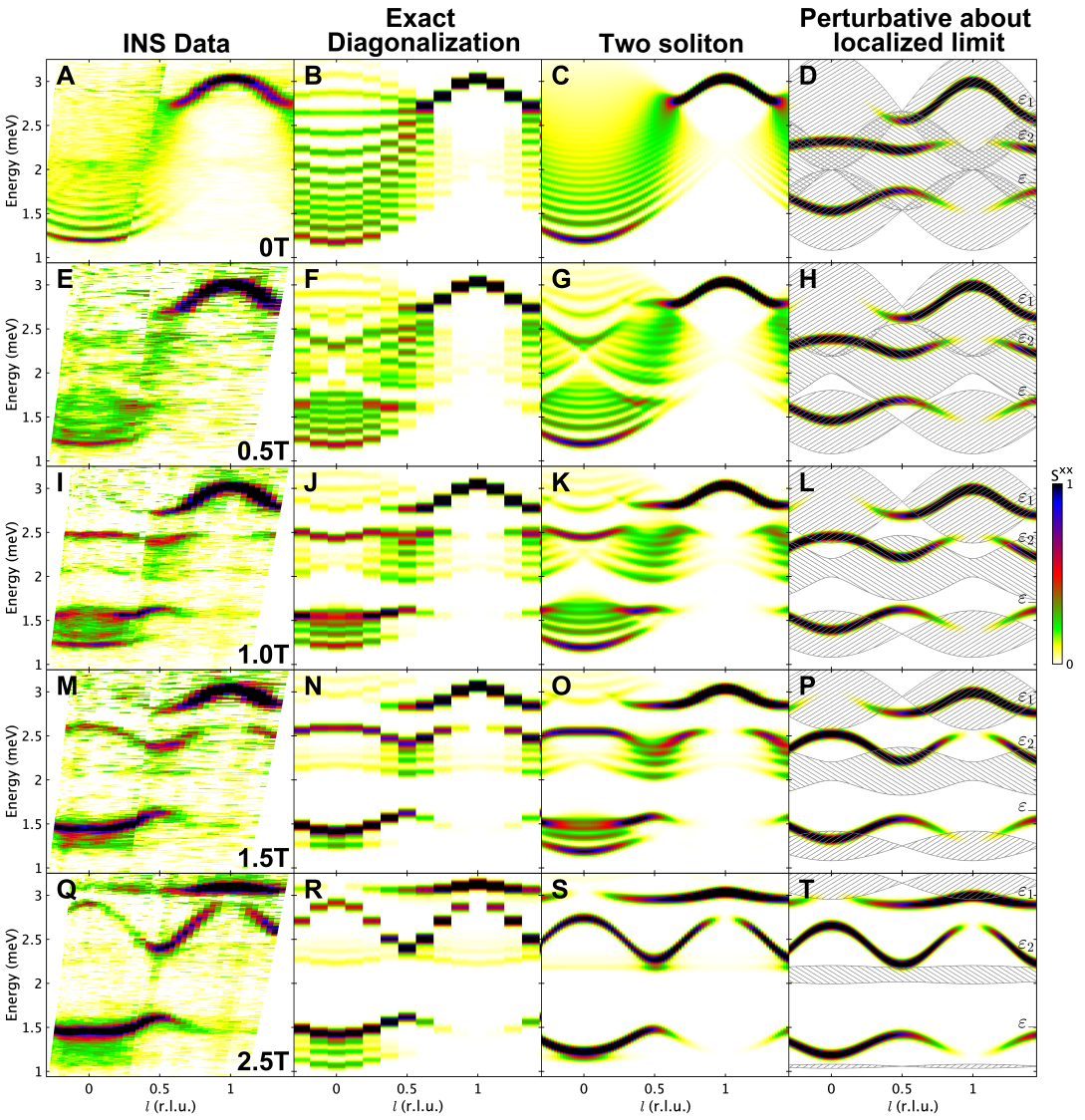

Figure 6.1: Evolution of the INS spectrum and calculated spectrum for the full Hamiltonian in (6.3), as a function of applied magnetic field, increasing from top to bottom. Columns left to right: Inelastic neutron scattering data (A adapted from [25]); S^{xx} as calculated by ED on 16 sites (8 unit cells) with periodic boundary conditions; S^{xx} as calculated by diagonalization of the two-soliton subspace (see Sec. 6.4.2) on 100 sites (50 unit cells) with periodic boundary conditions; S^{xx} as calculated analytically by perturbing about the localized limit for λ_{MF}=0 (see Sec. 6.5). In the right-most column, the hatched patches represent the two-soliton continua; in this approximation, the continua have no scattering intensity except where the bound states overlap them and create a resonance. In each panel, colour indicates S^{xx}, as defined in (6.1) and further normalized by the total number of sites, on a linear scale indicated by the colourbar. The calculations have been convolved with a Gaussian of FWHM 0.067 meV to mimic the estimated experimental resolution effects and calculated intensities are shown in absolute units of meV^{-1}. The intensities for the data in panels E, I, M, Q, have been multiplied by a common scale factor to bring them visually into agreement with the corresponding calculations in column 2. The data in A come from a different experiment so a separate scale factor was used for those intensities to bring them into agreement with those in panel B.

where

$$\mathcal{H}_1 = J\sum_j \Big[-S_j^z S_{j+1}^z - \lambda_S\left(S_j^x S_{j+1}^x + S_j^y S_{j+1}^y\right) + (-1)^j \lambda_{yz}\left(S_j^y S_{j+1}^z + S_j^z S_{j+1}^y\right)\Big] + \sum_j h_y S_j^y, \tag{6.4}$$

$$\mathcal{H}_2 = J\sum_j \Big[-\lambda_A\left(S_j^x S_{j+1}^x - S_j^y S_{j+1}^y\right) + \lambda_{\mathrm{AF}} S_j^z S_{j+2}^z + \lambda_{\mathrm{AF}}^{xy}\left(S_j^x S_{j+2}^x + S_j^y S_{j+2}^y\right)\Big], \tag{6.5}$$

and

$$\mathcal{H}_{\mathrm{MF}} = J\sum_j 2\lambda_{\mathrm{MF}}\left(\langle S^y\rangle S_j^y - \langle S^z\rangle S_j^z\right), \tag{6.6}$$

and where z is the Ising direction (in the crystallographic ac plane, defined as the direction of the moments in zero applied field), y is parallel to the crystallographic b-direction and x completes a right-handed coordinate system.

This Hamiltonian, with parameter values in Table 5.2, is a refinement of the minimal model proposed in Ref. [71] and was deduced using a simultaneous fit to the spectrum in zero field, large transverse field, and large near-longitudinal field, as discussed in the previous chapter. One can regard $\mathcal{H}_1$ as the minimal Hamiltonian needed to *qualitatively* reproduce all key features of the excitation spectrum, while the terms in $\mathcal{H}_2$ are sub-leading and are added in order to achieve *quantitative* agreement. This applies to both the data in Chapters 4 and 5 as well as data in low transverse field presented in this chapter. Finally, $\mathcal{H}_{\mathrm{MF}}$ captures the effects of the weak interchain interactions at a mean-field level. The given form with a constant $\lambda_{\mathrm{MF}} > 0$ applies throughout the field range explored here (0 to 2.5 T $\parallel b$) as the magnetic order pattern between chains does not change in this field range [123] and as, for this magnetic structure, all the interchain interactions that have a net contribution to the mean field are Heisenberg-like (see previous chapter). The relation between λ_{MF} and the interchain exchanges is given in the caption to Table 5.1. The different signs in front of the S_j^y and S_j^z terms reflect the fact that the S^y-components of spins on neighbouring chains are parallel (polarized by the applied field h_y), whereas the S^z components are (spontaneously) aligned antiparallel by the antiferromagnetic interchain interactions.

As discussed in the previous chapter, the spectrum in zero field (Fig. 6.1A data, 6.1B calculation) can be qualitatively understood in terms of the minimal Hamiltonian $\mathcal{H}_1 + \mathcal{H}_{\rm MF}$. A spin-flip neutron scattering event creates a pair of solitons (domain walls) and for the pure Ising chain, the energy is independent of the separation between these solitons [see Fig. 2.5A]. In the presence of the staggered off-diagonal exchange (λ_{yz}), the solitons become dispersive [71], resulting in a continuum of scattering in energy-momentum space, covering a large energy extent near $l = 0$ [25]. In zero field, the interchain mean field $\mathcal{H}_{\rm MF}$ is purely longitudinal and acts as an effective linear potential confining the solitons into a series of bound states, as seen in Fig. 6.1A near $l = 0$. The sharp mode in the data near $l = 1$ is a two-soliton kinetic bound state stabilized by the XY (λ_S) exchange [25]. Fig. 6.1B demonstrates that very good quantitative agreement has been achieved between the experimental zero-field data and exact diagonalization calculations using the full Hamiltonian (6.3), as noted in the previous chapter.

6.3.2 Spectrum in small to intermediate transverse field

The key feature of the evolution of the spectrum as a function of field, shown in the first column of Fig. 6.1, is the break-up of the observable spectrum into three parts, each evolving very differently upon increasing field. The top part, which evolves out of the zero-field high-energy kinetic bound state, is a sharp mode that becomes progressively flatter upon increasing field and spreads out over the whole Brillouin zone. In contrast, the middle part is dominated by a sharp mode that becomes progressively more dispersive upon increasing field and appears to trade intensity with the top mode. The lowest energy part is dominated by a continuum spread, with intensity moving from bottom to top upon increasing field. All features and trends in the INS data are quantitatively captured by exact diagonalization (ED) calculations using the full Hamiltonian in (6.3) with the expectation values $\langle S^y \rangle$ and $\langle S^z \rangle$ in the mean-field term $\mathcal{H}_{\rm MF}$ calculated self-consistently; these calculations are shown in the second column of Fig. 6.1.

The breakup of the spectrum in field is clearly illustrated in Fig. 6.1I at 1 T. The lowest energy part of the spectrum centred around 1.4 meV shows a set of excitations extending over a broad energy range with clear sharp modes visible both at the bottom and the top of this range. Those excitations are clearly separated from another set of states centred around 2.25 meV with a clear sharp mode near 2.5 meV. At higher energies still, there is the vestige of the zero-field kinetic bound state near $l = 1$, now clearly separated from the rest of the spectrum. All the observed features, both dispersions and wavevector-dependence of intensities, are well captured by the ED calculations in Fig. 6.1J.

The 2.5 T data (Fig. 6.1Q) shows even more contrasting behaviour between the different parts of the spectrum. The sharp mode at the top of the low energy continuum now extends all the way from the Brillouin zone center to $l \approx 0.6$ and has gained in intensity compared to the continuum below it. In the middle energy region the sharp mode has become strongly dispersive, with the middle continuum losing nearly all its scattering intensity, and the top sharp mode has become almost entirely flat and spread out over almost all of the Brillouin zone. Again, all these features are well reproduced in Fig. 6.1R. The spectra at 0.5 T (Figs. 6.1E and F) and 1.5 T (Figs. 6.1M and N) interpolate between 0, 1 and 2.5 T and show the gradual evolution of the spectrum.

The ED calculations quantitatively capture every feature and trend described above. It is important to note that the parameters used in this calculation were *not* fitted to the finite transverse field data presented here, but are fixed to the values proposed in the previous chapter. This excellent agreement between data and calculation gives further support to the Hamiltonian proposed in Chapter 5 and motivates the search for a physical picture of the excitations. In the following sections, a picture of solitons on the zigzag chains will be introduced and it will be shown that the breaking up of the spectrum and very different evolution of the different parts in field can be captured quantitatively and understood phenomenologically in terms of solitons hopping and forming bound states.

6.4 Two-soliton model

In (6.4) to (6.6), all λ terms are $\ll 1$ such that the dominant term is the ferromagnetic Ising term. This means that it is sufficient for the present purposes to consider two-soliton excitations, and neglect mixing with four-or-more-soliton excitations, since those occur at much higher energy.

The effect of the effective Hamiltonian which acts within subspaces of fixed soliton number is now considered: first its action on a single soliton, and then within the two-soliton sector. This effective Hamiltonian is related to the full Hamiltonian as

$$\mathcal{H}' \approx \sum_{i\geq 0} \mathcal{P}_i \mathcal{H} \mathcal{P}_i, \tag{6.7}$$

where $\mathcal{P}_i$ is the projector to the subspace with i solitons, and $i = 1, 2$. The main focus of the discussion will be the minimal Hamiltonian $\mathcal{H}_1 + \mathcal{H}_{\rm MF}$, as this yields a good qualitative understanding of the spectrum. As will be discussed further in Sec. 6.4.4, the assumption is also made that the spin vector expectation value in the ground state is $\langle \boldsymbol{S} \rangle = (0, 0, 1/2)$. As such, the mean field interchain coupling becomes an effective magnetic field along the z-direction,

$$\mathcal{H}_{\rm MF} = -h_z \sum_j S^z_j, \quad \text{with } h_z = 2J\lambda_{\rm MF}\langle S^z \rangle = J\lambda_{\rm MF}. \tag{6.8}$$

It will be convenient in the following to use the *unconventional* raising and lowering operators,

$$S^{\pm}_j = S^y_j \mp i S^x_j, \tag{6.9}$$

which obey the usual commutation relations. Note that this is equivalent to performing the calculations in a spin basis rotated by 90° around the z-axis, obtained via the canonical transformation $S^x_j \to -S^y_j$ and $S^y_j \to S^x_j$ in $\mathcal{H}$.

6.4.1 Action of the Hamiltonian on a single soliton

In this section the spectrum of deconfined solitons under the Hamiltonian $\mathcal{H}_1$ projected to the single soliton sector is considered. The confining mean field $\mathcal{H}_{\rm MF}$ will be introduced in Sec. 6.4.2, where the spectrum in the two-soliton sector is discussed.

Let $|j\rangle_L$ denote a 'left' soliton state, defined as a single domain wall between sites $j-1$ and j, separating up spins on the left from down spins on the right, i.e.,

$$|j\rangle_L = |\cdots\uparrow\uparrow\uparrow_{j-1}\downarrow_j\downarrow\downarrow\cdots\rangle\,. \tag{6.10}$$

Here, the arrows indicate the eigenstates of S_j^z with eigenvalues $\pm 1/2$. Now consider the action of the Hamiltonian $\mathcal{H}_1$ on this state, term by term.

- *Ising exchange:* The single-soliton state $|j\rangle_L$ is an eigenstate of the Ising interaction, with excitation energy $\epsilon_0 = J/2$ above the ground state.

- *XY exchange λ_S:* This term flips two adjacent spins in opposite directions. Acting on $|j\rangle_L$, it creates two additional domain walls by flipping the spins at sites $j-1$ and j, and can therefore be dropped as this term causes the state to leave the single soliton subspace.

- *Transverse field h_y:* This term flips a single spin,

$$V_y = \frac{h_y}{2}\sum_j \left(S_j^+ + S_j^-\right), \tag{6.11}$$

  where the unconventional raising and lowering operators (6.9) have been used. To conserve the number of solitons when acting on $|j\rangle_L$, the flipped spin must be either at j or $j-1$,

$$\mathcal{P}_1 V_y |j\rangle_L = \frac{h_y}{2}\left(|j+1\rangle_L + |j-1\rangle_L\right). \tag{6.12}$$

  Therefore, the transverse field gives rise to a nearest-neighbour hopping term for the domain wall.

- *Staggered off-diagonal exchange λ_{yz}*: Similarly to the transverse field h_y, this term results in a single spin flip,

$$V_{yz} = \frac{J\lambda_{yz}}{2}\sum_j (-1)^j \left(S_j^+ + S_j^-\right)\left(S_{j+1}^z - S_{j-1}^z\right). \tag{6.13}$$

Here, the operator $S_j^+ + S_j^-$ can flip the spin at site j if and only if the spins on sites $j+1$ and $j-1$ are opposite, due to the factor $S_{j+1}^z - S_{j-1}^z$. Therefore, V_{yz} leads to spin flip processes confined to domain walls, i.e.,

$$\mathcal{P}_1 V_{yz}|j\rangle_L = \frac{J\lambda_{yz}}{2}(-1)^{j+1}\left(|j+1\rangle_L - |j-1\rangle_L\right). \tag{6.14}$$

This is also a hopping term for the domain walls, similarly to the effect of the transverse field h_y, but with a different sign structure.

The spectrum of this hopping Hamiltonian is obtained by writing a Schrödinger equation for the soliton. First, define the state

$$|\psi_L\rangle = \sum_{j'} \psi_L(j')|j'\rangle_L, \tag{6.15}$$

where $\psi_L(j) = {}_L\langle j|\psi\rangle$ is the wavefunction of the soliton. Using the expressions derived for $\mathcal{P}_1\mathcal{H}_1|j\rangle_L$ above, the Schrödinger equation,

$${}_L\langle j|\mathcal{H}_1|\psi_L\rangle = \omega\,\psi_L(j), \tag{6.16}$$

can be rewritten as

$$\frac{1}{2}\sum_{\Delta=\pm1}\left(h_y + (-1)^j J\lambda_{yz}\Delta\right)\psi_L(j-\Delta) = \left(\omega - \frac{J}{2}\right)\psi_L(j). \tag{6.17}$$

This equation describes a staggered hopping of solitons, with hopping amplitudes

$$h_\pm = \frac{1}{2}\left(h_y \pm J\lambda_{yz}\right) \tag{6.18}$$

alternating on even/odd bonds.

Since $\mathcal{H}$ is invariant under translations by two lattice sites, the Bloch ansatz,

$$\psi_L(2p+\sigma) = \psi_{L\sigma}e^{ikpc}, \quad \text{with } \sigma = 0, 1, \tag{6.19}$$

can be used, where $k = 2\pi l/c$ is the soliton momentum. In the following, the symbols k and l will be used interchangeably when referring to momentum along the chain direction, with the only difference that k is in absolute units whereas l is in reciprocal lattice units. In the above equation, the coefficients $\psi_{L\sigma}$ differentiate between the even and odd sublattices, reflecting the two-site unit cell of the Hamiltonian. From

now on, the index p will be reserved for labelling the unit cells, whereas j will be used as a label of lattice sites. The Schrödinger equation then becomes

$$\begin{pmatrix} 0 & h_+e^{-ikc}+h_- \\ h_+e^{ikc}+h_- & 0 \end{pmatrix}\begin{pmatrix}\psi_{L0}\\ \psi_{L1}\end{pmatrix} = \left(\omega-\frac{J}{2}\right)\begin{pmatrix}\psi_{L0}\\ \psi_{L1}\end{pmatrix}. \tag{6.20}$$

The solution to this Schrödinger equation is a pair of bands, $\omega_\pm$, defined as

$$\begin{aligned}\left(\frac{J}{2}-\omega_\pm\right)^2 &= \left(h_+e^{-ikc}+h_-\right)\left(h_+e^{ikc}+h_-\right)\\ &= h_+^2+h_-^2+2h_+h_-\cos kc,\end{aligned} \tag{6.21}$$

which can be thought of as bonding / anti-bonding orbitals. Importantly, the dispersion of both bands vanishes if $h_+=0$ or $h_-=0$. In these limits, the hopping amplitude vanishes either on odd or on even bonds, and the domain wall can only hop backwards and forwards between two sites, resulting in flat localized bands, as previously noted in Ref. [125]. This localized limit will serve as a convenient starting point for perturbative considerations in Sec. 6.5, and will allow a simple qualitative picture to be obtained for the evolution of the INS spectrum with magnetic field h_y.

Note that, in the above, a single 'left' soliton was considered, which describes a domain wall with up spins on the left and down spins on the right. As well as these left solitons, it is also necessary to consider the other type of domain wall, i.e. 'right' solitons, which separate a domain of down spins on the left from up spins on the right,

$$|j\rangle_R = |\cdots\downarrow\downarrow\downarrow_{j-1}\uparrow_j\uparrow\uparrow\cdots\rangle\,. \tag{6.22}$$

The arguments described above can be repeated for right solitons, with the only difference being that the hopping induced by λ_{yz} is of opposite sign relative to the case when left solitons are considered. This sign change interchanges the hopping amplitudes h_+ and h_- in the Schrödinger equations, but leaves the dispersion (6.21) unaltered. Therefore, both types of soliton become localized at the same special magnetic field h_y.

6.4.2 Solution of the Hamiltonian in the two-soliton subspace

The spectrum of the effective Hamiltonian within the two-soliton subspace is now considered. In Sec. 6.4.1, two distinct soliton dispersions were obtained, $\omega_\pm$, corresponding to bonding/anti-bonding orbitals. Therefore, three continua are expected in the two-soliton subspace, arising from the combinations (ω_+, ω_+), (ω_+, ω_-) and (ω_-, ω_-). However, the solitons interact: this is due both to hard-core repulsion — if there are two domain walls in the same place, there is in fact only a single domain and the state is the fully aligned ground state — and to nearest-neighbour soliton-soliton interactions arising from terms in $\mathcal{H}_1$. Moreover, the full Hamiltonian also includes an effective confining magnetic field in the z-direction, $\mathcal{H}_{\rm MF}$, which leads to an attractive interaction between the two solitons in a pair. Below, all of these effects are taken into account; $\mathcal{H}_1 + \mathcal{H}_{\rm MF}$ is projected to the relevant subspace with $\mathcal{P}_2$ and it is shown that a full understanding of the spectrum cannot neglect these interactions.

Assuming $h_z > 0$, the relevant low energy excitations correspond to a single domain of down spins inserted into a background of up spins. Therefore, it is convenient to use the following basis, with a 'left' soliton on the left and a 'right' soliton on the right,

$$|j_L, j_R\rangle = |\cdots\uparrow\uparrow_{j_L-1}\downarrow_{j_L}\cdots\downarrow_{j_R-1}\uparrow_{j_R}\uparrow\cdots\rangle\,, \tag{6.23}$$

with $j_L < j_R$. Similarly to the procedure followed in Sec. 6.4.1, a Schrödinger equation can be derived within the two-soliton subspace by consideration of the effect of $\mathcal{P}_2\mathcal{H}_1$ and $\mathcal{H}_{\rm MF}$ on the basis states, as follows.

The transverse field h_y and staggered off-diagonal exchange λ_{yz} again give rise to hopping terms for the left and right solitons, with a correction term arising for nearest neighbour solitons $j_R = j_L + 1$ due to hard core repulsion, such that

$$\mathcal{P}_2 V_y |j_L, j_R\rangle = \frac{h_y}{2} {\sum_{\Delta=\pm1}}' \left(|j_L + \Delta, j_R\rangle + |j_L, j_R + \Delta\rangle\right), \tag{6.24}$$

and

$$\mathcal{P}_2 V_{yz}|j_L, j_R\rangle = \frac{J\lambda_{yz}}{2}\sum_{\Delta=\pm1}{}' \Delta\left((-1)^{j_L}|j_L-\Delta, j_R\rangle - (-1)^{j_R}|j_L, j_R-\Delta\rangle\right). \quad (6.25)$$

Here and throughout this subsection, $\sum'$ denotes a summation restricted to valid basis states, by dropping the unphysical terms $|j_L+1, j_R\rangle$ and $|j_L, j_R-1\rangle$ when solitons are on neighbouring sites, i.e., $j_R = j_L+1$, since this would lead to overlapping solitons.

Besides these terms, two new types of contribution arise compared to the single soliton case. The XY exchange term,

$$V_S = \frac{-J\lambda_S}{2}\sum_j \left(S_j^+ S_{j+1}^- + S_j^- S_{j+1}^+\right), \quad (6.26)$$

gives rise to a nearest neighbour interaction term between solitons,

$$\mathcal{P}_2 V_S|j_L, j_R\rangle = -\frac{J\lambda_S}{2}\delta_{j_R-j_L,1}\sum_{\Delta=\pm1}|j_L-\Delta, j_R-\Delta\rangle. \quad (6.27)$$

This term shifts the centre-of-mass coordinate of the soliton pair by one lattice site, without changing the relative coordinate $j_R - j_L$, i.e., it allows nearest neighbour solitons to hop together as a pair. In addition, the magnetic field h_z leads to an attractive potential between the left and right soliton,

$$\mathcal{H}_{\rm MF}|j_L, j_R\rangle = h_z(j_R-j_L)|j_L, j_R\rangle. \quad (6.28)$$

This is the same confinement effect as discussed in Chapter 4.

The two-soliton wavefunction $\Psi(j_L, j_R)$ is defined through

$$|\Psi\rangle = \sum_{j_L<j_R}\Psi(j_L, j_R)|j_L, j_R\rangle. \quad (6.29)$$

The two-soliton Schrödinger equation,

$$\langle j_L, j_R|\mathcal{H}_1\mathcal{P}_2 + \mathcal{H}_{\rm MF}|\Psi\rangle = \omega\Psi(j_L, j_R), \quad (6.30)$$

thus becomes

$$\frac{1}{2}\sum_{\Delta=\pm1}{}'\left[\left(h_y+\Delta(-1)^{j_L}J\lambda_{yz}\right)\Psi(j_L-\Delta, j_R)+\left(h_y-\Delta(-1)^{j_R}J\lambda_{yz}\right)\Psi(j_L, j_R-\Delta)\right]$$
$$-\frac{J\lambda_S}{2}\delta_{j_R-j_L,1}\sum_{\Delta=\pm1}\Psi(j_L-\Delta, j_R-\Delta)+h_z(j_R-j_L)\Psi(j_L, j_R) = (\omega-2\epsilon_0)\Psi(j_L, j_R), \quad (6.31)$$

where $\epsilon_0 = J/2$ is the energy cost of a single domain wall. Making use of lattice translational invariance for the centre of mass coordinate, it is convenient to write the wavefunction as

$$\Psi(2p_L + \sigma_L, 2p_R + \sigma_R) = e^{ikc(p_L+p_R)/2}\Phi^{(k)}_{\sigma_L\sigma_R}(p_R - p_L), \tag{6.32}$$

with $p_{L/R}$ labelling the two site unit cells, $\sigma_{L/R} = 0, 1$ distinguishing the even and odd sublattices and $c(p_L + p_R)/2$ being the position of the centre of mass of the soliton pair. For a fixed centre of mass momentum k, the Schrödinger equation (6.31) can be re-written in terms of $\Phi^{(k)}_{\sigma_L\sigma_R}(n)$, with n labelling the distance between two-site unit cells. The Schrödinger equation thus becomes

$$\begin{aligned}
&h_+e^{-ikc/2}\Phi^{(k)}_{10}(n+1) + h_-\Phi^{(k)}_{10}(n) + h_-e^{-ikc/2}\Phi^{(k)}_{01}(n-1) + h_+\Phi^{(k)}_{01}(n) \\
&\quad + 2nh_z\Phi^{(k)}_{0,0}(n) = (\omega - 2\epsilon_0)\Phi^{(k)}_{00}(n), && n \geq 1, \\
&h_-\Phi^{(k)}_{00}(n) + h_+e^{ikc/2}\Phi^{(k)}_{00}(n-1) + h_-e^{-ikc/2}\Phi^{(k)}_{11}(n-1) + h_+\Phi^{(k)}_{11}(n) \\
&\quad + h_z(2n-1)\Phi^{(k)}_{10}(n) - J\lambda_S\,\delta_{n,1}\cos\left(\frac{kc}{2}\right)\Phi^{(k)}_{01}(n-1) = (\omega - 2\epsilon_0)\Phi^{(k)}_{10}(n), && n \geq 1, \\
&h_+e^{-ikc/2}\Phi^{(k)}_{11}(n+1) + h_-\Phi^{(k)}_{11}(n) + h_+\Phi^{(k)}_{00}(n) + h_-e^{ikc/2}\Phi^{(k)}_{00}(n+1) \\
&\quad + h_z(2n+1)\Phi^{(k)}_{01}(n) - J\lambda_S\,\delta_{n,0}\cos\left(\frac{kc}{2}\right)\Phi^{(k)}_{10}(n+1) = (\omega - 2\epsilon_0)\Phi^{(k)}_{01}(n), && n \geq 0, \\
&h_-\Phi^{(k)}_{01}(n) + h_+e^{ikc/2}\Phi^{(k)}_{01}(n-1) + h_+\Phi^{(k)}_{10}(n) + h_-e^{ikc/2}\Phi^{(k)}_{10}(n+1) \\
&\quad + 2nh_z\Phi^{(k)}_{11}(n) = (\omega - 2\epsilon_0)\Phi^{(k)}_{11}(n), && n \geq 1,
\end{aligned} \tag{6.33}$$

with boundary conditions $\Phi^{(k)}_{00}(0) = \Phi^{(k)}_{11}(0) = \Phi^{(k)}_{10}(0) = 0$. This set of equations can be solved numerically using periodic boundary conditions on a finite ring.

To do this, the vector

$$\mathbf{\Phi}^{(k)} = \begin{pmatrix} \Phi^{(k)}_{01}(0) \\ \Phi^{(k)}_{00}(1) \\ \Phi^{(k)}_{11}(1) \\ \Phi^{(k)}_{10}(1) \\ \Phi^{(k)}_{01}(1) \\ \Phi^{(k)}_{00}(2) \\ \Phi^{(k)}_{11}(2) \\ \vdots \end{pmatrix}, \tag{6.34}$$

is introduced. This then yields a matrix equation, from which the low energy spectrum can be determined.

The correction terms arising from the subleading couplings in $\mathcal{H}_2$ to the two-soliton Schrödinger equation derived above can also be calculated by examining the action of $\mathcal{H}_2$ term by term. Note that following the convention defined above, $\mathcal{H}_2$ is rewritten in a rotated basis, $S^x_j \to -S^y_j$ and $S^y_j \to S^x_j$.

First, consider the anti-symmetric nearest-neighbour coupling,

$$V_A = \frac{J\lambda_A}{2} \sum_{\text{sites},j} \left(S^+_j S^+_{j+1} + S^-_j S^-_{j+1} \right), \tag{6.35}$$

raising or lowering two neighbouring spins. The effect of this term in the single soliton subspace is to move the soliton by two sites, i.e.,

$$\mathcal{P}_1 V_A |j\rangle_L = \frac{J\lambda_A}{2} \left(|j-2\rangle_L + |j+2\rangle_L \right). \tag{6.36}$$

In the two-soliton subspace, this becomes a next-to-nearest neighbour hopping term for the left and right solitons, with the constraint $j_R > j_L$ arising from the hard-core repulsion. Thus, the contribution of V_A to the left hand side of the Schrödinger equation for $(\omega - 2\epsilon_0)\Phi^{(k)}_{\sigma_L\sigma_R}(n)$ is

$$J\lambda_A \cos\left(\frac{kc}{2}\right) \left[\Phi^{(k)}_{\sigma_L\sigma_R}(n+1) + (1 - \delta_{n,0} - \delta_{n,1}(1 - \delta_{\sigma_L,0}\delta_{\sigma_R,1}))\, \Phi^{(k)}_{\sigma_L\sigma_R}(n-1) \right]. \tag{6.37}$$

Next, the perturbation

$$V_{\rm AF}^{xy} = \frac{J\lambda_{\rm AF}^{xy}}{2} \sum_{\text{sites},j} \left(S_j^+ S_{j+2}^- + S_j^- S_{j+2}^+ \right) \tag{6.38}$$

flips a pair of next-nearest-neighbour spins in opposite directions. Acting on a single soliton, $V_{\rm AF}^{xy}|j\rangle_L$ always leaves the single soliton subspace. In the presence of two solitons, $|j_L, j_R\rangle$, however, a non-vanishing short range contribution is found for $j_R \leq j_L + 2$,

$$\mathcal{P}_2 V_{\rm AF}^{xy}|j_L, j_R\rangle = \frac{J\lambda_{\rm AF}^{xy}}{2} \sum_{\Delta=\pm1} \left(\delta_{j_R,j_L+1} \, |j_L + 2\Delta, j_R + 2\Delta\rangle + \delta_{j_R,j_L+2} \, |j_L + \Delta, j_R + \Delta\rangle \right). \tag{6.39}$$

This term therefore shifts the centre-of-mass coordinate by ± 2 or ± 1 sites for a spin down domain of length $j_R - j_L = 1$ and $j_R - j_L = 2$, respectively. It leads to the following four extra contributions on the left hand side the Schrödinger equation (6.33)

$$\begin{aligned}
\cdots + J\lambda_{\rm AF}^{xy} \cos(kc) \Phi_{01}^{(k)}(0) &= (\omega - 2\epsilon_0) \Phi_{01}^{(k)}(0), \\
\cdots + J\lambda_{\rm AF}^{xy} \cos(kc) \Phi_{10}^{(k)}(1) &= (\omega - 2\epsilon_0) \Phi_{10}^{(k)}(1), \\
\cdots + J\lambda_{\rm AF}^{xy} \frac{1 + e^{-ikc}}{2} \Phi_{11}^{(k)}(1) &= (\omega - 2\epsilon_0) \Phi_{00}^{(k)}(1), \\
\cdots + J\lambda_{\rm AF}^{xy} \frac{1 + e^{ikc}}{2} \Phi_{00}^{(k)}(1) &= (\omega - 2\epsilon_0) \Phi_{11}^{(k)}(1).
\end{aligned} \tag{6.40}$$

Finally, the effect of the perturbation

$$V_{\rm AF} = J\lambda_{\rm AF} \sum_{\text{sites},j} S_j^z S_{j+2}^z \tag{6.41}$$

is to lower the energy of all states relative to the fully aligned (ground) state. This term is diagonal in the two-soliton basis $|j_L, j_R\rangle$, yielding an energy shift depending on the size of the spin down domain. If there is only a single spin flip, $j_R - j_L = 1$, only two antiferromagnetic bonds are satisfied, whereas if there are two or more spin flips, $j_R - j_L \geq 2$, four antiferromagnetic bonds are satisfied, i.e.,

$$\begin{aligned}
V_{\rm AF}|j, j+1\rangle &= -J\lambda_{\rm AF}|j, j+1\rangle \\
V_{\rm AF}|j, j+2\rangle &= -2J\lambda_{\rm AF}|j, j+2\rangle,
\end{aligned} \tag{6.42}$$

where only the energy difference between the excited state and the ground state has been kept. These considerations lead to the energy shifts

$$\omega - 2\epsilon_0 \longrightarrow \omega - 2\epsilon_0 + J\lambda_{\mathrm{AF}}, \quad \text{if } \; 2n + \sigma_R - \sigma_L = 1, \tag{6.43}$$

$$\omega - 2\epsilon_0 \longrightarrow \omega - 2\epsilon_0 + 2J\lambda_{\mathrm{AF}}, \quad \text{if } \; 2n + \sigma_R - \sigma_L > 1, \tag{6.44}$$

on the right hand side of the Schrödinger equation for $\Phi^{(k)}_{\sigma_L\sigma_R}(n)$.

6.4.3 Bound states in the two-soliton spectrum

The two-soliton Schrödinger equation derived above yields a spectrum consisting of three continua and three bound states across a wide range of parameters, as shown in Fig. 6.2. The left column of Fig. 6.2 shows the two-soliton spectrum as a function of field for the minimal Hamiltonian $\mathcal{H}_1$. In this case, the spectrum consists of three continua and three bound states at every non-zero field. As mentioned above, the origin of the three continua can be understood as due to the three different ways of combining the two bands of solitons into two-soliton continua. The origin of the bound states, which are here termed ε bound states for the avoidance of confusion, will be explored in the following section, Sec. 6.5.

The right hand column of Fig. 6.2 shows the same calculation for the full Hamiltonian $\mathcal{H}_1 + \mathcal{H}_2 + \mathcal{H}_{\mathrm{MF}}$, where $\mathcal{H}_{\mathrm{MF}}$ is the confining mean field. In this case, the mean field splits the continua into a series of confinement bound states, but the ε bound states are left mostly intact, because they are tightly bound.

6.4.4 Inelastic neutron scattering intensity in the two-soliton model

To conclude this section, a formula for the INS spectrum within the two-soliton model is derived, which shows that the dominant contribution stems from the three bound states.

As mentioned above, the assumption is made that the ground state $|\mathrm{GS}\rangle$ appearing in the dynamical structure factor S^{xx}, Eq. (6.1), can be approximated as the ground state of the Ising Hamiltonian, $|\mathrm{GS}\rangle \approx |... \uparrow\uparrow\uparrow ...\rangle$. Acting on this state

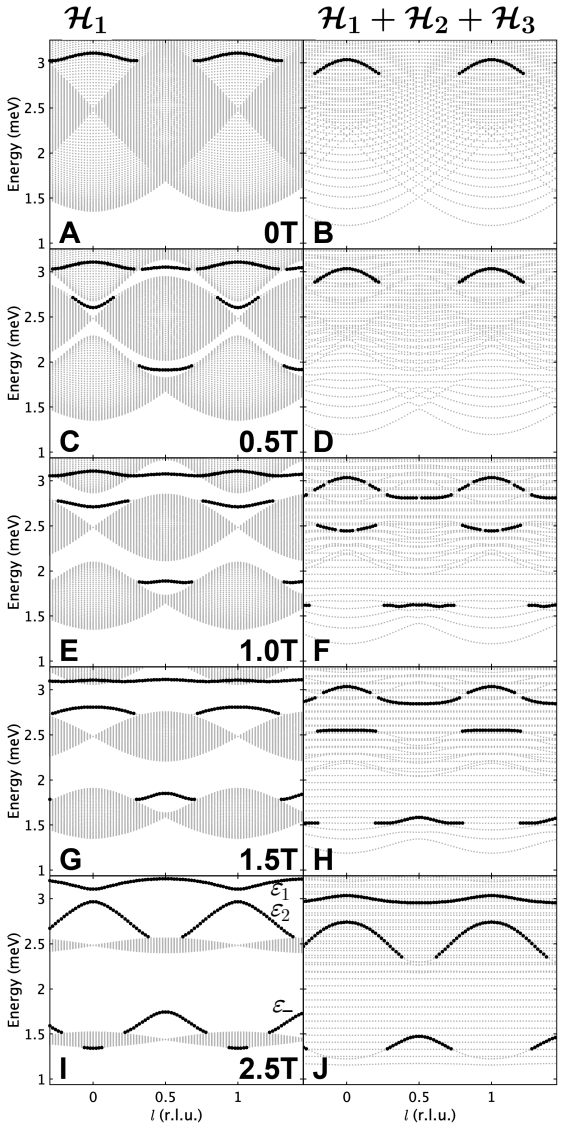

Figure 6.2: Eigenstates of the two-soliton Hamiltonian as a function of wavevector and energy at different fields, increasing from top to bottom. In each panel, states with the character of the ε bound states have been highlighted in black. These states have been identified by being well separated from other states in energy, or, where they overlap with other states, by having high INS intensity and discarding regions with strong hybridization. Left column: Solution of $\mathcal{H}_1$. Three continua and three bound states can be seen at every non-zero field. ε_1, ε_2 and ε_- are defined in Sec. 6.5.3. Right column: solution of $\mathcal{H} = \mathcal{H}_1 + \mathcal{H}_2 + \mathcal{H}_{\mathrm{MF}}$. This comparison illustrates the key effect of $\mathcal{H}_{\mathrm{MF}}$, i.e., the presence of a longitudinal mean field: all continua are split into confinement bound states, but the ε bound states are left essentially intact. This column is to be compared with the third column of Fig. 6.1, which shows the intensities under the same conditions.

with the spin operator $S^x(k)$ creates a pair of solitons. Using the unconventional raising and lowering operators $S_j^{\pm} = S_j^y \mp iS_j^x$, the resulting state can be written as

$$S^x(k)|\mathrm{GS}\rangle \approx -\frac{i}{2}\sum_j e^{ikjc/2}|j, j+1\rangle,$$

where $k = 2\pi l/c$ is the soliton pair centre-of-mass momentum. By substituting the eigenstates $|\lambda_f\rangle$ with the solutions of the two-soliton Schrödinger equation constructed above, the squared matrix element appearing in (6.1) is found to be

$$|\langle\lambda_f|S^x(k)|\mathrm{GS}\rangle|^2 = \frac{\left|\Phi_{01}^{(k)}(0) + \Phi_{10}^{(k)}(1)\right|^2}{4}. \tag{6.45}$$

Therefore, the ε bound states, which will be shown to have a large weight on the configurations with nearest-neighbour domain walls, give the dominant contribution to the dynamical spin structure factor (6.1).

The INS intensity as calculated above is shown in the third column of Fig. 6.1. The calculation uses the full Hamiltonian with the same parameters as in the ED calculations, except that the spin vector expectation value $\langle \boldsymbol{S}\rangle = (0, 0, 1/2)$ is assumed fixed, rather than using a self-consistent value, which is a consequence of assuming that the ground state is the ground state of the Ising Hamiltonian. This is a good approximation since even at 2.5 T, the self-consistent value as calculated by ED is $\langle \boldsymbol{S}\rangle = (0, -0.150, 0.473)$. The agreement between the observed spectrum and the model is still quantitative — all features and trends are captured — but not quite as strong as for the exact diagonalization calculation. For instance, there is a small overall energy shift, most visible by comparing Figs. 6.1R and S; in the latter, energies are shifted to lower values. However all key features are well reproduced at all measured fields.

To gain more insight into the structure and magnetic field dependence of this INS signal, the ε bound states are examined in the next section, using a perturbative expansion around the localized limit $h_- = 0$.

6.5 The localized limit

As derived in Sec. 6.4.1, the staggered off-diagonal exchange λ_{yz} and the transverse field h_y in the leading order Hamiltonian $\mathcal{H}_1$ lead to hopping terms of opposite sign for the solitons. A particularly interesting situation arises when these terms are matched, such that $h_- = 0$, resulting in localized single solitons. This localized limit serves as a convenient starting point for perturbative considerations, shedding light on the structure and magnetic field dependence of the ε bound states, as well as the three two-soliton continua. First, in Sec. 6.5.1, the case $h_- = 0$ is considered, and the two-soliton spectrum is studied, in particular, the nature of the two-soliton bound states. The effect of a small non-zero delocalizing term h_- is then examined in Sec. 6.5.2 while the effect of subleading terms is discussed in Sec. 6.5.3. Predictions for the evolution of the INS spectra with decreasing transverse field h_y, and comparisons of these to the experimental data, are discussed in Sec. 6.5.4. For most of this section, the focus is on the leading order Hamiltonian $\mathcal{H}_1$, with brief comments on the subleading Hamiltonian $\mathcal{H}_2$ in Sec. 6.5.3, and on the mean field $\mathcal{H}_{\text{MF}}$ at the end of the section.

6.5.1 Localized limit $h_- = 0$

For simplicity, the XY exchange λ_S is initially set to 0, and only the staggered off-diagonal exchange λ_{yz} and the transverse field h_y are kept. The effect of the nearest neighbour XY exchange λ_S will be discussed later. Under these simplifications, a left soliton can hop between the two sites of a unit cell p, $2p \leftrightarrow 2p+1$, with amplitude h_-, whereas it hops between neighbouring unit cells $p-1$ and p, i.e., sites $2p-1 \leftrightarrow 2p$, with amplitude h_+, see Fig. 6.3A. For $h_- = 0$, the following eigenstates are thus obtained for the left soliton with energies $\omega_\pm$,

$$|p\rangle_L^\pm \equiv \frac{1}{\sqrt{2}}\left(|2p-1\rangle_L \pm |2p\rangle_L\right), \quad \omega_\pm = \frac{J}{2} \pm h_+. \tag{6.46}$$

These eigenstates are respectively symmetric and antisymmetric under the inversion exchanging the even and odd sublattices. For a right soliton, the role of h_- and

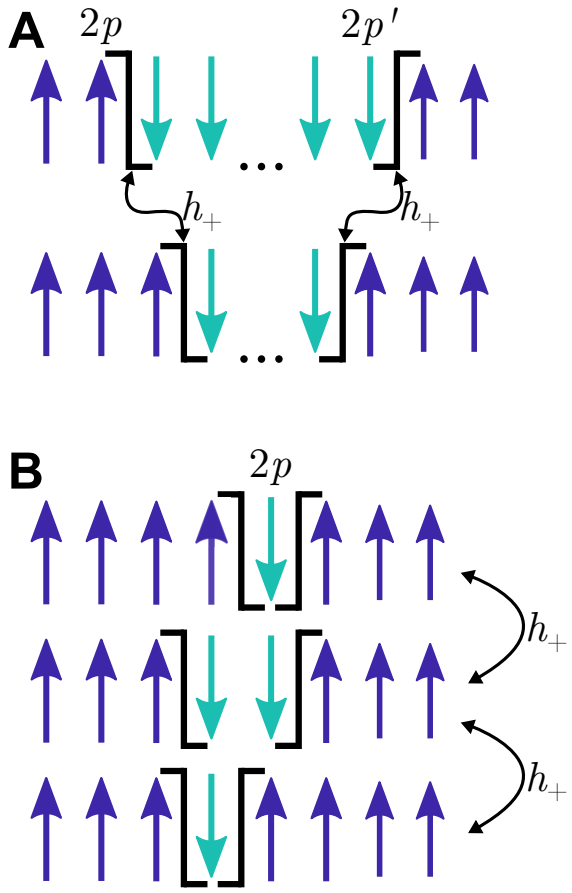

Figure 6.3: Soliton hopping in the localized limit. A) In the case of well separated solitons, they can hop independently, with each soliton hopping between two sites with matrix element h_+. B) When solitons are in adjacent unit cells, hopping is constrained by hard-core repulsion between solitons.

h_+ is interchanged, leading to symmetric / antisymmetric eigenstates localized within a single unit cell p,

$$|p\rangle_R^{\pm} \equiv \frac{1}{\sqrt{2}} \left(|2p\rangle_R \pm |2p+1\rangle_R \right), \text{ with } \omega_{\pm} = \frac{J}{2} \pm h_+. \tag{6.47}$$

Making use of these observations, the localized two-soliton eigenstates can then be constructed by considering a left soliton confined to hop between sites $2p-1$ and $2p$, and a right soliton confined to hop between sites $2p'$ and $2p'+1$. For $p' > p$, the solitons do not interact, and the eigenstates are

$$|p\rangle_L^- \otimes |p'\rangle_R^-, \text{ with energy } \omega_{--} = J - 2h_+, \tag{6.48}$$

$$\frac{1}{\sqrt{2}} \left[|p\rangle_L^+ \otimes |p'\rangle_R^- \pm |p\rangle_L^- \otimes |p'\rangle_R^+ \right], \text{ with } \omega_{+-} = J, \tag{6.49}$$

$$|p\rangle_L^+ \otimes |p'\rangle_R^+, \text{ with } \omega_{++} = J + 2h_+. \tag{6.50}$$

The eigenvalue $\omega_{+-} = J$ is doubly degenerate, and the eigenstates have been chosen to be symmetric / antisymmetric under inversion. The delocalized eigenstates with well-defined centre-of-mass momentum k are then

$$|n,k\rangle^{\pm} = \frac{1}{\sqrt{N}} \sum_{\text{cells},p} e^{ikc(2p+n)/2} |p\rangle_L^{\pm} \otimes |p+n\rangle_R^{\pm},$$
$$|n,k\rangle_{\pm}^{0} = \frac{1}{\sqrt{2N}} \sum_{\text{cells},p} e^{ikc(2p+n)/2} \left(|p\rangle_L^{+} \otimes |p+n\rangle_R^{-} \pm |p\rangle_L^{-} \otimes |p+n\rangle_R^{+} \right), \tag{6.51}$$

where N is the number of unit cells, and $n \geq 1$. These eigenstates correspond to the three two-soliton continua arising from the different pairing of bonding / anti-bonding orbitals. Note that in the localized limit considered here, the bands at energies $J \pm 2h_+$ and J are highly degenerate and flat; this is a reflection of the free index n which represents the relative coordinate between the left and right solitons.

If instead the left soliton is placed on sites $2p-1$ and $2p$, and the right soliton on $2p'$ and $2p'+1$ with $p = p'$, the hopping of the solitons is now constrained by the hard-core repulsion, see Fig. 6.3B. In this case, the eigenstates can be obtained by diagonalizing a 3×3 matrix acting on the three allowed configurations, yielding

$$|\varepsilon_{\pm}, p\rangle = \frac{1}{2} \left(|2p-1, 2p\rangle + |2p, 2p+1\rangle \pm \sqrt{2} |2p-1, 2p+1\rangle \right), \tag{6.52}$$
$$|\varepsilon_0, p\rangle = \frac{1}{\sqrt{2}} \left(|2p-1, 2p\rangle - |2p, 2p+1\rangle \right), \tag{6.53}$$

with energies $\varepsilon_{\pm} = J \pm \sqrt{2} h_+$ and $\varepsilon_0 = J$. The corresponding momentum eigenstates form non-degenerate flat bands (Fig. 6.4A) given by

$$|\varepsilon_\alpha, k\rangle = \frac{1}{\sqrt{N}} \sum_{\text{cells},p} e^{ikpc} |\varepsilon_\alpha, p\rangle, \text{ for } \alpha = \pm, 0. \tag{6.54}$$

These states are the origin of the ε bound states found through the numerical solution of the two-soliton Schrödinger equation in Sec. 6.4.3.

The effect of a weak symmetric exchange λ_S is now considered, while $h_- = 0$ remains fixed. As discussed in Sec. 6.4.2, this term only affects pairs of solitons when they are on nearest-neighbour sites, in which case it acts by shifting their centre-of-mass coordinate. Therefore, the three continua (6.51) are not affected, as these have solitons residing in different unit cells. In contrast, the symmetric

exchange acts non-trivially on the bound states (6.54), inducing an energy shift calculated perturbatively as

$$\varepsilon_\alpha \longrightarrow \varepsilon_\alpha(k) \approx \varepsilon_\alpha + \langle \varepsilon_\alpha, k | \, V_S \, | \varepsilon_\alpha, k \rangle, \tag{6.55}$$

yielding dispersive bands

$$\begin{aligned} \varepsilon_\pm(k) &= J \pm \sqrt{2} h_+ - \frac{J\lambda_S}{4} \left(1 + \cos kc\right), \\ \varepsilon_0(k) &= J + \frac{J\lambda_S}{2} \left(1 + \cos kc\right). \end{aligned} \tag{6.56}$$

The full spectrum in the localized limit $h_- = 0$, with weak symmetric exchange λ_S is illustrated in Fig. 6.4B, showing the three highly degenerate flat continua, and the three dispersive ε bound states, which become delocalized by λ_S. Note that in $CoNb_2O_6$, λ_S is large enough that the dispersion causes the ε_0 and ε_+ bands to cross, leading to band inversion. This effect is discussed quantitatively in Sec. 6.5.3 and illustrated in Fig. 6.4C. The band inversion further suppresses the dispersion of the top mode, as well as mixing the character of the top two bands.

6.5.2 Effects of weak delocalizing hopping h_-

As shown above, the localized limit $h_- = 0$ provides remarkable insight into the structure of the two-soliton spectrum obtained near to this limit. A more detailed understanding of the evolution of the spectrum with decreasing transverse field can be gained by perturbatively considering the effect of a weak delocalizing hopping term h_-. The first important effect of $h_- \neq 0$ is to lift the high degeneracy of the three continua and broaden these bands. Secondly, a finite h_- can mix the ε bound states constructed in the previous section with the continua in k regions where they overlap in energy.

The former effect is explored first, by focusing on the continua, and applying degenerate perturbation theory within each band separately. Note that for weak h_- and λ_S, the bottom and top bands remain well separated from the ε bound states. Assuming also $\lambda_S \gg h_-$, the middle continuum overlaps with the middle bound state only in the vicinity of $k = \pi/c$, see Fig. 6.4D. Therefore, the present

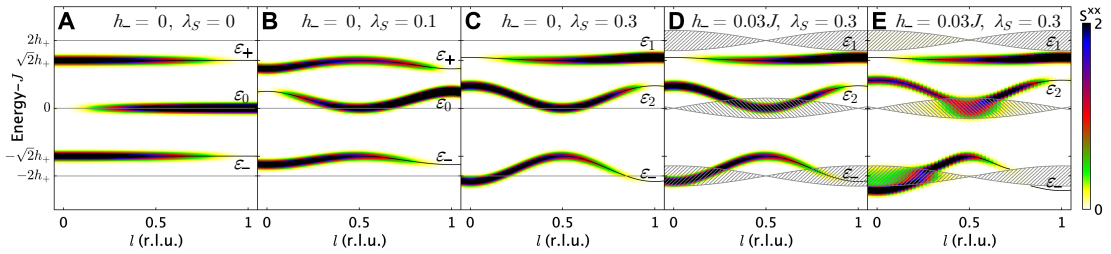

Figure 6.4: Dispersions and intensities as a function of wavevector and energy at different stages of perturbation away from the purely localized limit. The x-axis is momentum in reciprocal lattice units, $l = kc/(2\pi)$, vertical axis is energy relative to J. In each panel, colour indicates S^{xx}, as defined in (6.1) and further normalized by the total number of sites, on a linear scale indicated by the colourbar; black lines represent ε bound states while grey hatched patches represent continua. The calculated intensities have been convolved with a Gaussian of FWHM $0.033J$ and are shown in absolute units of $1/J$. In all panels, $h_+ = 0.2J$. In A-D) the calculation uses the perturbative regime of Sec. 6.5. A) Bound states and continua are both dispersionless for $h_- = 0$ and $\lambda_S = 0$. B) For finite λ_S, bound states become dispersive but continua remain flat and highly degenerate. C) Band inversion occurs between the top two bound states ε_+ and ε_0 for $J\lambda_S > 2\sqrt{2}h_+/3$ (see Sec. 6.5.3), resulting in modes labelled $\varepsilon_{1,2}$, such that ε_1 inherits the structure of the state ε_0 close to $l = 0$ and $l = 1$ while retaining the character of ε_+ elsewhere, with ε_2 showing the opposite behavior. This is reflected by the change in intensity distribution from B to C near $l = 0, 1$. D) Continua become dispersive for finite h_-. E) Same as D, but calculated using the full two-soliton model in Sec. 6.4, which predicts hybridization between the lowest two bound states, ε_2 and ε_-, and the continua they overlap.

treatment of neglecting the hybridization between the continua and the ε bound states is justified in the limit of weak couplings $h_+ \gg \lambda_S \gg h_-$, apart from the case of the middle band in the vicinity of $k = \pi/c$. While the experimental parameters lie outside of this well controlled region, it will be demonstrated below that a first order perturbative expansion nonetheless grants valuable insight into the evolution of the INS spectra for the whole range of applied transverse fields.

Denoting the hopping term by V_{h_-}, the matrix elements between the single-soliton eigenstates of the localized limit are found to be

$$ {}^{\pm}_{\alpha}\langle p'|V_{h_-}|p\rangle^{\pm}_{\alpha} = \pm\frac{h_-}{2}\left(\delta_{p',p+1} + \delta_{p',p-1}\right), \quad \alpha = L, R. \tag{6.57} $$

The energy shifts of the three continua can be evaluated up to first order in perturbation theory by considering the matrix elements of V_{h_-} between the two-soliton eigenstates of the localized limit (6.51) within each band separately. Using the

relations (6.57), the following expressions are obtained for the top and bottom bands:

$$ {}^{\pm}\langle n', k'|V_{h_-}|n, k\rangle^{\pm} = \pm\delta_{k,k'}\, h_- \cos\left(\frac{kc}{2}\right)(\delta_{n,n'+1} + \delta_{n,n'-1})\,. \tag{6.58} $$

For a fixed centre-of-mass momentum k, this equation corresponds to an effective nearest-neighbour hopping Hamiltonian for the relative coordinate n, with hopping amplitude $\pm h_- \cos(kc/2)$, subject to the hard-core constraint $n > 0$. Therefore, for the bottom and top bands, the spectrum

$$ \omega_{\sigma\sigma} = J + 2\sigma\left(h_+ + h_- \cos\left(\frac{kc}{2}\right)\cos\left(\frac{qc}{2}\right)\right), \quad \sigma = \pm 1, \tag{6.59} $$

is found, with unnormalized eigenstates

$$ |q, k\rangle^{\pm} \sim \sum_{\substack{\text{cell separation,}\\ n>0}} \sin\left(\frac{qnc}{2}\right)|n, k\rangle^{\pm}. \tag{6.60} $$

Here, k is the total momentum of the soliton pair and q is the relative momentum of the two solitons, and the factor $\sin(qnc/2)$ reflects hard-core repulsion which enforces $n > 0$. Thus, the weak hopping h_- broadens the bands, most strongly around $k = 0$, but the high degeneracy still persists at $k = \pi/c$, see Fig. 6.4D.

Turning now to the middle continuum, four types of matrix elements between the two-soliton states $|n, k\rangle^0_{\pm}$ must be calculated. The expressions

$$ \begin{aligned} {}^0_-\langle n', k'|V_{h_-}|n, k\rangle^0_+ &= {}^0_+\langle n', k'|V_{h_-}|n, k\rangle^0_- = \delta_{k,k'}\, i\, h_- \sin\left(\frac{kc}{2}\right)(\delta_{n',n+1} - \delta_{n',n-1})\,, \\ {}^0_-\langle n', k'|V_{h_-}|n, k\rangle^0_- &= {}^0_+\langle n', k'|V_{h_-}|n, k\rangle^0_+ = 0 \end{aligned} \tag{6.61} $$

are obtained. The broadening of this band can now be calculated by diagonalizing this matrix within a given total momentum sector k. The eigenstates in the middle band are found to remain at least twofold degenerate everywhere, yielding the spectrum

$$ \omega_{+-} = J - 2h_- \sin\left(\frac{kc}{2}\right)\sin\left(\frac{qc}{2}\right), \tag{6.62} $$

with unnormalized eigenstates

$$ \begin{aligned} |q, k\rangle^0_1 &\sim \sum_{\substack{\text{cell separation,}\\ n>0}} \left(e^{iqcn/2} - e^{-i(qc/2+\pi)n}\right)|n, k\rangle^0_{\xi(n)}, \\ |q, k\rangle^0_2 &\sim \sum_{\substack{\text{cell separation,}\\ n>0}} \left(e^{iqcn/2} - e^{-i(qc/2+\pi)n}\right)|n, k\rangle^0_{\xi(n+1)}, \end{aligned} \tag{6.63} $$

with $\xi(n) = \pm$ for n even/odd, and q again standing for the relative momentum. Thus, the middle band remains highly degenerate around $k = 0$, but it is broadened away from this point, most strongly around $k = \pi/c$.

Note that these dispersions of the continua can be understood based on the single-soliton spectrum as given in (6.21). In the limit of small h_-, (6.21) becomes

$$\omega_\pm = \frac{J}{2} \pm (h_+ + h_- \cos kc). \tag{6.64}$$

The three continua constructed above correspond to the three different types of soliton pairs. Denoting the individual solitons' momenta by k_1 and k_2, the energies

$$\begin{aligned}
\omega_{++} =& J + 2h_+ + h_-(\cos k_1 c + \cos k_2 c) = J + 2h_+ + 2h_- \cos\left(\frac{kc}{2}\right)\cos\left(\frac{qc}{2}\right), \\
\omega_{--} =& J - 2h_+ - h_-(\cos k_1 c + \cos k_2 c) = J - 2h_+ - 2h_- \cos\left(\frac{kc}{2}\right)\cos\left(\frac{qc}{2}\right), \\
\omega_{+-} =& J + h_-(\cos k_1 c - \cos k_2 c) = J - 2h_- \sin\left(\frac{kc}{2}\right)\sin\left(\frac{qc}{2}\right),
\end{aligned} \tag{6.65}$$

are obtained with total wavevector $k = k_1 + k_2$, and relative momentum $q = k_1 - k_2$, in accordance with the expressions derived above.

The second important effect of the hopping h_- is to mix the ε bound states with the continua where they overlap in energy. In these regions, the originally bound soliton pair can become delocalized, broadening out the INS signal, as shown in Fig. 6.4E.

6.5.3 Bound state inversion and matrix elements of $\mathcal{H}_2$ in the localized limit

The unperturbed bound states and their energies were given in (6.54). In the following, the effects of various other terms in the Hamiltonian in (6.4) to (6.6) are considered, starting with the second term in $\mathcal{H}_1$. Consider the matrix elements between the two highest energy modes ($|\varepsilon_+, k\rangle$ and $|\varepsilon_0, k\rangle$) for the perturbation

$$V_S = \frac{-J\lambda_S}{2} \sum_{\text{sites},j} S_j^+ S_{j+1}^- + S_j^- S_{j+1}^+. \tag{6.66}$$

As discussed above, this perturbation allows single spin flips to hop by one site. The diagonal matrix elements are

$$\begin{aligned}\langle\varepsilon_+,k|V_S|\varepsilon_+,k'\rangle =& \frac{-J\lambda_S}{4}(1+\cos kc)\,\delta_{k,k'}\\ \langle\varepsilon_0,k|V_S|\varepsilon_0,k'\rangle =& \frac{+J\lambda_S}{2}(1+\cos kc)\,\delta_{k,k'},\end{aligned} \tag{6.67}$$

as given in Sec. 6.5.1. Within the degenerate subspace, the off-diagonal matrix elements are

$$\langle\varepsilon_0,k|V_S|\varepsilon_+,k'\rangle = \frac{iJ\lambda_S}{2\sqrt{2}}\sin(kc)\,\delta_{k,k'} \tag{6.68}$$

and Hermitian conjugate. Eigenvalues and eigenvectors are then obtained by direct diagonalization (i.e., by diagonalizing this 2×2 matrix using the standard quadratic formula), with the dynamical correlations S^{xx} obtained from the eigenvectors as will be described in Sec. 6.5.4. The resulting modes are termed ε_1 and ε_2.

The matrix elements of the next-nearest-neighbour terms in $\mathcal{H}_2$ are also derived. Consistent with the considerations above, only diagonal matrix elements between bound states of the same type are kept, as well as the off-diagonal matrix elements between the middle and top modes ε_0 and ε_+, which show a strong mixing at the experimental parameters. The effect of the perturbation $V_{\rm AF}$, (6.41), is to lower the energy of all states relative to the fully aligned (ground) state. However, as discussed in Sec. 6.4.2, this energy shift is different for states with a single spin flip compared to states with at least two spin flips, corresponding to two and four satisfied antiferromagnetic bonds, respectively. This leads to matrix elements

$$\begin{aligned}\langle\varepsilon_+,k|V_{\rm AF}|\varepsilon_+,k'\rangle = \langle\varepsilon_-,k|V_{\rm AF}|\varepsilon_-,k'\rangle =& -\frac{3}{2}J\lambda_{\rm AF}\delta_{k,k'}\\ \langle\varepsilon_0,k|V_{\rm AF}|\varepsilon_0,k'\rangle =& -J\lambda_{\rm AF}\delta_{k,k'}\\ \langle\varepsilon_0,k|V_{\rm AF}|\varepsilon_+,k'\rangle =& \,0.\end{aligned} \tag{6.69}$$

This perturbation also shifts the energies of all the continua by $-2J\lambda_{\rm AF}$.

The effect of the perturbation $V_{\rm AF}^{xy}$, (6.38), is to hop single spin flips by two sites. This leads to matrix elements

$$\begin{aligned}\langle\varepsilon_+,k|V_{\rm AF}^{xy}|\varepsilon_+,k'\rangle = \langle\varepsilon_-,k|V_{\rm AF}^{xy}|\varepsilon_-,k'\rangle =& \frac{J\lambda_{\rm AF}^{xy}}{2}\cos(kc)\delta_{k,k'}\\ \langle\varepsilon_0,k|V_{\rm AF}^{xy}|\varepsilon_0,k'\rangle =& J\lambda_{\rm AF}^{xy}\cos(kc)\delta_{k,k'}\\ \langle\varepsilon_0,k|V_{\rm AF}^{xy}|\varepsilon_+,k'\rangle =& \,0.\end{aligned} \tag{6.70}$$

To first order, this perturbation vanishes when acting on the continua. However, it mixes the continua with the bound states.

The interchain mean field term, $\mathcal{H}_{\rm MF}$, is

$$V_z = -h_z \sum_{\text{sites},j} S_j^z \tag{6.71}$$

under the approximation that $\langle \boldsymbol{S}\rangle = (0,0,1/2)$. The effect of this term on the bound states is determined by the matrix elements

$$\begin{aligned}\langle\varepsilon_+,k|V_z|\varepsilon_+,k'\rangle = \langle\varepsilon_-,k|V_z|\varepsilon_-,k'\rangle =& \frac{3}{2}h_z\delta_{k,k'}\\ \langle\varepsilon_0,k|V_z|\varepsilon_0,k'\rangle =& h_z\delta_{k,k'}\\ \langle\varepsilon_0,k|V_z|\varepsilon_+,k'\rangle =& \,0.\end{aligned} \tag{6.72}$$

The effect of this term on the continua is to confine the soliton pairs into a series of bound states; this effect cannot be captured within the current picture.

Finally note that the first term in $\mathcal{H}_2$, V_A, (6.35), vanishes when projected to the subspace of bound states, since this term causes solitons to hop by two sites at a time. To understand the effect of this term on the continua, note that V_A, a hopping term to a neighbouring unit cell, shifts the single soliton dispersion relations as

$$\omega_\pm \longrightarrow \omega_\pm + J\lambda_A\cos(kc). \tag{6.73}$$

In contrast to the effect of the hopping h_-, V_A induces the same shift in the energies of both bonding and antibonding orbitals. As a result, this perturbation leads to the same energy change for the three continua,

$$\omega_{\sigma,\sigma'} \longrightarrow \omega_{\sigma,\sigma'} + J\lambda_A\left[\cos(k_1c)+\cos(k_2c)\right] = \omega_{\sigma,\sigma'} + J\lambda_A\cos\left(\frac{kc}{2}\right)\cos\left(\frac{qc}{2}\right), \tag{6.74}$$

for $\sigma, \sigma' = \pm$, with total and relative momenta given by $k = k_1 + k_2$ and $q = k_1 - k_2$, respectively.

Alternatively, these spectra can be obtained by applying first order perturbation theory around the localized limit, similarly to the analysis of the hopping h_- presented in Sec. 6.5.2. To this end, the effect of V_A on the states $|n,k\rangle$ constructed in Sec. 6.5.2 is evaluated. The expressions

$$ {}^{\pm}\langle n',k'|V_A|n,k\rangle^{\pm} =^0_{\pm} \langle n',k'|V_A|n,k\rangle^0_{\pm} = J\lambda_A \cos\left(\frac{kc}{2}\right)\left(\delta_{n',n+1}+\delta_{n',n-1}\right)\delta_{k,k'}, \tag{6.75} $$

are found, corresponding to an effective nearest-neighbour hopping Hamiltonian for the relative coordinate n, with hopping amplitude $J\lambda_A\cos(kc/2)$, subject to the hard-core constraint $n > 0$. For the top and bottom continua, the hopping amplitude due to V_{h_-} is also real, so the $|q,k\rangle^{\pm}$ states constructed in Sec. 6.5.2 are also eigenstates of V_A and the change in the energies is

$$ \frac{{}^{\pm}\langle q,k|V_A|q,k\rangle^{\pm}}{{}^{\pm}\langle q,k|q,k\rangle^{\pm}} = 2J\lambda_A\cos\left(\frac{kc}{2}\right)\cos\left(\frac{qc}{2}\right). $$

For the middle continuum, consider the effect of $V_{h_-}+V_A$ on the plane wave

$$ \sum_n e^{iqcn/2}(|n,k\rangle^0_+ + |n,k\rangle^0_-). $$

It is found that the perturbation corresponds to an effective nearest-neighbour hopping Hamiltonian for the relative coordinate n, with complex hopping amplitude $t = J\lambda_A\cos(kc/2) + ih_-\sin(kc/2) = t' + it'' = |t|e^{i\varphi}$. This yields the dispersion

$$ \begin{aligned} \omega^A_{+-} =& J + 2|t|\cos\left(\frac{qc}{2}+\varphi\right) = J + 2t'\cos\left(\frac{qc}{2}\right) - 2t''\sin\left(\frac{qc}{2}\right) \\ =& J - 2h_-\sin\left(\frac{kc}{2}\right)\sin\left(\frac{qc}{2}\right) + 2J\lambda_A\cos\left(\frac{kc}{2}\right)\cos\left(\frac{qc}{2}\right). \end{aligned} \tag{6.76} $$

The eigenstates satisfying the hard-core repulsion boundary condition at $n = 0$ can be obtained by noting that the plane wave with relative momentum q is degenerate with the plane wave with relative momentum $-q - 4\varphi/c$. Mixing these plane waves leads to the unnormalized eigenstates satisfying the hard-core constraint,

$$ \sum_{\substack{\text{cell separation,}\\ n>0}} \left(e^{iqcn/2} - e^{-i(qc/2+2\varphi)n}\right)\left(|n,k\rangle^0_+ + |n,k\rangle^0_-\right). \tag{6.77} $$

For the plane wave

$$\sum_n e^{iqcn/2}(|n,k\rangle_+^0 - |n,k\rangle_-^0), \tag{6.78}$$

the effect of $V_{h_-} + V_A$ corresponds to an effective nearest-neighbour hopping Hamiltonian for the relative coordinate n, with complex hopping amplitude t^*, such that the argument above applies with $\varphi \to -\varphi$. Thus, the effect of the perturbation V_A is to add $2J\lambda_A \cos(kc/2)\cos(qc/2)$ to the energies of all continua, as anticipated based on the single soliton dispersion relation. Also note that the argument above yields the following two degenerate eigenstates in the presence of V_{h_-} but without V_A, i.e. for $\varphi = \pi/2$,

$$\sum_{n>0}\left(e^{icq_\pm n/2} - e^{-i(cq_\pm/2+\pi)n}\right)\left(|n,k\rangle_+^0 \pm |n,k\rangle_-^0\right), \tag{6.79}$$

with $q_+ - q_- = \pi$. The eigenstates constructed in Sec. 6.5.2 are the symmetric / antisymmetric combinations of these eigenstates.

For $\lambda_A < 0$ and $h_- > 0$ such as is found experimentally, the perturbation V_A leads the top continuum to narrow and the bottom continuum to broaden, and the middle continuum to broaden around what would otherwise be the nodes. The plots in the right-most column of Fig. 6.1 include the effects of all terms in $\mathcal{H}_1$ and $\mathcal{H}_2$, but not $\mathcal{H}_{\rm MF}$ since it is not possible to include the effects of this last term on the continua in this framework.

6.5.4 Comparison with INS data

This section concludes with a description of the INS intensity predicted by these perturbative arguments. In the localized limit $h_- = 0$, the continua (6.51) have no overlap with nearest-neighbour soliton pairs $|j, j+1\rangle$ so do not contribute to the overlap (6.45) and to the resulting INS spectrum. The ε bound states (6.54), on the other hand, have the property that

$$\langle \varepsilon_\pm, k|S^x(k)|\mathrm{GS}\rangle = -i\sqrt{N}\frac{e^{ikc/2}+1}{4}, \tag{6.80}$$

$$\langle \varepsilon_0, k|S^x(k)|\mathrm{GS}\rangle = -i\sqrt{N}\frac{e^{ikc/2}-1}{2\sqrt{2}}, \tag{6.81}$$

where N is the number of unit cells, which follows from comparing (6.54) to (6.32). Therefore, the different bound states contribute differently to the INS spectrum $S^{xx}(\boldsymbol{Q},\omega)$. This structure is inherited by the bound states away from the limit $h_- = 0$.

In the absence of band inversion ($J\lambda_S < 2\sqrt{2}h_+/3$), the three bound states can be labelled by $\varepsilon_{\pm,0}$, such that the bottom and top modes $\varepsilon_\pm$ yield strong signals in the vicinity of $l = 0$ and are suppressed near $l = 1$ [note that $l = kc/(2\pi)$], whereas the middle band ε_0 behaves in the opposite way, see Fig. 6.4B. If λ_S is large enough for band inversion to occur, the top and middle bands acquire new labels $\varepsilon_{1,2}$, with ε_1 retaining the structure of ε_+ around $l = 0.5$ but inheriting the character of ε_0 around $l = 0$ and $l = 1$, and the reverse holding for ε_2. This results in a transfer of intensity between the top two bound states in the vicinity of $l = 0$ and $l = 1$. That is, the top mode is strong at $l = 1$ and weak at $l = 0$, and this is opposite to the middle band (Fig. 6.4C).

For small but finite h_-, the lowest ε bound state mode ε_-, which is strong around $l = 0$ in the limit $h_- = 0$, is pushed into the bottom continuum due to the strong broadening of the continuum with h_-. The mixing between these states leads to a signal smeared out across a larger range of energies. Similarly, the middle bound state mode mixes with the middle continuum around $l = 0.5$, smearing and eventually almost completely washing out the signal, see Fig. 6.4E. However, for λ_S large enough to lead to band inversion, the top mode does not hybridize with the continuum around $l = 1$, even for large h_-. This is because the upper continuum consists of states that are even under exchange of the even and odd sublattices, whereas the bound state ε_0 is odd, shedding light on the remarkably sharp INS spectrum of the top state around $l = 1$, even far from the localized limit $h_- = 0$. That is, the top mode ε_1 is sharp at all fields in Fig. 6.1 in the data (first column) and in the calculation (third column), even though there are regions where it overlaps with states originating from the top continuum, as illustrated in Fig. 6.1, last column.

This right-most column of Fig. 6.1 shows the INS intensity as calculated in this section, using the same parameters as for the middle two columns but with

no longitudinal mean field ($\mathcal{H}_{\rm MF} = 0$). Comparing Fig. 6.1T and P with Q and M respectively, it is seen that the above description is in remarkable qualitative agreement with the experimental results in large fields 2.5 T and 1.5 T. The agreement is especially good at 2.5 T (compare Figs. 6.1S and T), which is close to the localized limit. This agreement is strongly supportive of the model presented in this section, especially given that the model is relatively simple and completely analytically tractable. At lower fields, the agreement is expected to be less good as the solitons are now more delocalized and so a perturbative treatment around the localized limit is expected to be less quantitatively accurate. Nevertheless, several key trends are still reproduced: in particular, the top mode ε_1 is captured at all fields, the middle mode ε_2 is captured down to 1 T, and the lowest mode ε_- is captured down to 1.5 T.

The calculations in the right-most column of Fig. 6.1 include the effect of band inversion on the top two bound states, as well as the terms in $\mathcal{H}_2$, as explained in Sec. 6.5.3. Note that the full Hamiltonian also contains a z magnetic field, $\mathcal{H}_{\rm MF}$, changing the nature of the continua. This term introduces a linear confinement, splitting the continua into confinement bound states, which cannot be captured in this calculation. Despite these important effects, the tightly bound ε bound states remain relatively unaffected by the confinement, and the qualitative predictions for the INS spectra presented in this section still hold, see Sec. 6.4.3. Note that, at first order, a finite longitudinal mean field ($\mathcal{H}_{\rm MF}$) would be expected to increase the energies of all the ε-bound states, which would bring the calculated dispersions in the right-most column of Fig. 6.1 into closer agreement with the experimental data (left-most column).

6.6 Conclusions

The spectrum of the Ising chain material $CoNb_2O_6$ was investigated as a function of low to intermediate transverse field in the ordered phase using inelastic neutron scattering experiments. The measured spectrum was compared to predictions based on a recently refined Hamiltonian containing all relevant sub-leading terms beyond

the dominant Ising exchange and strong quantitative agreement was found. A physical picture of the excitations was then sought. It was found that by restricting the Hilbert space to the two-soliton subspace at first order in perturbation theory, very good agreement between the calculation and experiment was still achieved. The resulting spectrum in general has three continua and three bound states, of which only the bound states contribute significant weight to the inelastic neutron scattering intensity. In order to understand the character of the bound states, the localized limit was considered, in which the soliton hopping term on alternate bonds is zero. This occurs when the applied field matches the strength of the off-diagonal exchange. It was found that the bound states in this limit are of two solitons in adjacent unit cells, stabilized by hard-core repulsion leading to a change in delocalization energy. The bound states survive well away from the localized limit, suggesting that this picture has a broader domain of validity than might initially be expected. Using this physical picture, it has been possible to gain both a qualitative and a quantitative understanding of the low energy spectrum of $CoNb_2O_6$ in the low transverse field ordered phase.

7

Single crystal magnetization measurements of $CoNb_2O_6$

8

Excitation spectrum of the triangular lattice quantum XXZ antiferromagnet $Na_2BaCo(PO_4)_2$ in transverse field

In this chapter, the results of neutron scattering measurements on the triangular lattice Ising-like XXZ antiferromagnet material $Na_2BaCo(PO_4)_2$ are reported. The main focus of this chapter is inelastic neutron scattering measurements in transverse field. These observe that in high field, the excitations are sharp, resolution limited magnons which are well described by a minimal nearest-neighbour XXZ quantum spin Hamiltonian. A global fit is performed to data at several fields reported here, as well as to data previously reported in the literature for field applied along the easy-axis direction, in order to refine all the parameters in this minimal Hamiltonian independently and place upper bounds on any terms not included in this minimal model. In transverse fields below the transition to the paramagnetic phase there are two intermediate field phases, and significant continuum scattering is observed in both. The higher field phase evolves smoothly from the paramagnetic phase, with the magnons gradually broadening due to decay into the continuum as the field is decreased. At the lowest fields, no magnon-like features are observed at all and the spectrum is dominated by strong continuum scattering. The data are compared to the results of two-magnon scattering calculations in linear spinwave theory and it is

found that this semi-classical calculation cannot account for the strong continuum scattering observed experimentally, suggesting much stronger quantum fluctuations than can be captured by a spinwave approximation. In addition, neutron diffraction measurements in zero field are reported, which indicate that, as has previously been observed in the literature, this material orders magnetically at low temperatures with a propagation vector of (1/3, 1/3, 0.18), and refinement of the crystal structure using single crystal neutron diffraction at base temperature (0.036 K) supports a $P\bar{3}$ space group for this material.

Attribution note: *All the experiments described in this chapter were performed using single crystals grown by Ryutaro Okuma at the University of Oxford. The diffraction experiment was performed by an experimental team consisting of me, Daniel Antoniou and Radu Coldea (University of Oxford) and Pascal Manuel, Dmitry Khalyavin and Fabio Orlandi (ISIS Facility). For this experiment, I selected and prepared the sample, and was involved in the mounting and alignment. The data were converted from raw time-of-flight data to neutron scattering intensity in units of $S(\boldsymbol{Q})$ and the peaks were integrated by Radu Coldea using Mantid and custom-written code in Matlab. I performed the refinement, discussed in Sec. 8.3, with help from Pascal Manuel. This refinement started from a $P\bar{3}$ structure which had been refined by Ryutaro Okuma based on single crystal x-ray diffraction data before I became involved with the project. For the inelastic neutron scattering experiments, the crystals for the sample were co-aligned and mounted by Ryutaro Okuma. The experiments were performed by an experimental team consisting of me, Ryutaro Okuma and Radu Coldea (University of Oxford) and Ross Stewart and Christian Balz (ISIS Facility). I optimized the experimental configuration beforehand, processed the time-of-flight data into neutron scattering intensity in units of $S(\boldsymbol{Q},\omega)$ and have performed all the subsequent analysis. The analytical dispersion relations (8.14) and (8.17) were derived by Radu Coldea and Fig. 8.7B was made by Ryutaro Okuma.*

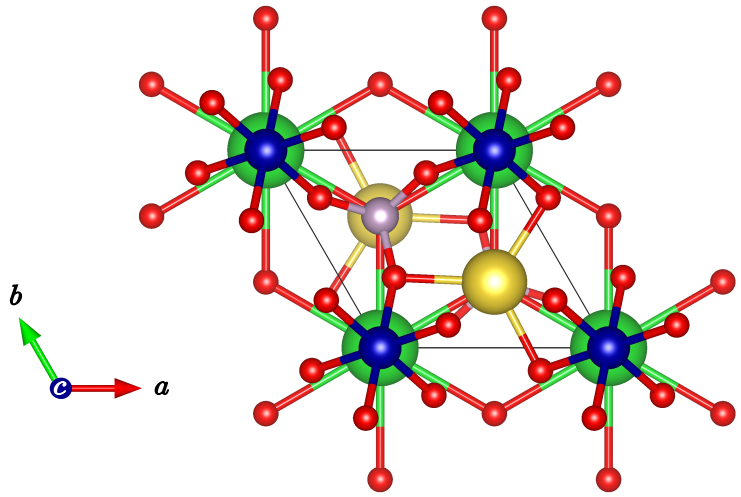

Figure 8.1: The crystal structure of $Na_2BaCo(PO_4)_2$, as refined in Sec. 8.3. Co^{2+} ions (blue) form a perfect triangular lattice, and are surrounded by oxygen octahedra (red). The layers of Co^{2+} alternate with layers of Ba^{2+} (green), and gaps within the layers are filled by Na^{+} (gold) and P^{5+} (pink). Figure made using VESTA [129].

8.1 Introduction

The triangular lattice antiferromagnet (TLAF) is the paradigmatic example of geometrical frustration, as discussed in Chapter 2. In the case of Heisenberg or XY-like (easy plane) spins, the true ground state in zero field is the semi-classical 120° ordered phase [20, 152, 153]. In the limit of pure Ising spins, however, a classical spin liquid is predicted [17]. For the intermediate Ising-like XXZ case, the ground state even in zero field has proved controversial [56, 57], and work is still ongoing to understand the spectrum and phase diagram [63, 154, 155], due in part to a lack of suitable experimental realizations until very recently.

The material $Na_2BaCo(PO_4)_2$ has recently been proposed to be well described by a nearest-neighbour XXZ Hamiltonian

$$\mathcal{H} = \sum_{\langle ij \rangle} J_{xy} \left(S_i^x S_j^x + S_i^y S_j^y \right) + J_z S_i^z S_j^z \tag{8.1}$$

with $J_z > 0$, $J_z/J_{xy} > 1$ and $\langle ij \rangle$ denoting a sum over nearest-neighbour bonds on the triangular lattice [64, 156, 157]. This material has a perfect triangular lattice, as shown in Fig. 8.1, with no chemical disorder [158]. Further, the energy scale of the interactions is small enough that the full phase diagram can be readily reached

within experimentally accessible magnetic fields [156]. In addition, the Co^{2+} ions are well described as effective spin-1/2 [6]. All these features make this material an ideal candidate for experimental investigation of the whole phase diagram of the quantum Ising-like triangular XXZ antiferromagnet. In comparison to another recently proposed easy-axis triangular lattice antiferromagnet, $K_2Co(SeO_3)_2$ [159, 160], the current material has a smaller value of J_z/J_{xy}, and the transitions to the field polarized phases happen at much more experimentally accessible fields, meaning that the Hamiltonian can be directly characterized [161].

While previous works on $Na_2BaCo(PO_4)_2$ have focussed on thermodynamic measurements across the phase diagram [156, 158, 162, 163] or on the spectrum in field along the out-of-plane (easy axis) direction [58, 157], this chapter focusses on the spectrum in field applied along an in-plane direction. It is found that above a critical field of about 1.6 T [157, 164], sharp magnons are observed, which are well described by an XXZ Hamiltonian as in (8.1). Through simultaneous fits to data observed at multiple fields along this direction, as well as to previously reported data for field along c [157], all the parameters of the XXZ Hamiltonian are independently refined, and an upper bound is placed on additional couplings beyond the minimal XXZ model. This thorough characterization of the Hamiltonian is crucial for comparisons of the lower field physics to theoretical models. As the field is decreased below the transition to the field polarized phase, a gradual increase is observed in the intensity of continuum scattering. Two distinct intermediate field magnetic phases are experimentally observed at the lowest temperature in this regime [64], see Fig. 8.2A. In the higher field phase, the spectrum is observed to evolve smoothly from the high field spectrum, with Brillouin zone folding occurring, and with the magnons becoming increasingly broadened as the field is decreased, but with the lowest energy magnons remaining sharp, as expected in a scenario of magnon decay [165]. These observations are in stark contrast to the sharp magnons observed throughout the Brillouin-zone in the easy-plane case [55], where magnons are thought to be prevented from decay by strong interactions with the continuum [54]. In the lowest field phase, no sharp modes are observed at all and

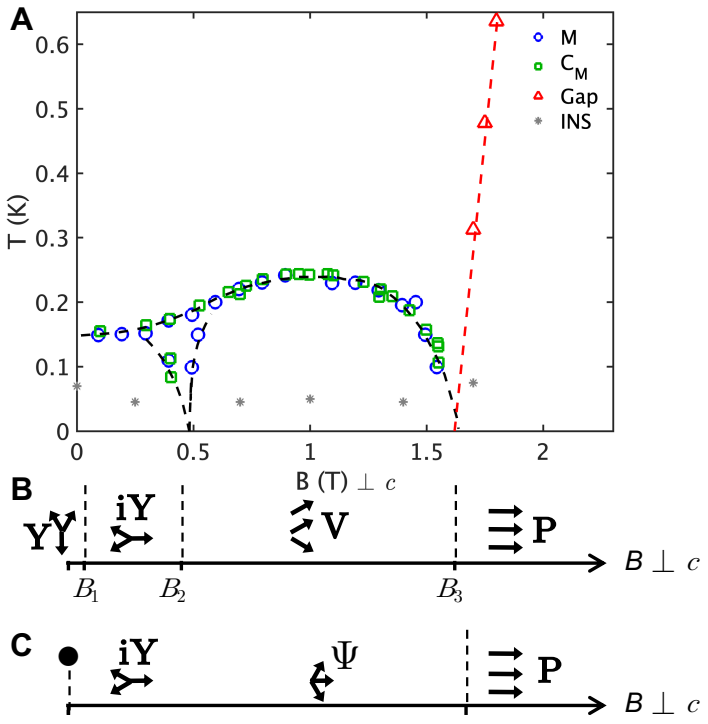

Figure 8.2: A) Phase diagram for $Na_2BaCo(PO_4)_2$ in an in-plane field. Heat capacity (green squares) and magnetization (blue open circles) data for the phase boundaries are taken from Ref. [157]. That data was taken with $B \parallel a^*$, which is symmetry equivalent to $B \parallel b^*$. Red triangles show the estimated magnon gap G, expected to close at the critical transition field B_C, just below 1.7 T, which was estimated from the observed minimum gap to excitations in the single orientation data. Dashed lines are guides to the eye. Grey stars indicate points at which the INS data in Fig. 8.10 were collected. B) The theoretically expected quantum phase diagram for field applied in the plane [63, 64], for the nearest-neighbour XXZ model (8.4). Black arrows show the three sublattice spin orientations in each phase. In zero field, the magnetic structure is a Y phase, with one spin pointing along the Ising axis and the other two have components along the Ising axis in the opposite direction to it. A small applied in-plane field induces an 'inverted Y' (iY) phase, in which one spin points along the field direction and the other two spins have one component opposite to the field direction, and the other component up the Ising axis for one spin and down for the other. This phase is not the same as the Y phase predicted in Heisenberg triangular antiferromagnets in small applied fields as in that case the unique spin points opposite to the field [19], and is instead related to the up-down-zero phase predicted in Ising triangular antiferromagnets [49]. Increasing field further leads to a V phase (V), in which two of the spins point parallel to each other, with the component of the spin along the Ising direction forming an up-up-down structure, with the up spins forming a honeycomb with a down spin in the centre of each hexagon. The highest field phase is the field polarized (paramagnetic, P) phase. C) The classical (mean-field) phase diagram for field applied in the plane. In zero field, the classical magnetic structure is highly degenerate (indicated by the • symbol) [57] but an infinitesimal field stabilises the iY phase. As the field is increased, the spins pointing away from the field gradually rotate to form a Ψ shaped structure with no phase transition up until the transition to the field polarized phase. Panels B and C are not drawn to scale.

only a broad continuum is seen, consistent with zero-field measurements reported in Refs. [58, 59]. The observed spectra are compared to the predictions of two-magnon calculations in linear spinwave theory and it is found that at all fields below the transition to the field polarized phase, the continuum spectral weight is too large to be explained semi-classically.

The rest of this chapter is organized as follows. Section 8.2 outlines the neutron scattering experiments, while Sec. 8.3 presents the results of neutron diffraction measurements in zero field and the refinement of the crystal structure. In Sec. 8.4, the results of inelastic neutron scattering (INS) measurements in the field polarized phase are reported, and a model Hamiltonian is refined based on these data. In Sec. 8.5, data taken in transverse field below the transition to the field polarized phase are reported, along with the results of linear spinwave theory calculations for this regime, and Sec. 8.6 contains the conclusions for this chapter.

8.2 Experimental details

Neutron diffraction measurements of the structural and magnetic Bragg peaks in zero field were made using the time-of-flight diffractometer WISH [85] at the ISIS facility. The sample was a 34.6 mg single crystal which had been filed down from a slightly larger crystal, see Fig. 8.3A, so that it would be a better approximation to a sphere for the purposes of absorption and extinction corrections. The sample was aligned with the b^* axis vertical such that the horizontal scattering plane was the $(2h, -h, l)$ plane of the trigonal unit cell and was cooled using a dilution refrigerator insert. The scattering was measured in three sample orientations rotated around the vertical axis, with the crystallographic c^*-direction at angles of 148°, 179° and -157° to the incident beam direction $\boldsymbol{k}_i$. In each orientation, the scattering was measured at both the base temperature of the dilution refrigerator (about 36 mK) and at 500 mK, well above the zero-field ordering temperature estimated around 148 mK [156] and the diffraction signal at this temperature was therefore used as a measurement of the non-magnetic background. The raw time-of-flight neutron data were converted to scattering intensities $S(\boldsymbol{Q})$ using MANTID [88]. The diffraction

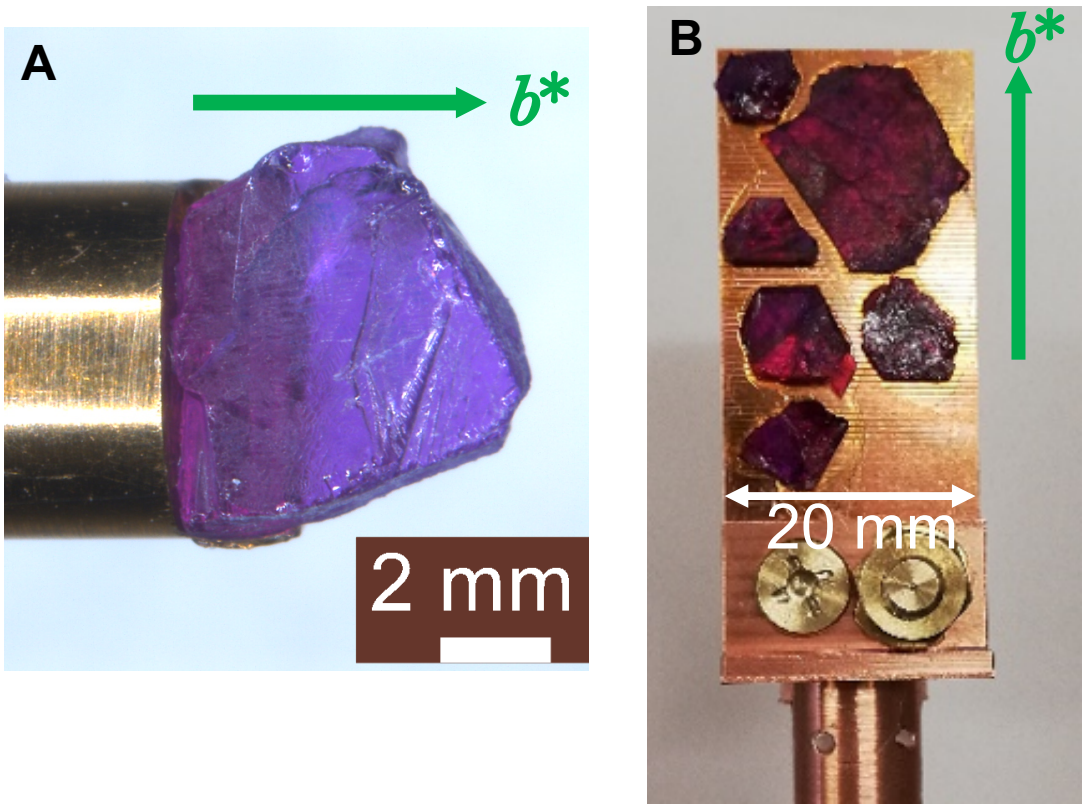

Figure 8.3: Samples of $Na_2BaCo(PO_4)_2$ used in the neutron scattering experiments. A) The sample used in the neutron diffraction experiment. The sample is shown on the mount used for preliminary x-ray diffraction screening, not the mount used for the neutron diffraction experiment. B) The sample used in the INS experiments. The sample consists of co-aligned crystals glued to three layers of copper sheets, of which only the front-most is visible. In both samples, the c^* axis is orthogonal to the large face of the crystals, i.e. orthogonal to the page.

intensities were normalized by the wavelength-dependent flux detected in a monitor, and then also normalized by a vanadium standard to account for detector efficiency, and corrected for the Lorentz factor to produce a three-dimensional data array of intensity as a function of (Q_x, Q_y, Q_z) which was used to extract the integrated intensities of the diffraction Bragg peaks.

Inelastic neutron scattering (INS) measurements of the magnetic excitation spectrum were performed on a sample of 19 co-aligned single crystals totalling 6.41 g, which were glued to oxygen-free copper sheets (see Fig. 8.3B). All crystals were mounted with the b^* axis vertically up and c^* normal to the vertical copper plates and the measured overall mosaicity was 3° (full width half maximum, FWHM). The

measurements were performed using the direct geometry time-of-flight spectrometer LET [84], also at the ISIS facility. A magnetic field up to 7 T was applied vertically along the crystallographic b^* direction, i.e., within the plane perpendicular to the easy axis of the spins, and such that the horizontal scattering plane was the crystallographic ac plane [reciprocal $(2h, -h, l)$ plane] of the trigonal unit cell. The incident beam came through the tunnel in the magnet wedges with the available range of scattering angles in the horizontal plane being $55° < 2\theta < 135°$; this made it possible to probe relatively high wavevector transfers with a high energy resolution given the low incident energies used. The sample was cooled using a dilution refrigerator insert and all data were collected below 80 mK, well below the zero-field ordering temperature of 148 mK [156], except for some data at 3.5 T in the high-field polarized phase (where the gap $G \approx 0.46$ meV ≈ 5.3 K), which were collected at temperatures < 165 mK, still cold enough to be in the low-temperature limit at this field. LET was operated to measure simultaneously the inelastic scattering of incident neutrons with energies of $E_i = 0.87$, 1.41 and 2.67 meV; the measured energy resolutions (FWHM) on the elastic line were 0.031(2), 0.057(3) and 0.142(3) meV, respectively. Multi-angle (Horace) scans were measured across two experiments, in order to obtain full four-dimensional data sets of the scattering intensity as a function of energy and momentum transfers. In the first experiment, measurements were taken at 0, 1.7, 3.5 and 7 T, while in the second, measurements were taken at 0.25, 0.7, 1, 1.4 and 3.5 T, with the repeated 3.5 T measurement used for comparison between the data sets and for background subtraction. For all fields, the sample was rotated about the vertical b^* axis through an angular range of 180° in steps of 2°. Each orientation was counted for 7 μAh of protons on target (at an average proton current of 40 μA) for the scans at 3.5, 1.7, 1.4, 1, 0.7 and 0.25 T, 10 μAh for the 0 T scan, 3 μAh for the 7 T scan, and 3.5 μAh for the second 3.5 T scan. Additional measurements to investigate the field evolution of the scattering near the point where the magnon gap is expected to close were collected between 3.5 and 1.55 T with a fixed sample orientation, with an angle of 3° between the incident beam direction and the crystallographic a-axis. For these,

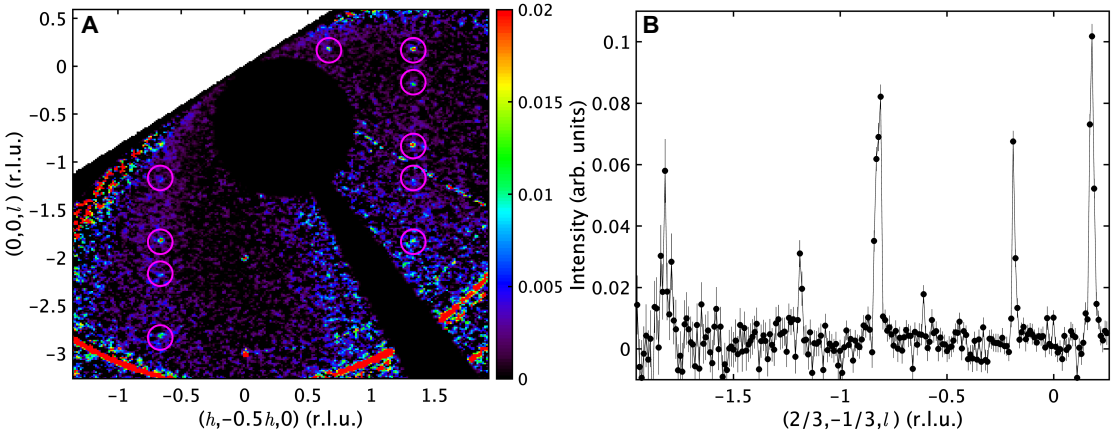

Figure 8.4: A) Diffraction data collected at the base temperature of 0.036 K in the first of the 3 crystal orientations probed. The higher temperature data has been subtracted off as background. The data have been corrected and normalized as described in Sec. 8.2 and averaged across a range $-0.15 < k < 0.15$ along the $(0\,k\,0)$ direction. Magnetic Bragg peaks are highlighted by circles. B) A cut through the data in (A) showing the sharp Bragg peaks along (2/3, -1/3, l). The data have been averaged across $1.31 < h < 1.36$ in the $(h, -0.5h, 0)$ direction and $-0.04 < k < 0.04$ in the $(0\,k\,0)$ direction. The observed sharp peaks correspond to magnetic Bragg peaks associated with two propagation vectors, $q_1 = (1/3, 1/3, +q_z)$ and $q_2 = (1/3, 1/3, -q_z)$ with $q_z = 0.18$.

an average counting time of 18 μAh was used. The raw time-of-flight neutron data were converted to scattering intensities $S(\boldsymbol{Q}, \omega)$ using MANTID [88]. It was found for the second experiment that in order for the energy of the incoherent elastic peak to remain centred at 0 to within better than 3, 5, and 5 μeV for E_i =0.87, 1.41 and 2.67 meV, respectively, as the sample was rotated, it was necessary to allow for an offset of 3 mm between the centre of the sample and the axis of rotation, which may be due to a small tilt in the sample rod. Taking into account this offset, the centre of the elastic line instead remained centred to within better than 0.5 μeV for all incident energies measured. The data were then analysed using the HORACE [90] and MSLICE [89] packages.

8.3 Diffraction

Diffraction data taken in zero field are shown in Fig. 8.4. The data shown are the difference between data taken at 36 mK and 500 mK, well below and above the ordering transition at 148 mK respectively [156]. Sharp peaks can be seen,

		This work ($P\bar{3}$)	This work ($P\bar{3}m$)	Ref. [166] ($P\bar{3}$)
T (K)		0.036	0.036	300
a (Å)		5.3	5.3	5.316830(5)
c (Å)		7.0	7.0	7.012398(16)
Na 2*d* (1/3 2/3 *z*)	*z*	0.8167(17)	0.8213 (17)	0.8203(3)
	B_{iso} (Å^2)	0	0	0.422(13)
Ba 1*b* (0 0 1/2)	B_{iso} (Å^2)	0	0	0.15(2)
Co 1*a* (0 0 0)	B_{iso} (Å^2)	0	18.8	0.182(13)
P 2*d* (1/3 2/3 z)	*z*	0.2607(11)	0.2712(12)	0.2583(2)
	B_{iso} (Å^2)	0	0	0.140(13)
O1 6*g* (*x y z*)	*x*	0.2406(18)	0.1765(18)	0.23137(16)
	y	0.8848(19)	0.8235(18)	0.87365(18)
	z	0.1833(7)	0.1850(16)	0.18036(13)
	B_{iso} (Å^2)	0	4.0(3)	0.364(13)
O2 2*d* (1/3 2/3 *z*)	*z*	0.4756(9)	0.4790(8)	0.47403(19)
	B_{iso} (Å^2)	0	0	0.28(2)

Table 8.1: Structural parameters refined in this work based on low temperature single crystal neutron diffraction compared to parameters from Ref. [166] based on room temperature powder neutron diffraction. The parameters in the first column, corresponding to a $P\bar{3}$ structure were used in Fig. 8.5A, while the parameters in the second column, corresponding to a $P\bar{3}m$ structure, were used in Fig. 8.5B.

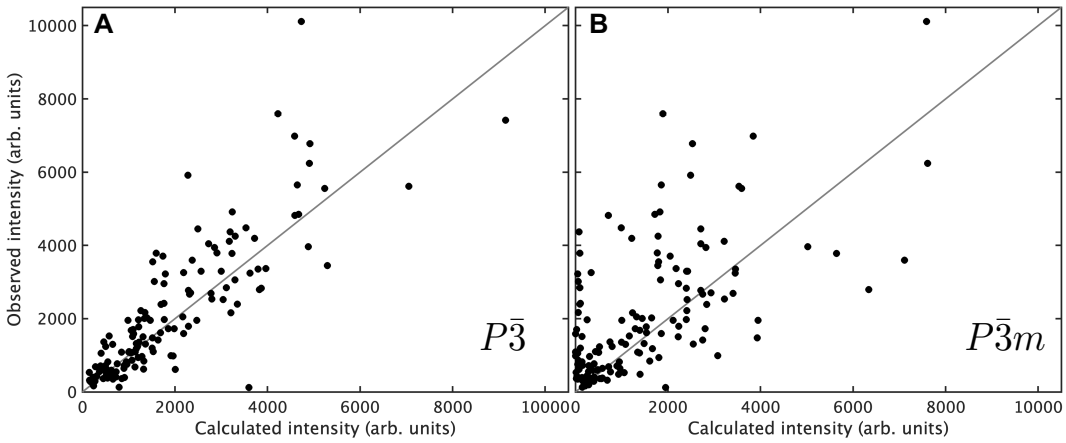

Figure 8.5: Comparisons between the observed intensities of Bragg peaks for $Na_2BaCo(PO_4)_2$ and calculated intensities using A) the parameters in the first column of Table 8.1, corresponding to a $P\bar{3}$ structure, B) the parameters in the second column of $Na_2BaCo(PO_4)_2$, corresponding to a $P\bar{3}m$ structure. In A, the calculation assumes two twins, whose volume fractions were also refined. The grey line in both panels is a guide to the eye indicating one-to-one agreement. The agreement in A is much better than in B.

corresponding to magnetic Bragg peaks with propagation vectors $(1/3, 1/3, \pm q_z)$, with $q_z \approx 0.18$, consistent with the data reported in Ref. [157].

In order to understand the magnetic structure, it is important first to refine the crystal structure. It was found that the agreement obtained between the observed and calculated intensities was poor if the refinement was done within the previously proposed $P\bar{3}m$ structure [158], see Fig. 8.5B. Much better agreement was found if it was assumed that the sample was instead composed of two twins of a $P\bar{3}$ structure. This structure differs from the $P\bar{3}m$ structure only by a rotation of the oxygen octahedra, which breaks the mirror planes orthogonal to the hexagonal a and b axes, with the two twins corresponding to opposite senses of rotation. As oxygen is a light element, this difference only produces subtle differences in x-ray diffraction data (although a difference can be seen in the refined anisotropic displacement parameters for the oxygens), but is much easier to detect in neutron diffraction data, which is much more sensitive to the oxygen positions. The parameters obtained from the structural refinement are shown in Table 8.1 and the quality of the agreement obtained using these parameters is shown in Fig. 8.5A. This refinement was carried out using JANA [93], and the isotropic displacement parameters B_{iso} were set to zero as they otherwise refined to unphysical negative values. The parameters obtained agree well with the $P\bar{3}$ structural parameters recently reported in Ref. [166], which are also listed for comparison in Table 8.1.

Note that as well as the $P\bar{3}$ structure accounting much better for the intensities of the structural peaks than the $P\bar{3}m$ structure, it is also not possible to account for the observed incommensurate magnetic propagation vector within a $P\bar{3}m$ crystal structure [167]. This will be discussed in more detail in Sec. 8.4.1. It is assumed that the peaks corresponding to propagation vector $(1/3, 1/3, q_z)$ are due to one of the structural twins, while the propagation vector $(1/3, 1/3, -q_z)$ is due to the other structural twin.

The presence of structural twins, each of which is likely to contain several magnetic domains corresponding to the incommensurate propagation vector, makes the process of refining the magnetic structure difficult. The (1/3,1/3) in-plane

propagation vector is consistent with the theoretically expected Y phase, but it is as yet unclear what the nature of the interlayer modulation is. Further work is needed to complete the analysis of this data.

8.4 Excitations in high transverse field

In the limit of high field along any direction, the excitations are expected to be sharp magnons. These are indeed observed at all fields above the transition field of about 1.6 T, as shown in Fig. 8.6.

8.4.1 Interlayer interactions

In order to verify the two-dimensional nature of the magnetic interactions, the dispersion of magnons in the direction perpendicular to the plane of the layers was measured; results are shown in Fig. 8.7.

Some assumptions can be made about the couplings between the layers based on the magnetic propagation vector observed in zero field as described in Sec. 8.3, $(1/3, 1/3, q_z)$ with $|q_z| = 0.18$. For a model in which the interactions are approximately Heisenberg, and assuming that the structure within each layer is a 120° structure, the classical mean field energy is, following Ref. [167],

$$\frac{E}{S^2} = -\frac{3}{2}J_1 + \left[J_2 - \frac{3}{2}(J_a + J_b)\right]\cos 2\pi q_z + \frac{3\sqrt{3}}{2}(J_a - J_b)\sin 2\pi q_z, \tag{8.2}$$

where J_1 is the nearest-neighbour in-plane exchange and $J_{2,a,b}$ are defined in Fig. 8.7A.[1] Differentiating with respect to q_z to find the minimum in energy implies that the magnetic propagation vector must satisfy [167]

$$\tan(2\pi q_z) = \frac{3\sqrt{3}(J_a - J_b)}{2J_2 - 3J_a - 3J_b}. \tag{8.3}$$

Note that in the limit $|J_a| \gg |J_{2,b}|$, the solution is $q_z = -1/6$, which is close to what is seen experimentally. This limit will be assumed for simplicity, as there is not enough data to distinguish between the different possibilities, but note that there is

[1] $J_{a,b}$ has been defined with a factor of 3 difference to Ref. [167], such that $J_{a,b}$ refer to the energy per bond.

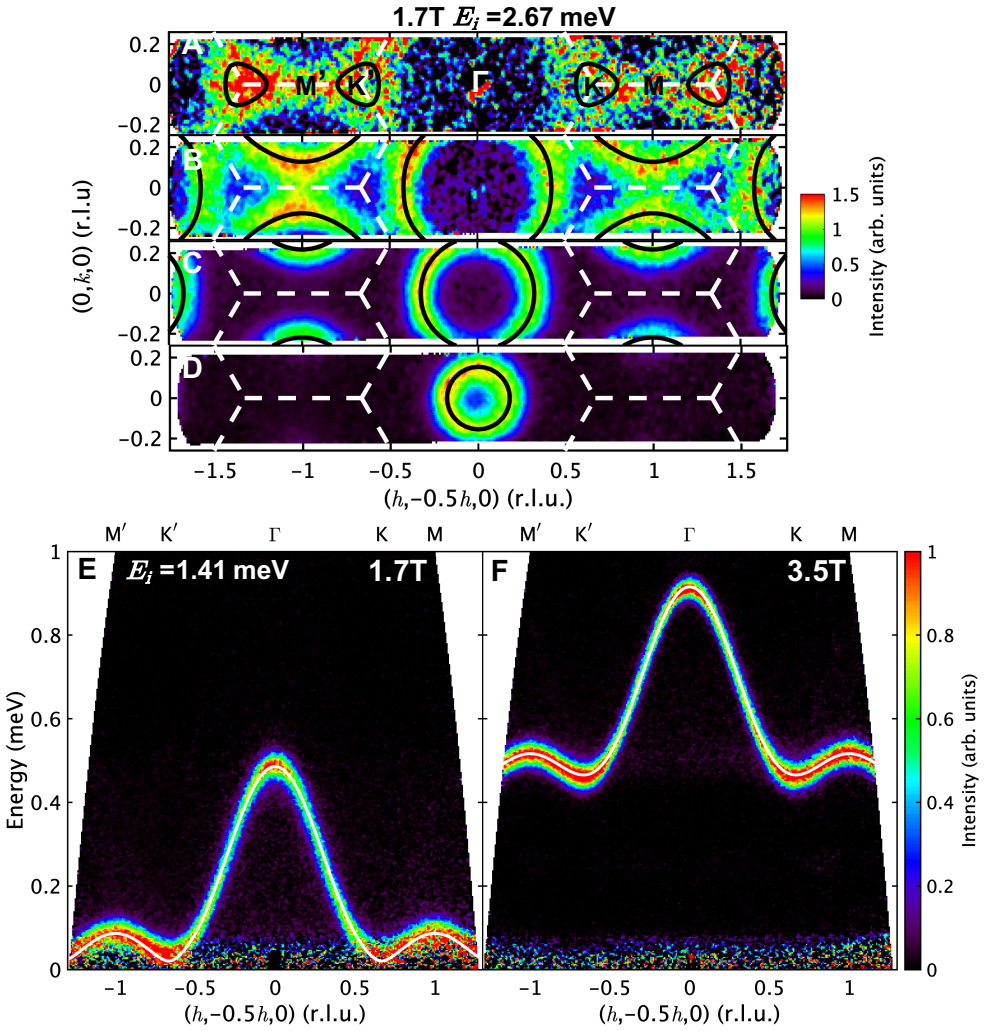

Figure 8.6: A-D) Constant energy slices through the Horace scan at 1.7 T. Slices correspond to energy transfers of 0.05, 0.15, 0.25 and 0.40 meV respectively, increasing from top to bottom. The two-dimensional nature of the dispersion can be clearly seen, as well as the 3-fold symmetry around the K points. Dashed white lines indicate boundaries of the two-dimensional Brillouin zones, while black contours are contours of the dispersion (8.6) using the parameters in Table 8.2. In A, high symmetry points of the two-dimensional Brillouin zone are indicated, showing the path used for the scans in E, F and in Figs. 8.10, 8.13 and 8.14. The data were averaged across a range ±0.025 meV relative to the nominal energy transfer and the whole range of the data in the (001) direction. The incident energy used was $E_i = 2.67$ meV. Colour indicates the neutron scattering intensity on an arbitrary scale. E, F) The spectrum seen along the (1,-0.5,0) direction [path indicated in A] in the quantum paramagnetic phase above the transition field B_c, at 1.7 T (E) and at 3.5 T (F), extracted from Horace scans with an incident energy $E_i = 1.41$ meV. In both cases, intensities were averaged in the range $-0.025 < k < 0.025$ in the (010) direction and across the full range of data in the (001) direction. Sharp, resolution limited magnons are seen in both cases. The white curves are linear spinwave theory fits as described in Sec. 8.4.2 using the parameters in Table 8.2. Colour indicates the neutron scattering intensity on an arbitrary scale [different to panels A-D]. In all panels, an estimate of the non-magnetic background has been subtracted off.

a whole family of other possible solutions. All of these, however, require $J_a \neq J_b$ to achieve an incommensurate propagation vector, which is only symmetry allowed in the $P\bar{3}$ structure refined in Sec. 8.3 and not in the previously assumed $P\bar{3}m$ structure [158], where the J_a and J_b exchange paths are symmetry equivalent via the mirror m.

In the present macroscopic size sample, both twins of the $P\bar{3}$ structure are present, related by swapping J_a and J_b. This means that for any dispersion present along the l direction, there will be two modes, one with minimum at $q_z \approx 1/6$ and the other at $q_z \approx -1/6$. The spectrum along the $(-2/3, 1/3, l)$ direction at 3.5 T is shown in Fig. 8.7A. It is not possible to resolve any clear modulation in the energy, either in the intensity map [Fig. 8.7A] or after extracting peak positions through taking cuts and doing fits to Gaussians (not shown). There is, however, some modulation in the linewidths beyond the experimental error bars, as shown in Fig. 8.7D. This is expected if there are two unresolvable modes, since they will cross at $l = 0, \pm 0.5$, as illustrated in Fig. 8.7C. Based on the variation in linewidth, and making the assumption that this is due to two modes dispersing due to only J_a, the value $J_a \approx 0.003$ meV is estimated, i.e. about 2.5% of the value of the nearest-neighbour Ising component J_z refined in Sec. 8.4.2. The linewidth calculated based on these assumptions, by fitting a single Gaussian peak to a sum of two Gaussians with energies corresponding to the dispersions in each twin, as given in Appendix C, is shown by the solid line in Fig. 8.7D. Calculations of the expected inelastic neutron scattering spectrum based on this model are shown in Fig. 8.7C. There is clear modulation in energy in the calculation which is not present in the data, suggesting that a more complex model perhaps involving non-zero values for J_2 and J_b might be needed. There is not, however, sufficient data to refine such a model, so this is considered beyond the scope of this work. This estimated value of J_a is therefore considered to be an upper bound on the size of the interlayer interactions.

Both because there is no visible modulation in the magnon energies due to interlayer couplings (neither at 3.5 T, nor at the other fields investigated in Horace scans), and because the estimated interlayer couplings are so much smaller than the nearest-neighbour couplings, their effect is neglected in the rest of this chapter.

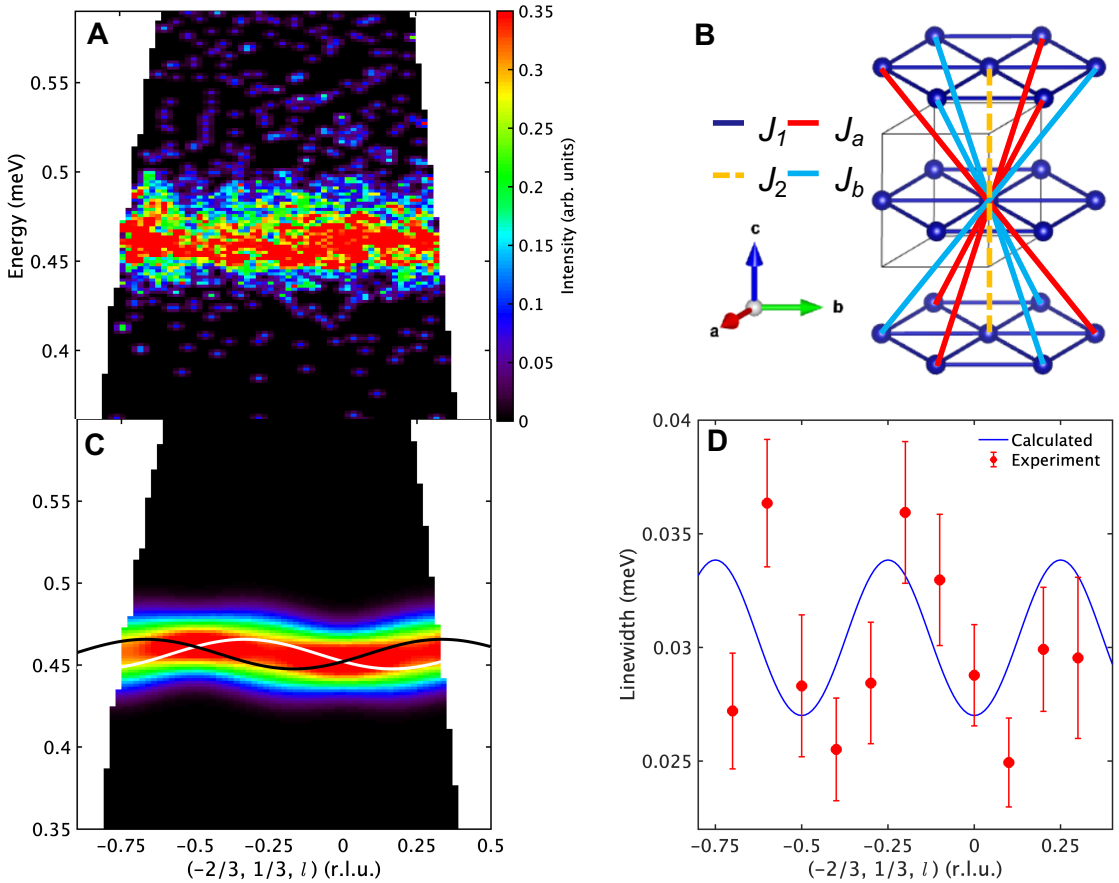

Figure 8.7: Interlayer dispersion effects. A) INS data taken at 3.5 T with $E_i = 0.87$ meV, showing the spectrum along the $(-2/3, 1/3, l)$ direction. The data have been averaged over a width of ± 0.025 r.l.u. along both the $(1, -1/2, 0)$ and (010) directions. B) Schematic diagram of the different interlayer exchange paths. The J_a (red) and J_b (light blue) paths are inequivalent in the $P\bar{3}$ structure refined in Sec. 8.3. C) Calculation in linear spinwave theory of the expected inelastic neutron scattering intensity, for the range of data shown in A, taking into account the two different structural $P\bar{3}$ twins, related by the m mirror, as well as the Co^{2+} magnetic form factor. The calculation takes $J_a = 0.003$ meV and $J_b = J_2 = 0$ and the linewidth for isolated magnons is set to 0.027 meV. The dispersions for the two twins are overplotted in white and black respectively. In A and C, colour indicates INS intensity on an arbitrary scale. D) Experimental and calculated line widths along this same direction. The experimental data points are extracted from fitting Gaussians to constant wavevector scans through the data in A. The calculation uses the same parameters as in C. The expressions for the dispersions and intensities in linear spinwave theory used in C and D are given in Appendix C.

The inelastic neutron scattering data are therefore averaged across the entire range in the $(00l)$ direction to improve counting statistics, and the dynamics are treated as fully two dimensional in all calculations.

8.4.2 Linear spinwave theory fits

In order to refine the parameters of the proposed XXZ Hamiltonian, fits were done to the magnon dispersion observed in the high-field polarized phase, simultaneously to the data reported here, for several in-plane fields, and to the data taken in field along c (reported in Ref. [157]). First, cuts were done through the data, to which Gaussian peak shapes were then fit, in order to extract several hundred dispersion points. Fits were then done in linear spinwave theory to the Hamiltonian

$$\mathcal{H} = \sum_{\langle ij \rangle} J_{xy} \left(S_i^x S_j^x + S_i^y S_j^y \right) + J_z S_i^z S_j^z - \mu_B \sum_i \left(g_c B_z S_i^z + g_{ab} B_y S_i^y \right) \tag{8.4}$$

where $\langle ij \rangle$ denotes nearest-neighbour bonds in the plane and x, y, z are along the (1,-0.5,0), (010) and (001) directions respectively. The magnon dispersions for this Hamiltonian in the field-polarized phase in linear spinwave theory are given by

$$\hbar\omega(\boldsymbol{Q}) = g_c \mu_B B_z - 3J_z + J_{xy}\gamma(\boldsymbol{Q}) \tag{8.5}$$

for field applied along the c direction and

$$\hbar\omega(\boldsymbol{Q}) = \sqrt{\mathcal{A}^2 - \mathcal{B}^2} \tag{8.6}$$

$$\mathcal{A} = g_{ab}\mu_B B_y - 3J_{xy} + \frac{J_z + J_{xy}}{2}\gamma(\boldsymbol{Q}) \tag{8.7}$$

$$\mathcal{B} = \frac{J_z - J_{xy}}{2}\gamma(\boldsymbol{Q}) \tag{8.8}$$

for field applied in the plane, where

$$\gamma(\boldsymbol{Q}) = \cos 2\pi h + \cos 2\pi k + \cos 2\pi(h + k), \tag{8.9}$$

and where $S = 1/2$ has been taken. Note that the dispersion (8.5) has the same functional form as for a pure Heisenberg model with $J = J_{xy}$, $g = (g_c \mu_B B_z - 3J_z + 3J_{xy}) / (g\mu_B B_z)$, so INS measurements at a single field along c cannot distinguish between the pure Heisenberg and the XXZ scenarios.

The fits were done simultaneously to the data taken at 3.5 and 7 T $\parallel b^*$ and 3.5 T $\parallel c$, the latter extracted from Ref. [157]. The data for 1.7 T $\parallel b^*$ were not included in these fits because 1.7 T is below the classical transition field of 1.72 T

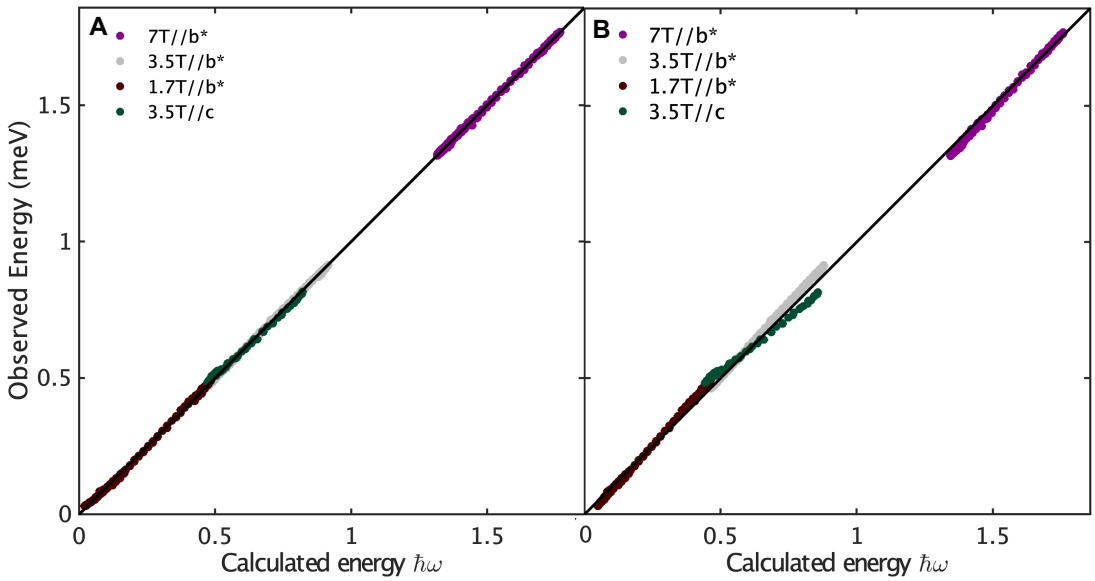

Figure 8.8: Observed energy vs calculated energy using different Hamiltonian models. A) The XXZ model (8.4) to (8.9) with the parameters of Table 8.2. B) The Heisenberg-Kitaev model (8.10) to (8.17) with best fit parameters in Table 8.3, using the same fitting procedure as for the XXZ model, as outlined in Sec. 8.4.2. The dispersion data points for 3.5 T $\parallel c$ were extracted by digitizing Fig. 4B in Ref. [157] using Ref. [168].

J_z	0.1225(10) meV
J_{xy}	0.0779(7) meV
g_c	4.716(7)
g_{ab}	4.200(7)
δB	0.041(4) T at $B = 1.7$ T $\parallel b^*$

Table 8.2: Hamiltonian parameters refined in Sec. 8.4.2, as defined in (8.4).

and so dispersion renormalization effects are expected to be important [139]. It was empirically found that the dispersion seen at 1.7 T could be approximately captured by fixing the Hamiltonian parameters to those obtained from the fits to high field data, and adding a variable effective field offset δB, i.e. the fitted Zeeman term in (8.4) was $-\mu_B \sum_i g_{ab}(B_y + \delta B) S_i^y$. The fitted parameters are shown in Table 8.2 and the obtained one-to-one agreement is shown in Fig. 8.8A. This good agreement is also illustrated by the agreement between the inelastic neutron scattering data and the overlaid white curves indicating the linear spinwave theory dispersions in Fig. 8.6.

It is also possible to use these data to test alternative parameterizations of the Hamiltonian. It has been proposed that rather than an XXZ Hamiltonian,

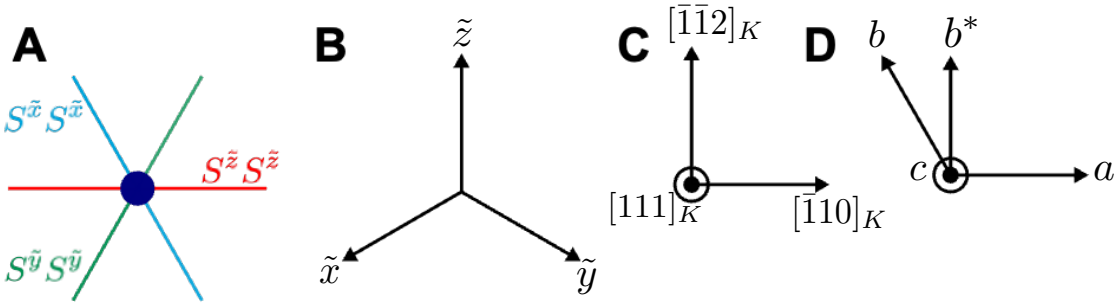

Figure 8.9: A) Nearest-neighbour bonds colour coded by the corresponding Kitaev exchange axis. B) Projection of cubic Kitaev axes $\tilde{x}\tilde{y}\tilde{z}$ onto the crystallographic ab plane (D) to illustrate the relation to hexagonal axes. C) The orthogonal crystallographic directions a, b^* and c expressed in terms of the Kitaev $\tilde{x}, \tilde{y}, \tilde{z}$ axes.

$Na_2BaCo(PO_4)_2$ could instead be described by a Heisenberg-Kitaev Hamiltonian [169]. This is defined as

$$\mathcal{H} = \sum_{\langle ij \rangle} \left(J \boldsymbol{S}_i \cdot \boldsymbol{S}_j + K S_i^\gamma S_j^\gamma \right), \tag{8.10}$$

where the second term contains the Kitaev couplings, where the bond-dependent Ising axis for each of the 6 nearest neighbour bonds is indicated by the bond colour in Fig. 8.9A. The Ising axes γ are a set of cubic axes $\tilde{x}\tilde{y}\tilde{z}$ defined such that

$$\boldsymbol{a} \parallel [\bar{1}10]_K, \tag{8.11}$$

$$\boldsymbol{b}^* \parallel [\bar{1}\bar{1}2]_K, \tag{8.12}$$

$$\boldsymbol{c} \parallel [111]_K, \tag{8.13}$$

where $[]_K$ refers to the cubic Kitaev axes. The projection of the Kitaev axes onto the ab plane is illustrated in Fig. 8.9B. For each bond, the Kitaev axis is perpendicular to the bond direction. The magnon dispersion relation for high field $\parallel c$ or in plane can be obtained analytically, as discussed below, and these expressions were checked against SpinW [65] calculations. The dispersion in the model (8.10) in field applied in the out-of-plane direction is (taking S=1/2)

$$\hbar\omega(\boldsymbol{Q}) = \sqrt{\mathcal{A}^2 - |\mathcal{B}|^2} \tag{8.14}$$

$$\mathcal{A} = g_c \mu_B B_z - 3\left(J + \frac{K}{3}\right) + \left(J + \frac{K}{3}\right)\gamma(\boldsymbol{Q}) \tag{8.15}$$

$$\mathcal{B} = \frac{K}{2}\left[\left(\frac{1}{\sqrt{3}} - \frac{i}{3}\right)\cos 2\pi h + \frac{2i}{3}\cos 2\pi k + \left(-\frac{1}{\sqrt{3}} - \frac{i}{3}\right)\cos 2\pi(h+k)\right], \tag{8.16}$$

J	0.0900 meV
K	0.0063 meV
g_c	4.230
g_{ab}	4.340
ΔB	0.142 T at $B = 1.7$ T$\|\| b^*$

Table 8.3: Best fit Hamiltonian parameters using the alternative Heisenberg-Kitaev model, as defined in (8.10) and used in Fig. 8.8B.

where $\gamma(\boldsymbol{Q})$ is defined in (8.9). When $|\mathcal{A}| \gg |\mathcal{B}|$, which is equivalent to being significantly above the transition to the field polarized phase, (8.14) can be Taylor expanded, such that $\hbar\omega(\boldsymbol{Q}) \approx \mathcal{A}$. This is of the same form as (8.5) with $g_c\mu_B B_z - 3J_z \rightarrow g_c\mu_B B_z - 3\,(J + K/3)$ and $J_{xy} \rightarrow (J + K/3)$. In the limit of high field (i.e., significantly above the critical field), this dispersion is therefore equivalent to that of a Heisenberg model with renormalized J. However, if field is applied instead in the plane, the dispersions are more distinct. In particular, when the field is applied along b^*, the dispersions become

$$\hbar\omega(\boldsymbol{Q}) = \sqrt{\mathcal{A}^2 - |\mathcal{B}|^2} \tag{8.17}$$

$$\mathcal{A} = g_{ab}\mu_B B_y - 3\left(J + \frac{K}{3}\right) + \left(J + \frac{K}{6}\right)\cos 2\pi h + \left(J + \frac{5K}{12}\right)\left[\cos 2\pi(h+k) + \cos 2\pi k\right] \tag{8.18}$$

$$\mathcal{B} = \frac{K}{2}\left[\frac{i}{3}\cos 2\pi h + \left(\sqrt{\frac{2}{3}} + \frac{i}{6}\right)\cos 2\pi k + \left(\sqrt{\frac{2}{3}} + \frac{i}{6}\right)\cos 2\pi(h+k)\right]. \tag{8.19}$$

This has a different functional form to the XXZ dispersion (8.6). Therefore, if data taken in high in-plane field are also taken into account, these two scenarios can be readily distinguished, as illustrated by the poor agreement between calculated and observed energies shown in Fig. 8.8B. The parameters used in that calculation are shown in Table 8.3.

The presence of Kitaev terms (K) or next-nearest-neighbour in-plane exchanges (J_3) as small perturbations to the XXZ Hamiltonian was also investigated. Allowing either of these terms did not significantly improve the fits, and gave values of K and J_3 at most of order 5% of J_z, i.e. the same order of magnitude as the neglected

interlayer couplings. Therefore, in the following, the XXZ Hamiltonian parameters in Table 8.2 will be used, as these already provide a very good quantitative description of the high field dispersions in field along two orthogonal directions, see Fig. 8.8A.

Note that the magnon linewidth at high fields is found to be resolution-limited, with no evidence for any intrinsic width. In particular, the observed linewidth can be accounted for by the time-of-flight energy resolution as predicted by PyChop [88] and accounting for the finite sample extent and crystal mosaic. It is therefore possible to rule out for the present sample the existence of exchange disorder as proposed in Ref. [170], i.e. a variation in J_z of 0.025 meV, which would result in a 0.075 meV variation in the Γ point energy, as this would have effects on the linewidth readily measurable within the current experimental set-up and which are not observed.

8.5 Excitations in low transverse field

8.5.1 Results

In stark contrast to the sharp magnons in the field polarized phase, the spectrum at lower fields has significant continuum scattering and broadened excitations, as illustrated in Fig. 8.10. While at 1.7 T, just above the transition field, sharp magnons are observed [Fig. 8.10F shows the same information as Fig. 8.6A but in a higher resolution configuration], substantial continuum scattering is seen at 1.4 T [Fig. 8.10E] and at all lower fields. For some qualitative insight into the evolution of the spectrum in the ordered phase immediately below B_c, consider the fact that the ordered magnetic structure for a pure 2D model is illustrated in Fig. 8.2B (V phase), and is expected to have a 3 site unit cell, with ordering wavevector at the K point. Thus, the change in the one-magnon spectrum from 1.7 T to 1.4 T can be seen as due to Brillouin zone folding, with shadow copies of the main mode appearing shifted by $(2/3, -1/3)$ and $(-2/3, 1/3)$ in the (h, k) plane, along with some additional splitting of the mode at the K point. In addition, these magnons then become broadened through interactions with the continuum, whereas the very lowest energy modes near K and K' appear to remain sharp with a quadratic dispersion around the K point. As the applied field is further decreased to 1 T [Fig. 8.10D] and 0.7 T [Fig.

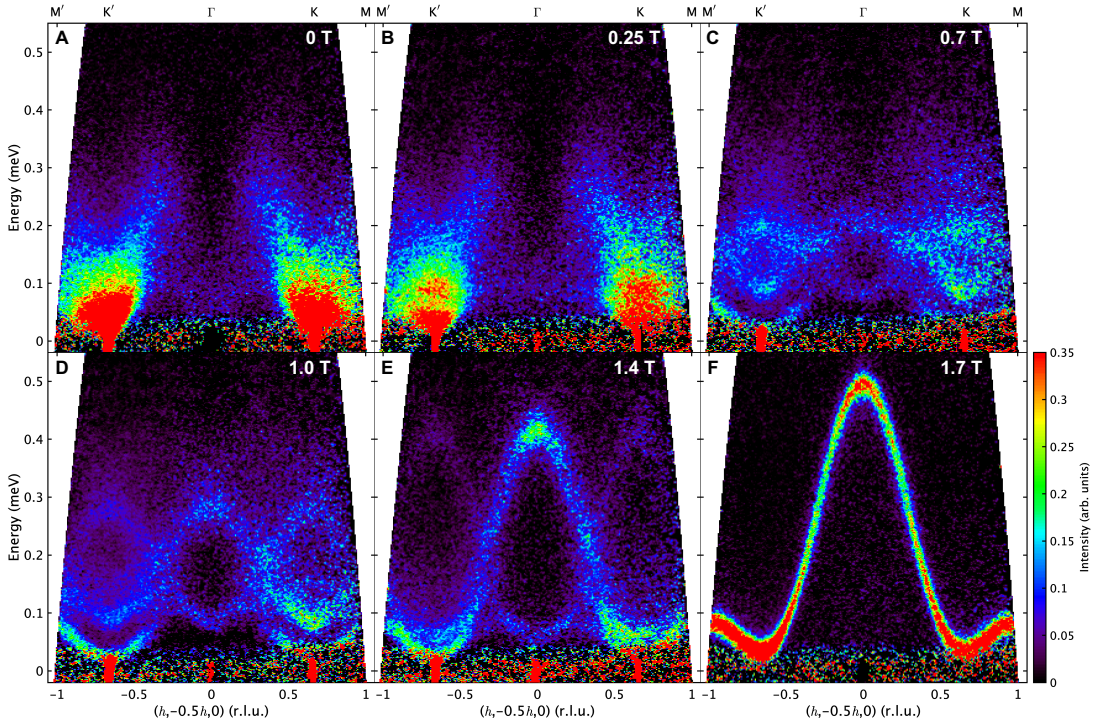

Figure 8.10: Inelastic neutron scattering data showing the evolution of the spectrum as a function of in-plane field, increasing from left to right and top to bottom. Colour is the measured intensity with an estimate of the non-magnetic background subtracted off, including the incoherent scattering on the elastic line. In each panel, the data are shown for wavevector along the $(1, -0.5, 0)$ direction, and are averaged over the range $-0.025 < k < 0.025$ in the (010) direction, and over the full range of the data in the (001) direction. The data were taken with $E_i = 0.87$ meV. Labels on the top x-axis indicate positions equivalent to high symmetry points in the two-dimensional hexagonal Brillouin zone.

8.10C], the energy of what remains of the magnon at the Γ point decreases, due to the decrease in Zeeman energy, while the splitting at the K points increases and the continuum increases in intensity. The broadening of the linewidth as field is decreased is studied more systematically in Fig. 8.11A. This shows that the linewidth at low field is far greater than the experimentally expected linewidth.

Between 0.7 T and 0.25 T [Fig. 8.10B], there is believed to be a first order phase transition between a V phase and an iY phase [64], thus the spectrum is not expected to evolve continuously. Indeed, the spectrum at 0.25 T no longer has any magnon-like features, such as are seen down to 0.7 T near the K points. Instead, the spectrum closely resembles the very strong continuum scattering seen in zero field [Fig. 8.10A], which has also been reported previously [58, 59]. The

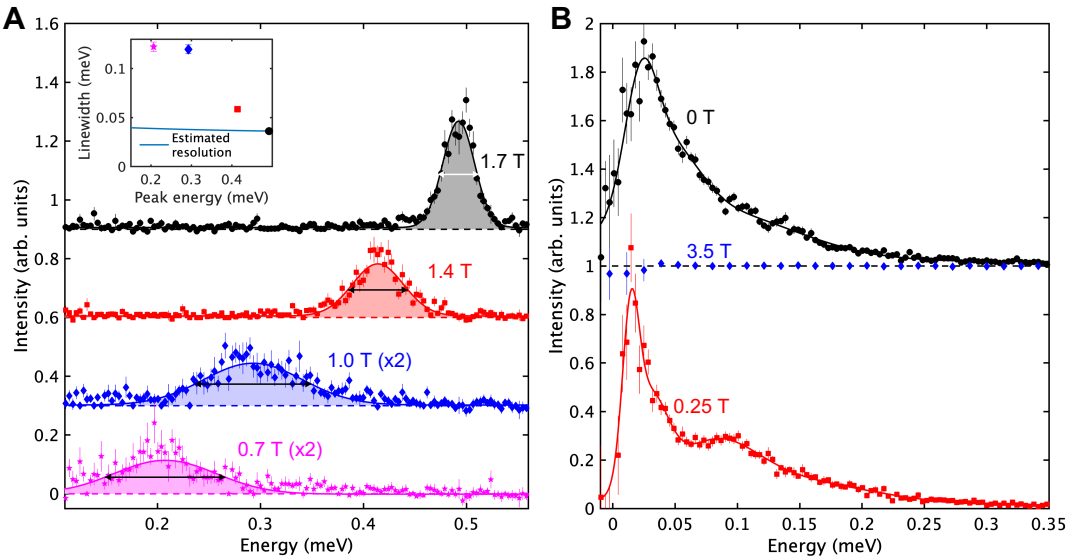

Figure 8.11: A) Energy scans at constant wavevector extracted from the data in Fig. 8.10 near $h = 0, k = 0$ showing the increasing magnon linewidth with decreasing field. Data points are neutron scattering intensities in arbitrary units with an estimate of the non-magnetic background subtracted off. Data were averaged across $-0.025 < h < 0.025$ in the $(h, -0.5h, 0)$ direction, $-0.025 < k < 0.025$ in the $(0, k, 0)$ direction and $-1.2 < l < 0.3$ in the $(0, 0, l)$ direction. Solid lines are Gaussian fits to the peak shape; horizontal double headed arrows indicate the corresponding FWHM. For clarity, curves have been offset vertically (by 0.3) as a function of increasing field, and the intensities at 0.7 T and 1.0 T have been multiplied by a factor of 2. Inset: Linewidths (FWHM) extracted from Gaussian peak shapes in A, as a function of peak energy. The symbols used are the same as in A. An estimate of the experimental resolution (solid line) is shown for reference. This was obtained by assuming that the difference between the output of PyChop and the experimentally observed value at 1.7 T is due to finite sample size and mosaicity and that these result in a constant linewidth contribution which adds to the theoretical resolution in quadrature. B) Cuts through data at 0 T (black circles), 0.25 T (red squares) and 3.5 T (blue diamonds), with an estimate of the non-magnetic background subtracted off in each case. There is strong continuum scattering across a significant energy range at 0 T and 0.25 T, but the data at 0.25 T are seen to have additional structure with a second broad hump around 0.1 meV. The data at 3.5 T are shown to illustrate the quality of the background subtraction. The data at 0 T and 3.5 T have been offset by 1 unit for clarity. Solid lines are guides to the eye. The data were averaged across $-0.05 < h + 2/3 < +0.05$ in the $(h, -0.5h, 0)$ direction, $-0.05 < k < 0.05$ in the $(0, k, 0)$ direction and $-0.75 < l < -0.25$ in the $(0, 0, l)$ direction. In both panels, the data were taken with $E_i = 0.87$ meV.

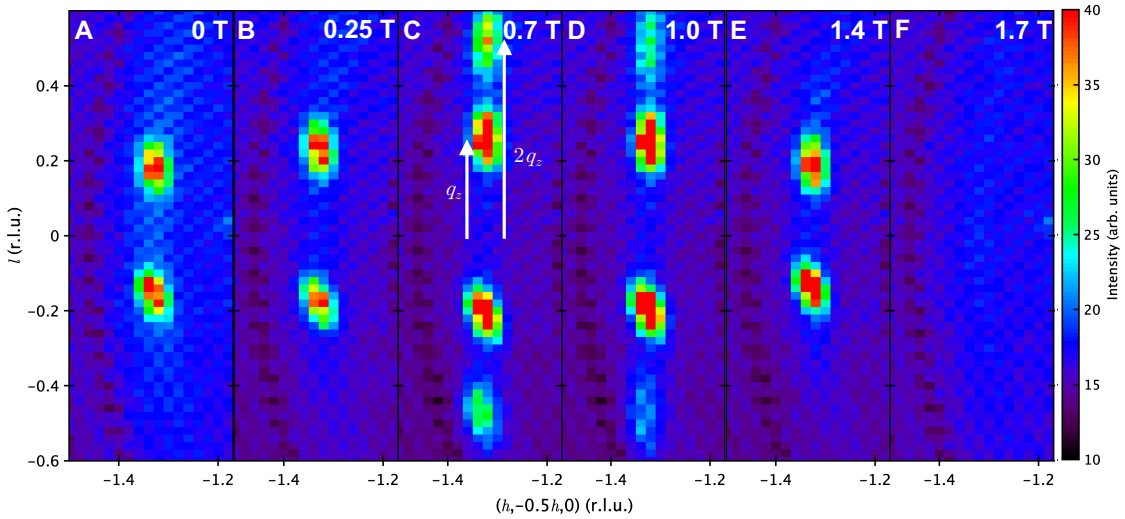

Figure 8.12: The evolution of the elastic line as a function of increasing magnetic field from left to right. The sharp spots are Bragg peaks associated with the magnetic order. In each panel, the horizontal direction shows the distance along $(h, -0.5h, 0)$; all peaks shown are at $h = -4/3$, indicating 3-sublattice in-plane magnetic ordering. In panels C and D weak peaks are also observed at the second harmonic $\pm 2q_z$ positions in addition to the primary peaks at $\pm q_z$. The vertical axis is the $(0, 0, l)$ direction. In all panels, colour shows the raw neutron scattering intensity on an arbitrary scale. The data have been averaged across $-0.1 < k < 0.1$ in the $(0, k, 0)$ direction and $-0.1 < E < 0.1$ where E is the energy transfer in meV. The incident energy used was $E_i = 2.67$ meV.

one qualitative difference observed between the spectrum at 0 T and 0.25 T is that while at 0 T the intensity at the K point seems to smoothly decrease with energy, at 0.25 T, there appears to be more structure in the form of a second broad hump at the intermediate energy of 0.1 meV, as illustrated in Fig. 8.11B.

Finally, the evolution of the magnetic Bragg peaks in this regime, shown in Fig. 8.12, is briefly discussed. It can be seen that at all fields, the magnetic ordering vector is of the form $(1/3, 1/3, q_z)$, but with a field-dependent q_z. As discussed in Sec. 8.3, in zero field, $q_z = 0.18 \approx 1/6$. When the field is increased to 0.25 T, q_z increases slightly. After the transition to what is believed to be the V phase [64], the structure changes somewhat. Here, q_z is seen to increase further to nearly 1/4, and a second set of weaker diffraction peaks appear at positions $\pm 2q_z$ [see Fig. 8.12C]. These are suppressed faster than the main peaks (at $\pm q_z$) upon increasing field [see Fig. 8.12C-E]. The second harmonic component indicates that a single Fourier component cannot fully capture the magnetic structure in this intermediate

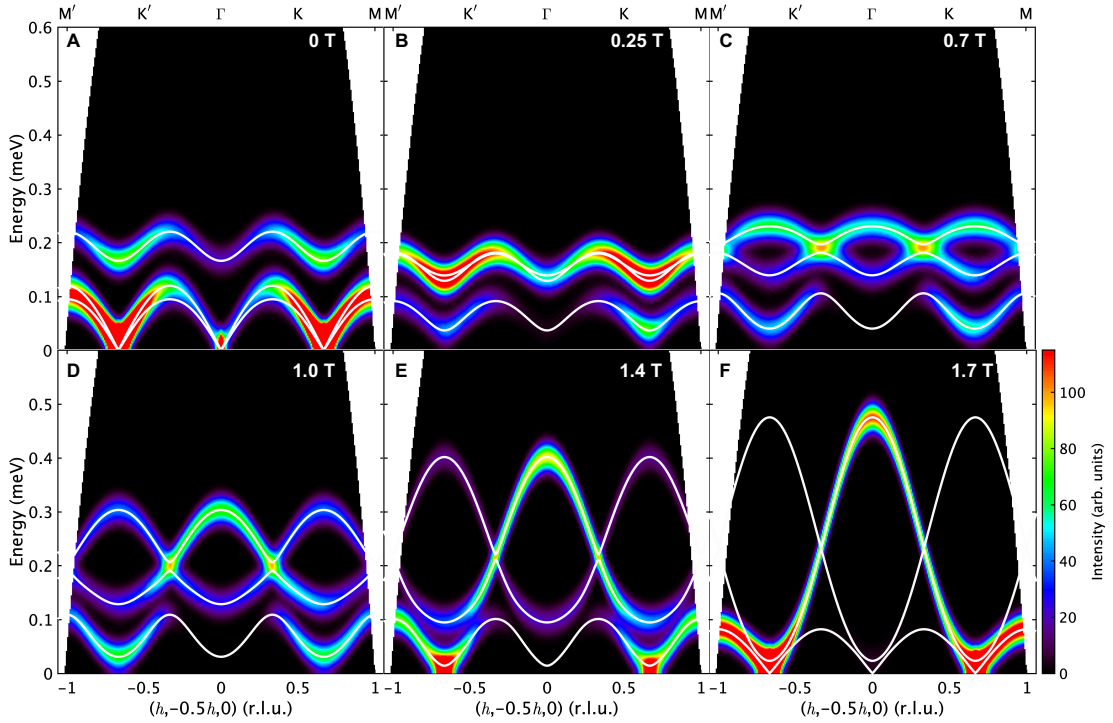

Figure 8.13: Calculations of the one-magnon contribution to the spectrum as a function of in-plane field. Colour shows predicted neutron scattering intensity on an arbitrary scale, chosen such that the intensity at the Γ point in the 1.7 T calculation matches the data. White lines show the corresponding magnon dispersions. The calculation uses the classical ground state at all fields (see Fig. 8.2C); for field ≥ 0.7 T, this is not the same as the quantum prediction for the ground state (see Fig. 8.2B). In particular, 1.7 T is below the classical transition field to the field polarized phase so there are still three modes in this calculation at 1.7 T. The calculation was averaged over a range $-0.025 < k < 0.025$ in the $(0, k, 0)$ direction and over the full range of data in the $(0, 0, l)$ direction, as in Fig. 8.10. The calculation was performed using SpinW [65] and has been broadened by convolution with a Gaussian of 0.04 meV FWHM to simulate the estimated experimental energy resolution.

field regime. As the field increases above 0.7 T, q_z decreases again towards 1/6 and at 1.7 T all magnetic peaks have disappeared, confirming the transition to the high-field polarized phase. The fact that q_z evolves with field is intriguing, but an understanding of this is beyond the scope of the current work.

8.5.2 Linear spinwave theory calculations

In order to understand the evolution of the spectrum in low field, it is instructive first to consider the predictions of linear spinwave theory, as shown in Fig. 8.13. These calculations show the one-magnon contribution to the spectrum and were

performed using SpinW [65]. From 0.7 T upwards, the shape of the top two modes is qualitatively captured, but the gap to the lowest mode is predicted to be higher than is seen experimentally and its shape is not well captured. At 0 T and 0.25 T by contrast, the calculation does not even qualitatively capture the data. As these calculations are one-magnon calculations, they cannot include any continuum scattering, and so cannot capture the strong continua seen in the data.

The next step was therefore to clarify the nature of the continuum excitations, in particular whether they can be understood semi-classically. The two-magnon contribution to the linear spinwave theory prediction for the scattering intensity was therefore calculated. For this, it is convenient to introduce a local reference frame $x'y'z'$, with z' along the local ordered spin. The transverse directions x', y' are defined according to the convention used by the SpinW package [65]: defining $\hat{x}', \hat{y}', \hat{z}', \hat{a}, \hat{b}$ to be unit vectors along the local x', y', z' and the crystallographic a, b directions respectively, this convention is that $\hat{y}'$ is along $\hat{z}' \times \hat{a}$ (unless $\hat{z}' \parallel \hat{a}$, in which case $\hat{y}'$ is along $\hat{a} \times \hat{b}$), and $\hat{x}' = \hat{y}' \times \hat{z}'$. In this local frame, the ground state is ferromagnetically polarized along z' and the two-magnon scattering occurs entirely in the longitudinal ($z'z'$) polarization, and is given by[2]

$$S^{z'z'}(\boldsymbol{Q}, \omega) = \sum_{\lambda_f} |\langle \lambda_f | S^{z'}(\boldsymbol{Q}) | \mathrm{GS} \rangle|^2 \delta \left(E_{\lambda_f} - \hbar\omega \right), \tag{8.20}$$

where the sum extends over all excited states $|\lambda_f\rangle$ of energy E_{λ_f} relative to the ground state $|\mathrm{GS}\rangle$ and where $S^{z'}(\boldsymbol{Q}) = \sum_j \exp(i\boldsymbol{Q} \cdot \boldsymbol{r}_j) S^{z'}_j$, with j running over all magnetic sites. One-magnon scattering occurs in the transverse correlations $S^{x'x'}$, $S^{y'y'}$ and $S^{x'y'}$, $S^{y'x'}$.

In linear spinwave theory, at zero temperature, $S^{z'z'}$ comes from terms with two magnon creation operators. Working now in the original global frame, the two-magnon contribution to the $\alpha\beta$ component of the dynamical structure fac-

[2]The g-factor (and Bohr magneton) has been omitted for the purposes of working in this local frame but will be reintroduced when working in the global frame.

tor is given by

$$S^{\alpha\beta}_{2M}(\boldsymbol{Q},\omega) = Z_{2M}\mu_B^2 g^\alpha g^\beta \sum_{\boldsymbol{k},\boldsymbol{k'},\boldsymbol{\tau}} \delta\left(\boldsymbol{Q}-\boldsymbol{k}-\boldsymbol{k'}-\boldsymbol{\tau}\right) \sum_{j,j'} \delta\left(\hbar\omega - E^j_{\boldsymbol{k}} - E^{j'}_{\boldsymbol{k'}}\right) f_{j,j'}(\boldsymbol{k},\boldsymbol{k'}), \tag{8.21}$$

$$f_{j,j'}(\boldsymbol{k},\boldsymbol{k'}) = \sum_{m,m'} e^m_{z'\alpha} e^{m'}_{z'\beta} u^*_{mj}(\boldsymbol{k}) v^*_{mj'}(\boldsymbol{k'}) u_{m'j}(\boldsymbol{k}) v_{m'j'}(\boldsymbol{k'}), \tag{8.22}$$

where $\alpha,\beta = x,y$ and z. Here, $\boldsymbol{k},\boldsymbol{k'}$ run over the first structural Brillouin zone, j,j' label the different magnon modes, m,m' label the sites in the magnetic unit cell, $E^j_{\boldsymbol{k}}$ is the energy of the jth magnon mode with wavevector $\boldsymbol{k}$, $e^m_{z'\alpha}$ is the component of $\hat{z}'$ on the mth sublattice along the global α direction and $\boldsymbol{k}+\boldsymbol{k'} = \boldsymbol{Q}-\boldsymbol{\tau}$ is the total wavevector reduced to the first Brillouin zone ($\boldsymbol{\tau}$ are reciprocal lattice vectors). The overall pre-factor Z_{2M} is introduced here to allow for an overall renormalization of the intensity due to quantum fluctuations beyond LSWT, for which $Z_{2M} = 1$. The quantities $u_{mj}(\boldsymbol{k})$, $v_{mj}(\boldsymbol{k})$ transform between the boson operators $a_{\boldsymbol{k},m}$ for the N different magnetic sublattices, $m = 1$ to N, and the normal mode boson operators $b_{\boldsymbol{k},j}$ as

$$a_{\boldsymbol{k},m} = \sum_j u^*_{mj}(-\boldsymbol{k}) b_{\boldsymbol{k},j} + v_{mj}(\boldsymbol{k}) b^\dagger_{-\boldsymbol{k},j} \tag{8.23}$$

$$a^\dagger_{-\boldsymbol{k},m} = \sum_j v^*_{mj}(-\boldsymbol{k}) b_{\boldsymbol{k},j} + u_{mj}(\boldsymbol{k}) b^\dagger_{-\boldsymbol{k},j}, \tag{8.24}$$

where $j = 1$ to N, the number of magnetic sublattices. Here, N=3 for $B < B_3$ and $N = 1$ for $B \geq B_3$, for B_3 the transition field to the field polarized phase (see Fig. 8.2). The corresponding 1-magnon expression is

$$S^{\alpha\beta}_{1M}(\boldsymbol{Q},\omega) = Z_{1M}\mu_B^2 g^\alpha g^\beta \sum_{\boldsymbol{k},\boldsymbol{\tau}} \delta\left(\boldsymbol{Q}-\boldsymbol{k}-\boldsymbol{\tau}\right) \sum_j \delta\left(\hbar\omega - E^j_{\boldsymbol{k}}\right) \tilde{f}_j(\boldsymbol{k}), \tag{8.25}$$

$$\tilde{f}_j(\boldsymbol{k}) = \sum_{m,m'} \left[e^m_{x'\alpha}\left(u_{mj}+v_{mj}\right) + e^m_{y'\alpha} i\left(v_{mj}-u_{mj}\right)\right]^* \left[e^{m'}_{x'\beta}\left(u_{m'j}+v_{m'j}\right) + e^{m'}_{y'\beta} i\left(v_{m'j}-u_{m'j}\right)\right]. \tag{8.26}$$

In this expression, the u_{ij}, v_{ij} are all implicitly evaluated at $\boldsymbol{k}$, Z_{1M} is an overall intensity renormalization factor due to quantum fluctuations beyond LSWT and $e^m_{\{x',y'\}\alpha}$ is the component of $\hat{x}', \hat{y}'$ on the mth sublattice along the global α direction

The integral equations for the dynamical correlations $S^{\alpha\beta}(\boldsymbol{Q},\omega)$ in (8.21) were calculated numerically using a Monte-Carlo method as in Ref. [171]. The SpinW

package [65], was used to determine the classical magnetic ground state at a given field and calculate the local spin projection components $e^m_{z'\alpha}$ and the functions $u_{mj}(\boldsymbol{k})$, $v_{mj}(\boldsymbol{k})$, $E^j_{\boldsymbol{k}}$. The intensity prefactors Z_{1M} and Z_{2M} were determined such that the dynamical correlations satisfied the sum rules in the local frame. These rules state that for a spin-half system in the case of an isotropic g-tensor [172],

$$M^{\alpha\beta} = \frac{1}{N}\sum_{\boldsymbol{Q}}\int \mathrm{d}(\hbar\omega) S^{\alpha\beta}(\boldsymbol{Q},\omega) = \frac{1}{4}(g\mu_B)^2\delta_{\alpha\beta}, \tag{8.27}$$

where the sum is over all $\boldsymbol{Q}$ in the first Brillouin zone and N is the total number of magnetic sites. The contributions to $M^{x'x'}$ and $M^{y'y'}$ come from single-magnon excitations, and a common overall scale factor Z_{1M} has been assumed for all 1-magnon contributions, such that $M^{x'x'} + M^{y'y'} = \frac{1}{2}(g\mu_B)^2$. There are two contributions to $M^{z'z'}$: the magnetic Bragg peaks on the elastic line, and the inelastic part due to two-magnon scattering, as described above. The magnetic Bragg peaks have total intensity per magnetic site

$$M^{z'z'}_{\mathrm{BP}} = \left(S^2 - 2S\overline{\Delta S} + \overline{(\Delta S)^2}\right)(g\mu_B)^2, \tag{8.28}$$

where

$$(\Delta S)_m = \frac{1}{N}\sum_{\boldsymbol{k}}\sum_j |v_{mj}|^2 \tag{8.29}$$

is the spin reduction on sublattice m and overlines denote averages across the different magnetic sublattices. Setting $S = 1/2$, the two magnon contribution to the scattering is therefore required to sum to $\overline{\Delta S} - \overline{(\Delta S)^2}$. It was found that without normalization, the intensities were off by about 30% (but correct to within an order of magnitude), as shown in Table 8.4.

The results of these calculations are shown in Fig. 8.14E-H, where the intensities are shown on a log scale in order for the calculated continuum intensities to be visible. Just above the transition field [Figs. 8.14D data, H calculation] the spectrum is well captured by the one-magnon calculation; the two-magnon contribution may be present but if so, it is below the noise level of the experiment. When calculating the spectrum for the V phase, there is the additional difficulty that the classical ground state is an inverted-Y type phase (also called a Ψ phase) all the way to the

	0 T	0.25 T	1.4 T	1.7 T	3.5 T	Sum rules
$M^{x'x'}$	0.3293	0.3045	0.2435	0.2253	0.2482	0.25
$M^{y'y'}$	0.3475	0.2650	0.2723	0.2968	0.2522	0.25
$M^{z'z'}_{\text{total}}$	0.3218	0.2624	0.2524	0.2558	0.2499	0.25
$M^{z'z'}_{2M}$	0.2135	0.0769	0.0179	0.0275	0.0003	
$M^{z'z'}_{\text{BP}}$	0.1083	0.1855	0.2345	0.2283	0.2496	

Table 8.4: The sum total of the intensity contribution in each channel in the local $x'y'z'$ frame before normalization in units of $(g\mu_B)^2$ assuming an isotropic g-tensor, as calculated in LSWT before normalization. The first and second rows correspond to the two different polarizations of single magnon scattering. Each of these should sum to 1/4 according to the sum rule (8.27). In the fixed frame, it is not possible to normalize these polarizations separately so a common overall scale factor has been assumed for all one-magnon contributions such that $M^{x'x'} + M^{y'y'} = 1/2$. The third row shows the longitudinal polarization $M^{z'z'}$, which has contributions from Bragg peaks and from two-magnon excitations, and which should also sum to 1/4 as per (8.27). The last two rows show the two contributions separately, with the fourth row showing the two-magnon contribution, calculated using (8.21), while the fifth row shows the Bragg peak contribution to $S^{z'z'}$ as per (8.28). It is assumed that the calculation of the Bragg peak intensity is accurate, so the two-magnon intensity is normalized such that the sum is 1/4. At low field, the sum rules are only very approximately satisfied, but the relative intensities of the single-magnon and two-magnon scattering are nevertheless close to what is expected from the sum rules. The 3.5 T column shows that well into the paramagnetic phase, linear spinwave theory is an asymptotically good approximation as the sum rules are very close to being exactly satisfied.

field polarized phase, as per Fig. 8.2C. In order to stabilize the V phase at 1.4 T, which is believed to be the correct quantum ground state for the XXZ model with the experimentally relevant parameters [64], a small nearest-neighbour biquadratic exchange $-J_{bq}\sum_{\langle ij\rangle}\left(\boldsymbol{S}_i\cdot\boldsymbol{S}_j\right)^2$ (J_{bq}=0.008 meV) was added to the Hamiltonian in order to approximate the effects of quantum fluctuations [173]. This value was chosen as being slightly above the minimal value needed to stabilize the V phase; note that analytic expressions for J_{bq} for the case of pure Heisenberg exchange were given in Ref. [173], but they are not applicable here because of the strong XXZ anisotropy, so the value used was instead chosen empirically. Within the V phase, calculations were only done at 1.4 T, as at 0.7 T and 1 T, the required size of the biquadratic exchange is of similar size to the bilinear exchange interactions, which would therefore significantly affect the physics. At 1.4 T, the gross features of the spectrum can be understood starting from the linear spinwave theory calculation,

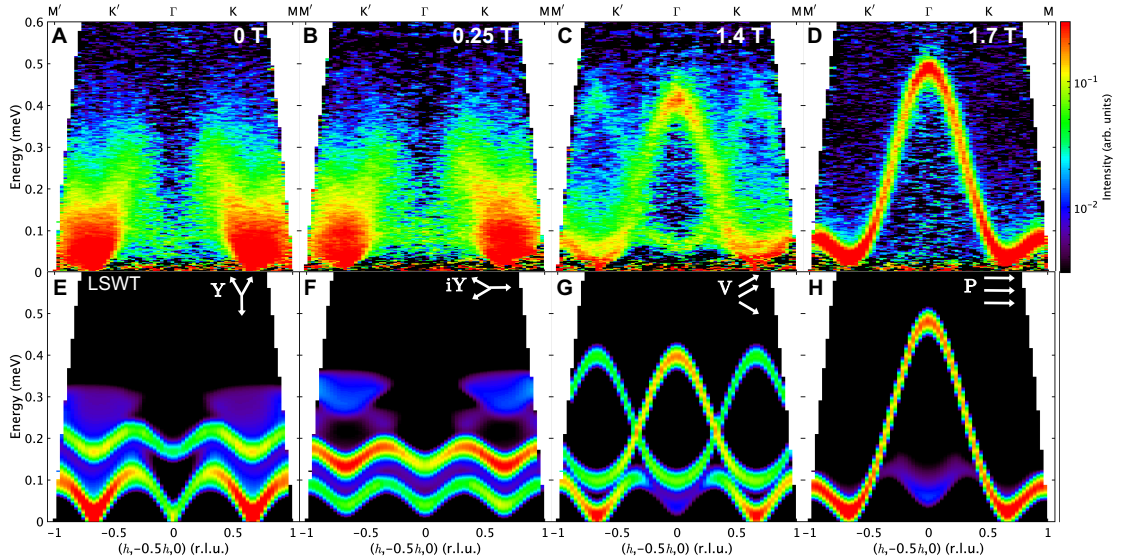

Figure 8.14: A-D) Evolution of the spectrum as a function of field. The averaging range in these panels is different to that used in Fig 8.10, and in particular, the l range was chosen so as not to include magnetic Bragg peaks. E-H) Calculations of the inelastic neutron scattering intensity in linear spinwave theory, as described in Sec. 8.5.2, including both the 1-magnon and 2-magnon contributions, normalized to satisfy the sum rules as described in the text. The calculations have been convolved with a Gaussian in energy of 0.04 meV FWHM, corresponding to the estimated experimental energy resolution. The data have been averaged across the range $-0.05 < k < 0.05$ in the $(0, k, 0)$ direction and $-0.75 < l < -0.25$ in the $(0, 0, l)$ direction, and have had an estimate of the non-magnetic background subtracted off. The calculations take into account the averaging range, polarization factor and Co^{2+} magnetic form factor. In all panels, colour represents scattering intensity on an arbitrary scale. A common overall intensity scale in the calculations was chosen such as to get a good match with the 1-magnon intensity in the 1.7 T data. A log scale has been used in order for the continuum scattering to be visible in the calculation panels.

although the shape of the bands around the K points is not very well captured and there is significantly more continuum scattering seen in the experiment than in the calculations. Strong magnon decays into magnon pairs are expected at all in-plane fields below the transition to the field polarized phase due to the non-collinear order [174], and the spectrum observed at 1.4 T looks like it could plausibly be described in terms of magnons which are both broadened and somewhat renormalized in their dispersion due to interactions with the two-magnon continuum. In the Y phase [Figs. 8.14A, B data, E, F calculation], however, the linear spinwave spectrum looks very different from the experimental data; the data have no detectable sharp modes, contrary to what is predicted, and the continuum in the calculations is

both far weaker than what is seen experimentally and a very different shape. This indicates that the semi-classical model does not work in this regime and that the spectrum is fundamentally much more quantum in nature. Numerical calculations in zero field based on tensor network states suggest that the continuum observed is an intrinsic feature of the Ising-like XXZ TLAF model and not due to additional in-plane exchange terms in the Hamiltonian or to effects of interlayer interactions [58, 59], although there is currently disagreement as to whether there could be some low energy sharp modes which current experiments have been unable to resolve [60]. Similar physics could be expected to be at play also at 0.25 T.

8.6 Conclusions

In summary, neutron scattering measurements have been performed on the Ising-like TLAF material $Na_2BaCo(PO_4)_2$. Diffraction measurements in zero field indicate an incommensurate (1/3,1/3,0.18) magnetic propagation vector as previously reported. Both this incommensurate propagation vector and a refinement of the structural peaks support the crystallographic space group being $P\bar{3}$ rather than $P\bar{3}m$. High resolution inelastic neutron scattering measurements were performed as a function of in-plane field. In the limit of high field, sharp magnons are observed which are well described by linear spinwave theory. The data in this regime were used to confirm that this material is well described by a nearest-neighbour XXZ model. Below the critical field however, strong continuum scattering is seen, much stronger than what is expected semi-classically in linear spinwave theory. While, the spectrum down to 0.7 T can be approximately described by magnons strongly broadened by interaction with the continuum, the spectrum at 0.25 T and 0 T has no sharp features at all. This suggests that there is novel intrinsically quantum physics describing the spectrum in this regime. Further experimental work to understand the field-dependence of the ground state and further theoretical work to understand the spectrum are needed to fully understand this physics.

9 Conclusions

This thesis presented neutron scattering and magnetization results as a function of applied field on two low-dimensional Ising-like quantum magnetic materials.

The first of these materials was the ferromagnetic Ising chain material $CoNb_2O_6$. First the excitations of this material were studied using inelastic neutron scattering with a magnetic field applied along the crystallographic a-direction, such that there was a large longitudinal (along Ising axis) field component, which tuned the confinement potential between domain walls. In the low field, weak confinement regime, a Zeeman ladder of bound states was found, with their energy varying as field to the 2/3 power. Upon increasing field, higher-order bound states increased more quickly in energy and progressively disappeared from the spectrum such that in the limit of high field, in the strong confinement regime, only two bound states were found, whose energies depend linearly on field.

The Hamiltonian for $CoNb_2O_6$ was then revisited in order to be able to account for the data observed in high field applied along this direction. In order to capture the interchain dispersion as well as bound states and renormalization effects, a two step fitting method was developed using a combination of linear spinwave theory and exact diagonalization of the Hamiltonian on finite chains in order to capture both the interchain couplings as well as the variety of different bound states. By performing a global fit to the full wavevector dependent spectrum

observed in various fields, a microscopic Hamiltonian was proposed, including both in-chain and inter-chain interactions, down to 2% of the dominant Ising exchange. This Hamiltonian quantitatively reproduces the INS data obtained across a wide range of field conditions including zero field, high near-longitudinal field and high transverse field, as well as intermediate fields to which the Hamiltonian was not fit, leading to a fully consistent description of the spin dynamics using a single set of exchange parameters.

In particular, exact diagonalization calculations using this refined Hamiltonian quantitatively reproduced the rich evolution of the spectrum observed as a function of low to intermediate transverse field in the ordered phase of $CoNb_2O_6$. A physical picture of the excitations was then sought by restricting the Hilbert space to the two-domain wall subspace, resulting in a spectrum that in general has three continua and three bound states, of which only the bound states contribute significant weight to the inelastic neutron scattering intensity. It was found that these bound states of domain walls can be understood in the localized limit when the hopping on alternate bonds is zero, as being stabilized by hardcore repulsion leading to a change in the delocalization energy. Using this physical picture, it was possible to gain both a qualitative and a quantitative understanding of the low energy spectrum of $CoNb_2O_6$ in the low transverse field ordered phase.

Finally, the magnetization of $CoNb_2O_6$ was measured for field applied along each of the a, b, c crystallographic axes in fields up to 16 T. Using these data, it was possible to observe signatures of the presence of the transverse field induced quantum critical point. The magnetization curves were compared to predictions based on the Hamiltonian refined in Chapter 5, achieving good agreement. Further work would be useful to fully understand the behaviour of the magnetization. In particular, further work is needed in order to understand the source of the small discrepancies observed between the predictions of the refined Hamiltonian and the measured magnetization. An understanding of these discrepancies may allow for a further refinement of the g-tensor. In addition, lower temperature magnetization measurements, which would

be possible with a SQUID magnetometer equipped with a helium-3 option, could be instructive to reveal more quantitative universal behaviour.

As one of the best experimental realizations of an Ising chain, a paradigmatic model in quantum magnetism, $CoNb_2O_6$ is still being actively studied, both experimentally and theoretically. Recent studies have focussed both on the universal aspects of the transverse field Ising chain behaviour exhibited in $CoNb_2O_6$ [124, 175] but also on understanding the effect of terms in the Hamiltonian beyond the pure Ising limit [139, 176–179] and how they arise microscopically [126, 127]. The work presented in this thesis makes a valuable contribution to this field of study. The various bound states discussed in this thesis arise due to effects beyond the pure one-dimensional Ising limit and understanding them is therefore an important step to understanding the effects of these perturbations. In particular, the Hamiltonian refined here could be useful for understanding future experimental results, comparing to microscopic calculations (as was indeed done in Refs. [126, 127]) and as a starting point for further theoretical explorations.

Neutron scattering measurements were also performed on the Ising-like triangular lattice antiferromagnet material $Na_2BaCo(PO_4)_2$. Diffraction measurements in zero field support the crystallographic space group being $P\bar{3}$ rather than $P\bar{3}m$. High resolution inelastic neutron scattering measurements were performed as a function of in-plane magnetic field. In the limit of high field, sharp magnons were observed which could be well described by linear spinwave theory. A global fit was performed to data in this regime as well as previously published data to refine a minimal XXZ Hamiltonian and rule out unambiguously other exchange models proposed previously. In fields below the transition to the field polarized phase however, much stronger continuum scattering is seen than what is expected semi-classically in linear spinwave theory. While the spectrum at and above 0.7 T can be approximately described by magnons strongly broadened by interaction with the continuum, the spectrum at 0.25 T and 0 T has no sharp features at all, suggesting that there is novel intrinsically quantum physics describing the spectrum in this regime, which has not been previously explored experimentally or theoretically. Further work to study the

field dependence of the ground state magnetic structure via neutron diffraction would be instructive to gain further understanding of the physics both of this material and in general of the spin-1/2 Ising-like triangular lattice antiferromagnet, which is a canonical model system for two-dimensional frustrated quantum magnetism.

9.1 Contributions

In this thesis I have made the following contributions to the field of low dimensional quantum magnetism.

- I performed detailed analysis of inelastic neutron scattering data from the quasi-one-dimensional Ising-like magnet $CoNb_2O_6$ as a function of field applied along the a-axis. I parameterized the dispersions of all modes at every field in the data set in order to understand the behaviour in both the high and low field regimes. I performed quantitative fits to the behaviours expected in both regimes, observing a crossover during which the number of modes visible in the spectrum gradually decreases and found that modes do *not* decay as soon as they overlap with the continuum. This crossover between the regimes of weak and strong confinement of domain walls had not been previously observed experimentally in Ising chain systems.

- I used a combination of data taken in high field along two orthogonal directions as well in zero field to refine a quantum spin Hamiltonian for $CoNb_2O_6$. This required the development of a novel two-step technique. I first used analytic linear spinwave theory expressions to parameterize the three-dimensional dispersion, and then set the interchain coupling terms in those parameterizations to zero in order to obtain effective one-dimensional dispersions. I then used custom-written exact diagonalization code to fit a single-chain Hamiltonian to these effective one-dimensional dispersions so that the various bound states in the spectrum could be captured. This algorithm allowed the refinement of both the interchain and the in-chain parameters down to less than 2% of the dominant Ising exchange, and resulted in a

quantitative description of not only the data to which the Hamiltonian was fit, but also the spectra at intermediate fields, within a single Hamiltonian.

- I used this refined Hamiltonian to gain a numerical understanding of the rich behaviour of the spectrum observed in $CoNb_2O_6$ in low to intermediate transverse field. I performed analytic calculations and numerical computations of the spectrum within a two-domain-wall model, and extended an analytic model of bound states in the localized limit to account for additional terms in the refined Hamiltonian for comparison with experiment. This model provides a very good qualitative understanding of the spectrum and thus provides evidence for novel bound states being present in $CoNb_2O_6$ in this regime.

- I performed magnetization measurements of $CoNb_2O_6$ up to 16 T and down to 2K with field applied along each of the *abc* crystallographic axes, including aligning the sample and designing an adaptor to verify the alignment. I found that signatures of the proximate transverse field quantum critical point could be observed and that the measured magnetization curves agree well with the refined Hamiltonian, providing a further test of this model.

- I performed detailed analysis of inelastic neutron scattering data on the triangular Ising-like quantum antiferromagnet $Na_2BaCo(PO_4)_2$ as a function of externally applied transverse field, as well as taking an active role in planning and performing the experiments. Using the data in high field, I performed fits in linear spinwave theory to refine a minimal nearest-neighbour XXZ triangular lattice antiferromagnet model, and place bounds on couplings beyond this minimal model, including on the interlayer couplings. In low field, strong continuum scattering is observed, and I performed linear spinwave theory calculations including both one- and two-magnon contributions, using custom written code, in order to test whether this continuum scattering can be understood semi-classically. I found that the continuum scattering observed experimentally is far stronger than what could be explained by this semi-classical model.

Appendices

A

Parameter correlations in the single-chain Hamiltonian for $CoNb_2O_6$

The correlations between the parameters fitted for the single chain Hamiltonian for $CoNb_2O_6$ in Chapter 5.4 are given in this appendix.

The correlation matrix between parameters is

$$
\begin{array}{c}
 \\
J \\
\lambda_S \\
\lambda_{\mathrm{AF}} \\
\lambda_{yz} \\
h_z \\
g_x \\
g_z \\
g_y \\
\lambda_{\mathrm{AF}}^{xy} \\
\lambda_A
\end{array}
\begin{array}{c}
\begin{array}{ccccccccccc}
J & \lambda_S & \lambda_{\mathrm{AF}} & \lambda_{yz} & h_z & g_x & g_z & g_y & \lambda_{\mathrm{AF}}^{xy} & \lambda_A
\end{array} \\
\left(\begin{array}{cccccccccc}
1 & -0.998 & 0.982 & -0.909 & -0.034 & 0.988 & -0.949 & 0.945 & -0.986 & 0.738 \\
-0.998 & 1 & -0.975 & 0.902 & 0.053 & -0.993 & 0.958 & -0.949 & 0.979 & -0.743 \\
0.982 & -0.975 & 1 & -0.948 & 0.073 & 0.976 & -0.880 & 0.928 & -0.979 & 0.739 \\
-0.909 & 0.902 & -0.948 & 1 & 0.082 & -0.931 & 0.819 & -0.902 & 0.893 & -0.844 \\
-0.034 & 0.053 & 0.073 & 0.082 & 1 & -0.077 & 0.273 & -0.082 & -0.034 & -0.216 \\
0.988 & -0.993 & 0.976 & -0.931 & -0.077 & 1 & -0.948 & 0.955 & -0.968 & 0.781 \\
-0.949 & 0.958 & -0.880 & 0.819 & 0.273 & -0.948 & 1 & -0.925 & 0.909 & -0.760 \\
0.945 & -0.949 & 0.928 & -0.902 & -0.082 & 0.955 & -0.925 & 1 & -0.908 & 0.853 \\
-0.986 & 0.979 & -0.979 & 0.893 & -0.034 & -0.968 & 0.909 & -0.908 & 1 & -0.683 \\
0.738 & -0.743 & 0.739 & -0.844 & -0.216 & 0.781 & -0.760 & 0.853 & -0.683 & 1
\end{array}\right)
\end{array}
\tag{A.1}
$$

There are strong correlations between many of the parameters. This is probably in part because J was used as an overall scale factor. It is therefore important to use the full covariance matrix when further propagating uncertainties. It is nonetheless possible to be reasonably confident in the refined parameters. This is because i) the uncertainties even along the largest eigenvector of the covariance matrix are not that large, ii) multiple methods of doing the fits gave very similar answers and

iii) the parameter set reported in this work gave better agreement to features of the data that were not included in the fit than other parameter sets that were tested. In particular, it is possible to be confident that $\lambda_{\mathrm{AF}}^{xy}$ and λ_A are definitely non-zero.

B

Formulae used in exact diagonalization calculations of the magnetization of $CoNb_2O_6$

This appendix provides extra details about how the exact diagonalization predictions of the magnetization were calculated in Chapter **??**.

As discussed in Chapter 2, the expectation value of the spin component S^α per site at a temperature T can be calculated as

$$\langle \tilde{S}^\alpha \rangle = \frac{1}{Z} \sum_\lambda e^{-\frac{\Omega_\lambda}{k_B T}} \langle \lambda | \tilde{S}^\alpha | \lambda \rangle, \tag{B.1}$$

where λ labels eigenstates, Z is the partition function $Z = \sum_\lambda \exp\{[-\Omega_\lambda/(k_B T)]\}$, Ω_λ is the energy of state λ, and $\tilde{S}^\alpha$ is the α component of the spin operator in the energy eigenstate basis averaged over all the sites in the chain.

The crystallographic b direction coincides with the y direction for the spins, so the calculated magnetization is simply

$$M^b = g_y \mu_B \langle \tilde{S}^y \rangle. \tag{B.2}$$

For fields along a and c, the magnetization has more complex expressions as these crystallographic directions do not coincide with principal axes of the g-tensor. As discussed in Chapter **??**, the inelastic neutron scattering measurements with

field applied along a were only sensitive to the component of the magnetic moment projected along the a direction. For field along a, this is also what the magnetization measurements were sensitive to, so the g-factors could be parameterized according to (**??**) and (**??**). The Zeeman term in the Hamiltonian then becomes

$$\sum_j \mu_B \left(g_x \cos 30^\circ S_j^x + g_z \sin 30^\circ S_j^z \right) H^a. \tag{B.3}$$

The magnetization along the a direction was then calculated as

$$M^a = \mu_B \left(g_x \cos 30^\circ \langle \tilde{S}^x \rangle + g_z \sin 30^\circ \langle \tilde{S}^z \rangle \right). \tag{B.4}$$

For field along c, the full form of the magnetic moment according to (**??**) was used. Therefore, the Zeeman term in the Hamiltonian was expressed as

$$\sum_j \mu_B \left[\left(-g_{xx} \sin\gamma + g_{xz} \cos\gamma \right) S_j^x + \left(-g_{xz} \sin\gamma + g_{zz} \cos\gamma \right) S_j^z \right] H^c, \tag{B.5}$$

and the magnetization along c was calculated as

$$M^c = \mu_B \left[\left(-g_{xx} \sin\gamma + g_{xz} \cos\gamma \right) \langle \tilde{S}^x \rangle + \left(-g_{xz} \sin\gamma + g_{zz} \cos\gamma \right) \langle \tilde{S}^z \rangle \right]. \tag{B.6}$$

C

Linear spinwave theory in the field polarized phase for $Na_2BaCo(PO_4)_2$ including interlayer coupling effects

This appendix provides expressions for the dispersions and dynamical structure factor components in the field-polarized phase for the minimal exchange model for $Na_2BaCo(PO_4)_2$ including a minimal parameterization of the interlayer coupling effects.

As discussed in Chapter 8.4.1, the minimal Hamiltonian for $Na_2BaCo(PO_4)_2$ including interlayer couplings is

$$\begin{aligned}\mathcal{H} =& \frac{1}{2}\sum_{\boldsymbol{R}}\left[\sum_{\boldsymbol{\delta}_1}\left(J_{xy}\left(S^x_{\boldsymbol{R}}S^x_{\boldsymbol{R}+\boldsymbol{\delta}_1}+S^y_{\boldsymbol{R}}S^y_{\boldsymbol{R}+\boldsymbol{\delta}_1}\right)+J_z S^z_{\boldsymbol{R}}S^z_{\boldsymbol{R}+\boldsymbol{\delta}_1}\right)+\sum_{\boldsymbol{\delta}_2}J_a\boldsymbol{S}_{\boldsymbol{R}}\cdot\boldsymbol{S}_{\boldsymbol{R}+\boldsymbol{\delta}_2}\right] \\ &-\mu_B\sum_{\boldsymbol{R}}\left(g_c B_z S^z_{\boldsymbol{R}}+g_{ab}B_y S^y_{\boldsymbol{R}}\right), \end{aligned} \tag{C.1}$$

where $\boldsymbol{R}$ runs over the positions of magnetic sites, located at the vertices of a stacked triangular lattice and $\boldsymbol{\delta}_1$ runs over the vectors connecting sites to their nearest neighbours, that is, $\boldsymbol{\delta}_1 = \boldsymbol{a}, \boldsymbol{b}, \boldsymbol{a}+\boldsymbol{b}, -\boldsymbol{a}, -\boldsymbol{b}, -\boldsymbol{a}-\boldsymbol{b}$. The vector $\boldsymbol{\delta_2}$ connects sites to neighbours in adjacent layers, as indicated in Fig. 8.7B and runs over $\boldsymbol{a}+\boldsymbol{c}, \boldsymbol{b}+\boldsymbol{c}, -\boldsymbol{a}-\boldsymbol{b}+\boldsymbol{c}, -\boldsymbol{a}-\boldsymbol{c}, -\boldsymbol{b}-\boldsymbol{c}, \boldsymbol{a}+\boldsymbol{b}-\boldsymbol{c}$ in one of the twins of the $P\bar{3}$ crystal structure. Note that a macroscopic crystal sample is expected to contain almost equal amounts of two $P\bar{3}$ twins related by a mirror in the b^*c^* plane, or

equivalently a 2-fold rotation around the a-axis, and the effects of this twinning are included in the comparison with the data in Fig. 8.7.

In the field-polarized phase in high magnetic field applied in the plane (along the y direction), the magnon dispersion in linear spinwave theory is obtained as

$$\hbar\omega(\boldsymbol{Q}) = \sqrt{\mathcal{A}^2 - \mathcal{B}^2}, \tag{C.2}$$

$$\mathcal{A} = g_{ab}\mu_B B_y - 3J_{xy} + \frac{J_z + J_{xy}}{2}\gamma(\boldsymbol{Q}) + J_a(-3 + \gamma_a(\boldsymbol{Q})), \tag{C.3}$$

$$\mathcal{B} = \frac{J_z - J_{xy}}{2}\gamma(\boldsymbol{Q}), \tag{C.4}$$

where

$$\gamma_a(\boldsymbol{Q}) = \cos 2\pi(h+l) + \cos 2\pi(k+l) + \cos 2\pi(-h-k+l) \tag{C.5}$$

for an untwinned single crystal with the $P\bar{3}$ structure, and where $\gamma(\boldsymbol{Q})$ is given in (8.9). The non-zero components of the dynamical structure factor are then given by

$$S^{xx}(\boldsymbol{Q},\omega) = \frac{\mathcal{A}(\boldsymbol{Q}) + \mathcal{B}(\boldsymbol{Q})}{\hbar\omega(\boldsymbol{Q})}\delta(\hbar\omega - \hbar\omega(\boldsymbol{Q})), \tag{C.6}$$

$$S^{zz}(\boldsymbol{Q},\omega) = \frac{\mathcal{A}(\boldsymbol{Q}) - \mathcal{B}(\boldsymbol{Q})}{\hbar\omega(\boldsymbol{Q})}\delta(\hbar\omega - \hbar\omega(\boldsymbol{Q})). \tag{C.7}$$

The above expressions also apply for the mirrored $P\bar{3}$ twin by replacing $l \to -l$ in the expression for γ_a. These formulae are used in the calculations shown in Fig. 8.7C and D.

Bibliography

[1] S. Blundell, *Magnetism in condensed matter* (Oxford University Press, Oxford, 2001).

[2] U. Schollwöck, J. Richter, D. J. J. Farnell, and R. F. Bishop, eds., *Quantum Magnetism*, 1st ed., Lecture Notes in Physics (Springer Berlin Heidelberg, Berlin, Heidelberg, 2004).

[3] A. Abragam and B. Bleaney, *Electron paramagnetic resonance of transition ions* (Dover Publications, New York, 1986).

[4] M. Elliot, P. A. McClarty, D. Prabhakaran, R. D. Johnson, H. C. Walker, P. Manuel, and R. Coldea, Order-by-disorder from bond-dependent exchange and intensity signature of nodal quasiparticles in a honeycomb cobaltate, Nat. Commun. **12**, 3936 (2021).

[5] J. A. Ringler, A. I. Kolesnikov, and K. A. Ross, Single-ion properties of the transverse-field Ising model material $CoNb_2O_6$, Phys. Rev. B **105**, 224421 (2022).

[6] B. S. Mou, X. Zhang, L. Xiang, Y. Xu, R. Zhong, R. J. Cava, H. Zhou, Z. Jiang, D. Smirnov, N. Drichko, and S. M. Winter, Comparative Raman scattering study of crystal field excitations in Co-based quantum magnets, Phys. Rev. Mater. **8**, 084408 (2024).

[7] S. M. Winter, Magnetic couplings in edge-sharing high-spin d7 compounds, J. Phys.: Mater. **5**, 045003 (2022).

[8] P. W. Anderson, Theory of magnetic exchange interactions: Exchange in insulators and semiconductors (Academic Press, 1963) pp. 99–214.

[9] K. P. Sinha and N. Kumar, *Interactions in magnetically ordered solids* (Oxford University Press, Oxford, 1980).

[10] G. Jackeli and G. Khaliullin, Mott insulators in the strong spin-orbit coupling limit: From Heisenberg to a quantum compass and Kitaev models, Phys. Rev. Lett. **102**, 017205 (2009).

[11] S. Sachdev, *Quantum phase transitions*, 2nd ed. (Cambridge University Press, Cambridge, 2011).

[12] P. Coleman and A. J. Schofield, Quantum criticality, Nature **433**, 226 (2005).

[13] N. Goldenfeld, *Lectures On Phase Transitions And The Renormalization Group*, 1st ed., Frontiers in physics ; 85 (CRC Press, Boca Raton, 1992).

[14] J. Cardy, *Scaling and Renormalization in Statistical Physics*, Cambridge Lecture Notes in Physics (Cambridge University Press, Cambridge, 1996).

[15] N. D. Mermin and H. Wagner, Absence of ferromagnetism or antiferromagnetism in one- or two-dimensional isotropic Heisenberg models, Phys. Rev. Lett. **17**, 1133 (1966).

[16] L. Balents, Spin liquids in frustrated magnets, Nature **464**, 199 (2010).

[17] G. H. Wannier, Antiferromagnetism. the triangular Ising net, Phys. Rev. **79**, 357 (1950).

[18] P. Anderson, Resonating valence bonds: A new kind of insulator?, Mat. Res. Bull. **8**, 153 (1973).

[19] A. V. Chubukov and D. I. Golosov, Quantum theory of an antiferromagnet on a triangular lattice in a magnetic field, J. Phys.: Condens. Matter **3**, 69 (1991).

[20] B. Bernu, P. Lecheminant, C. Lhuillier, and L. Pierre, Exact spectra, spin susceptibilities, and order parameter of the quantum Heisenberg antiferromagnet on the triangular lattice, Phys. Rev. B **50**, 10048 (1994).

[21] A. Kitaev, Anyons in an exactly solved model and beyond, Ann. Phys. **321**, 2 (2006).

[22] W. Brzezicki, J. Dziarmaga, and A. M. Oleś, Quantum phase transition in the one-dimensional compass model, Phys. Rev. B **75**, 134415 (2007).

[23] Y.-D. Li, X. Wang, and G. Chen, Anisotropic spin model of strong spin-orbit-coupled triangular antiferromagnets, Phys. Rev. B **94**, 035107 (2016).

[24] Z. Zhou, C. Liu, Z. Yan, Y. Chen, and X.-F. Zhang, Quantum dynamics of topological strings in a frustrated Ising antiferromagnet, npj Quantum Mater. **7**, 60 (2022).

[25] R. Coldea, D. A. Tennant, E. M. Wheeler, E. Wawrzynska, D. Prabhakaran, M. Telling, K. Habicht, P. Smeibidl, and K. Kiefer, Quantum criticality in an Ising chain: Experimental evidence for emergent E8 symmetry, Science **327**, 177 (2010).

[26] R. B. Laughlin, Anomalous quantum Hall effect: An incompressible quantum fluid with fractionally charged excitations, Phys. Rev. Lett. **50**, 1395 (1983).

[27] H. Bethe, Zur Theorie der Metalle, Z. Physik **71**, 205 (1931).

[28] B. Lake, D. A. Tennant, J.-S. Caux, T. Barthel, U. Schollwöck, S. E. Nagler, and C. D. Frost, Multispinon continua at zero and finite temperature in a near-ideal Heisenberg chain, Phys. Rev. Lett. **111**, 137205 (2013).

[29] H. Jacobsen, S. M. Gaw, A. J. Princep, E. Hamilton, S. Tóth, R. A. Ewings, M. Enderle, E. M. H. Wheeler, D. Prabhakaran, and A. T. Boothroyd, Spin dynamics and exchange interactions in CuO measured by neutron scattering, Phys. Rev. B **97**, 144401 (2018).

[30] T. Fennell, P. P. Deen, A. R. Wildes, K. Schmalzl, D. Prabhakaran, A. T. Boothroyd, R. J. Aldus, D. F. McMorrow, and S. T. Bramwell, Magnetic Coulomb phase in the spin ice $Ho_2Ti_2O_7$, Science **326**, 415 (2009).

[31] C. Castelnovo, R. Moessner, and S. L. Sondhi, Spin ice, fractionalization, and topological order, Annu. Rev. Condens. Matter Phys. **3**, 35 (2012).

[32] R. Dusad, F. K. K. Kirschner, J. C. Hoke, B. R. Roberts, A. Eyal, F. Flicker, G. M. Luke, S. J. Blundell, and J. C. S. Davis, Magnetic monopole noise, Nature **571**, 234 (2019).

[33] L. Facheris, S. D. Nabi, A. Glezer Moshe, U. Nagel, T. Rõõm, K. Y. Povarov, J. R. Stewart, Z. Yan, and A. Zheludev, Confinement of fractional excitations in a triangular lattice antiferromagnet, Phys. Rev. Lett. **130**, 256702 (2023).

[34] Z. Zhu and S. R. White, Spin liquid phase of the $S = 1/2$ $J_1 - J_2$ Heisenberg model on the triangular lattice, Phys. Rev. B **92**, 041105 (2015).

[35] M. Hermanns, I. Kimchi, and J. Knolle, Physics of the Kitaev model: Fractionalization, dynamic correlations, and material connections, Annu. Rev. Condens. Matter Phys. **9**, 17 (2018).

[36] T. Giamarchi, *Quantum Physics in One Dimension* (Oxford University Press, 2003).

[37] P. Pfeuty, The one-dimensional Ising model with a transverse field, Ann. Phys. **57**, 79 (1970).

[38] E. Lieb, T. Schultz, and D. Mattis, Two soluble models of an antiferromagnetic chain, Ann. Phys. **16**, 407 (1961).

[39] S. T. Carr and A. M. Tsvelik, Spectrum and correlation functions of a quasi-one-dimensional quantum Ising model, Phys. Rev. Lett. **90**, 177206 (2003).

[40] H. C. Fogedby, The Ising chain in a skew magnetic field, J. Phys. C: Solid State Phys. **11**, 2801 (1978).

[41] B. M. McCoy and T. T. Wu, Two-dimensional Ising field theory in a magnetic field: Breakup of the cut in the two-point function, Phys. Rev. D **18**, 1259 (1978).

[42] A. B. Zamolodchikov, Integrals of motion and S matrix of the (scaled) T=T_c Ising model with magnetic field, Int. J. Mod. Phys. A **4**, 4235 (1989).

[43] K. Amelin, J. Engelmayer, J. Viirok, U. Nagel, T. Rõõm, T. Lorenz, and Z. Wang, Experimental observation of quantum many-body excitations of E8 symmetry in the Ising chain ferromagnet $CoNb_2O_6$, Phys. Rev. B **102**, 104431 (2020).

[44] R. Orbach, Linear antiferromagnetic chain with anisotropic coupling, Phys. Rev. **112**, 309 (1958).

[45] F. Franchini, *An Introduction to Integrable Techniques for One-Dimensional Quantum Systems*, Lecture Notes in Physics (Springer International Publishing, Cham, 2017).

[46] J. Stephenson, Ising-model spin correlations on the triangular lattice. III. Isotropic antiferromagnetic lattice, J. Math. Phys. **11**, 413 (1970).

[47] H. W. J. Blöte and M. P. Nightingale, Antiferromagnetic triangular Ising model: Critical behavior of the ground state, Phys. Rev. B **47**, 15046 (1993).

[48] M. Vojta, Frustration and quantum criticality, Rep. Prog. Phys. **81**, 064501 (2018).

[49] R. Moessner and S. L. Sondhi, Ising models of quantum frustration, Phys. Rev. B **63**, 224401 (2001).

[50] S. V. Isakov and R. Moessner, Interplay of quantum and thermal fluctuations in a frustrated magnet, Phys. Rev. B **68**, 104409 (2003).

[51] V. Kalmeyer and R. B. Laughlin, Equivalence of the resonating-valence-bond and fractional quantum Hall states, Phys. Rev. Lett. **59**, 2095 (1987).

[52] D. A. Huse and V. Elser, Simple variational wave functions for two-dimensional Heisenberg spin-½ antiferromagnets, Phys. Rev. Lett. **60**, 2531 (1988).

[53] T. Jolicoeur and J. C. Le Guillou, Spin-wave results for the triangular Heisenberg antiferromagnet, Phys. Rev. B **40**, 2727 (1989).

[54] R. Verresen, R. Moessner, and F. Pollmann, Avoided quasiparticle decay from strong quantum interactions, Nat. Phys. **15**, 750 (2019).

[55] D. Macdougal, S. Williams, D. Prabhakaran, R. I. Bewley, D. J. Voneshen, and R. Coldea, Avoided quasiparticle decay and enhanced excitation continuum in the spin-$\frac{1}{2}$ near-Heisenberg triangular antiferromagnet $Ba_3CoSb_2O_9$, Phys. Rev. B **102**, 064421 (2020).

[56] P. Fazekas and P. W. Anderson, On the ground state properties of the anisotropic triangular antiferromagnet, Philos. Mag. **30**, 423 (1974).

[57] B. Kleine, E. Müller-Hartmann, K. Frahm, and P. Fazekas, Spin-wave analysis of easy-axis quantum antiferromagnets on the triangular lattice, Z. Phys. B: Condens. Matter **87**, 103 (1992).

[58] J. Sheng, L. Wang, W. Jiang, H. Ge, N. Zhao, T. Li, M. Kofu, D. Yu, W. Zhu, J.-W. Mei, Z. Wang, and L. Wu, Continuum of spin excitations in an ordered magnet, arXiv:2402.07730 (2024).

[59] Y. Gao, C. Zhang, J. Xiang, D. Yu, X. Lu, P. Sun, W. Jin, G. Su, and W. Li, Double magnon-roton excitations in the triangular-lattice spin supersolid, Phys. Rev. B **110**, 214408 (2024).

[60] R. Chi, J. Hu, H.-J. Liao, and T. Xiang, Dynamical spectra of spin supersolid states in triangular antiferromagnets, arXiv:2404.14163 (2024).

[61] H. Jia, B. Ma, Z. D. Wang, and G. Chen, Quantum spin supersolid as a precursory Dirac spin liquid in a triangular lattice antiferromagnet, Phys. Rev. Res. **6**, 033031 (2024).

[62] S. Miyashita and H. Kawamura, Phase transitions of anisotropic Heisenberg antiferromagnets on the triangular lattice, J. Phys. Soc. Jpn. **54**, 3385 (1985).

[63] D. Yamamoto, G. Marmorini, M. Tabata, K. Sakakura, and I. Danshita, Magnetism driven by the interplay of fluctuations and frustration in the easy-axis triangular XXZ model with transverse fields, Phys. Rev. B **100**, 140410 (2019).

[64] Y. Gao, Y.-C. Fan, H. Li, F. Yang, X.-T. Zeng, X.-L. Sheng, R. Zhong, Y. Qi, Y. Wan, and W. Li, Spin supersolidity in nearly ideal easy-axis triangular quantum antiferromagnet $Na_2BaCo(PO_4)_2$, npj Quantum Mater. **7**, 89 (2022).

[65] S. Toth and B. Lake, Linear spin wave theory for single-Q incommensurate magnetic structures, J. Phys.: Condens. Matter **27**, 166002 (2015).

[66] T. Holstein and H. Primakoff, Field dependence of the intrinsic domain magnetization of a ferromagnet, Phys. Rev. **58**, 1098 (1940).

[67] C. Kittel and C. Y. Fong, *Quantum theory of solids*, 2nd ed. (Wiley, New York, 1987).

[68] R. M. White, M. Sparks, and I. Ortenburger, Diagonalization of the antiferromagnetic magnon-phonon interaction, Phys. Rev. **139**, A450 (1965).

[69] J. H. P. Colpa, Diagonalization of the quadratic boson Hamiltonian, Physica A **93**, 327 (1978).

[70] A. T. Boothroyd, *Principles of Neutron Scattering from Condensed Matter* (Oxford University Press, Oxford, 2020).

[71] M. Fava, R. Coldea, and S. A. Parameswaran, Glide symmetry breaking and Ising criticality in the quasi-1d magnet $CoNb_2O_6$, Proc. Natl. Acad. Sci. U.S.A. **117**, 25219 (2020).

[72] MATLAB version: 9.11.0 (R2021b) (2021).

[73] P. Weinberg and M. Bukov, QuSpin: a Python package for dynamics and exact diagonalisation of quantum many body systems part I: spin chains, SciPost Phys. **2**, 003 (2017).

[74] G. L. Squires, *Introduction to the theory of thermal neutron scattering*, 3rd ed. (Cambridge University Press, Cambridge, 2012).

[75] S. W. Lovesey, *Theory of neutron scattering from condensed matter*, Oxford Science Publications (Clarendon Press, Oxford, 1984).

[76] J. M. Carpenter and C.-K. Loong, *Elements of slow-neutron scattering : basics, techniques, and applications* (Cambridge University Press, Cambridge, 2015).

[77] G. E. Bacon, *Neutron diffraction*, 3rd ed., Monographs on the physics and chemistry of materials (Clarendon Press, Oxford, 1975).

[78] J. Binney and D. Skinner, *The Physics of Quantum Mechanics* (Oxford University Press, Oxford, 2014).

[79] T. Chatterji, ed., *Neutron scattering from magnetic materials* (Elsevier, Amsterdam, 2006).

[80] K. N. Trueblood, H.-B. Bürgi, H. Burzlaff, J. D. Dunitz, C. M. Gramaccioli, H. H. Schulz, U. Shmueli, and S. C. Abrahams, Atomic dispacement parameter nomenclature. Report of a subcommittee on atomic displacement parameter nomenclature, Acta Crystallogr., Sect. A: Found. Crystallogr. **52**, 770 (1996).

[81] O. Steinsvoll, G. Shirane, R. Nathans, M. Blume, H. A. Alperin, and S. J. Pickart, Magnetic form factor of terbium, Phys. Rev. **161**, 499 (1967).

[82] P. J. Brown, Form factors for 3d transition elements and their ions, `https://www.ill.eu/sites/ccsl/ffacts/ffactnode5.html` (2001).

[83] B. T. M. Willis and C. J. Carlile, *Experimental neutron scattering* (Oxford University Press, Oxford, 2008).

[84] R. I. Bewley, J. W. Taylor, and S. M. Bennington, LET, a cold neutron multi-disk chopper spectrometer at ISIS, Nucl. Instrum. Methods Phys. Res., Sect. A **637**, 128 (2011).

[85] L. C. Chapon, P. Manuel, P. G. Radaelli, C. Benson, L. Perrott, S. Ansell, N. J. Rhodes, D. Raspino, D. Duxbury, E. Spill, and J. Norris, WISH: The new powder and single crystal magnetic diffractometer on the second target station, Neutron News **22**, 22 (2011).

[86] R. I. Bewley, R. S. Eccleston, K. A. McEwen, S. M. Hayden, M. T. Dove, S. M. Bennington, J. R. Treadgold, and R. L. S. Coleman, MERLIN, a new high count rate spectrometer at ISIS, Physica B **385-386**, 1029 (2006).

[87] M. Russina and F. Mezei, First implementation of repetition rate multiplication in neutron spectroscopy, Nucl. Instrum. Methods Phys. Res., Sect. A **604**, 624 (2009).

[88] O. Arnold, J. C. Bilheux, J. M. Borreguero, A. Buts, S. I. Campbell, L. Chapon, M. Doucet, N. Draper, R. F. Leal, M. A. Gigg, V. E. Lynch, A. Markvardsen, D. J. Mikkelson, R. L. Mikkelson, R. Miller, K. Palmen, P. Parker, G. Passos, T. G. Perring, P. F. Peterson, S. Ren, M. A. Reuter, A. T. Savici, J. W. Taylor, R. J. Taylor, R. Tolchenov, W. Zhou, and J. Zikovsky, Mantid—data analysis and visualization package for neutron scattering and μsr experiments, Nucl. Instrum. Methods Phys. Res., Sect. A **764**, 156 (2014).

[89] R. Coldea, MSlice: Matlab visualization software for single crystal and powder time-of-flight neutron data, `http://mslice.isis.rl.ac.uk/Main_Page` (2000).

[90] R. A. Ewings, A. Buts, M. D. Le, J. van Duijn, I. Bustinduy, and T. G. Perring, Horace: Software for the analysis of data from single crystal spectroscopy experiments at time-of-flight neutron instruments, Nucl. Instrum. Methods Phys. Res., Sect. A **834**, 132 (2016).

[91] K. H. Andersen, D. Martín y Marero, and M. J. Barlow, The OSIRIS diffractometer and polarisation-analysis backscattering spectrometer, Appl. Phys. A **74**, s237 (2002).

[92] J. Rodríguez-Carvajal, Recent advances in magnetic structure determination by neutron powder diffraction, Physica B **192**, 55 (1993).

[93] V. Petříček, M. Dušek, and L. Palatinus, Crystallographic computing system JANA2006: General features, Z. Kristallogr. - Cryst. Mater. **229**, 345 (2014).

[94] *Physical Property Measurement System Vibrating Sample Magnetometer (VSM) Option User's Manual*, Quantum Design, 4th ed. (2008).

[95] A. Zieba and S. Foner, Detection coil, sensitivity function, and sample geometry effects for vibrating sample magnetometers, Rev. Sci. Instrum. **53**, 1344 (1982).

[96] K. MacFarquharson, *Magnetometry and Thermodynamic Studies of Anisotropic Honeycomb and Hyperhoneycomb Magnets*, Ph.D. thesis, University of Oxford (2023).

[97] B. Dodrill and J. R. Lindemuth, Vibrating sample magnetometry, in *Magnetic Measurement Techniques for Materials Characterization*, edited by V. Franco and B. Dodrill (Springer International Publishing, Cham, 2021) pp. 15–37.

[98] L. Woodland, D. Macdougal, I. M. Cabrera, J. D. Thompson, D. Prabhakaran, R. I. Bewley, and R. Coldea, Tuning the confinement potential between spinons in the Ising chain compound $CoNb_2O_6$ using longitudinal fields and quantitative determination of the microscopic Hamiltonian, Phys. Rev. B **108**, 184416 (2023).

[99] A. W. Kinross, M. Fu, T. J. Munsie, H. A. Dabkowska, G. M. Luke, S. Sachdev, and T. Imai, Evolution of quantum fluctuations near the quantum critical point of the transverse field Ising chain system $CoNb_2O_6$, Phys. Rev. X **4**, 031008 (2014).

[100] T. Liang, S. M. Koohpayeh, J. W. Krizan, T. M. McQueen, R. J. Cava, and N. P. Ong, Heat capacity peak at the quantum critical point of the transverse Ising magnet $CoNb_2O_6$, Nat. Commun. **6**, 7611 (2015).

[101] K. Amelin, J. Viirok, U. Nagel, T. Rõõm, J. Engelmayer, T. Dey, A. A. Nugroho, T. Lorenz, and Z. Wang, Quantum spin dynamics of quasi-one-dimensional Heisenberg-Ising magnets in a transverse field: confined spinons, E8 spectrum, and quantum phase transitions, J. Phys. A: Math. Theor. **55**, 484005 (2022).

[102] C. M. Morris, R. V. Aguilar, A. Ghosh, S. M. Koohpayeh, J. Krizan, R. J. Cava, O. Tchernyshyov, T. M. McQueen, and N. P. Armitage, Hierarchy of bound states in the one-dimensional ferromagnetic Ising chain $CoNb_2O_6$ investigated by high-resolution time-domain terahertz spectroscopy, Phys. Rev. Lett. **112**, 137403 (2014).

[103] T. Kunimoto, M. Sato, K. Nagasaka, and K. Kohn, Hybridized mode of phonon and spin-cluster excitation in quasi-one-dimensional magnet $CoNb_2O_6$, J. Phys. Soc. Jpn. **68**, 1404 (1999).

[104] S. Kobayashi, S. Mitsuda, M. Ishikawa, K. Miyatani, and K. Kohn, Three-dimensional magnetic ordering in the quasi-one-dimensional Ising magnet $CoNb_2O_6$ with partially released geometrical frustration, Phys. Rev. B **60**, 3331 (1999).

[105] H. Weitzel and S. Klein, Magnetische Struktur von Columbiten $MnTa_2O_6$ und $CoNb_2O_6$, Solid State Commun. **12**, 113 (1973).

[106] B. Wanklyn, B. Garrard, and G. Garton, Flux growth of crystals of MNb_2O_6 (M = Ni, Co, Mn, Fe), Mat. Res. Bull. **11**, 1497 (1976).

[107] I. Maartense, I. Yaeger, and B. M. Wanklyn, Field-induced magnetic transitions of $CoNb_2O_6$ in the ordered state, Solid State Commun. **21**, 93 (1977).

[108] W. Scharf, H. Weitzel, I. Yaeger, I. Maartense, and B. M. Wanklyn, Magnetic-structures of $CoNb_2O_6$, J. Magn. Magn. Mater. **13**, 121 (1979).

[109] T. Hanawa, M. Ishikawa, and K. Miyatani, Disappearance of ferromagnetism at low temperatures in $CoNb_2O_6$, J. Phys. Soc. Jpn. **61**, 4287 (1992).

[110] S. Mitsuda, K. Hosoya, T. Wada, H. Yoshizawa, T. Hanawa, M. Ishikawa, K. Miyatani, K. Saito, and K. Kohn, Magnetic ordering in one-dimensional system $CoNb_2O_6$ with competing interchain interactions, J. Phys. Soc. Jpn. **63**, 3568 (1994).

[111] T. Hanawa, K. Shinkawa, M. Ishikawa, K. Miyatani, K. Saito, and K. Kohn, Anisotropic specific heat of $CoNb_2O_6$ in magnetic fields, J. Phys. Soc. Jpn. **63**, 2706 (1994).

[112] S. Mitsuda, S. Kobayashi, K. Aga, H. Katagiri, H. Yoshizawa, I. Masayasu, K. Miyatani, and K. Kohn, Disappearance of 2d magnetic character in quasi-1d system $CoNb_2O_6$ under magnetic field, J. Phys. Soc. Jpn. **64**, 2325 (1995).

[113] S. Kobayashi, S. Mitsuda, K. Hosoya, H. Yoshizawa, T. Hanawa, M. Ishikawa, K. Miyatani, K. Saito, and K. Kohn, Competition between the inter-chain interaction and single-ion anisotropy in $CoNb_2O_6$, Physica B **213**, 176 (1995).

[114] C. Heid, H. Weitzel, P. Burlet, M. Bonnet, W. Gonschorek, T. Vogt, J. Norwig, and H. Fuess, Magnetic phase-diagram of $CoNb_2O_6$ - a neutron-diffraction study, J. Magn. Magn. Mater. **151**, 123 (1995).

[115] C. Heid, H. Weitzel, P. Burlet, M. Winkelmann, H. Ehrenberg, and H. Fuess, Magnetic phase diagrams of $CoNb_2O_6$, Physica B **234-236**, 574 (1997).

[116] H. Weitzel, H. Ehrenberg, C. Heid, H. Fuess, and P. Burlet, Lifshitz point in the three-dimensional magnetic phase diagram of $CoNb_2O_6$, Phys. Rev. B **62**, 12146 (2000).

[117] S. Kobayashi, S. Mitsuda, and K. Prokes, Low-temperature magnetic phase transitions of the geometrically frustrated isosceles triangular Ising antiferromagnet $CoNb_2O_6$, Phys. Rev. B **63**, 024415 (2001).

[118] S. Lee, R. K. Kaul, and L. Balents, Interplay of quantum criticality and geometric frustration in columbite, Nat. Phys. **6**, 702 (2010).

[119] T. Kunimoto, K. Nagasaka, H. Nojiri, S. Luther, M. Motokawa, H. Ohta, T. Goto, S. Okubo, and K. Kohn, Submillimeter wave ESR study of magnetic excitations in the Ising ferromagnetic chain $CoNb_2O_6$, J. Phys. Soc. Jpn. **68**, 1703 (1999).

[120] R. C. Pullar, The synthesis, properties, and applications of columbite niobates ($M^{2+}Nb_2O_6$): A critical review, J. Am. Ceram. Soc. **92**, 563 (2009).

[121] C. Balamurugan, A. R. Maheswari, and D.-W. Lee, Structural, optical, and selective ethanol sensing properties of p-type semiconducting $CoNb_2O_6$ nanopowder, Sens. Actuators, B **205**, 289 (2014).

[122] Y. De Luna, S. Ma, G. Li, and N. Bensalah, Highly stable free-standing cobalt niobate with orthorhombic structure as anode material for Li-ion batteries, ChemElectroChem **11**, e202300627 (2024).

[123] E. M. Wheeler, *Neutron scattering from low-dimensional quantum magnets*, Ph.D. thesis, University of Oxford (2007).

[124] A. Hauspurg, K. Matsuura, T. Arima, S. Zherlitsyn, and J. Wosnitza, Quantum critical fluctuations in a transverse-field Ising magnet, J. Phys.: Condens. Matter **36**, 325801 (2024).

[125] C. M. Morris, N. Desai, J. Viirok, D. Hüvonen, U. Nagel, T. Rõõm, J. W. Krizan, R. J. Cava, T. M. McQueen, S. M. Koohpayeh, R. K. Kaul, and N. P. Armitage, Duality and domain wall dynamics in a twisted Kitaev chain, Nat. Phys. **17**, 832 (2021).

[126] A. A. Konieczna, D. A. S. Kaib, S. M. Winter, and R. Valentí, Understanding the microscopic origin of the magnetic interactions in $CoNb_2O_6$, arXiv:2406.17854 (2024).

[127] D. Churchill and H.-Y. Kee, Transforming from Kitaev to disguised Ising chain: Application to $CoNb_2O_6$, Phys. Rev. Lett. **133**, 056703 (2024).

[128] E. Husson, Y. Repelin, Q. Dao, and H. Brusset, Characterization of different bondings in some divalent metal niobates of columbite structure, Mat. Res. Bull. **12**, 1199 (1977).

[129] K. Momma and F. Izumi, *VESTA3* for three-dimensional visualization of crystal, volumetric and morphology data, J. Appl. Crystallogr. **44**, 1272 (2011).

[130] J. B. Torrance and M. Tinkham, Excitation of multiple-magnon bound states in $CoCl_2 \cdot 2H_2O$, Phys. Rev. **187**, 595 (1969).

[131] U. B. Hansen, O. F. Syljuåsen, J. Jensen, T. K. Schäffer, C. R. Andersen, M. Boehm, J. A. Rodriguez-Rivera, N. B. Christensen, and K. Lefmann, Magnetic bloch oscillations and domain wall dynamics in a near-Ising ferromagnetic chain, Nat. Commun. **13**, 2547 (2022).

[132] D. Prabhakaran, F. R. Wondre, and A. T. Boothroyd, Preparation of large single crystals of ANb_2O_6 (A = Ni, Co, Fe, Mn) by the floating-zone method, J. Cryst. Growth **250**, 72 (2003).

[133] S. B. Rutkevich, Energy spectrum of bound-spinons in the quantum Ising spin-chain ferromagnet, J. Stat. Phys. **131**, 917 (2008).

[134] I. Cabrera, J. D. Thompson, R. Coldea, D. Prabhakaran, R. I. Bewley, T. Guidi, J. A. Rodriguez-Rivera, and C. Stock, Excitations in the quantum paramagnetic phase of the quasi-one-dimensional Ising magnet $CoNb_2O_6$ in a transverse field: Geometric frustration and quantum renormalization effects, Phys. Rev. B **90**, 014418 (2014).

[135] S. Kobayashi, S. Mitsuda, S. Hosaka, H. Tamatsukuri, T. Nakajima, H. Koorikawa, K. Prokeš, and K. Kiefer, Neutron diffraction study of low-temperature magnetic phase diagram of an isosceles-triangular-lattice Ising antiferromagnet $CoNb_2O_6$, Phys. Rev. B **94**, 134427 (2016).

[136] S. B. Rutkevich, On the weak confinement of kinks in the one-dimensional quantum ferromagnet $CoNb_2O_6$, J. Stat. Mech: Theory Exp. **2010**, P07015 (2010).

[137] J. A. Kjäll, F. Pollmann, and J. E. Moore, Bound states and E8 symmetry effects in perturbed quantum Ising chains, Phys. Rev. B **83**, 020407 (2011).

[138] N. J. Robinson, F. H. L. Essler, I. Cabrera, and R. Coldea, Quasiparticle breakdown in the quasi-one-dimensional Ising ferromagnet $CoNb_2O_6$, Phys. Rev. B **90**, 174406 (2014).

[139] C. A. Gallegos and A. L. Chernyshev, Magnon interactions in the quantum paramagnetic phase of $CoNb_2O_6$, Phys. Rev. B **109**, 014424 (2024).

[140] L. Woodland, I. Lovas, M. Telling, D. Prabhakaran, L. Balents, and R. Coldea, Excitations of quantum Ising chain $CoNb_2O_6$ in low transverse field: Quantitative description of bound states stabilized by off-diagonal exchange and applied field, Phys. Rev. B **108**, 184417 (2023).

[141] J. H. Robertson, R. Senese, and F. H. L. Essler, A simple theory for quantum quenches in the ANNNI model, SciPost Phys. **15**, 032 (2023).

[142] M. Nandi, D. Prabhakaran, and P. Mandal, Spin-charge-lattice coupling in quasi-one-dimensional Ising spin chain $CoNb_2O_6$, J. Phys.: Condens. Matter **31**, 195802 (2019).

[143] F. Museur, Development of software to align crystals in a Laue diffractometer (2017).

[144] D.-X. Chen, E. Pardo, and A. Sanchez, Demagnetizing factors of rectangular prisms and ellipsoids, IEEE Trans. Magn. **38**, 1742 (2002).

[145] P. Calabrese, F. H. L. Essler, and M. Fagotti, Quantum quench in the transverse field Ising chain: I. time evolution of order parameter correlators, J. Stat. Mech: Theory Exp. **2012**, P07016 (2012).

[146] L. Zhu, M. Garst, A. Rosch, and Q. Si, Universally diverging Grüneisen parameter and the magnetocaloric effect close to quantum critical points, Phys. Rev. Lett. **91**, 066404 (2003).

[147] A. Zheludev, Quantum critical dynamics and scaling in one-dimensional antiferromagnets, J. Exp. Theor. Phys. **131**, 34 (2020).

[148] M. Garst and A. Rosch, Sign change of the Grüneisen parameter and magnetocaloric effect near quantum critical points, Phys. Rev. B **72**, 205129 (2005).

[149] S. Thota, S. Ghosh, R. Maruthi, D. C. Joshi, R. Medwal, R. S. Rawat, and M. S. Seehra, Magnetic ground state and exchange interactions in the Ising chain ferromagnet $CoNb_2O_6$, Phys. Rev. B **103**, 064415 (2021).

[150] D.-X. Chen, J. A. Brug, and R. B. Goldfarb, Demagnetizing factors for cylinders, IEEE Trans. Magn. **27**, 3601 (1991).

[151] J. D. Thompson, P. A. McClarty, D. Prabhakaran, I. Cabrera, T. Guidi, and R. Coldea, Quasiparticle breakdown and spin Hamiltonian of the frustrated quantum pyrochlore $Yb_2Ti_2O_7$ in a magnetic field, Phys. Rev. Lett. **119**, 057203 (2017).

[152] R. R. P. Singh and D. A. Huse, Three-sublattice order in triangular- and kagomé-lattice spin-half antiferromagnets, Phys. Rev. Lett. **68**, 1766 (1992).

[153] L. Capriotti, A. E. Trumper, and S. Sorella, Long-range Néel order in the triangular Heisenberg model, Phys. Rev. Lett. **82**, 3899 (1999).

[154] M. Ulaga, J. Kokalj, A. Wietek, A. Zorko, and P. Prelovšek, Finite-temperature properties of the easy-axis Heisenberg model on frustrated lattices, Phys. Rev. B **109**, 035110 (2024).

[155] Y. Xu, J. Hasik, B. Ponsioen, and A. H. Nevidomskyy, Simulating spin dynamics of supersolid states in a quantum Ising magnet, Phys. Rev. B **111**, L060402 (2025).

[156] N. Li, Q. Huang, X. Y. Yue, W. J. Chu, Q. Chen, E. S. Choi, X. Zhao, H. D. Zhou, and X. F. Sun, Possible itinerant excitations and quantum spin state transitions in the effective spin-1/2 triangular-lattice antiferromagnet $Na_2BaCo(PO_4)_2$, Nat. Commun. **11**, 4216 (2020).

[157] J. Sheng, L. Wang, A. Candini, W. Jiang, L. Huang, B. Xi, J. Zhao, H. Ge, N. Zhao, Y. Fu, J. Ren, J. Yang, P. Miao, X. Tong, D. Yu, S. Wang, Q. Liu, M. Kofu, R. Mole, G. Biasiol, D. Yu, I. A. Zaliznyak, J.-W. Mei, and L. Wu, Two-dimensional quantum universality in the spin-1/2 triangular-lattice quantum antiferromagnet $Na_2BaCo(PO_4)_2$, Proc. Natl. Acad. Sci U.S.A. **119**, e2211193119 (2022).

[158] R. Zhong, S. Guo, G. Xu, Z. Xu, and R. J. Cava, Strong quantum fluctuations in a quantum spin liquid candidate with a Co-based triangular lattice, Proc. Natl. Acad. Sci. U.S.A. **116**, 14505 (2019).

[159] M. Zhu, V. Romerio, N. Steiger, S. D. Nabi, N. Murai, S. Ohira-Kawamura, K. Y. Povarov, Y. Skourski, R. Sibille, L. Keller, Z. Yan, S. Gvasaliya, and A. Zheludev, Continuum excitations in a spin supersolid on a triangular lattice, Phys. Rev. Lett. **133**, 186704 (2024).

[160] T. Chen, A. Ghasemi, J. Zhang, L. Shi, Z. Tagay, L. Chen, E.-S. Choi, M. Jaime, M. Lee, Y. Hao, H. Cao, B. Winn, R. Zhong, X. Xu, N. P. Armitage, R. Cava, and C. Broholm, Phase diagram and spectroscopic evidence of supersolids in quantum Ising magnet $K_2Co(SeO_3)_2$ (2024), arXiv:2402.15869 .

[161] R. Coldea, D. A. Tennant, K. Habicht, P. Smeibidl, C. Wolters, and Z. Tylczynski, Direct measurement of the spin Hamiltonian and observation of condensation of magnons in the 2d frustrated quantum magnet Cs_2CuCl_4, Phys. Rev. Lett. **88**, 137203 (2002).

[162] Y. Y. Huang, D. Z. Dai, C. C. Zhao, J. M. Ni, L. S. Wang, B. L. Pan, B. Gao, P. Dai, and S. Y. Li, Thermal conductivity of triangular-lattice antiferromagnet $Na_2BaCo(PO_4)_2$: Absence of itinerant fermionic excitations, arXiv:2206.08866 (2022).

[163] X.-Y. Liu, Y. Gao, H. Li, W. Jin, J. Xiang, H. Jin, Z. Chen, W. Li, and G. Su, Quantum spin liquid candidate as superior refrigerant in cascade demagnetization cooling, Commun. Phys. **5**, 233 (2022).

[164] S. Lee, C. H. Lee, A. Berlie, A. D. Hillier, D. T. Adroja, R. Zhong, R. J. Cava, Z. H. Jang, and K.-Y. Choi, Temporal and field evolution of spin excitations in the disorder-free triangular antiferromagnet $Na_2BaCo(PO_4)_2$, Phys. Rev. B **103**, 024413 (2021).

[165] A. L. Chernyshev and M. E. Zhitomirsky, Spin waves in a triangular lattice antiferromagnet: Decays, spectrum renormalization, and singularities, Phys. Rev. B **79**, 144416 (2009).

[166] Y. Kajita, T. Nagai, S. Yamagishi, K. Kimura, M. Hagihala, and T. Kimura, Ferroaxial transitions in glaserite-type $Na_2BaM(PO_4)_2$ (M = Mg, Mn, Co, and Ni), Chem. Mater. 10.1021/acs.chemmater.4c01406 (2024).

[167] A. J. Hearmon, F. Fabrizi, L. C. Chapon, R. D. Johnson, D. Prabhakaran, S. V. Streltsov, P. J. Brown, and P. G. Radaelli, Electric field control of the magnetic chiralities in ferroaxial multiferroic $RbFe(MoO_4)_2$, Phys. Rev. Lett. **108**, 237201 (2012).

[168] A. Rohatgi, Webplotdigitizer: Version 4.2 (2019).

[169] C. Wellm, W. Roscher, J. Zeisner, A. Alfonsov, R. Zhong, R. J. Cava, A. Savoyant, R. Hayn, J. van den Brink, B. Büchner, O. Janson, and V. Kataev, Frustration enhanced by Kitaev exchange in a j=1/2 triangular antiferromagnet, Phys. Rev. B **104**, L100420 (2021).

[170] A. Tsirlin, Frustration and randomness in spin-1/2 triangular antiferromagnets (2024), paper presented at the International Conference on Magnetism, Bologna.

[171] R. Coldea, D. A. Tennant, and Z. Tylczynski, Extended scattering continua characteristic of spin fractionalization in the two-dimensional frustrated quantum magnet Cs_2CuCl_4 observed by neutron scattering, Phys. Rev. B **68**, 134424 (2003).

[172] J. Lorenzana, G. Seibold, and R. Coldea, Sum rules and missing spectral weight in magnetic neutron scattering in the cuprates, Phys. Rev. B **72**, 224511 (2005).

[173] C. Griset, S. Head, J. Alicea, and O. A. Starykh, Deformed triangular lattice antiferromagnets in a magnetic field: Role of spatial anisotropy and dzyaloshinskii-moriya interactions, Phys. Rev. B **84**, 245108 (2011).

[174] M. E. Zhitomirsky and A. L. Chernyshev, Colloquium: Spontaneous magnon decays, Rev. Mod. Phys. **85**, 219 (2013).

[175] N. Xi, Y. Gao, C. Li, S. Liang, R. Yu, X. Wang, and W. Li, Thermal tensor network approach for spin-lattice relaxation in quantum magnets, arXiv:2403.11895 (2024).

[176] S. Birnkammer, J. Knolle, and M. Knap, Signatures of domain-wall confinement in Raman spectroscopy of Ising spin chains, Phys. Rev. B **110**, 134408 (2024).

[177] G. Sim, J. Knolle, and F. Pollmann, Nonlinear spectroscopy of bound states in perturbed Ising spin chains, Phys. Rev. B **107**, L100404 (2023).

[178] P. Laurell, G. Alvarez, and E. Dagotto, Spin dynamics of the generalized quantum spin compass chain, Phys. Rev. B **107**, 104414 (2023).

[179] G. Sim, F. Pollmann, and J. Knolle, Microscopic details of two-dimensional spectroscopy of one-dimensional quantum Ising magnets, Phys. Rev. B **108**, 134423 (2023).